

University of Groningen

Finite-Volume Filtering in Large-Eddy Simulations Using a Minimum-Dissipation Model

Verstappen, Roel

Published in:

Notes on Numerical Fluid Mechanics and Multidisciplinary Design

DOI:

[10.1007/978-3-030-65820-5_8](https://doi.org/10.1007/978-3-030-65820-5_8)

IMPORTANT NOTE: You are advised to consult the publisher's version (publisher's PDF) if you wish to cite from it. Please check the document version below.

Document Version

Publisher's PDF, also known as Version of record

Publication date:

2021

[Link to publication in University of Groningen/UMCG research database](#)

Citation for published version (APA):

Verstappen, R. (2021). Finite-Volume Filtering in Large-Eddy Simulations Using a Minimum-Dissipation Model. In *Notes on Numerical Fluid Mechanics and Multidisciplinary Design* (pp. 91-100). (Notes on Numerical Fluid Mechanics and Multidisciplinary Design; Vol. 149). Springer. https://doi.org/10.1007/978-3-030-65820-5_8

Copyright

Other than for strictly personal use, it is not permitted to download or to forward/distribute the text or part of it without the consent of the author(s) and/or copyright holder(s), unless the work is under an open content license (like Creative Commons).

The publication may also be distributed here under the terms of Article 25fa of the Dutch Copyright Act, indicated by the "Taverne" license. More information can be found on the University of Groningen website: <https://www.rug.nl/library/open-access/self-archiving-pure/taverne-amendment>.

Take-down policy

If you believe that this document breaches copyright please contact us providing details, and we will remove access to the work immediately and investigate your claim.

Downloaded from the University of Groningen/UMCG research database (Pure): <http://www.rug.nl/research/portal>. For technical reasons the number of authors shown on this cover page is limited to 10 maximum.

Notes on Numerical Fluid Mechanics
and Multidisciplinary Design 149

Michel Deville · Christophe Calvin ·
Vincent Couaillier ·
Marta De La Llave Plata ·
Jean-Luc Estivalèzes · Thiên Hiệp Lê ·
Stéphane Vincent *Editors*

Turbulence and Interactions

Proceedings of the TI 2018 Conference,
June 25–29, 2018, Les Trois-Îlets,
Martinique, France

 Springer

Notes on Numerical Fluid Mechanics and Multidisciplinary Design

Volume 149

Founding Editor

Ernst Heinrich Hirschel, Zorneding, Germany

Series Editor

Wolfgang Schröder, Aerodynamisches Institut, RWTH Aachen, Aachen, Germany

Editorial Board Members

Bendiks Jan Boersma, Delft University of Technology, Delft, The Netherlands

Kozo Fujii, Institute of Space & Astronautical Science (ISAS), Sagamihara,
Kanagawa, Japan

Werner Haase, Hohenbrunn, Germany

Michael A. Leschziner, Department of Aeronautics, Imperial College, London, UK

Jacques Periaux, Paris, France

Sergio Pirozzoli, Department of Mechanical and Aerospace Engineering,
University of Rome 'La Sapienza', Roma, Italy

Arthur Rizzi, Department of Aeronautics, KTH Royal Institute of Technology,
Stockholm, Sweden

Bernard Roux, Ecole Supérieure d'Ingénieurs de Marseille, Marseille CX 20,
France

Yurii I. Shokin, Siberian Branch of the Russian Academy of Sciences, Novosibirsk,
Russia

Managing Editor

Esther Mäteling, RWTH Aachen University, Aachen, Germany

Notes on Numerical Fluid Mechanics and Multidisciplinary Design publishes state-of-art methods (including high performance methods) for numerical fluid mechanics, numerical simulation and multidisciplinary design optimization. The series includes proceedings of specialized conferences and workshops, as well as relevant project reports and monographs.

More information about this series at <http://www.springer.com/series/4629>

Michel Deville · Christophe Calvin ·
Vincent Couaillier · Marta De La Llave Plata ·
Jean-Luc Estivalèzes · Thiên Hiệp Lê ·
Stéphane Vincent
Editors

Turbulence and Interactions

Proceedings of the TI 2018 Conference,
June 25–29, 2018, Les Trois-Îlets,
Martinique, France

Editors

Michel Deville
EPFL-STI-DO
Lausanne, Vaud, Switzerland

Christophe Calvin
FR-91191 Gif-sur-Yvette cedex
CEA/DRF, CEA/Paris-Saclay
Sainte-Geneviève-des-Bois, France

Vincent Couaillier
Centre de Châtillon
ONERA - The French Aerospace Lab
Châtillon, France

Marta De La Llave Plata
ONERA Toulouse
Toulouse Cedex, France

Jean-Luc Estivalèzes
ONERA Toulouse
Toulouse Cedex 4, France

Thiên Hiệp Lê
ONERA Châtillon
Châtillon Cedex, France

Stéphane Vincent
MSME Laboratory
University of Paris-Est
Champs-sur-Marne, France

ISSN 1612-2909 ISSN 1860-0824 (electronic)
Notes on Numerical Fluid Mechanics and Multidisciplinary Design
ISBN 978-3-030-65819-9 ISBN 978-3-030-65820-5 (eBook)
<https://doi.org/10.1007/978-3-030-65820-5>

© Springer Nature Switzerland AG 2021

This work is subject to copyright. All rights are reserved by the Publisher, whether the whole or part of the material is concerned, specifically the rights of translation, reprinting, reuse of illustrations, recitation, broadcasting, reproduction on microfilms or in any other physical way, and transmission or information storage and retrieval, electronic adaptation, computer software, or by similar or dissimilar methodology now known or hereafter developed.

The use of general descriptive names, registered names, trademarks, service marks, etc. in this publication does not imply, even in the absence of a specific statement, that such names are exempt from the relevant protective laws and regulations and therefore free for general use.

The publisher, the authors and the editors are safe to assume that the advice and information in this book are believed to be true and accurate at the date of publication. Neither the publisher nor the authors or the editors give a warranty, expressed or implied, with respect to the material contained herein or for any errors or omissions that may have been made. The publisher remains neutral with regard to jurisdictional claims in published maps and institutional affiliations.

This Springer imprint is published by the registered company Springer Nature Switzerland AG
The registered company address is: Gewerbestrasse 11, 6330 Cham, Switzerland

Contents

Keynote Lectures

Fluid-Structure Interactions in Discrete Mechanics	3
Jean-Paul Caltagirone and Philippe Angot	
HPC and Data: When Two Becomes One	14
Christophe Calvin and France Boillod-Cerneux	
LES of the Flow Past a Circular Cylinder Using a Multiscale Discontinuous Galerkin Method	26
Marta de la Llave Plata, Fabio Naddei, and Vincent Couaillier	
A Volume-of-Fluid Dual-Scale Approach for Simulating Turbulent Liquid/Gas Interactions	39
Dominic Kedelty, James Uglietta, and Marcus Herrmann	
Influence of Particle Anisotropy and Motility on Preferential Concentration in Turbulence	52
Cristian Marchioli, Harshit Bhatia, and Diego Dotto	
Reference Solutions and URANS Model Characterization for Turbulent Forced Convection Around Heated Square Cylinders	66
Xavier Nicolas, Hua Sun, and Yannick Sommerer	
A Convergence Study of the One-Fluid Formulation in a Phase Inversion Application at Moderate Reynolds and Weber Numbers	80
Taraneh Sayadi, Stéphane Zaleski, Stéphane Popinet, Vincent Le Chenadec, and Stéphane Vincent	
Finite-Volume Filtering in Large-Eddy Simulations Using a Minimum-Dissipation Model	91
Roel Verstappen	

Contributed Papers

Simulation of a Particulate Flow in 3D Using Volume Penalization Methods	103
Philippe Angot, Léa Batteux, Jacques Laminie, and Pascal Poullet	
Simulation of a Confined Turbulent Round Jet at Moderate Reynolds Number	110
Georges Halim Atallah, Emmanuel Belut, Sullivan Lechêne, Benoît Trouette, and Stéphane Vincent	
Effect of Very-Large-Scale Motions on One- and Two-Point Statistics in Turbulent Pipe Flow Investigated by Direct Numerical Simulations	117
Christian Bauer and Claus Wagner	
Large Eddy Simulation of Turbulent Heat Transfer in Pipe Flows of Temperature Dependent Power-Law Fluids	123
Paulin Sourou Ganmbode, Meryem Ould-Rouiss, Xavier Nicolas, and Paolo Orlandi	
The Flow Around a Surface Combatant at 10° Static Drift: Assessment of Turbulence Models	130
Emmanuel Guilmineau, Michel Visonneau, and Ginevra Rubino	
Experiments and Large Eddy Simulations on Particle Interaction with a Turbulent Air Jet Impacting a Wall	136
Syphax Ikardouchene, Xavier Nicolas, Stéphane Delaby, and Meryem Ould-Rouiss	
A Review of Geometrical Interface Properties for 3D Front-Tracking Methods	144
Désir-André Koffi Bi, Mathilde Tavares, Éric Chénier, and Stéphane Vincent	
Soft-Sphere DEM Simulation of Coarse Particles Transported by a Fully Developed Turbulent Gas Vertical Channel Flow	150
Ainur Nigmatova, Yann Dufresne, Enrica Masi, Vincent Moureau, and Olivier Simonin	
Rod-Bundle Thermalhydraulics Mixing Phenomena: 3D Analysis with CATHARE-3 of ROSA-2/LSTF Experiment	161
Raphaël Préa and Anouar Mekkas	
Sensitivity of Approximate Deconvolution Model Parameters in a <i>Posteriori</i> LES of Interfacial Turbulence	169
Mahdi Saeedipour, Stéphane Vincent, and Stefan Pirker	

Time-Resolved High-Density Particle Tracking Velocimetry of Turbulent Rayleigh-Bénard Convection in a Cubic Sample 176
 Daniel Schiepel, Sebastian Herzog, and Claus Wagner

Sub-grid Deconvolution Approach for Filtered Two-Fluid Models and the Application to Fluidized Gas-Particle Suspensions 183
 Simon Schneiderbauer and Mahdi Saeedipour

A Front-Tracking Method for Multiphase Flows with a Sharp Interface Representation 189
 Mathilde Tavares, Désir-André Koffi Bi, Eric Chénier, and Stéphane Vincent

Bayesian Estimation of Turbulent Flow Intermittency 196
 Adaté Tossa, Didier Bernard, and Richard Emilion

Lagrangian Scheme for Scalar Advection-Diffusion. Application to Pollutant Transport 202
 Benoît Trouette, Georges Halim Atallah, and Stéphane Vincent

Spreading Time of Liquid Droplets Impacting on Non-wetting Solid Surfaces 208
 Yang Xu, Stéphane Vincent, Q.-C. He, and H. Le-Quang

Author Index 217

Keynote Lectures



Fluid-Structure Interactions in Discrete Mechanics

Jean-Paul Caltagirone¹ and Philippe Angot²(✉)

¹ Institut Ingénierie Mécanique de Bordeaux, Dept. TREFLE, CNRS UMR5295, Université de Bordeaux, 16 Avenue Pey-Berland, 33607 Pessac Cedex, France
calta@ipb.fr

² Institut de Mathématiques de Marseille, CNRS UMR7373, Aix-Marseille Université, Centrale Marseille, 13453 Marseille Cedex, France
philippe.angot@univ-amu.fr

Abstract. The primary objective of discrete mechanics is to unify various laws from different areas of physics, such as fluid mechanics and solid mechanics. The same objective was also pursued by continuum mechanics, but the latter has not been entirely successful in accomplishing it. The Galilean invariance and the principle of equivalence make it possible to rewrite the law of dynamics as an equality between accelerations, the one undergone by the medium and the external accelerations applied to it. The derivation of the equation of discrete motion leads to writing the acceleration as a Hodge-Helmholtz decomposition, *i.e.* the sum of a gradient of a scalar potential and the rotational of a vector potential. By choosing the acceleration as being a primary variable, we can express the velocity and the displacement simply as quantities that accumulate over time. Potentials represent energies per unit mass and are also stored over time. The resulting formulation is able to describe the motion and dynamics of complex media, that can be both fluid and solid, under large deformations and large displacements. Two examples of fluid-structure coupling, an analytical solution and a numerical solution used for a benchmark, are presented here. They show the ability of the model to reproduce the behavior of interacting fluid and solid media.

1 Introduction

The continuum mechanics is supposed to unify the mechanics of both solid and fluids. Most of the numerous differences between these two mechanical modelings result in the fact that the equation of motion is not the same for them, for example the Navier-Stokes equation are formulated in terms of velocity in fluids whereas the Navier-Lamé equation are expressed in displacement in solids. Multiple differences between the two domains, fluid and solid, are related to one of the principal cause, the annexation of the conservation of mass to the Navier-Stokes equations. In fact, the initial decoupling between velocity and pressure requires the use of the law of mass conservation whatever the chosen coupling way between pressure and velocity. In fact, number of difficulties make this unification impossible in the concept of continuous medium [5].

Discrete mechanics differs in particular in that it does not require the use of tensors: the notion of vector itself is associated with a constant scalar on an oriented edge. The

concept of tensor introduced in the 18th century has made it possible to synthesize the normal and tangential stresses within the same operator applied to second-order tensors; if it is necessary for the Navier-Stokes equation to express the local deformation rate according to variable properties, it proves useless for the Navier-Lamé equation in rotational formulation. This is an original confusion between the tensor properties of anisotropic media and the formulation of the equation of motion. Although it is possible to use the tensorial form, it is not strictly necessary.

Multiple difficulties and artifacts still enameled the conservation laws for fluid and solid media. In fluids, the hypothesis of Stokes that $3\lambda + 2\mu = 0$ is wrong [8, 11]. Even putting aside the Stokes hypothesis, the continuum mechanics consider for an isotropic medium that the tensor of elasticity of the fourth order \mathbf{C} is reduced to the two Lamé coefficients, these are conditioned by the Clausius-Duhem $3\lambda + 2\mu \geq 0$ inequality that can potentially define a negative viscosity. In solids, the use of tensors leads to the writing of compatibility conditions to link constraints to displacements.

The discrete mechanics [5] proceeds from another vision, relying on the fact that vector quantities are assigned to a finite-length bipoint saving the direction in any homothetic reduction. A vector, velocity for example, will be a constant scalar attached to this oriented segment. The derivation of the equation of discrete motion is initiated from two principles emitted by Galileo, the relativity of motion and the principle of equivalence between masses associated with gravity and inertia. The fundamental law of the dynamics established in terms of forces by I. Newton then becomes an equality between accelerations, namely the acceleration undergone by a medium is the sum of the accelerations applied to it. This conservation law of the acceleration leads to express conservation equations in terms of velocities for the fluids but also for the solids. The principle of constraint accumulation makes it possible to derive accelerations relative to inertia, diffusion, dissipation and all the other forces per unit of mass which contribute to modify movement, gravitation, capillary effects, etc.

The equation of discrete motion is representative of all phenomena observed in fluid flows, solids with complex constitutive laws representative of large displacements and large deformations as well as the propagation of linear waves or shock waves. In classical cases with constant material properties, it allows to recover all the solutions obtained previously with the Navier-Stokes and Navier-Lamé equations.

2 Bases of Discrete Mechanics

2.1 Physical Model of Discrete Approach

Discrete mechanics is based on classical principles and postulates of physics; one of the most emblematic is the principle of equivalence introduced by Galileo that assigns an equivalent effect to the gravitational acceleration and the one due to inertia. This principle, now called the Weak Equivalence Principle (WEP), has been verified by numerous experiments quantified by the Eötvös ratio $\eta = 2 |\gamma_1 - \gamma_2| / |\gamma_1 + \gamma_2|$ where γ_1 and γ_2 are the accelerations of the two masses. The measurement of the acceleration is independent of any reference and can be achieved with an absolute precision. The current state leads to estimating that the WEP is exact with a ratio of Eötvös $\eta < 10^{-17}$; Will's [13] review cites the various experiments carried out for a century.

For gravitational effects only, this principle makes it possible to eliminate the mass of Newton's second law in order to obtain equality between the acceleration of the medium and the gravitational acceleration. In fact the fundamental law of dynamics in a more modern form $\rho \boldsymbol{\gamma} = \mathbf{f}$ where \mathbf{f} is the sum of the volume forces applied to the medium is modified in discrete mechanics as follows:

$$\boldsymbol{\gamma} = \mathbf{g} \quad (1)$$

where \mathbf{g} , the sum of the forces per unit mass, is an acceleration.

By dissecting all the physical quantities and associated units by which they are expressed, it can be noticed that each time the mass appears in these units, this is only with a first order. It is therefore possible to define equivalent quantities but per unit mass. It appears that only two fundamental units, *i.e.* a length and a time, are required to quantify any physical variable.

Thus the notion of velocity \mathbf{V} is degraded, this one appears as a secondary variable whose value in absolute does not need to be known, it will not be present as such in the system of equations. The acceleration $\boldsymbol{\gamma}$ takes on the contrary a fundamental status. It will be considered as an absolute quantity which can be measured in any place and at any moment. It possesses the essential property of satisfying the rule of vector summation, which is not the case with velocity, in any case for velocities close to the speed of light. The principle of relativity, also understood by Galileo, is therefore satisfied from the outset. A uniform translational motion is thus completely impaired in the equation of the discrete motion as the velocity appears only through discrete operators that filter this contribution. This is a little more complex for uniform rotation movements [5]. However at the end, these motions are also filtered by the same operators. These two stiffening movements have no effect on the acceleration of the particle or the material medium.

Another foundation of discrete mechanics is the Hodge-Helmholtz decomposition, see [1]. It establishes that every vector is the sum of a solenoidal component with null divergence and another irrotational one. A third component is sometimes associated, of harmonic type, being at the same time divergence and rotational free or constant. The vector is thus the sum of a gradient of a scalar potential ϕ and a rotational of a vector potential $\boldsymbol{\psi}$. These are only defined to harmonic functions, the decomposition is not unique and depends on the boundary conditions. There are many potentials in physics and not all of them have the same importance. In discrete mechanics the vector considered is the acceleration $\boldsymbol{\gamma}$, an absolute quantity in a local reference frame. It is written naturally:

$$\boldsymbol{\gamma} = -\nabla\phi + \nabla \times \boldsymbol{\psi} \quad (2)$$

The harmonic term sometimes added is absent from this decomposition, it physically represents the movements of rectilinear translation and uniform rotation which disappear by application of the discrete operators. All undulatory physics are implicitly based on this relation: the terms of the right hand side are derived from orthogonal fields. The gradient and dual rotational operators project these fields on the same Γ edge and the sum of these two contributions is the acceleration applied to the medium. For example, in electromagnetism, the electric and magnetic fields \mathbf{E} and \mathbf{B} are orthogonal

to each other at any moment and themselves orthogonal to the wave vector \mathbf{k}_0 . Thus a current can be applied from a potential difference or produced by induction from a magnetic field. The unification of the laws of macroscopic physics is thus considered under the undulatory point of view for any phenomenon of any nature, mechanical, acoustic, electrical, magnetic, optical [10].

2.2 Geometrical Topologies and Definitions

The notion of continuous medium is abandoned, as is that of global reference frame. There is a local discrete geometrical structure represented in Fig. 1 composed of primal and dual elementary structures. The term discrete geometric structure or geometric topology defines a set of links between connected elementary objects, here points, segments, surfaces. These notions are identical to those that can be found in mesh structures, for example resulting from spatial discretization in finite elements. The segment Γ of unit vector oriented \mathbf{t} and of ends a and b defines the basic element of the primal topology which, with two other segments, forms the planar surface \mathcal{S} whose unit-oriented normal is \mathbf{n} such that $\mathbf{t} \cdot \mathbf{n} = 0$ (Fig. 1(a)). The scalar potential ϕ is only defined at the ends of the primal topology. A possible contact discontinuity or shock wave Σ intersects the segment Γ into c . The normal to the \mathcal{S} plane is associated with a pseudo-vector $\boldsymbol{\psi}$ such that the rotation of vector \mathbf{V} is itself associated with the segment Γ . Figure 1(b) represents the primal surface \mathcal{S} as a planar polygon; the δ outline and the Δ surface form the dual topology. The material medium, a flux of particles or an isolated particle represented by a p sphere in Fig. 1(a) has a velocity and a spin but only their components are explicitly represented on each Γ segment.

The thus defined primal and dual topologies intrinsically satisfy two essential discrete properties $\nabla_h \times \nabla_h \phi = 0$ and $\nabla_h \cdot (\nabla_h \times \boldsymbol{\psi}) = 0$. They are verified whatever the topologies based on planar surfaces, polygons or polyhedra and whatever the regular functions ϕ and $\boldsymbol{\psi}$. These conditions are absolutely necessary for a complete Hodge-Helmholtz decomposition applied here to acceleration. Each vector can be decomposed into a solenoidal part and an irrotational component, but the scalar and vectorial potentials are not of the same importance according to the nature of the vector.

It should be noted that ϕ^o and $\boldsymbol{\psi}^o$ are the stresses at time t , *i.e.* all the forces applied before this instant are “remembered” and stored. The formalism presented here enables us to take into account the entire history of the medium, *i.e.* its evolution over time from an initial neutral state. For a given instantaneous state of strain, there may be multiple paths by which this state can be reached, and $(\phi^o, \boldsymbol{\psi}^o)$ will, alone, contain the whole of the medium’s history. It is not helpful to know the local and instantaneous stresses, in that these two potentials will have accumulated stresses over time. These quantities are also called “accumulators” or “storage potentials”. These potentials can therefore be used to take into account the behavior of media with continuous memory.

2.3 Discrete Motion Equation

The discrete motion equation is derived from the conservation equation of acceleration (2) by expressing the deviations of potentials ϕ and $\boldsymbol{\psi}$ as a function of velocity \mathbf{V} . These “deviators” are obtained on the basis of the physical analysis of the storage-release

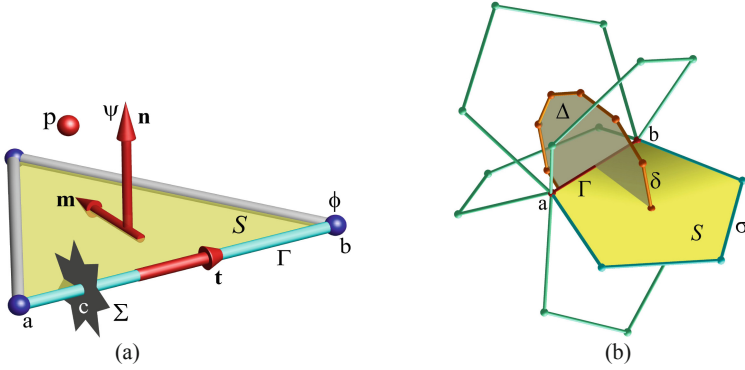


Fig. 1. (a) Elementary geometrical structure of discrete media mechanics in direct referential $(\mathbf{m}, \mathbf{n}, \mathbf{t})$: three straight Γ edges delimited by dots define a planar face \mathcal{S} . The unit normal vectors \mathbf{n} to the face and the vector carried by Γ are orthogonal, $\mathbf{t} \cdot \mathbf{n} = 0$. The edge Γ can be intercepted by a discontinuity Σ located in c , between the ends a and b of Γ . ϕ and $\boldsymbol{\psi}$ are the scalar and vector potentials respectively. (b) The virtual machine of motion in Discrete Mechanics: the acceleration of the medium along the edge Γ is due to the difference of the scalar potential ϕ between the ends of the edge $[a, b]$ of unit vector \mathbf{t} , to the circulation action of the vector \mathbf{V} on the contour of the different primal facets \mathcal{S} inducing an acceleration on Γ and the projection $\mathbf{g} \cdot \mathbf{t}$ imposed other accelerations as gravity. The particle p has a velocity and an acceleration whose projections on the Γ edges are named respectively $\boldsymbol{\gamma}$ and \mathbf{V} .

processes of compression and shear energies. The first is written as the divergence of velocity and the second as a dual rotational velocity. The physical modeling of these terms is developed in a book devoted to discrete mechanics [5].

The vectorial equation of movement and its upgrades are written as:

$$\left\{ \begin{array}{l} \boldsymbol{\gamma} = -\nabla(\phi^o - dt c_l^2 \nabla \cdot \mathbf{V}) + \nabla \times (\boldsymbol{\psi}^o - dt c_t^2 \nabla \times \mathbf{V}) + \mathbf{g} \\ \alpha_l \phi^o - dt c_l^2 \nabla \cdot \mathbf{V} \mapsto \phi^o \\ \alpha_t \boldsymbol{\psi}^o - dt c_t^2 \nabla \times \mathbf{V} \mapsto \boldsymbol{\psi}^o \\ \mathbf{V}^o + \boldsymbol{\gamma} dt \mapsto \mathbf{V} \end{array} \right. \quad (3)$$

The quantities ϕ^o and $\boldsymbol{\psi}^o$ are the equilibrium potentials, the same ones that allow the equation to be satisfied exactly at the discrete instants t and $t + dt$. c_l and c_t are the longitudinal and transverse celerities, intrinsic quantities in the medium that can vary according to physical parameters. The terms $dt c_l^2 \nabla \cdot \mathbf{V}$ and $dt c_t^2 \nabla \times \mathbf{V}$ are respectively the deviators of the compression and shear effects. The second member is thus composed of two oscillators in which ϕ^o and $\boldsymbol{\psi}^o$, which represent energies per unit mass, exchange these energies with their respective deviators. The two terms in gradient and in dual rotational are orthogonal and can not exchange energy directly. If an imbalance due to an external event occurs on one of these effects, acceleration is modified and energy is then redistributed towards the other term. The acceleration \mathbf{g} represents gravity or

any other source quantity and will also be written in the form of a Hodge-Helmholtz decomposition.

The physical parameters α_l and α_t are the attenuation factors of the compression and shear waves. They also depend only on the considered medium: for example, a Newtonian fluid retains the shear stresses only for very weak relaxation time constants, of order of magnitude of 10^{-12} s and the coefficient α_t can be taken as zero. The updating of potentials at time $t + dt$ is thus affected by these coefficients ranging from zero to unity. The velocity and possibly the displacement \mathbf{U} are also upgraded. In the case where the density is not constant, it is also updated using the conservation of mass in the form $\rho = \rho^o - dt \rho^o \nabla \cdot \mathbf{V}$. This quantity is only a function of the divergence of velocity.

The acceleration $\boldsymbol{\gamma}$ and the particle derivative of the velocity are written as $\partial \mathbf{V} / \partial t + \mathbf{V} \cdot \nabla \mathbf{V}$ or using the Lamb vector $\partial \mathbf{V} / \partial t - \mathbf{V} \times \nabla \times \mathbf{V} + \nabla (\|\mathbf{V}\|^2 / 2)$ in continuum mechanics. These expressions can not be transformed into a Hodge-Helmholtz decomposition, the notion of tensor being non-existent in discrete mechanics. Similarly, the Lamb term is not a rotational one. The acceleration is thus rewritten in the form of irrotational and solenoidal components of a Hodge-Helmholtz decomposition of inertial potential $\phi_i = \|\mathbf{V}\|^2 / 2$. All other source terms applied to the medium or particle can also be written as a Hodge-Helmholtz decomposition.

3 Validation of the DM Model

The formulation of discrete mechanics makes it possible to find all the results obtained with the Navier-Stokes equation in the case of a medium with constant properties, mainly the density, the viscosity and the coefficient of compressibility (or the celerity of the waves). In the case where the properties are variable in space, the formulations differ.

The exact solutions of the Navier-Stokes equations corresponding to physical cases such as the Poiseuille or Couette flows are also exact solutions of the equation of discrete mechanics when these solutions are formulated in the form of polynomials of degree equal to or less than two. In the case of any continuous functions, the numerical solution obtained by the discrete formulation proves orders of convergence in time and in space equal to two. This is for example the case of the synthetic solution of the Green-Taylor vortex. Simulations of simple constraints applied to solids, compression, bending, torsion make it possible to find the theoretical solutions also. Benchmarks on fluid-structure interactions [3,4], compare very favorably with solutions obtained by other authors.

The few validation cases presented here make it possible to confirm that the Navier-Stokes equation and the discrete mechanics have the same solutions but above all, to show the versatility of the latter unifying the representation of fluid flows, of complex materials behaviors in an unsteady unified approach.

3.1 Oscillatory Fluid-Solid Interaction

Even if the rheology of the medium is more complex, e.g. viscoelastic fluids, non-linear viscosity laws, viscoplastic fluids, time-dependent properties, and so on, we should still

be able to represent its behavior under various types of applied stress. In some cases, the shear-rotation stresses may only be partially accumulated. We can describe viscoelastic behavior by weighting the accumulation term of $\boldsymbol{\Psi}^o$ by an accumulation factor $0 \leq \alpha_t \leq 1$. Fluids with thresholds can also easily be represented by specifying a value of $\boldsymbol{\Psi}^o = \boldsymbol{\Psi}_c$ below which the medium behaves like an elastic solid. Many of the difficulties that are typically encountered in rheologies with non-linear viscosities are no longer an issue with DM.

In discrete mechanics, the concepts of viscosity and shear-rotation are exclusively associated with the faces of the primal topology, where the stress may be expressed in the form $\mathbf{v} \nabla \times \mathbf{V}$ in fluids and $dt \mathbf{v} \nabla \times \mathbf{V}$ in solids. As an example, let us consider the interaction between an incompressible viscous Newtonian fluid and a neo-Hookean elastic solid. The stress tensor of an incompressible isotropic hyperelastic material is as follows in the neo-Hookean model:

$$\boldsymbol{\sigma}_s = -p \mathbf{I} + \mu_s \mathbf{B}, \quad (4)$$

where $\mathbf{B} = \mathbf{F}\mathbf{F}^T$ is the left Cauchy-Green deformation tensor. In two spatial dimensions, the Cayley-Hamilton theorem can be used to show that the Mooney-Rivlin model of a hyperelastic material is equivalent to the neo-Hookean model.

We shall study a problem that was published by Sugiyama in 2011 [12]. Consider an elastic band with an applied shear stress generated by the periodic flow of an incompressible Newtonian fluid. The flow is laminar and periodic in x . Given that there are no compression terms, we can solve the problem in one spatial dimension along the y -axis for $y \in [0, 1]$. Suppose that the upper interface follows the periodic motion $V(t) = V_0 \sin(\omega t)$, where $V_0 = 1$ and $\omega = \pi$. The velocity of the lower surface is imposed at zero. The solid occupies the lower part of the domain, and the fluid occupies the upper part of the domain; the position of the interface is $y = 1/2$. The theoretical solution found by Sugiyama was obtained by separating the spatial variable y from the time variable t . A homogeneous solution is found by considering a basis of Fourier functions on the interval $y \in [0, 1]$ and exponential functions on the time interval in each of the fluid and solid domains separately. The sequence of Fourier coefficients can be determined from the coupling at the interface by requiring the velocity and the stress to be continuous.

We can find a solution $V(y, t)$ directly from the equations of discrete mechanics [1] simply by imposing the relevant conditions at $y = 0$ and $y = 1$. The coupling conditions at the interface, namely the continuity of the velocity and the stress, are implicitly guaranteed to hold by the dual curl operator. The notion of a 2D or 3D space does not exist in discrete mechanics. Instead, the operators define the orientations of the normal and tangent directions within a three-dimensional space. Despite this, the assumptions made in this example enable us to solve along a single spatial dimension. The time step is chosen to be $\delta t = 10^{-4}$ to ensure good overall levels of accuracy. By comparing against the theoretical analytic solution, it can be shown that the numerical solution is second-order in space and time.

Figure 2 plots the velocity and the displacement of the interface Σ over time. The velocity of the upper wall is also shown. The solution establishes itself very quickly. After just a few periods, the velocity becomes fully periodic. The velocity profiles are

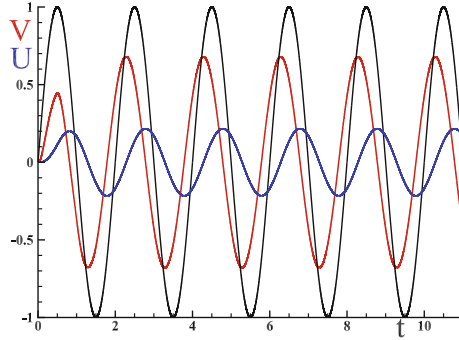


Fig. 2. Study of a periodic fluid-structure interaction between a viscous fluid and an elastic solid. The kinematic viscosity of the fluid is $\nu = 1$ and the shear modulus of the solid is $\nu = 4$. The velocity of the fluid at the upper wall is shown in black, the velocity of the interface Σ is shown in red, and the displacement over time of the solid U at the interface is shown in blue.

shown until $t = 10$. The displacement of the solid over time may be deduced from the relation $\mathbf{U} = \mathbf{U}^o + \mathbf{V} dt$, where dt represents both the differential element and the time increment $\delta t = dt$. Note that the displacement is strongly out of phase with the velocity of the interface.

A selection of the velocity profiles in the y -direction are shown in Fig. 3 once the periodic regime is fully established. The results converge to second order in space and time. Given the absolute accuracy (of the order of 10^{-4} s) obtained using a coarse mesh ($n = 32$), we can conclude that there is no observable error between the theoretical solution and the numerical solution.

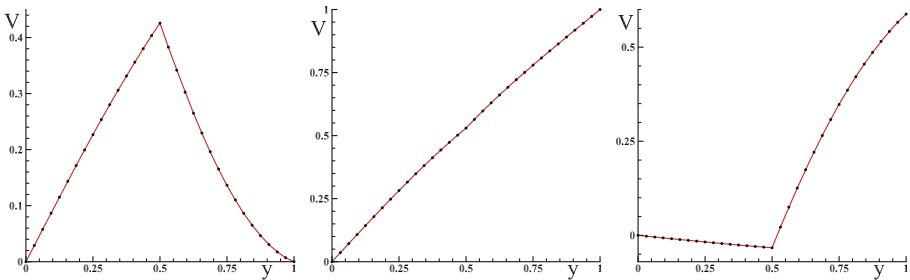


Fig. 3. Study of a periodic fluid-structure interaction between a viscous fluid and an elastic solid. The viscosity of the fluid is $\nu = 1$ and the shear modulus of the solid is $\nu = 4$. The figures show the velocity profiles as a function of y at time $t = 10$, $t = 10.5$, $t = 10.8$. The solid line holds for the theoretical solution whereas the points represent the spatial approximation obtained with 32 cells.

One advantage of the fluid-structure interaction for a neo-Hookean model described by Sugiyama is that it has a theoretical solution. This allows us to compare the numeri-

cal solutions that we obtain more precisely, but also allows us to develop new concepts, as we did for discrete mechanics in this section. Sugiyama obtained a first-order error in the L_2 and L_∞ norms, whereas the model [1] achieves second-order results with much lower absolute errors. This improvement is ultimately attributable to the separation of the properties at the interface, as well as the fact that no interpolation is performed, despite a fully monolithic and implicit treatment of the fluid-solid coupling.

Fluid-structure interactions in 2D or 3D geometries with a moving interface can of course also be solved using the system [1]. However, without an analytic solution for comparison, there is little benefit in doing so, since the errors of the various methodologies accumulate over each step of the process. Other more complex constitutive laws can also be modeled.

3.2 Lid-Driven Open Cavity Flow with Flexible Bottom Wall

The lid-driven cavity with flexible bottom is an example that we can reasonable deal with. This case corresponds to that proposed in reference [9]. It was also considered by others authors [2,6]. A fluid, characterized by density $\rho_f = 1 \text{ kg m}^{-3}$ and viscosity $\mu = 10^{-2} \text{ Pa.s}$, is driven by the velocity boundary condition of the top of the cavity which varies with time: $u(x,t) = 1 - \cos(2\pi t/T)$, where the period is equal to $T = 5 \text{ s}$.

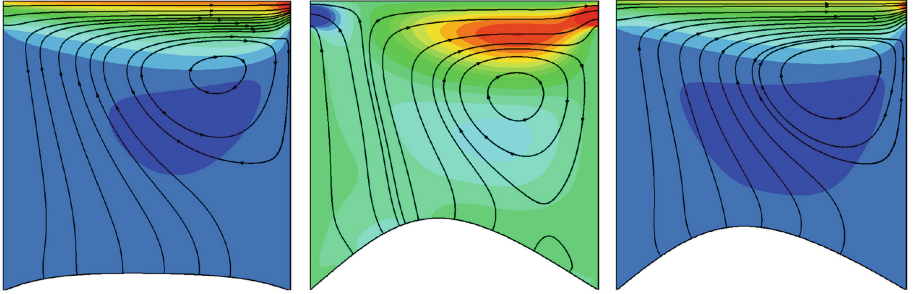


Fig. 4. Lid-driven open cavity flow with flexible bottom wall, velocity and streamlines at $t = 2.5, 15, 20 \text{ s}$.

The elastic structure density is $\rho_s = 500 \text{ kg m}^{-3}$, the Young modulus is $E = 250 \text{ Pa}$ and the Poisson coefficient $\sigma = 0$. The fluid is considered as incompressible. Neumann boundary conditions are imposed on the two holes localized at the top of the vertical walls. As we resolve at the same time, the velocity field and the displacement field in the fluid and the elastic membrane respectively, using a fixed grid, we have to take a relative large thickness for the membrane (2% of the cavity length) compared to other simulations of the literature, in order to prevent using a very fine grid. A one dimensional deformation of the membrane can be dealt using another numerical scheme. The formulation and the equations used are that proposed in the article. Only the procedure

related to the membrane deformation and the numerical scheme are different. The differential discrete operators, such as gradient, divergence and rotational properties have the properties of continuum $\nabla \cdot \nabla \times \boldsymbol{\psi} = 0$ and $\nabla \times \nabla \phi = 0$ on every type of unstructured polyhedral meshes. This methodology is close the Discrete Exterior Calculus one [7]. In the present case, adaptive quadrangle mesh is used with initially 2562 cells. The resolution of the motion equation of the fluid allows to obtain the pressure on the top surface of the membrane, the lower surface being maintained at a constant pressure $p = 0$. The force acting on the membrane, proportional to the pressure difference, allows to calculate its displacement. The mesh is then modified and this at each time steps. This is what we call the Arbitrary Lagrangian Eulerian method.

The results obtained are presented in the Fig. 4 where the horizontal velocity maps in the fluid and the membrane shape are shown together with the streamlines for different time steps.

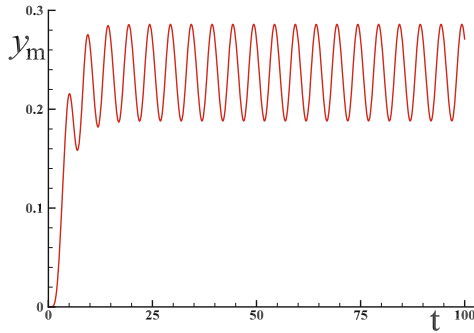


Fig. 5. Lid-driven open cavity flow with flexible bottom wall. Evolution of maximum deviation of membrane y_m over time.

These results are in good agreement with those of [2] and [6]. After an unsteady phase of a few cycles, the regime becomes totally periodic, of period $T = 5$ s (Fig. 5). The divergence of the velocity remains less than 10^{-8} throughout the calculation. The celerity of air, which is equal to $c \approx 340 \text{ms}^{-1}$, maintains the flow in the incompressibility approximation for the selected time period $dt = 10^{-2}$ s. Indeed the discrete model clearly shows that the Mach number $M = v/c$ does not define the incompressibility of a flow: this is the product $dt c_l^2$. For example water, an essentially incompressible fluid, propagates the waves at a celerity of $c_l \approx 1500 \text{ms}^{-1}$ which induces the fact that water is a compressible medium if the observation time constant dt is sufficiently low.

4 Towards a Unification of Solid and Fluid Mechanics

The most significant achievements of the discrete approach are as follows:

- discrete mechanics proposes a unique formulation of the equations of motion in terms of the velocity to represent the motion of both fluids and solids;

- the velocity variable, the displacement, and the stresses ($p^o, \boldsymbol{\omega}^o$) or ($\phi^o = p^o/\rho, \boldsymbol{\psi}^o = \boldsymbol{\omega}^o/\rho$) are calculated simultaneously and accumulated by simple differential operators;
- the accumulation process for the stress holds for large displacements and large deformations.

This theory describes the motion and displacements of solids and fluids consistently, but the scope of the proposed description also extends to the dynamic behavior of these materials and the propagation of waves within them. Possibly, the most important result of discrete mechanics for fluids and solids is the formal Hodge-Helmholtz decomposition of the equations of motion. The decomposition into irrotational and solenoidal components enables us to understand the mechanisms governing the equilibrium of a medium, and the divergence and curl of the velocity can be used to deduce the stresses, namely the equilibrium pressure p^o and the rotation stress $\boldsymbol{\omega}^o$.

References

1. Angot, Ph., Caltagirone, J.-P. and Fabrie, P.: Fast discrete Helmholtz-Hodge decomposition in bounded domains. *Appl. Math. Lett.* **26**(4), 445–451 (2013)
2. Bathe, K.-J., Zhang, H.: A mesh adaptivity procedure for CFD and fluid-structure interactions. *Comput. Struct.* **87**, 604–617 (2009)
3. Bordère, S., Caltagirone, J.-P.: A unifying model for fluid flow and elastic solid deformation: a novel approach for fluid structure interaction. *J. Fluid Struct.* **51**, 344–353 (2014)
4. Bordère, S., Caltagirone, J.-P.: A multi-physics and multi-time scale approach for modeling fluid-solid interaction and heat transfer. *Comput. Struct.* **164**, 38–52 (2016)
5. Caltagirone, J.-P.: *Discrete Mechanics, Concepts and Applications*, ISTE. Wiley, London (2018)
6. Kassiotis, C., Ibrahimbegovic, A., Niekamp, R., Matthies, H.: Nonlinear fluid-structure problem, part I: implicit partitioned algorithm, nonlinear stability proof and validation examples. *Comput. Mech.* **47**, 305–323 (2011)
7. Desbrun, M., Hirani, A.N., Leok, M., Marsden, J.E.: Discrete exterior calculus. *arXiv-math/0508341v2*, pp. 1–53 (2005)
8. Gad-El-Hak, M.: Stokes hypothesis for a Newtonian, isotropic fluid. *J. Fluids Eng.* **117**, 3–5 (1995)
9. Gerbeau, J.F., Vidrascu, M.: A quasi-Newton algorithm based on a reduced model for fluid-structure interaction problems in blood flows. *Math. Modell. Numer. Anal.* **37**, 3–5 (2003)
10. Marsden, J.E., Ratiu, T., Abraham, R.: *Manifolds, Tensor Analysis, and Applications*, 3rd edn. Springer, New York (2002)
11. Rajagopal, K.R.: A new development and interpretation of the Navier-Stokes fluid which reveals why the “Stokes assumption” is inapt. *Int. J. Non-Linear Mech.* **50**, 141–151 (2013)
12. Sugiyama, K., Ii, S., Takeuchi, S., Takagi, S., Matsumoto, Y.: A full Eulerian finite difference approach for solving fluid-structure coupling problems. *J. Comput. Phys.* **230**, 596–627 (2011)
13. Will, C.M.: The confrontation between general relativity and experiment. *Space Sci. Rev.* **148**, 3–13 (2009)



HPC and Data: When Two Becomes One

Christophe Calvin^(✉) and France Boillod-Cerneux

CEA Saclay, DRF, Gif Sur Yvette, France
{christophe.calvin, france.boillod-cerneux}@cea.fr

Abstract. As claimed for many years, High Performance Computing (HPC) and high performance numerical simulation are necessary tools for fundamental science and engineering. Big data and artificial intelligence are some newcomers in the landscape, but not that new, especially in science. Finally, open data and open science are becoming now mandatory for trustable and reproducible science.

This paper presents the recent evolution of HPC with the spectacular arising of AI. HPC and AI share at least one common point: Data. Many HPC communities are struggling with data, whether they are coming from simulation and wait to be analyzed, or coming from large instruments (experiments, observatories) and wait to be treated.

Data was not a major focus in the last decades for HPC community but it reshapes HPC paradigms by introducing data as a “scientific pillar”.

We will first present the current HPC context and how AI changed the current HPC landscape. We will then focus about data use in HPC and how AI can improve HPC simulations. We will also present the concept of FAIR data and why this concern shall be treated soon and embraced by HPC and AI community. We will finally conclude on the data issue and present our point of view regarding the future evolution of HPC market.

Keywords: HPC · AI · Open Science · Data

1 Introduction

With exascale challenge, Top500 [1] has really mutated, either regarding the supercomputers listed and regarding its weight to estimate a supercomputer’s compute power.

The first mutation comes from the exascale challenge itself. Power wall is hard to cross and so far, (safe) decision has been made to promote low consumption processors or high multicore processors while trying to keep a reasonable power consumption of the overall machine.

Top500 is heckled by new rankings, such as Green500 [3] that proposes to classify supercomputers by Flops per Watts rather than just Flops/s capacities. This rank strategy deeply reshapes the Top500 ranking, as very few of the top 10 coming from Top500 can reach Green500 first ranks. Green500 also emphasizes

Japan's effort to build low energy consumption machines, as 6 over 10 of the best Green500 machines come from Japan.

HPCG500 (High Performance Conjugate Gradients) [4] is either getting more and more attention from HPC community: Indeed, Linpack benchmark for Top500 provides an efficiency from 50% to 80% from peak compute capacity, while real users applications have about 10% efficiency from peak performance. Few of real applications can address the compute bound profile of High Performance Linpack (HPL): In this context, HPCG is raised as a "more representative" benchmark, closer to "real HPC applications" profile. It is not surprising to see that HPCG500 and Top500 present very different ranking, but the difference is less striking than Green500. However, if we compare the HPL peak performance and HPCG peak performance, then the reality of supercomputer compute capacity becomes closer to reality.

Even though the change is unavoidable, it is either not quite smooth. Last petaflop homogeneous supercomputers propose mostly massive parallel processors, and users must take care of their application parallelism (especially multi-level parallelism) if they really want to see a performance gain on the last petaflop computers.

On the other side, Top500 is fastly tainted by hybrid architecture (classic processors with accelerators such as Graphic Process Units), which is a direct consequence of exascale power wall. NVIDIA[®] GPUs strike hard the 2018 Top500: Half of top 10 most powerful supercomputers (November 2018 Top500 list [2]) contains nodes with NVIDIA[®] GPUs. However, taking full advantage of hybrid nodes efficiency requires large effort for HPC community. Choosing GPUs acceleration is mostly a tradeoff portability versus efficiency (in terms of compute power and energy consumption). This trend is justified by the excellent ratio of Flops per Watts of NVIDIA[®] GPUs but also by the ongoing evolution (that is actually not far from a revolution) of HPC landscape.

"Hybrid" word must be used with caution: indeed, we traditionally referred to hybrid architecture as compute nodes with accelerators (such as GPUs), but hybrid may now, depending on the context, refer to the community addressed by the supercomputer. Looking closely at the top 10 of the Top500 November 2018 list, we observe that 2 of them, Summit (USA) and ABCI (Japan) clearly expose their membership to AI research: That is to say, Summit and ABCI are not HPC dedicated but at the best, AI dedicated and at the worst, HPC and AI dedicated. This recent trend is likely to be spread to the other Top500 computers and might contaminate very quickly the full Top500.

The fusion of HPC and AI is clearly illustrated by many HPC centers that are enlarging their scope of action: As an example, Argonne Leadership Computing Facility (ALCF) from Argonne National Laboratory (ANL) has officially announced the integration of Machine and Deep Learning as one of their scientific pillars. Most of the historic and HPC actors made similar declarations.

In what follows we will focus on how AI reshapes the HPC community and can help to consider data as a key point in their simulation process. We will then

focus on the data issue, and address the FAIR data concept, which may lead in the future both HPC and AI scientific research.

2 HPC (R)evolution

2.1 When AI Shakes HPC

Since the end of 2018, many HPC media relay the announcements of supercomputers dedicated to AI as well as strong positions to promote AI science and development. The recent appearance and success of Deep500 [5], the ranking of most powerful computers dedicated to AI (or HPC and AI) is a very good illustration of Machine and Deep Learning success in industry and scientific fields.

AI Adoption. The Deep Learning (DL) success can be attributed to enterprises and industries who have massively used it to improve their process, or wisely address their (future) customers. Deep learning is currently widely adopted by public at large scale. This might be seen as a very “late recognition” as AI discipline was born many decades ago, around 1950. Success of AI and more specifically Deep Learning is largely due to the GAFAM (Google, Apple, Amazon, Facebook and Microsoft) but not only. At a more global scale, in the last decades, every industry, every organization and everyone has gathered massive amount of data. The convergence of a large amount of data and the maturity of available computing hardware drove AI from “theoretical” discipline to “executable” discipline, and currently, “unavoidable” discipline.

AI and HPC Fusion. Deep Learning is driven by data and HPC is generating huge amount of data. Therefore, it is not very surprising to observe the collision of these two disciplines. On another level, HPC community is quite mature now and organized. It has access to a large panel of HPC platforms, addressing many different needs in terms of hardware and compute capacity needs. The progression of AI inside the HPC community is coming from four needs:

- AI needs large platforms to run specific experimentations, and HPC can offer such platforms,
- HPC is struggling with data and their analyses,
- Many HPC applications cannot cross petaflop or exaflop scale due to their algorithms and/or the physics model and numeric used,
- Governments have identified AI as a strategic point, at least as important as HPC.

AI Supercomputers Might Cross Exascale First. Machine Learning and Deep Learning completely reshape exascale challenge thanks to their ability to reduce the compute precision. Though many HPC simulations require a fine precision, Machine Learning and Deep Learning applications can be satisfied with very low precision.

For many years, reduced and/or mixed precision compute kernels have been considered as a strategic key to overcome the exascale challenge. Even if this strategy has been adopted for some applications, we must admit its success remains very limited and did not drastically change the performance as expected: Whether reduced/mixed precision kernels are too small to increase scalability significantly, whether their numerical impacts imply to keep them very limited. For now, reduced or mixed precision in HPC simulations is far from sufficient to cross a new computing scale.

New cards are given with the rise of Machine Learning and Deep Learning and their execution on hybrid processors that support as well classic HPC and Deep Learning simulations. One may see that “AI” dedicated or “mixed” processors and GPU addressing the market are able to deal with low precision compute. This is one of the key points when these processors are presented, showing very attractive compute capacity especially with low precision. It would not be surprising if first exascale application were a Deep Learning simulation running in low precision. In that case, Exascale should not be late for 2020 as it is expected since a few years, and might even be “greener” as expected if very low precision is used.

Economic Market Drives Technologies. Deep learning market is more sensitive to the economy than HPC. HPC remains a strategic point for many industries, but HPC use is restricted most of the time to very large enterprises who can afford the infrastructure costs and human resources with a specific knowledge to address large simulations (computer science, algorithms and IT). In contrast, Deep Learning is widely accessible thanks to:

- The amount of data each industry has accumulated over time,
- The “black-box” frameworks, requiring few IT knowledge to build an AI application,
- AI platform proposed by GAFAM, with reasonable costs.

A recent report coming from Market Research Future estimates that deep learning economic market is about to reach \$18 billion in 2023. This is no surprise that governments provide massive efforts to support AI research and community, and fund the acquisition of proprietary infrastructure to host AI research community applications.

On the other side, vendors have greatly addressed this market by proposing either dedicated AI solution or HPC & AI compliant solutions.

Consequently, many HPC vendors either get into the AI market with “pure” AI processors or “mixed” processors, which can address the HPC or Machine Learning and Deep Learning issues.

- Intel[®] has recently proposed its AI dedicated processor, the Intel[®] Nervana processor. Intel[®] either integrates, in its “HPC” processors, new instructions set, dedicated to Deep Learning, making these processors a really good target for “converged” architecture.

- NVIDIA[®] proposed AI supercomputers, with a “ready to go” box named DGX[®]. On the other side, NVIDIA[®] was able to penetrate the market thanks to its GPU Volta[®] V100 and P100, which propose very interesting features for AI but still remains extremely good candidates for HPC applications.

We did not mention above the Google[®] TPU (Tensor Process Unit) as they are not for sale, and we do believe that Google and Facebook are not likely to commercialize their solutions.

The large economic growth of Machine Learning and Deep Learning market are either due to the vendors themselves: Classic vendors such as Intel[®] and NVIDIA[®] largely and actively contribute to AI framework development and optimization. AI success is partly due to an active and efficient contribution of vendors to the most used Machine Learning and Deep Learning frameworks, allowing AI researchers and enterprises to focus only on the algorithm side, and not on the development and performance issues.

This is also one major advantage of Machine Learning and Deep Learning communities compared to HPC, as they directly made a massive use of open source frameworks, and started their work on, mostly, private cloud platforms. GAFAM very quickly offered to the AI community very advanced and smooth platforms, with free access first to attract people, and low prices when addiction or need is established.

HPC and AI communities have very different “habits” when it comes to production and science: HPC community executes its simulation on proprietary or governmental platforms, develops its own frameworks and is reluctant to share its data, as most of them are sensitive data: Therefore, platforms of execution run in a closed and secured environment that is hardly compatible with “open-science”. The path to open-science for HPC community is harder than it is for AI community. AI community mostly started to run on cloud platforms, non-proprietary, with simulations based on open source frameworks, using data that are not sensitive or whose security is not a major concern. AI community does not need to migrate towards open-science: it directly started with open-science mind.

3 Rethink HPC: Think Data

Regarding the recent market evolution and government decisions, HPC will have to deal with AI community. This must not appear as a constraint, as many HPC simulations can take advantage of Deep Learning or Machine Learning algorithms and improve either their performance or data analysis process. Mostly, these two scientific worlds collision is an opportunity to improve their simulation and scientific research.

3.1 Data Struggling

Many scientific domains, such as astrophysics, materials, fusion... that are massively using HPC to execute their simulations are currently struggling with data.

It can be data coming from real experimentations or HPC simulations and both can be either output or input data.

Analyzing these data is vital for some scientific domains, as they might improve drastically research and therefore theory. However, analysis part is often not up to the HPC simulation level: Whether the analysis part is done manually and is excessively long and fastidious to do, including lack of resources, whether the platforms to do post treatment are inexistent or not adapted.

We recall that for very large set of data, we can hardly move Terabytes or Petabytes of data from one HPC center where data were generated to another where data could be analyzed. HPC centers hosting data consumer applications will need to find solutions to the following issues:

- For long term and interactive storage: the storage capacities and functions (which was, so far, limited to archive treatment) that we encouraged so far cannot be considered anymore. The major risk is a loss of generated data and inhibit research discoveries.
- The use of Machine Learning and/or Deep Learning solutions for analysis (pre or post-treatment) of HPC data. Data analysis can be done in situ, depending on the application workflow and needs.

It is often observed that data management is treated with a lower priority compared to the compute capacity issue. This bad habit is now changing, because of the fast and drastic rise of Deep Learning and Machine Learning in the HPC landscape.

Big-data-driven models featuring machine learning and deep learning can incredibly improve scientific research, as presented in [10]. In the Fusion energy domain, such techniques enable key discoveries and/or provide considerable time saving to produce results and simulations. The project EuroFusion Joint European Torus (JET) is faced to very large scale perturbations in modelling tokamak systems.

The JET team realized great improvements regarding the predictive capability (which currently is 80%) for disruptions that happen before to deterioration incident: such success largely overcome the “classic” HPC simulations. This work is still ongoing as upcoming International Thermonuclear Experimental Reactor (ITER) aims to provide a predictive capability of 95%, which requires a large refinement of physical models, and this challenge can be crossed with machine learning methods.

3.2 HPC Community Must Think Data

Unfortunately, the data issue has not been sufficiently addressed both in terms of infrastructures and in terms of development frameworks. Many applications generate massive amounts of data, but the post treatment and storage management is not sharp enough to deal with the amount of data. Many codes do not embed the post treatment procedures and data compression is either not enough, not adapted or inexistent.

HPC community really needs to rethink their applications, especially the community with data issues. For this community, the power compute capacity is currently their focus, while data should be the first focus as it will be -soon enough- the bottleneck for their applications scalability.

Some HPC communities have understood that Machine Learning and/or Deep Learning can be a very good alternative to classic HPC compute paradigms.

Current HPC applications are overwhelmed with:

- Data captured by observations/production instruments
- Data generated by simulations that must be treated and/or analyzed
- Data generated by sensors networks.

Some HPC applications are therefore in needs of Deep Learning methods to automatize and accelerate the data treatment. This treatment can be used either as pure analysis or as a quality comparison between data coming from the simulation and data coming from real experimentations.

This can help to value the efficiency and accuracy of simulations, eventually its limits and potential. The paper [11] gives a good overview of the data issue in the context of turbulence modeling. Decades ago, the compute power was the driving metric while now the data-driven model is favored. The amount of experimental data are now used to estimate a model relevance or to improve the model itself. A data-driven model is based on making a program that is able to give results, based on large data set. Such approach is adequate for any scientific model struggling with data.

Many numerical simulations in which turbulent flows appear use Large-Eddy Simulation (LES). In [14], the turbulent flow in LES are decomposed into Grid Scale (GS) flow field and filtered with SubGrid-Scale (SGS): The scientists have used Artificial Neural Network (ANN) to find a new subgrid model of the SubGrid-Scale (SGS) applied to LES. The team trained an ANN with a backward propagation using direct numerical simulation data coming from turbulent channel flow. Such configuration improved the correlation between the GS flow field and the SGS stress tensor in LES.

As an illustration, the climate community is directly concerned by data challenge. An international consortium was built to design a climate model and make predictions. Climate community is consuming and generating massive amount of data. The recent use of Deep Learning in climate models can allow comparing simulation results with observational ones, and therefore evaluating the accuracy of simulations. Machine Learning can also help to deal with forecasting problems: Data accumulated about the climate can be effectively used to build predictors for inferring dependencies between past and short-term future values of observed values [7].

Many scientific applications are inundated with data, and for some framework, using Hadoop is a nice option as Hadoop is one of the most used framework to manage big data. Its success comes from his resilience, ease of use and very good portability. In Computational Fluid Domain (CFD), Hadoop is used to manage data analyses as CFD applications can generate large files to stock information on the systems and associated time-steps. In [12], the authors used

a one-dimensional MagnetoHydroDynamics simulation to show that Hadoop is a good approach for CFD applications struggling with large data volume. HaDooP File System (HDFS) success is also described in [13], especially because HDFS proposes any plugins that apply to each problem depending on the issue (large files, number of files, MapReduce issues...).

HPC community needs to rethink its old paradigms, where data was not an issue. Many simulations have evolved, without considering the data as a key point in both algorithms and code developments. For a long time it was assumed that HPC was based on three pillars, namely, theory, experimentation and simulation. This paradigm is not true anymore for any HPC simulation struggling with data. Data is another pillar of science and should get at least as much attention as the three others [8].

It will be tough to rethink the current HPC paradigms, especially introducing a new “key parameter” in the center of the simulations. Many HPC applications will need a complete strategy regarding data management and get educated to Data Science. There is an urge to establish, for every data consumer/producer code, data strategy: establishing a fast and efficient data treatment, that can be executed with machine learning or deep learning. Though Data science is somehow not new, and a large community has addressed this problem, the HPC community is not yet fully aware of their needs of Data Science.

3.3 FAIR Data

Most of the current HPC platform treats the storage as an “archive” process, while this cannot be true anymore with the current amount of data and the converged platform “AI-HPC”. In the context of converged architectures, data are the key of the simulation rather than a simple input and/or output. Such application profile requires to get architecture able to feed large volume of data to the CPU with a high bandwidth and very low latency. This large data transfer is neither a pre/post process nor an input/output step, it is the “main compute process”. This raises some questions as HPC centers can currently provide large compute capabilities but are not ready to sustain dynamic and open software stacks as well as dynamic and large storage capacities. One must always remember that (large amount and quality) data is the center of all AI applications. Recently, a consortium seriously treats the data-tsunami issue. This consortium proposed the concept of FAIR data [9] and [16], meaning that they must be:

- Findable: One must be able to find a data easily and quickly. This implies a standardization and strict processes for data storage and more precisely archive whatever the infrastructure is. Metadata associated to archived data must be rich enough to precisely describe the stored data themselves and respect a unique identifier.
- Accessible: Data must be accessible by scientists responsible of the data or any scientists wishing to use these data for scientific purpose. Data storage infrastructures must propose a standard protocol for data access: security and clear conditions of access (license access, use agreement...) at least.

- Interoperability: Data must be usable on any infrastructure and compatible with any platforms and other data. This will be a direct consequence of the “Findable” aspect in the FAIR data conception. The interoperability aspect can be achieved if and only if standardization around metadata and archive policies are defined.
- Re-usable: The re-usable access is also nested with the “Findable” and “Accessible” characteristics presented above. A perishable data should not be integrated in the FAIR process, in this part, only re-usable data matters, data that can enrich several research activities.

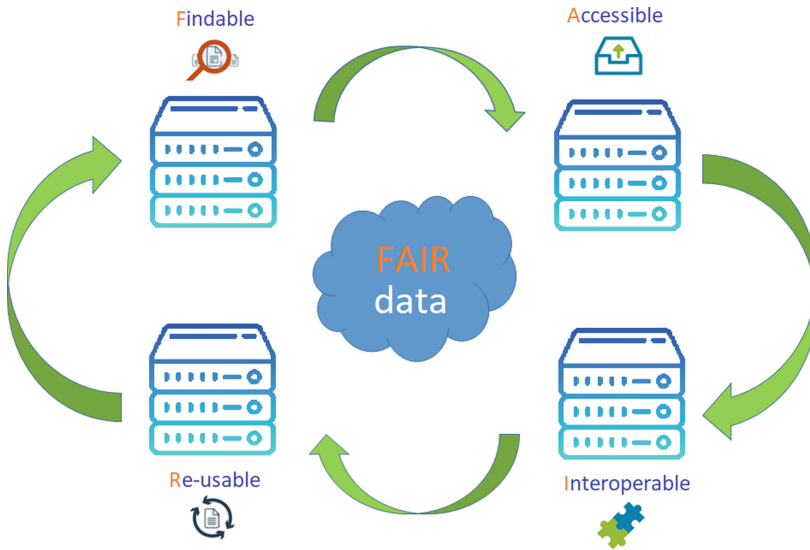


Fig. 1. FAIR data

Data shall not be considered as passive, stored and pending for a treatment, but active, whether we talk about “rough” or “treated” data. This implies a deep adaptation of HPC community to satisfy these requirements, but the effort coming from research community cannot happen before the establishment of FAIR standard. A direct consequence is to protect and ensure the usability/viability of scientific data.

The “DATA FAIR” consortium aims to provide guides and specifications to describe the minimal required protocols, formats and interface that will help to satisfy the Findable, Accessible, Interoperable and Reusable characteristics. The consortium gathers scientists that are involved in data issue to develop into a generic data principle, with different implementations in communities and organizations. The aims of this existing consortium is to extend and share the concept of FAIR data in order to ensure data management issue in each application design.

One danger is that data is a major economic market that jeopardizes the scientific community: Indeed, technologies for data management will very likely not be driven by science. Data issued from scientific applications (whether we talk about HPC or AI applications) are highly valuable in terms of scientific knowledge but for some security and ethical issues, those data can't be used for economic purpose, or under very strict and identified conditions.

Towards Open Science. FAIR data presented above is not exactly the same as open data, where the accessibility is mostly the only concern for open-data. However, FAIR data implicitly leads HPC community towards the open science concept: indeed, FAIR data is one of the corner-stone of open science.

AI scientific community has a major difference with HPC: AI success is (in part) due to the massive open-source culture. Indeed, the massive use of Deep Learning applications is a consequence of release as open source from major frameworks coming from industries.

Globally, AI community started directly with the “open source” culture while HPC went to open source more by necessity than by design.

Getting benefit from AI also implies that HPC must reconsider its “partition” design and get toward open science: namely using and contributing to open source codes, with an open access, and most of all, allowing FAIR data. Of course these paradigms do not address the defense and army sector, but many HPC scientific domains do not require secret defense or closed development and could largely get benefit from open science.

The open science issues concern the biology and medical scientific communities. More precisely, the genomic studies are facing to the problem of data struggling and FAIR data: They generate about 250 000 genomes per year. Nowadays genomic analysis are used for clinical R&D and under pressure regarding the confidentiality issues. The project sponsored by French government called “France genomic plan” [6] aims to combined the use of big data and HPC to implement an efficient use of genomics in healthcare pathway. Today, it could take between days to weeks to obtain a feedback from biology experts in charge of genomic analysis. Due to the huge increase of data and since we will be in healthcare pathway, the genome's analysis should be done in 2 or 3 days, and has to be reproducible. HPC and AI are two solutions to reach this objective, such as using a specific hardware to genome alignment process, which produces the differences between the sequenced genome to analyze and a references one. The use of deep learning is also a solution to genomic studies issues, and could help to analyze the genome and identify the “defaults”: Annotation phase, which needs lots of cross-comparisons, correlation and data analysis with many other data (existing annotated genomes, databases, bibliography, clinical data, medical images...).

Such scientific domains can get a large benefit from open science; sharing genomic data can greatly accelerate the research. Medical topics are clearly caught between the data protection issue and the needs of open science.

4 Conclusion

Data is the new gold and both AI and HPC communities must take this very seriously. It is urgent to treat the data issue, and the FAIR concept and consortiums around are very promising. However, both HPC and AI community must get involved in this consortium to make sure it contributes to scientific research.

FAIR data is not easy to set up as it involves not only the scientific community but also vendors, HPC centers, legal sector... Nevertheless, this is an unavoidable step to ensure a viable and substantial improvement of scientific research (HPC and AI areas). The FAIR consortium is a good protection to protect scientific data and limit their use in an economic context. The current approach of FAIR to address the data issue enables the communities to prepare their frameworks to big data issues and exploiting/analyzing these data.

HPC community will have large benefit from FAIR data but either from AI community, as it can drastically help simulations scalability and data treatment. We believe that HPC will be strongly impacted by Deep Learning applications. It is very likely that the first exaflop computer will be in fact a supercomputer dedicated to Deep Learning frameworks, which illustrates well the HPC strong evolution facing the AI rising.

References

1. Top500. <https://www.top500.org>
2. Top500 November 2018. <https://www.top500.org/lists/2018/11>
3. Green500. <https://www.top500.org/green500>
4. HPCG500. <http://www.hpcg-benchmark.org>
5. Deep500. <https://www.deep500.org>
6. Plan France Médecine Génomique 2025. <https://solidarites-sante.gouv.fr/systeme-de-sante-et-medico-social/recherche-et-innovation/france-genomique>
7. Bontempi, G., Ben Taieb, S., Le Borgne, Y.A.: Machine learning strategies for time series forecasting. In: Aufaure, M.A., Zimányi, E. (eds.) *Business Intelligence; eBISS 2012. Lecture Notes in Business Information Processing*, vol. 138. Springer, Heidelberg (2013)
8. Tolle, K.M., Tansley, D.S.W., Hey, A.J.G.: The fourth paradigm: data-intensive scientific discovery. *Proc. IEEE* **99**(8) (2011). <https://doi.org/10.1109/JPROC.2011.2155130>
9. Wilkinson, M.D., et al.: The FAIR Guiding Principles for scientific data management and stewardship. *Sci. Data* <https://doi.org/10.1038/sdata.2016.18>
10. Big Data and Extreme-Scale Computing: Pathways to Convergence; BDEC report; Tech Report No. ICL-UT-17-08; <http://www.exascale.org/bdec>; January 2018. *Int. J. High Performance Comput. Appl.* **32**(4) (2018)
11. Duraisamy, K., Iaccarino, G., Xiao, H.: Turbulence modeling in the age of data. *Annu. Rev. Fluid Mech.* **51**, 357–77 (2019)
12. Kim, M., Lee, Y., Park, H.-H., Hahn, S.J., Lee, C.-G.: Computational fluid dynamics simulation based on Hadoop Ecosystem and heterogeneous computing. *Comput. Fluids* **115**, 1–10 (2015)

13. Lange, B., Nguyen, T.: A Hadoop distribution for engineering simulation; [Research Report] INRIA Grenoble - Rhône-Alpes (2014). fhal-01130630; <https://hal.inria.fr/hal-01130630/document>
14. Gamahara, M., Hattori, Y.: Searching for turbulence models by artificial neural network. *Phys. Rev. Fluids* **2**, 054604 (2017)
15. Wilkinson, M., Dumontier, M., Aalbersberg, I.J., Appleton, G., Axton, M., Baak, A., Blomberg, N. and Boiten, J.W., da Silva Santos, B., Olavo, L., Bourne, P.E., Bouwman, J., Brookes, A.J., Clark, T., Crosas, M., Dillo, I., Dumon, O., Edmunds, S., Evelo, C.T., Finkers, R., Richard and Mons, B.: The FAIR Guiding Principles for scientific data management and stewardship. *Sci. Data* **3** (2016). <https://doi.org/10.1038/sdata.2016.18>
16. FAIR data consortium. <http://www.datafairport.org/>



LES of the Flow Past a Circular Cylinder Using a Multiscale Discontinuous Galerkin Method

Marta de la Llave Plata^(✉), Fabio Naddei, and Vincent Couaillier

ONERA – Université Paris-Saclay, 92320 Châtillon, France
marta.de_la_llave_plata@onera.fr
<https://www.onera.fr/>

Abstract. The variational multiscale (VMS) approach based on a modal discontinuous Galerkin (DG) method is used to perform LES of the sub-critical flow past a circular cylinder at Reynolds numbers 20 000 and 140 000, based on the cylinder diameter. The potential of using p-adaption in combination with DG-VMS is illustrated for the case at $Re = 140\,000$ by considering a non-uniform distribution of the polynomial degree based on a recently developed error estimation strategy [15].

Keywords: Discontinuous Galerkin · P-adaptivity · Large-eddy simulation · Variational multiscale approach

1 Introduction

The study of flows past cylinders is of relevance to many engineering applications, such as noise prediction in aircraft landing gears. A characteristic feature of bluff body aerodynamics is the appearance of a large-scale vortex shedding in the near wake which can lead to flow-induced sound and vibration of the structure. The ability to accurately predict this phenomenon across a wide range of Reynolds numbers using numerical methods is especially challenging, in particular because the location of the separation point on the cylinder wall is very sensitive to small disturbances in the flow. On the other hand, the geometrical representation of the cylinder adds an extra level of complexity in the context of high-order methods, due to the necessity to use large curved elements around the wall when the order of the polynomial approximation is increased (p-refinement).

In this work, the scale-resolving capabilities of the DG solver *Aghora* [4, 18] are illustrated by performing LES of the flow past a cylinder in the sub-critical regime at $Re = 20\,000$ and $140\,000$. The subgrid-scale (SGS) modelling approach adopted here is based on the VMS approach developed in [5] in the context of a modal DG method (DG-VMS). The potential of using p-adaptation for LES is demonstrated for the case at $Re = 140\,000$ by defining a non-uniform distribution of local polynomial degrees based on a recently developed error estimation strategy [15].

A limited number of LES simulations of this configuration have been reported in the literature for these two Reynolds numbers. We can cite the work presented in [13, 14, 19] for $Re = 20\,000$ and in [2, 9] for $Re = 140\,000$ based on second-order finite-volume methods (FVM) and different SGS models, and grid resolutions. The outcome of our DG-VMS simulations is compared with the high-resolution LES results reported by Lysenko et al. [13] for $Re = 20\,000$, and by Breuer [2] for $Re = 140\,000$ using low-dissipation second-order FVM. The material presented in these two articles is well documented and, in our view, constitutes a valuable reference to assess the performance of the present approach.

2 Governing Equations

Let $\Omega \subset \mathbb{R}^3$ be a bounded domain. The compressible Navier-Stokes (N-S) equations, with appropriate boundary conditions in $\partial\Omega$, read

$$\frac{\partial \mathbf{u}}{\partial t} + \nabla \cdot (\mathcal{F}_c(\mathbf{u}) - \mathcal{F}_v(\mathbf{u}, \nabla \mathbf{u})) = 0, \text{ in } \Omega \quad (1)$$

where $\mathbf{u} = (\rho, \rho \mathbf{v}, \rho E)^T$ is the vector of conservative variables. The vectors \mathcal{F}_c , and \mathcal{F}_v are the convective and viscous fluxes, respectively,

$$\mathcal{F}_c = \left(\rho, \rho \mathbf{v} \otimes \mathbf{v} + p \bar{\bar{\mathbf{I}}}, (\rho E + p) \mathbf{v} \right)^T, \quad \mathcal{F}_v = (0, \bar{\bar{\boldsymbol{\tau}}}, \bar{\bar{\boldsymbol{\tau}}} \cdot \mathbf{v} - \mathbf{q})^T \quad (2)$$

In (2), $\bar{\bar{\boldsymbol{\tau}}}$ represents the shear-stress tensor, given by

$$\bar{\bar{\boldsymbol{\tau}}} = \mu \left(2\bar{\bar{\mathbf{S}}} - \frac{2}{3}\bar{\bar{\mathbf{S}}}\bar{\bar{\mathbf{I}}} \right) \quad \text{with} \quad \bar{\bar{\mathbf{S}}} = \frac{1}{2}(\nabla \mathbf{v} + \nabla \mathbf{v}^T) \quad (3)$$

μ is the dynamic viscosity and $\bar{\bar{\mathbf{S}}}$ the rate-of-strain tensor. The heat-flux vector is written as $\mathbf{q} = -k\nabla T$, with T the temperature and k the thermal diffusivity.

3 The DG-VMS Formulation

Let Ω_h be a shape-regular partition of the domain Ω , into N non-overlapping and non-empty cells κ of characteristic size h . We also define the sets \mathcal{E}_i and \mathcal{E}_b of interior and boundary faces in Ω_h , such that $\mathcal{E}_h = \mathcal{E}_i \cup \mathcal{E}_b$. Let $\mathcal{V}_h^p = \{\phi \in L^2(\Omega_h) : \phi|_\kappa \in \mathcal{P}^p(\kappa), \forall \kappa \in \Omega_h\}$ be the functional space of piecewise polynomials of degree at most p , and $(\phi_\kappa^1, \dots, \phi_\kappa^{N_p}) \in \mathcal{P}^p(\kappa)$ a hierarchical and orthonormal modal basis of \mathcal{V}_h^p , of dimension N_p , confined to κ [1]. The solution in each element is thus expressed as a linear expansion of basis functions, the coefficients of which constitute the degrees of freedom (DOFs) of the problem at hand.

The LES technique used in this research is based on the projection of the N-S equations onto a the functional space \mathcal{V}_h^p . This projection operation implicitly defines a partitioning of the solution such that a turbulent field \mathbf{u} is decomposed

into its resolved, \mathbf{u}_h , and unresolved components, $\mathbf{u} - \mathbf{u}_h$. The variational form of the LES equations thus reads: find \mathbf{u}_h in \mathcal{V}_h^p such that $\forall \phi_h \in \mathcal{V}_h^p$ we have

$$\frac{\partial}{\partial t} \int_{\Omega_h} \phi_h \mathbf{u}_h dV + \mathcal{L}_c(\mathbf{u}_h, \phi_h) + \mathcal{L}_v(\mathbf{u}_h, \phi_h) = \mathcal{L}_{sgs}(\mathbf{u}, \mathbf{u}_h, \phi_h), \quad (4)$$

where we have used the definition of the L^2 -projection, i.e. $\int_{\Omega_h} (\mathbf{u} - \mathbf{u}_h) \phi_h = 0, \forall \phi_h \in \mathcal{V}_h^p$. In Eq. (4) \mathcal{L}_c and \mathcal{L}_v represent the weak form of the convective and viscous terms, respectively. The term \mathcal{L}_{sgs} on the right-hand-side of Eq. (4), is the variational form of the SGS residual representing the effect of the unresolved scales $\mathbf{u} - \mathbf{u}_h$ on the resolved field \mathbf{u}_h .

We now introduce the following notation: for a given interface in \mathcal{E}_i we define the average operator $\{\mathbf{u}\} = (\mathbf{u}^+ + \mathbf{u}^-)/2$ and the jump operator $\llbracket \mathbf{u} \rrbracket = \mathbf{u}^+ \otimes \mathbf{n} - \mathbf{u}^- \otimes \mathbf{n}$, where \mathbf{u}^+ and \mathbf{u}^- are the traces of the variable vector \mathbf{u} at the interface between elements κ^+ and κ^- , and \mathbf{n} denotes the unit outward normal vector to an element κ^+ . The DG discretization of the convective terms reads

$$\begin{aligned} \mathcal{L}_c(\mathbf{u}_h, \phi_h) \cong & - \int_{\Omega_h} \mathcal{F}_c(\mathbf{u}_h) \cdot \nabla_h \phi_h dV \\ & + \int_{\mathcal{E}_i} \llbracket \phi_h \rrbracket \mathbf{h}_c(\mathbf{u}_h^+, \mathbf{u}_h^-, \mathbf{n}) dS + \int_{\mathcal{E}_b} \phi_h^+ \mathcal{F}_c(\mathbf{u}_b) \cdot \mathbf{n} dS \end{aligned} \quad (5)$$

where the boundary values $\mathbf{u}_b = \mathbf{u}_b(\mathbf{u}_h^+, \mathbf{u}_{\text{ext}}, \mathbf{n})$, with \mathbf{u}_{ext} a reference external state, are computed so that the boundary conditions are satisfied on \mathcal{E}_b . In this paper, a modified version of the local Lax-Friedrichs (LLF) flux and the Roe scheme have been employed for the simulations at the lower and higher Reynolds numbers, respectively,

$$\mathbf{h}_c(\mathbf{u}_h^+, \mathbf{u}_h^-, \mathbf{n}) = \frac{1}{2} (\mathcal{F}_c(\mathbf{u}_h^+) \cdot \mathbf{n} + \mathcal{F}_c(\mathbf{u}_h^-) \cdot \mathbf{n} + \alpha \mathcal{D}(\mathbf{u}_h^+, \mathbf{u}_h^-, \mathbf{n})) \quad (6)$$

where $\mathcal{D}(\mathbf{u}_h^+, \mathbf{u}_h^-, \mathbf{n})$ is the upwinding dissipation function associated with the selected numerical flux. This is scaled by a coefficient α to calibrate the amount of numerical dissipation introduced. Based on numerical experiments, $\alpha = 0.1$ in this study. Indeed, for this value the simulation remains stable while minimizing the numerical dissipation introduced via the numerical flux.

The discretization of the viscous terms is performed using the *symmetric interior penalty* (SIP) method proposed by Hartmann and Houston [8],

$$\begin{aligned} \mathcal{L}_v(\mathbf{u}_h, \phi_h) \cong & \int_{\Omega_h} \mathcal{F}_v(\mathbf{u}_h, \nabla_h \mathbf{u}_h) \cdot \nabla_h \phi_h dV \\ & - \int_{\mathcal{E}_i} \llbracket \phi_h \rrbracket \{ \mathcal{F}_v(\mathbf{u}_h, \nabla_h \mathbf{u}_h) \} \cdot \mathbf{n} dS - \int_{\mathcal{E}_b} \phi_h^+ \mathcal{F}_v(\mathbf{u}_b, \nabla \mathbf{u}_b) \cdot \mathbf{n} dS \\ & - \int_{\mathcal{E}_i} \llbracket \mathbf{u}_h \rrbracket \{ \mathbf{G}^T(\mathbf{u}_h) \nabla_h \phi_h \} \cdot \mathbf{n} dS - \int_{\mathcal{E}_b} (\mathbf{u}_h^+ - \mathbf{u}_b) \{ \mathbf{G}^T(\mathbf{u}_b) \nabla_h \phi_h^+ \} \cdot \mathbf{n} dS \\ & + \int_{\mathcal{E}_i} \llbracket \phi_h \rrbracket \boldsymbol{\delta}(\mathbf{u}_h) \cdot \mathbf{n} dS + \int_{\mathcal{E}_b} \phi_h^+ \boldsymbol{\delta}_b(\mathbf{u}_h^+, \mathbf{u}_b) \cdot \mathbf{n} dS \end{aligned} \quad (7)$$

where $\mathbf{G}(\mathbf{u}_h) = \partial \mathcal{F}_v(\mathbf{u}_h, \nabla_h \mathbf{u}_h) / \partial (\nabla_h \mathbf{u}_h)$ is the so-called homogeneity tensor. The viscous fluxes may thus be written as $\mathcal{F}_v(\mathbf{u}_h, \nabla_h \mathbf{u}_h) = \mathbf{G}(\mathbf{u}_h) \nabla_h \mathbf{u}_h$. The penalty function is defined following the approach proposed in [8] as

$$\delta(\mathbf{u}_h) = \eta_{IP} \frac{p^2}{h} \mathbf{G}(\mathbf{u}_h) \llbracket \mathbf{u}_h \rrbracket \quad (8)$$

with η_{IP} the penalty parameter, which must be chosen sufficiently large.

The integrals in Eqs. (5) and (7) are computed by means of the Gauss-Legendre quadrature with $q = p + 1 + m$ points in each space direction, where m depends on the test case considered.

As regards the SGS term, the effect of the subgrid scales can be approximated by a closure term that depends only on the resolved field, $\mathcal{L}_{sgs}(\mathbf{u}, \mathbf{u}_h, \phi_h) \approx \mathcal{L}_m(\mathbf{u}_h, \phi_h)$. The compressible LES formalism of [11] is used here, which consists in introducing a SGS flux vector of the form,

$$\mathcal{F}_m = (0, \bar{\boldsymbol{\tau}}^{sgs}, -\mathbf{q}^{sgs})^T \quad (9)$$

Using the eddy-viscosity assumption, the SGS stress tensor $\bar{\boldsymbol{\tau}}^{sgs}$ is written as

$$\tau_{ij}^{sgs} = \rho_h \nu_t \left(2S_{ij} - \frac{2}{3} S_{kk} \delta_{ij} \right) \quad (10)$$

where ρ_h is the resolved density, S_{ij} are the components of the resolved rate-of-strain tensor $\bar{\mathbf{S}}$, and ν_t the turbulent eddy viscosity. The SGS heat-flux vector is given by

$$q_i^{sgs} = -\rho_h C_p \frac{\nu_t}{Pr_t} \frac{\partial T_h}{\partial x_i} \quad (11)$$

where T_h denotes the resolved temperature and Pr_t is the turbulent Prandtl number, assumed to be constant and equal to 0.6.

In this work, the Smagorinsky model is used, for which ν_t is expressed as

$$\nu_t = (C_s \Delta)^2 |\bar{\mathbf{S}}| \quad ; \quad |\bar{\mathbf{S}}| = \sqrt{2S_{ij}S_{ij}} \quad (12)$$

In (12), C_s is the model constant which usually takes a value between 0.1 and 0.2, and Δ is the filter size associated with a given element, defined here as $\Delta = \frac{h}{p+1}$, with h the characteristic size of the element.

Based on the formalism laid out above, the model term $\mathcal{L}_m(\mathbf{u}_h, \phi_h)$ is discretized using the same scheme employed to discretize the viscous fluxes. This amounts to replacing \mathcal{F}_v by \mathcal{F}_m in Eq. (7). For more details on the DG-LES formalism implemented in *Aghora* the reader is referred to [5, 6].

In VMS we assume that the effect of the unresolved scales on the largest resolved scales is negligible and thus the effect of the SGS model is confined to a range of small resolved scales. This is obtained in the DG-VMS framework by splitting the polynomial solution space \mathcal{V}_h^p into a low-order component $\mathcal{V}^l \equiv \mathcal{V}_h^{p_L} \subseteq \mathcal{V}_h^p$, associated with the large scales, and a high-order component $\mathcal{V}^s \equiv \mathcal{V}_h^p \setminus \mathcal{V}^l$ presenting the small scales, where p_L is called the scale-partition parameter. In this work, the SGS term is computed from the full resolved field, as proposed in [5], and the effect of the SGS model is removed from all scales belonging to \mathcal{V}^l by enforcing $\mathcal{L}_m(\mathbf{u}_h, \phi_h) = 0, \forall \phi_h \in \mathcal{V}^l$.

4 DG-VMS of the Flow Past a Circular Cylinder

The sections that follow report the results from the DG-VMS simulations of the cylinder flow at $Re = 20\,000$ and $140\,000$. At these sub-critical Reynolds numbers the boundary layer separates laminarly from the cylinder surface and transition to turbulence takes place in the free-shear layer. It is worth noting that in the version of the VMS algorithm used in this work, the scale-partition parameter p_L that sets the limit between large and small scales is constant across the domain. This implies that the SGS model will also be active in the cells covering the (laminar) boundary layer region. This is, however, not an issue in VMS, as, by definition, only the small scales are affected by the SGS dissipation, while the mean flow is let free of SGS dissipation. In the DG-VMS simulations presented in this paper a partition number $p_L = 1$ has been used (see Sect. 3 and [5]).

In both simulations a curved O-type mesh is considered in a computational domain with radial and spanwise extension of $25D$ and πD , respectively. The number of elements in the azimuthal and radial directions is 36, and in the spanwise direction 16 elements are used. This amounts to a total number of elements equal to 20736. In the case of the higher Reynolds number, a higher stretching factor is used in a region closer to the cylinder, which leads to a more pronounced clustering of the elements in the vicinity of the wall, with respect to the lower-Reynolds-number case. As will be shown below, this is consistent with the shorter length of the recirculation bubble expected and the resolution requirements of the boundary layer at this higher Reynolds number. The focus in this work is therefore on capturing the flow dynamics in the near-wake behind the cylinder, by putting most of the computational effort in this region. The region beyond the recirculation area can thus be considered as under-resolved.

Periodicity of the flow is assumed in the spanwise direction, and an isothermal no-slip boundary condition is imposed on the cylinder wall. A laminar free-stream flow at $M = 0.2$ is imposed via a far-field condition on the outer boundary of the computational domain. Finally, the time integration is performed using an explicit third-order accurate Runge-Kutta method.

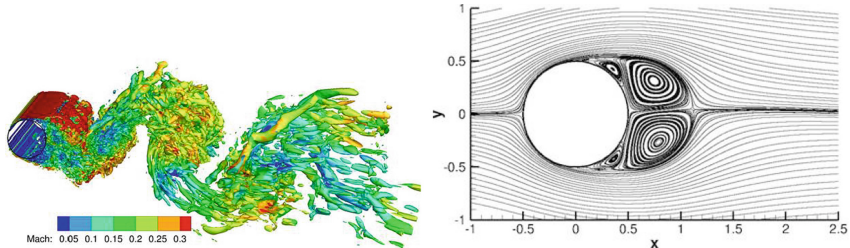
The present simulations were carried out on the Bull supercomputer Occigen at CINES. The total cost per convective time step in TauBench work units was 293160 for $Re = 20\,000$ (420 cores), and $1.27 \cdot 10^6$ for $Re = 140\,000$ (3360 cores).

4.1 Simulation Results at $Re = 20\,000$

For this lower-Reynolds-number case, the polynomial degree is set to $p = 4$, which leads to fifth-order accuracy in space and a number of DOFs of 2.59 million (Mdofs). The effective resolution at the wall is $\Delta r / (p + 1) = 0.01D$. Over-integration is used to reduce aliasing errors and increase the accuracy of the solution. A horizontal uniform flow at $M = 0.2$ is used as initial condition. After a transient period, a statistically steady (periodic) state is reached, from which the flow statistics are gathered for approximately 95 vortex-shedding cycles. Table 1 compares our DG-VMS results with those obtained by Lysenko et al. [13] using a second-order low-dissipative FV compressible solver at the same Mach number

Table 1. Cylinder flow at $Re = 20\,000$: integral flow quantities.

Data	$\Delta \left(\frac{U_c}{D} \right)$	$\frac{\Delta r_{min}}{D}$	Mdofs	N_{vs}	C_d	Cl_{rms}	S_t	$\frac{L_r}{D}$
Exp. [12, 16]	–	–	–	–	1.20	0.48	1.19	–
FV – $\mathcal{O}(2)$ [13]	–	$5.6 \cdot 10^{-4}$	12.4	75	[1.33–1.36]	[0.61–0.70]	[0.18–0.19]	[0.57–0.69]
DG – $\mathcal{O}(5)$	$2 \cdot 10^{-4}$	10^{-2}	2.59	95	1.39	0.64	0.19	0.67

**Fig. 1.** Flow past a circular cylinder at $Re = 20\,000$. Left: iso-surfaces of the Q-criterion coloured by the Mach number. Right: streamlines of mean flow.

$M = 0.2$ and for the same dimension of the computational domain as in the present simulation. The main integral flow quantities are shown in this table. The range of values shown for the reference simulation correspond to the use of different numerical schemes and SGS modelling approaches. More details about the FV simulations by Lysenko et al. can be found in their original paper [13].

We can see from this table that the results yielded by the DG-VMS fifth-order simulation are in fairly good agreement with the reference LES results. Only the value of the drag coefficient C_d is slightly above the upper-most value of the reference range, by about 2.2%. This is despite the fact that the DG simulation involves nearly five times fewer DOFs than the FV simulation. It is worth noting the much smaller effective size of the grid cells at the wall, which in the DG simulation is about 18 times smaller with respect to the reference value. The good prediction achieved with our DG approach is partly a consequence of the excellent approximation properties of polynomial expansions in representing thin boundary layers, as pointed out by Gottlieb and Orszag [7]. This coarseness of the mesh in the vicinity of the wall does not seem to impact the accuracy with which the integral quantities, and in particular the size of the recirculation bubble L_r , are captured. In fact, the value of L_r is well within the range of values reported in [13]. The different C_d and C'_l found in the experiment and the simulations might be due to compressibility effects linked to the use of $M = 0.2$.

Figure 1 shows a snapshot of the iso-surfaces of Q-criterion coloured by the Mach number (left) as well as the streamlines of the time-averaged flow field (right). We can see that the mean flow is characterised by the presence of a main recirculation bubble, and the appearance of two symmetrical secondary bubbles near the separation point in accordance with the literature. The value of the primal separation angle is estimated from the profile of the wall-shear

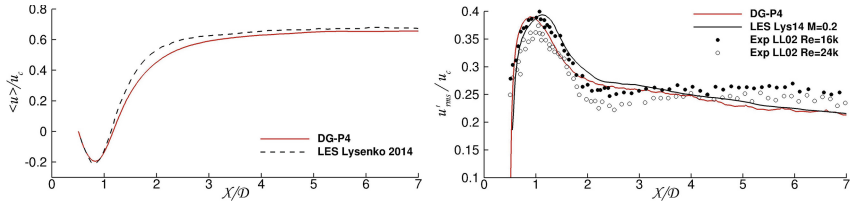


Fig. 2. Cylinder flow at $Re = 20\,000$: streamwise velocity statistics on wake centreline. Left: mean streamwise velocity; solid line: $DG - p4$, dashed line: incompressible FV simulation (TKE-I in [13]). Right: rms of streamwise velocity; red solid line: $DG - p4$, black solid line: compressible FV simulation (SMAG- γ in [13]), symbols: experimental data of Lim and Lee [12] at $Re = 16\,000$ (dots) and $Re = 24\,000$ (circles).

stress, which leads to $\theta_{sep} = 88^\circ$. This estimated value is in good agreement with the results of Lysenko et al. who predicted from their LES a value in the range $\theta_{sep} = 86^\circ - 88^\circ$. As pointed out by the author, these values are about 13% above the value predicted in the experiments of Son and Hanratty [20] and Norberg [16]. The cause for these discrepancies might be an insufficient resolution of the boundary layer, or else possible differences between the simulation and the experimental conditions.

To further assess the quality of our results, the statistics in the near-wake region are also analysed. Figure 2 therefore shows the mean streamwise velocity along the wake centreline (left), as well as the profile of root-mean-square (rms) of the axial velocity fluctuations (right). The present results are compared with the available data from [13]. For the first, the only data available is that from an incompressible FV simulation using the dynamic k -equation SGS model (see [13] for more details). Despite the different equation models used, the two mean streamwise velocity profiles are in relatively good agreement. As regards the profiles of rms of the axial velocity, our results are compared with the compressible CFD results from [13] on the fine mesh and the experimental data of Son and Hanratty [20] for Reynolds numbers $Re = 16\,000$ and $24\,000$. We can see that, overall, our results are in rather good agreement with the reference numerical data, and well within the range of the values predicted by the experiment. However, the discrepancies with the experimental data become visible from approximately $x/D = 2$. These differences are also observed for the reference CFD data. This is partly a consequence of the lack of resolution in this region. It is interesting to note that this under-resolution does not seem to have a strong effect on the quality of the prediction in the wall region and near-wake dynamics.

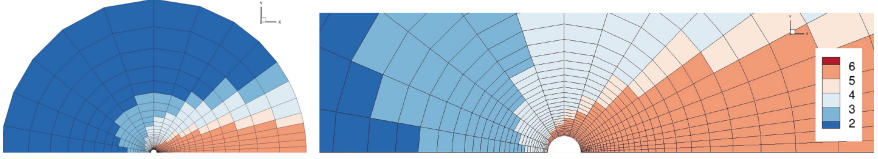


Fig. 3. p-adapted DG-VMS of cylinder flow at $Re = 140\,000$: distribution of p .

4.2 Static p-Adapted Simulation Results at $Re = 140\,000$

The use of p-adaptation, involving refinement as well as coarsening, allows for an important reduction of the number of DOFs with respect to uniform refinement, as well as an increased level of accuracy.

Description of the p-Adapted Algorithm

The p-adaptive algorithm employed here is that developed in [15]. The algorithm is initialised by specifying a uniform polynomial degree distribution. A first simulation is then carried out based on the prescribed polynomial degree that will serve as initial solution for the next iteration of the p-adaptive algorithm. At each iteration of the algorithm, a new distribution of polynomial degrees is defined based on local error estimates and a new numerical solution is computed. The error estimator used in this work is the small-scale energy density (SSED) estimator proposed in [15], which can also be interpreted as a measure of the kinetic energy associated with the highest-order modes representing the solution within the element.

For the simulations presented here, an initial uniform distribution of polynomial degree $p = 4$ is used. The DG simulation is then run until the flow is fully developed and reaches a statistically periodic state. From this point, the element-wise values of the SSED estimator are computed over approximately five vortex-shedding cycles.

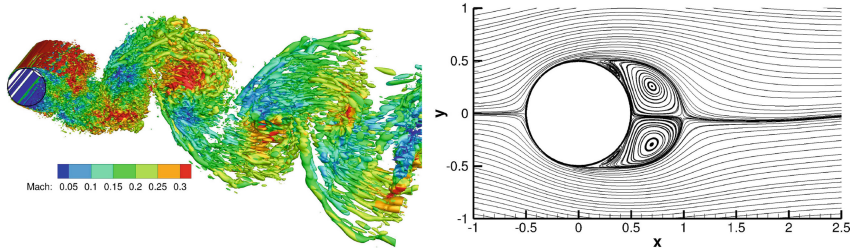
Based on the p-adaptation strategy just described, a new distribution of polynomial degrees is obtained. A new iteration of the p-adaptation algorithm is then applied. In this work, two iterations of the adaptive algorithm have been performed leading to the p-pattern shown in Fig. 3, with p varying from 2 to 6. In the spanwise direction p is kept constant. This is consistent with the statistically 2D character of the flow. The polynomial degree in the first element layer around the cylinder is $p = 6$. This yields an effective size of the first element at the wall of $\Delta r/(p+1) = 4 \cdot 10^{-3}$. This value is about 2.5 smaller than that corresponding to $Re = 20\,000$, in accordance with the fact that the boundary layer thickness is inversely proportional to \sqrt{Re} as predicted by the theory.

DG-VMS Results at $Re = 140\,000$

The p-adapted DG solution at this higher Re is compared with the numerical data reported by Breuer [2], as well as the experimental data from Cantwell and Coles [3]. In [2], the author performed a number of simulations using different levels of resolution and spanwise extensions of the computational domain.

Table 2. Circular cylinder flow at $Re = 140\,000$: comparison of integral flow quantities with the simulation results of Breuer [2] and Cantwell and Coles [3].

Data	$\Delta t \left(\frac{U_c}{D}\right)$	Mdofs	$\frac{\Delta r_{min}}{D}$	N_{vs}	C_d	$-C_{p,b}$	S_t	$\frac{L_r}{D}$
Experiment [3]	–	–	–	–	1.24	1.21	0.18	0.50
Breuer-C3 [2]	$2 \cdot 10^{-4}$	1.74	$4 \cdot 10^{-4}$	13–34	1.28	1.51	0.22	0.46
Breuer-D3 [2]	$2 \cdot 10^{-4}$	6.76	$4 \cdot 10^{-4}$	13–34	1.37	1.60	0.21	0.42
DG- $\mathcal{O}(3-7)$	$1.5 \cdot 10^{-4}$	4.98	$4 \cdot 10^{-3}$	71	1.43	1.59	0.19	0.50

**Fig. 4.** Cylinder at $Re = 140\,000$. Left: iso-surfaces of the Q-criterion coloured by the Mach number. Right: streamlines of mean flow.

Here we consider for comparison the simulations $C3$ and $D3$ corresponding to a spanwise length of the cylindrical domain of πD and a radial extension of $15D$. The number of DOFs was 1.74 and 6.76 Mdofs, respectively, for simulations $C3$ and $D3$. They are both based on the Smagorinsky model for SGS modelling. Table 2 compiles the values of the integral quantities obtained from the present simulation and for the reference data used for comparison. As regards the values of drag, C_d , and base pressure, $-C_{p,b}$, coefficients, our results are in good agreement with the CFD data from Breuer, though substantially larger than the experimental value. The Strouhal number, S_t , is in between the experimental and the numerical reference values. The S_t measured by Cantwell and Coles [3] appears, however, very low with respect to what has been found in other experimental works. In particular, Son and Hanratty [20] report a value slightly above 0.19 which is consistent with the value found in the present work. Finally, the recirculation length, L_r , predicted by the DG simulation is in perfect agreement with the experimental value and slightly higher than the numerical reference. We have however observed, that the value of this quantity is very sensitive to the averaging period, in agreement with the observations made in [17]. This might explain the differences found between our value and that reported by Breuer, who considered an averaging time considerably lower. As pointed out in [17], and from our own observations, this quantity is actually a very reliable indicator of the level of accuracy in the simulation. It is indeed very sensitive to the mesh resolution in the near-wake region, as well as to the amount of numerical and SGS dissipation in the simulation.

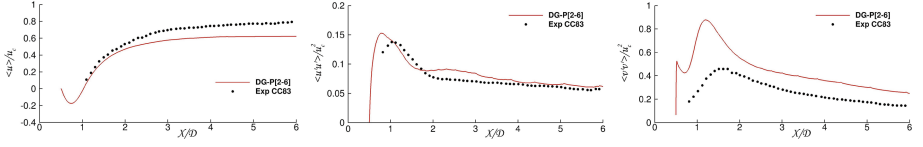


Fig. 5. Flow past a circular cylinder at $Re = 140\,000$. Wake centreline statistics. \bullet : Experiments [3], red solid line: p-adapted DG-VMS.

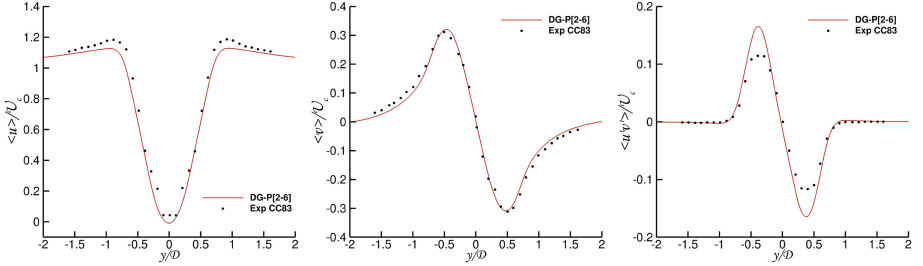


Fig. 6. Flow past a circular cylinder at $Re = 140\,000$. Wake statistics at $x=1$. \bullet : Experiments [3], red solid line: p-adapted DG-VMS.

Figure 4 shows a snapshot of the iso-surfaces of Q-criterion coloured by the Mach number (left) and the streamlines of the time-averaged flow field (right). We can observe the laminar separation that takes place on the cylinder surface and the significantly larger-scale vortex shedding originating from this separation, as compared to the case at $Re = 20\,000$. The separation angle is estimated to be about 94° in agreement with the value reported by Breuer for simulation *C3* on the coarser mesh, and slightly higher than the value 92° obtained by the author on the finer grid (simulation *D3*). On the right, we can see the plots of the streamlines of the mean flow. The most salient feature is the length of the recirculation bubble that shrinks as the Re number is increased. It is also worth noting the two small secondary bubbles showing up in our simulation, not observed in the experiments, nor in the simulation by Breuer. These two small secondary bubbles have also been found, however, in the simulation performed by Karabelas [10]. No clear explanation for this discrepancy with the experiments can be given today, and further research will be necessary to clarify this point. As regards the *rms* of the drag and lift coefficients we obtain the following values, $C'_d = 0.094$ and $C'_l = 0.79$.

In Fig. 5, the wake centreline statistics are also compared with those obtained from the experiment. As regards the mean velocity profile, we can see that the length of the recirculation region matches very well the experimental value (see also Table 2). It is apparent from these results, however, that as we move further downstream from the recirculation region, the streamwise velocity levels are significantly under-predicted. This is partly due to the very coarse mesh used in the wake beyond the recirculation region. This is in contrast with the profiles

of *rms* of the streamwise velocity $\langle u' u' \rangle$, better predicted over a longer distance beyond the recirculation zone. This might be a consequence of the higher levels, with respect to the reference, found in the region closer to the cylinder base. As regards the cross-stream Reynolds stresses $\langle v' v' \rangle$, their magnitude is significantly higher than the experimental value, although in fairly agreement with the values predicted by Breuer on his fine-grid simulations (see [2], not shown here). We have also inspected the wake statistics at a location $x = 1$ and compared to the experimental data of Cantwell and Coles [3]. The outcome from this comparison can be seen in Fig. 6. We can observe the overall good agreement found with the experiment for these quantities. The most significant discrepancies appear in the profile of the shear stresses $\langle u' v' \rangle$, although their magnitude is in line with the differences found by Breuer on his fine-grid simulations. These discrepancies might be linked to the different conditions between the experiment and the simulations (e.g. zero turbulence level at the inlet in the simulation). In fact, regarding the study carried out in [2], the author mentioned that grid refinement did not appear to provide convergence towards the experimental values.

5 Conclusions

The scale-resolving capabilities of the DG solver Aghora [4, 18] have been illustrated by performing high-order LES of the flow past a circular cylinder in the sub-critical regime. The SGS modelling approach adopted here is based on the DG-VMS formalism described in [5]. The static p-adaptive algorithm recently proposed in [15] has been successfully applied to cylinder flow at $Re = 140\,000$. The maximum order of accuracy used in these simulations amounts to fifth and seventh-order for $Re = 20\,000$ and $140\,000$, respectively.

The outcome of our simulations has been compared with the high-resolution LES results reported by Lysenko et al. [13] for $Re = 20\,000$, and by Breuer [2] for $Re = 140\,000$, using low-dissipation second-order FVM, as well as with the available experimental data. An overall good agreement with the reference CFD data is found in terms of integral flow quantities and near-wake statistics. This is despite the fact that the DG-VMS simulations involve much fewer DOFs than the FV LES. For the higher Re , some discrepancies with the experimental data have been found. These differences are, however, in line with those found in the work of Breuer [2] and, based on published research, might be explained by the different flow conditions between the simulations and the experiment.

It is noteworthy that the effective height of the first grid cell off the wall in the DG simulations is one order of magnitude larger than in the reference LES. This highlights the excellent approximation properties of DG approximations in representing boundary layers.

Acknowledgements. This research has been partly funded by the European Union's Horizon 2020 TILDA project (grant agreement number 635962). This work was performed using HPC resources from GENCI (Grants A0022A10129 and A0032A10309).

References

1. Bassi, F., Botti, L., Colombo, A., Di Pietro, D.A., Tesini, P.: On the flexibility of agglomeration based physical space DG discretizations. *J. Comput. Phys.* **231**(1) (2012)
2. Breuer, M.: A challenging test case for large-eddy-simulation: high Reynolds number circular cylinder flow. *Int. J. Heat Fluid Flow* **21**(5) (2000)
3. Cantwell, B., Coles, D.: An experimental study of entrainment and transport in the turbulent near wake of a circular cylinder. *J. Fluid Mech.* **136** (1983)
4. Chapelier, J.B., de la Llave Plata, M., Renac, F., Lamballais, E.: Evaluation of a high-order discontinuous Galerkin method for the DNS of turbulent flows. *Comput. Fluids* **95** (2014)
5. Chapelier, J.B., de la Llave Plata, M., Lamballais, E.: Development of a multiscale LES model in the context of a modal DG method. *Comput. Methods Appl. Mech. Eng.* **307** (2016)
6. de la Llave Plata, M., Couaillier, V., Le Pape, M.C.: On the use of a high-order discontinuous Galerkin method for DNS and LES of wall-bounded turbulence. *Comput. Fluids* **176** (2018)
7. Gottlieb, D., Orszag, S.A.: *Numerical Analysis of Spectral Methods: Theory and Applications*. SIAM (1977)
8. Hartmann, R., Houston, P.: An optimal order interior penalty DG discretization of the compressible Navier-Stokes equations. *J. Comput. Phys.* **227**(22) (2008)
9. Fröhlich, J., Rodi, W., Bertoglio, J.P., Bieder, U., Touil, H.: LES of flow around circular cylinders on structured and unstructured grids, II. In: Hirschel, E.H. (eds.) *Numerical Flow Simulation II. Notes on Numerical Fluid Mechanics*, vol. 75. Springer (2001)
10. Karabelas, S.J.: LES of high-Reynolds number flow past a rotating cylinder. *Int. J. Heat Fluid Flow* **31**(4) (2010)
11. Lesieur, M., Métais, O., Comte, P.: *Large-Eddy Simulation of Turbulence*. Cambridge University Press, Cambridge (2005)
12. Lim, H.C., Lee, S.J.: Flow control of circular cylinders with longitudinal grooved surfaces. *AIAA J.* **40**(10) (2002)
13. Lysenko, D.A., Ertesvåg, I.S., Rian, K.E.: LES of the flow over a circular cylinder at Reynolds number 2×10^4 . *Flow Turbul. Combust.* **92**(3) (2014)
14. Moussaed, C., Wornom, S., Salvetti, M.-S., Koobus, B., Dervieux, A.: Impact of dynamic subgrid-scale modeling in variational multiscale large-eddy simulation of bluff-body flows. *Acta Mech.* **225**(12) (2014)
15. Naddei, F., de la Llave Plata, M., Couaillier, V.: A comparison of refinement indicators for p-adaptive simulations of steady and unsteady flows using DG methods. *J. Comput. Phys.* **376** (2019)
16. Norberg, C.: Fluctuating lift on a circular cylinder: review and new measurements. *J. Fluids Struct.* **17** (2003)
17. Parnaudeau, P., Carlier, J., Heitz, D., Lamballais, E.: Experimental and numerical studies of the flow over a circular cylinder at Reynolds number 3900. *Phys. Fluids* **20**(8) (2008)
18. Renac, F., de la Llave Plata, M., Martin, E., Chapelier, J.-B., Couaillier, C.: Aghora: a high-order DG solver for turbulent flow simulations. In: Kroll, et al. (eds.) *IDIHOM: Industrialization of High-Order Methods - A Top-Down Approach. Notes on Numerical Fluid Mechanics and Multidisciplinary Design*, vol. 128. Springer (2015)

19. Salvatici, E., Salvetti, M.V.: Large-eddy simulations of the flow around a circular cylinder: effects of grid resolution and subgrid scale modeling. *Wind Struct.* **6**(6) (2003)
20. Son, J., Hanratty, T.: Velocity gradients at the wall for flow around a cylinder at Reynolds numbers from 5×10^3 to 10^5 . *J. Fluid Mech.* **35** (1969)



A Volume-of-Fluid Dual-Scale Approach for Simulating Turbulent Liquid/Gas Interactions

Dominic Kedelty^(✉), James Uglietta, and Marcus Herrmann

Arizona State University, Tempe, AZ 85284, USA

dkedelty@asu.edu

<http://www.multiphase.asu.edu>

Abstract. Advances to a dual-scale modeling approach (Gorokhovski and Herrmann, 2008) are presented to describe turbulent phase interface dynamics in a Large Eddy Simulation spatial filtering context. Spatial filtering of the governing equations to decrease the burden of Direct Numerical Simulation introduces several sub-filter terms that require modeling. Instead of developing individual closure models for the interface associated terms, the dual-scale approach uses an exact closure by explicitly filtering a fully resolved realization of the phase interface. This resolved realization is maintained on a high-resolution over-set mesh using a Refined Local Surface Grid approach (Herrmann, 2008) employing an un-split, geometric, bounded, and conservative Volume-of-Fluid method (Owkes and Desjardins, 2014). Advection of the phase interface on this DNS scale requires a reconstruction of the fully resolved interface velocity. This velocity is the sum of the filter scale velocities, readily available from an LES solver, and sub-filter velocity fluctuations. These fluctuations can be due to sub-filter turbulent eddies, which can be reconstructed on-the-fly using a local fractal interpolation technique (Scotti and Meneveau, 1999) to generate time evolving sub-filter velocity fluctuations. In this work, results from the dual-scale LES model are compared to DNS results for four different realizations of a unit density and viscosity contrast interface in a homogeneous isotropic turbulent flow at infinite Weber number. Introduction of a sub-filter turbulent velocity reconstruction in a passive scalar context is the first step towards use of a dual-scale model for multiphase applications.

Keywords: Volume-of-fluid · Dual-scale · Fractal interpolation · RLSG

1 Introduction

Atomization in turbulent environments involves a vast range of length and time scales. Predictive simulations aiming to resolve all relevant scales thus require

The support of NASA TTT grant NNX16AB07A is gratefully acknowledged.

© Springer Nature Switzerland AG 2021

M. Deville et al. (Eds.): TI 2018, NNF 149, pp. 39–51, 2021.

https://doi.org/10.1007/978-3-030-65820-5_4

enormous computational resources, taxing even the most powerful computers available today [5]. Since primary atomization is governed by the dynamics of the interface, a need therefore exists for appropriate interface models that make the computational cost of predicting the atomization outcome more tractable.

A wide range of phenomenological models aiming to represent statistically the essential features of atomization have been proposed in the past. Although these aim to introduce the dominant mechanisms for breakup, they often use round blobs injected from the nozzle exit and hence neglect all details of the interface dynamics.

Other modeling approaches to atomization include stochastic models [6, 7] representing the interface by constituent stochastic particles and the mean interface density transport equation model for Reynolds-Averaged Navier-Stokes (RANS) approaches [21, 22]. The former treats the interface dynamics in a stochastic sense but requires the *a priori* knowledge of the breakup mechanism, whereas the latter is affected by the drawbacks of the RANS approach: the transport of the mean interface density is modeled by a diffusion-like hypothesis, thereby neglecting the spatial grouping effects of liquid elements [5].

In the context of Large Eddy Simulations (LES), [12, 18–20] have proposed models to close the unclosed terms arising from the introduction of spatial filtering into the governing equations. However, these models typically neglect the contribution of the sub-filter surface tension term and are based on a cascade process hypothesis that may be questionable in the context of surface tension-driven atomization. An exception is the model for the sub-filter surface tension term proposed in [1]. In [9, 11], a dual-scale approach for LES of interface dynamics was proposed and a model for the sub-filter surface tension induced motion of phase interfaces was developed.

The purpose of this contribution is to develop a model for the sub-filter phase interface motion induced by sub-filter turbulent velocity fluctuations. Combining such a model with the surface tension model proposed in [9, 11] will result in a LES model applicable to atomizing flows.

2 Governing Equations

The equations governing the fully resolved motion of an unsteady, incompressible, immiscible, two-fluid system in the absence of surface tension are the Navier-Stokes equations,

$$\frac{\partial \rho \mathbf{u}}{\partial t} + \nabla \cdot (\rho \mathbf{u} \otimes \mathbf{u}) = -\nabla p + \nabla \cdot (\mu (\nabla \mathbf{u} + \nabla^T \mathbf{u})), \quad (1)$$

where \mathbf{u} is the velocity, ρ the density, p the pressure, and μ the dynamic viscosity. Here, we neglect surface tension to solely focus on the turbulence induced dynamics of phase interfaces. Furthermore, the continuity equation results in a divergence-free constraint on the velocity field

$$\nabla \cdot \mathbf{u} = 0. \quad (2)$$

Assuming ρ and μ are constant within each fluid, density and viscosity can be calculated from

$$\rho = \psi\rho_l + (1 - \psi)\rho_g \quad (3)$$

$$\mu = \psi\mu_l + (1 - \psi)\mu_g, \quad (4)$$

where indices l and g denote values in liquid and gas, respectively, and ψ is a volume-of-fluid scalar that is $\psi = 0$ in the gas and $\psi = 1$ in the liquid with

$$\frac{\partial\psi}{\partial t} = -\mathbf{u} \cdot \nabla\psi = -\nabla \cdot (\mathbf{u}\psi) + \psi\nabla \cdot \mathbf{u}. \quad (5)$$

Here, the last term on the right-hand side is zero for incompressible flows, see Eq. (2). In this work, unit density and viscosity ratios are considered making this a single-phase flow, therefore Eqs. (3) and (4) are unnecessary but are included for completeness sake.

2.1 Filtered Governing Equations

Introducing spatial filtering into Eqs. (1) and (2) and assuming that the filter commutes with both the time and spatial derivatives, the filtered governing equations can be derived [20],

$$\frac{\partial\bar{\rho}\bar{\mathbf{u}}}{\partial t} + \nabla \cdot (\bar{\rho}\bar{\mathbf{u}} \otimes \bar{\mathbf{u}}) = -\nabla\bar{p} + \nabla \cdot (\bar{\mu}(\nabla\bar{\mathbf{u}} + \nabla^T\bar{\mathbf{u}})) + \boldsymbol{\tau}_1 + \nabla \cdot (\boldsymbol{\tau}_2 + \boldsymbol{\tau}_3), \quad (6)$$

$$\nabla \cdot \bar{\mathbf{u}} = 0, \quad (7)$$

where $\bar{\cdot}$ indicates spatial filtering, and

$$\boldsymbol{\tau}_1 = \frac{\partial\bar{\rho}\bar{\mathbf{u}}}{\partial t} - \frac{\partial\rho\bar{\mathbf{u}}}{\partial t} \quad (8)$$

$$\boldsymbol{\tau}_2 = \bar{\rho}\bar{\mathbf{u}} \otimes \bar{\mathbf{u}} - \overline{\rho\mathbf{u} \otimes \mathbf{u}} \quad (9)$$

$$\boldsymbol{\tau}_3 = \overline{\mu(\nabla\mathbf{u} + \nabla^T\mathbf{u})} - \bar{\mu}(\nabla\bar{\mathbf{u}} + \nabla^T\bar{\mathbf{u}}), \quad (10)$$

where $\boldsymbol{\tau}_1$, $\boldsymbol{\tau}_2$, and $\boldsymbol{\tau}_3$ are associated, respectively, with acceleration, advection, and viscous effects [20]. Using Eqs. (3) and (4), the filtered density and viscosity in Eq. (6) are

$$\bar{\rho} = \rho_l\bar{\psi} + \rho_g(1 - \bar{\psi}) \quad (11)$$

$$\bar{\mu} = \mu_l\bar{\psi} + \mu_g(1 - \bar{\psi}), \quad (12)$$

where

$$\bar{\psi} = \int \mathcal{G}(\mathbf{x})\psi d\mathbf{x}, \quad (13)$$

and \mathcal{G} is a normalized spatial filter function.

3 The Dual-Scale Approach to Modeling Sub-filter Interface Dynamics

Instead of relying on a cascade process by which dynamics on a sub-filter scale can be inferred from the dynamics on the resolved scale, the dual-scale approach proposed in [11] aims to maintain a fully resolved realization of the immiscible interface geometry at all times, expressed, for example, in terms of a volume-of-fluid scalar ψ . Then $\overline{\psi}$ can be calculated exactly by explicit filtering using Eq. (13).

Although this is an exact closure, the problem of modeling is of course simply shifted to the problem of maintaining a fully resolved realization of the interface geometry, i.e., describing the fully resolved motion of the interface, Eq. (5). Since the fully resolved velocity is the sum of the filtered velocity and the sub-grid velocity, $\mathbf{u} = \overline{\mathbf{u}} + \mathbf{u}_{sg}$, this results in

$$\frac{\partial \psi}{\partial t} = -\nabla \cdot ((\overline{\mathbf{u}} + \mathbf{u}_{sg}) \psi) + \psi \nabla \cdot (\overline{\mathbf{u}} + \mathbf{u}_{sg}), \quad (14)$$

where the only term requiring modeling is \mathbf{u}_{sg} . In [11], a model for \mathbf{u}_{sg} is proposed consisting of three contributions,

$$\mathbf{u}_{sg} = \mathbf{u}' + \delta \mathbf{u} + \mathbf{u}_\sigma, \quad (15)$$

where \mathbf{u}' is due to sub-filter turbulent eddies, $\delta \mathbf{u}$ is attributed to the interface velocity increment due to relative sub-filter motion between the two immiscible fluids, and \mathbf{u}_σ is due to sub-filter velocities induced by sub-filter surface tension forces. The focus of the current contribution is on the first term; for a modeling outline of the second term, the reader is referred to [10, 11], and for modeling of the last term, the reader is referred to [9].

3.1 Sub-filter Turbulent Fluctuation Velocity Models

We propose to reconstruct the sub-filter turbulent fluctuation velocity \mathbf{u}' using fractal interpolation [17]. To demonstrate fractal interpolation in one dimension, consider 3 adjacent LES scale nodes x_0 , x_1 , and x_2 with velocities \overline{u}_0 , \overline{u}_1 , and \overline{u}_2 . Following [4, 17] the fractal interpolation operator \mathcal{W}_{FI} can be written as

$$\begin{aligned} \mathcal{W}_{FI}(x) = & \overline{u}_0 + \frac{\overline{u}_1 - \overline{u}_0}{x_1 - x_0}(x - x_0) \\ & + d_1 \left(u(2x - x_0) - \overline{u}_0 - \frac{\overline{u}_2 - \overline{u}_0}{x_2 - x_0}(2x - x_0) \right) \text{ if } x \in [x_0, x_1] \end{aligned} \quad (16)$$

$$\begin{aligned} \mathcal{W}_{FI}(x) = & \overline{u}_1 + \frac{\overline{u}_2 - \overline{u}_1}{x_2 - x_1}(x - x_1) \\ & + d_2 \left(u(2x - x_0) - \overline{u}_0 - \frac{\overline{u}_2 - \overline{u}_0}{x_2 - x_0}(2x - x_0) \right) \text{ if } x \in [x_1, x_2] \end{aligned} \quad (17)$$

Here $|d_1| < 1$ and $|d_2| < 1$ are stretching factors making \mathcal{W}_{FI} a contractive mapping [17]. Successively applying the fractal interpolation operator \mathcal{W}_{FI} starting with the LES filter velocities, generates the fully resolved turbulent fluctuation velocity. In order to extend the method into three dimensions, the fractal interpolation operator is first performed in one spatial direction only, followed by separate 1D fractal interpolations in the other two directions [17].

The determination of the values of the stretching factors d_1 and d_2 follows the so-called ZE1 model of [17] by using $d_1 = -d_2 = \pm 2^{-1/3}$ with the sign chosen randomly with equal probability. This choice of d_i generates a velocity signal that satisfies the $-5/3$ kinetic energy spectrum of turbulence at all sub-filter scales.

4 Numerical Methods

Equation (14) is solved using an unsplit geometric transport scheme for volume-of-fluid scalars that ensures both discrete volume conservation of each fluid and boundedness of the volume-of-fluid scalar, ψ [13]. Geometric reconstruction of the interface within each computational cell is done using PLIC reconstruction, employing analytical formulas [16] using ELVIRA estimated normals [14, 15].

To efficiently solve Eq. (14) for the fully resolved immiscible interface, the RLSG method [8] is employed. By design, it solves the interface capturing advection equation on a separate, highly resolved Cartesian overset grid of mesh spacing h_G , independent of the underlying LES flow solver grid of mesh spacing h . In the dual-scale LES approach, h_G needs to be chosen sufficiently small to maintain a fully resolved realization of the phase interface.

The velocity \mathbf{u} at RLSG scale h_G is calculated from

$$\mathbf{u} = \mathcal{W}_{FI}^k \bar{\mathbf{u}}, \quad (18)$$

where the superscript k indicates k -times application of the fractal interpolation operator \mathcal{W}_{FI} , with

$$k = \frac{\log\left(\frac{h}{h_G}\right)}{\log(2)}. \quad (19)$$

Since the LES flow solver used in this work utilizes a staggered mesh layout, the face normal velocities in each spatial direction are not co-located and hence the fractal interpolation has to be performed for different locations depending on the spatial component of the velocity vector.

The unsplit, geometric advection scheme of [13] requires face-centered velocities that are discretely divergence-free to ensure both conservation and boundedness. While discretely divergence free filtered velocities $\bar{\mathbf{u}}$ are available on the flow solver mesh in a standard fractional step method, i.e., $\nabla_h \cdot \bar{\mathbf{u}} = 0$, the fractal interpolated velocities \mathbf{u} are not necessarily divergence free on the fine overset mesh. To ensure $\nabla_{h_G} \cdot \mathbf{u} = 0$, \mathbf{u} is projected into the subspace of solenoidal velocity fields using the projection/correction step of a standard fractional step method applied to the overset mesh contained within each LES cell separately.

Note that the resulting Poisson systems that need to be solved to determine the Lagrange multiplier for projection of \mathbf{u} are defined on a per LES cell basis, necessitating an additional step to make the LES cell face average of \mathbf{u} equal to the LES scale filtered velocity $\bar{\mathbf{u}}$. This is achieved by computing and applying a per cell face constant correction velocity to \mathbf{u} , similar to the approach used to determine an outlet correction velocity in the fractional step method to make the approach satisfy the continuity equation on the entire domain. Here the correction velocity applied to each cell face ensures satisfying the continuity equation for u on the LES filter scale h .

The fractal interpolation reconstruction is performed at every LES time step such that the resolved scale velocity \mathbf{u} is actively evolving with the LES velocity $\bar{\mathbf{u}}$ on the LES time scale.

Finally, to calculate $\bar{\psi}$, Eq. (13) is evaluated by setting the filter size to the local flow solver mesh spacing h and evaluating the integral by explicitly summing the volume-of-fluid scalar ψ of those overset-mesh cells that are contained within a given LES flow solver cell.

4.1 Comparison Metrics

Assuming that the phase interface is initially planar with normal orientation in the y -direction, we define $\alpha(x, z, t)$ as the liquid volume fraction that is contained within a square column in the y -direction with cross sectional area equal to h_G^2 . Using the definition of $\alpha(x, z, t)$, the RMS sum of the time evolution of α can be defined as

$$\alpha'_0(t) = \sqrt{\frac{1}{L^2} \int_L \int_L ((\alpha(x, z, t) - \alpha(x, z, 0))^2 dx dz}. \quad (20)$$

This quantity depends predominantly on the large scale movement of the interface. Defining $\bar{\alpha}(x, z, t)$ as the liquid volume fraction contained within a square column in the y -direction with cross sectional area equal to the LES filter scale h^2 , we define the sub-filter liquid column height RMS as

$$\alpha'(t) = \sqrt{\frac{1}{L^2} \int_L \int_L ((\alpha(x, z, t) - \bar{\alpha}(x, z, t))^2 dx dz}, \quad (21)$$

This quantity depends predominantly on the sub-filter transport of the volume fraction.

To take into account that even on an LES mesh scale, the PLIC reconstruction of the filtered phase interface geometry provides a level of sub-filter geometry resolution beyond the mere liquid column height $\bar{\alpha}$, we define a local quantity C_{mix} that measures the sub-filter variation of the phase interface on the overset mesh compared to the LES mesh. C_{mix} is calculated by first performing a PLIC reconstruction on the LES mesh using the filtered volume fraction $\bar{\psi}$, see Fig. 1. The reconstructed planar representation of the phase interface is then used to calculate liquid volume fractions on the overset mesh $\bar{\psi}_{h_G}$. The root mean square

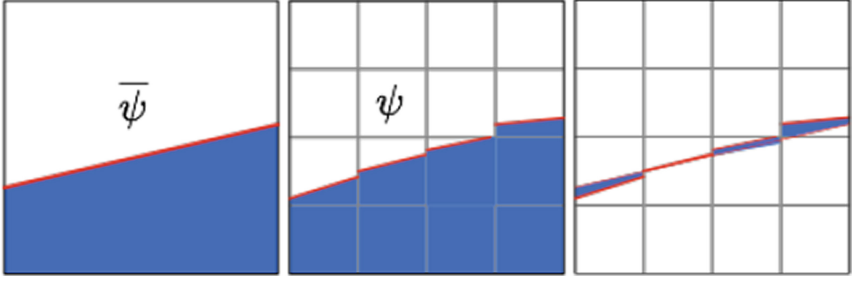


Fig. 1. PLIC geometry on LES mesh cell (left), fully resolved PLIC geometry (center), difference used to calculate C_{mix} (right).

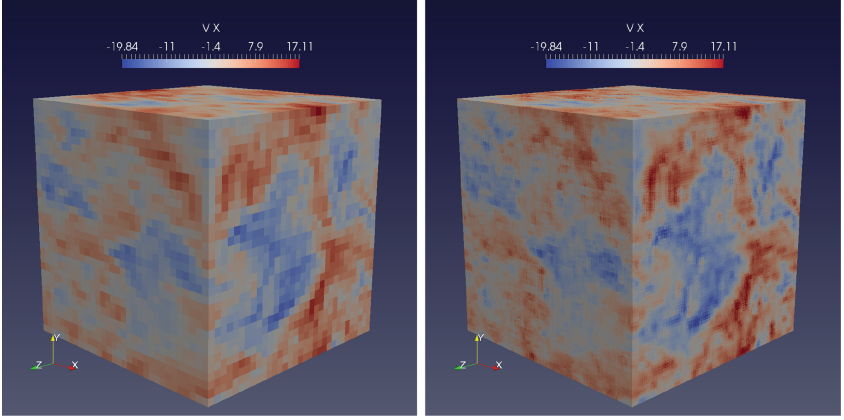


Fig. 2. Comparison of LES filtered velocity (left) and fractal interpolated velocity (right).

of the difference of these volume fractions and the fully resolved volume fractions ψ , see Fig. 1, is C_{mix} ,

$$C_{mix}(t) = \sqrt{\frac{1}{L^3} \int_L \int_L \int_L (\psi - \bar{\psi}_{h_G})^2 dx dy dz}. \quad (22)$$

It should be pointed out that both α' and C_{mix} will remain zero for all time without a dual-scale model.

The probability density function (PDF) of interface curvature is used as a final comparison metric. The curvature that is sampled is the mean curvature calculated by height function [3]. Samples are taken from every RLSG cell that contains an interface and $|\kappa|$ is used to create the PDF.

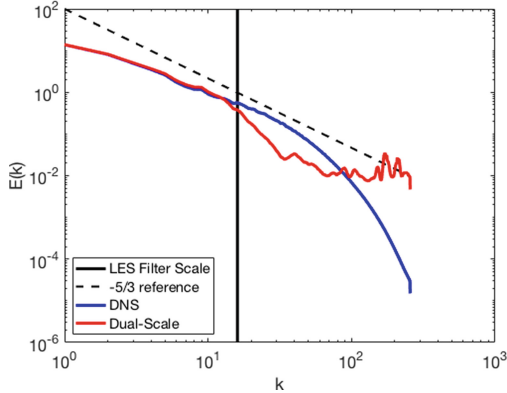


Fig. 3. Resulting 3D spatial kinetic energy spectra for 512^3 overset mesh using fractal interpolation (red). DNS (blue) and $-5/3$ reference line (dashed) are also provided. Vertical solid black line denotes the LES filter scale.

5 Results and Discussion

An initially flat interface is placed inside a box of fully developed isotropic turbulence. The fully developed isotropic turbulence field was graciously provided by R. Chiodi and O. Desjardins [2]. Both density and viscosity ratio are unity, and no surface tension forces are present with a Reynolds number of $Re_\lambda = 156$ and $We_\lambda = \infty$. Here, we present DNS and LES results using the dual-scale approach employing a LES mesh resolution of 32^3 and an overset mesh resolution of 512^3 for four different realizations generated by placing the phase interface at different initial heights in the turbulent velocity field. The four different initial heights listed from realization 1–4 are $y = \pi, y = \pi/2, y = 0, y = 3\pi/2$. DNS results were obtained using a 512^3 mesh for both the flow solver and interface advection scheme.

Figure 2 shows, as an example, a comparison of the LES filtered velocity field and the fractal interpolated velocity. Noticeably more small scale structure is visible in the fractal interpolated velocity compared to the filter scale LES velocity. This is corroborated by the kinetic energy spectrum shown in Fig. 3 that compares the kinetic energy spectrum of the fractal interpolated velocities to the DNS velocities. The fractal interpolation kinetic energy spectrum does show a noticeable dip before beginning to follow the $-5/3$ energy cascade. Note the absence of any viscous dissipation range in the fractal interpolated velocities.

Figure 4 compares one realization of the phase interface geometry using fractal interpolation and the interface geometry that would be obtained without any dual-scale model. Including the fractal interpolated sub-filter velocity in the advection velocity of the resolved realization of the interface clearly leads to significantly more surface corrugations, as expected.

Figure 5a–b shows the liquid column height RMS α'_0 with respect the initially flat interface. In Fig. 5a, comparison of the four different realizations show a large

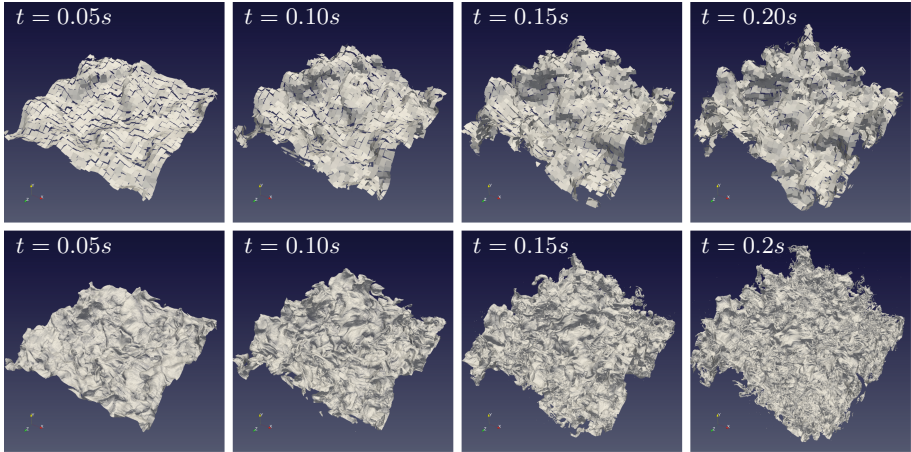


Fig. 4. Comparison of time evolving phase interface geometry for Realization #1 of homogeneous isotropic turbulence at several time steps: no dual-scale model (top) and fractal interpolation velocity (bottom).

effect on α'_0 , because α'_0 depends strongly on the large scale motion of the interface that are noticeably different from realization to realization. However, each of the individual LES results shows very good agreement with its corresponding DNS result. Figure 5b compares the LES results with and without dual-scale model to the DNS results for one realization. It can be seen that the dual-scale LES result agrees more closely with the DNS, although the results without dual-scale model are not too different from the DNS results since α'_0 depends mostly on the large scale motion on the LES filter scale.

Figure 5c shows the sub-filter liquid column height RMS α' for the different realizations. The results presented are only shown until the periodic boundary condition in the interface normal direction impacts the measurement. The difference between the realizations is very small, consistent with the observation that α' is a sub-filter quantity exhibiting a degree of universality of the small scales. The dual-scale LES simulations consistently over-predict α' at later times compared to the DNS results. However, it should be noted that α' is always zero if no dual-scale LES model is applied and the dual-scale model is therefore a significant improvement.

Figure 5d compares the sub-filter variation C_{mix} for the different realizations. Again, the difference between the realizations is small, indicating that C_{mix} is a sub-filter quantity that exhibits a degree of universality on the small scales. The dual-scale LES simulations consistently under-predict C_{mix} compared to the DNS results. However, again it should be noted that C_{mix} is always zero if no dual-scale LES model is applied and the dual-scale model is therefore a significant improvement.

Finally, Fig. 6 compares the PDF of interfacial curvature. Interestingly, no difference in the PDFs can be observed between the four different realizations

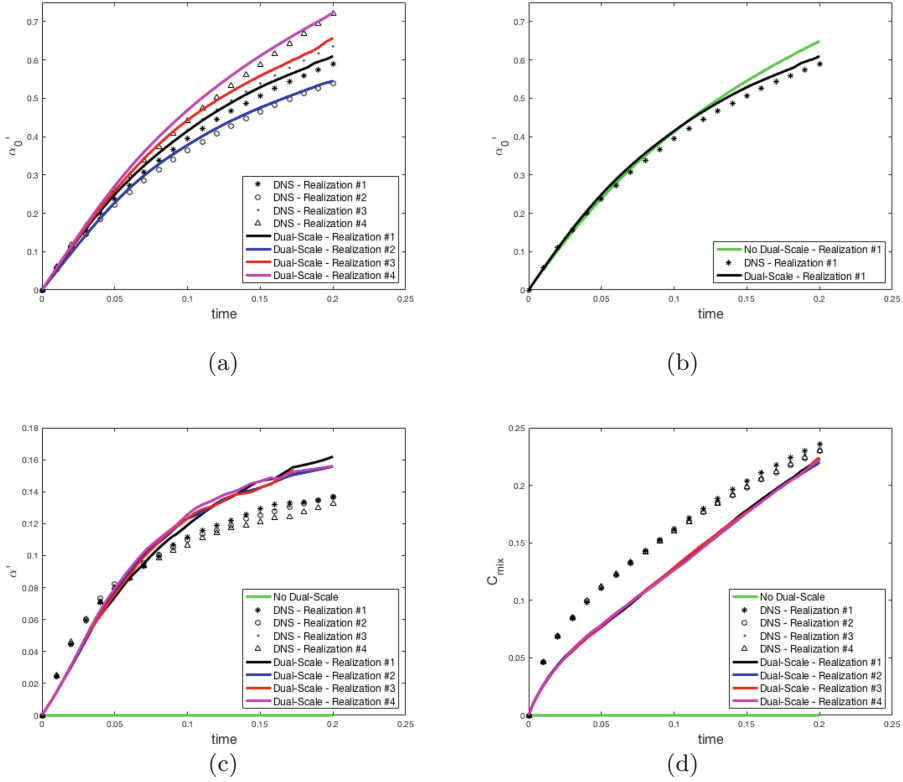


Fig. 5. Comparison of column height RMS α'_0 for: (a) Different realizations of Re_λ . (b) No sub-filter velocity, DNS, and fractal interpolation. (c) Comparison of sub-filter liquid column height RMS α' . (d) Comparison Metric C_{mix} .

of Re_λ . While this is not surprising on the small scales, this also holds true for the larger scales as well. The dual-scale LES results show good agreement with the DNS results while the LES results without the dual-scale model are significantly different. Between $\kappa = 1/h$ and $\kappa = 1/h_G$ the dual-scale model overpredicts the population of curvature by approximately 1% as compared to the DNS results. Comparison of dual-scale LES and DNS results at $\kappa < 10^{-1}$, i.e., at radii of curvature that are larger than the computational box size of 2π , shows a difference of less than 0.01%. Note that both dual-scale LES and DNS results show a peak curvature probability at $\kappa = 1/h_G$, whereas the LES results without dual-scale model are limited to $\kappa = 1/h$. Since the present simulations are for infinite Weber number, the Hinze scale, aka Komogorov's critical radius, is zero and hence the appearance of larger and larger curvatures with time is only limited by the available mesh resolution.

It should be stressed that the dual-scale LES result using the time evolving fractal interpolation generates the same population of curvatures as the DNS and

hence it can be conjectured that the dual-scale LES model might generate similar droplet sizes in atomization cases, if drop generation is initiated by turbulent velocity fluctuations.

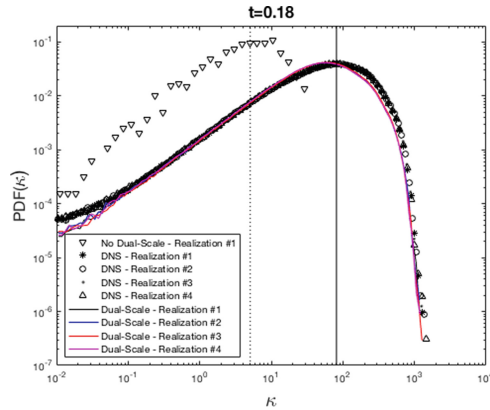


Fig. 6. Comparison of probability density function of curvature after the interface has had time to deform. Vertical reference lines denote the curvature of: $1/h_G$ (solid) $1/h$ (dotted).

6 Summary and Conclusions

A dual-scale modeling approach for phase interface dynamics in turbulent flows is presented that is based on a fractal interpolation technique to generate fully resolved turbulent velocity fields. The method uses overset high-resolution meshes to capture a resolved realization of the phase interface geometry that can be explicitly filtered to close the terms that require modeling in the filtered Navier-Stokes equations. Comparison of DNS and dual-scale LES results show good agreement for the case of an initially planar phase interface of unit density and viscosity contrast at infinite Weber number placed into a homogeneous isotropic decaying turbulence field. This favorable comparison includes the probability density function of interfacial curvature, an earlier indicator that the proposed dual-scale LES model may be applicable to atomization cases where droplet generation is initiated by turbulent eddies.

The dual-scale method has also shown significant improvements in computational cost. Proper implementation of the dual-scale method can be orders of magnitude faster than a pure DNS simulation when only a small portion of the domain contains an interface, as is the case for primary atomization. In the case where the entire domain is filled with interface, the dual-scale method has shown to be as fast as pure DNS.

Future work will focus on incorporating the dual-scale model for surface tension and an analysis on the impact of sub-filter surface tension on the interface dynamics.

References

1. Aniszewski, W., Bogusławski, A., Marek, M., Tyliczszak, A.: A new approach to sub-grid surface tension for LES of two-phase flows. *J. Comput. Phys.* **231**(21), 7368–7397 (2012). <http://www.sciencedirect.com/science/article/pii/S002199112003890>
2. Chiodi, R., Desjardins, O.: DNS of turbulent phase interfaces (2017)
3. Cummins, S.J., François, M.M., Kothe, D.B.: Estimating curvature from volume fractions. *Comput. Struct.* **83**, 425–434 (2005)
4. Ding, K.Q., Zhang, Z.X., Shi, Y.P., She, Z.S.: Synthetic turbulence constructed by spatially randomized fractal interpolation. *Phys. Rev. E* **82**(3), 036311 (2010). <https://doi.org/10.1103/PhysRevE.82.036311>
5. Gorokhovski, M., Herrmann, M.: Modeling primary atomization. *Annu. Rev. Fluid Mech.* **40**(1), 343–366 (2008). <http://arjournals.annualreviews.org/doi/abs/10.1146/annurev.fluid.40.111406.102200>
6. Gorokhovski, M., Jouanguy, J., Chtab, A.: Simulation of air-blast atomization: “floating guard” statistic particle method for conditioning of LES computation; stochastic models of break-up and coalescence. In: *Proceedings of International Conference on Liquid Atomization and Spray Systems* (2006)
7. Gorokhovski, M., Jouanguy, J., Chtab, A.: Stochastic simulation of the liquid jet break-up in a high-speed air coflow. In: *International Conference on Multiphase Flow*, Leipzig, Germany (2007)
8. Herrmann, M.: A balanced force refined level set grid method for two-phase flows on unstructured flow solver grids. *J. Comput. Phys.* **227**(4), 2674–2706 (2008). <http://www.sciencedirect.com/science/article/B6WHY-4R53WMC-7/2/bd0eb9d6157d8845efeb734b0aa6a6cf>
9. Herrmann, M.: A sub-grid surface dynamics model for sub-filter surface tension induced interface dynamics. *Comput. Fluids* **87**(0), 92–101 (2013). <https://doi.org/10.1016/j.compfluid.2013.02.008>. <http://www.sciencedirect.com/science/article/pii/S0045793013000637>
10. Herrmann, M., Gorokhovski, M.: An outline of a LES subgrid model for liquid/gas phase interface dynamics. In: *Proceedings of the 2008 CTR Summer Program*, pp. 171–181. Center for Turbulence Research, Stanford University, Stanford (2008)
11. Herrmann, M., Gorokhovski, M.: A large eddy simulation subgrid model for turbulent phase interface dynamics. In: *ICLASS 2009, 11th Triennial International Annual Conference on Liquid Atomization and Spray Systems*, Vail, CO (2009)
12. Labourasse, E., Lacanette, D., Toutant, A., Lubin, P., Vincent, S., Lebaigue, O., Caltagirone, J.P., Sagaut, P.: Towards large eddy simulation of isothermal two-phase flows: governing equations and a priori tests. *Int. J. Multiphase Flow* **33**(1), 1–39 (2007). <http://www.sciencedirect.com/science/article/pii/S0301932206000905>
13. Owkes, M., Desjardins, O.: A computational framework for conservative, three-dimensional, unsplit, geometric transport with application to the volume-of-fluid (VOF) method. *J. Comput. Phys.* **270**, 587–612 (Aug 2014). <https://doi.org/10.1016/j.jcp.2014.04.022>, <http://linkinghub.elsevier.com/retrieve/pii/S00219911400285X>
14. Pilliod, J.E.: An analysis of piecewise linear interface reconstruction algorithms for volume-of-fluid methods. Master’s thesis, University of California Davis (1992)

15. Pilliod Jr., J.E., Puckett, E.G.: Second-order accurate volume-of-fluid algorithms for tracking material interfaces. *J. Comput. Phys.* **199**(2), 465–502 (2004). <https://doi.org/10.1016/j.jcp.2003.12.023>. <http://www.sciencedirect.com/science/article/pii/S0021999104000920>
16. Scardovelli, R., Zaleski, S.: Analytical relations connecting linear interfaces and volume fractions in rectangular grids. *J. Comput. Phys.* **164**(1), 228–237 (2000). <https://doi.org/10.1006/jcph.2000.6567>. <http://www.sciencedirect.com/science/article/pii/S0021999100965677>
17. Scotti, A., Meneveau, C.: A fractal model for large eddy simulation of turbulent flow. *Phys. D: Nonlinear Phenomena* **127**(3–4), 198–232 (1999). [https://doi.org/10.1016/S0167-2789\(98\)00266-8](https://doi.org/10.1016/S0167-2789(98)00266-8). <http://linkinghub.elsevier.com/retrieve/pii/S0167278998002668>
18. Toutant, A., Chandesris, M., Jamet, D., Lebaigue, O.: Jump conditions for filtered quantities at an under-resolved discontinuous interface. Part 1: theoretical development. *Int. J. Multiphase Flow* **35**(12), 1100–1118 (2009). <http://www.sciencedirect.com/science/article/pii/S030193220900130X>
19. Toutant, A., Chandesris, M., Jamet, D., Lebaigue, O.: Jump conditions for filtered quantities at an under-resolved discontinuous interface. Part 2: a priori tests. *Int. J. Multiphase Flow* **35**(12), 1119–1129 (2009). <http://www.sciencedirect.com/science/article/pii/S0301932209001293>
20. Toutant, A., Labourasse, E., Lebaigue, O., Simonin, O.: DNS of the interaction between a deformable buoyant bubble and a spatially decaying turbulence: a priori tests for LES two-phase flow modelling. *Comput. Fluids* **37**(7), 877–886 (2008). <http://www.sciencedirect.com/science/article/pii/S004579300700165X>
21. Vallet, A., Borghi, R.: An Eulerian model of atomization of a liquid jet. In: *Proceedings of International Conference on Multiphase Flow, Lyon, France* (1998)
22. Vallet, A., Burluka, A., Borghi, R.: Development of an eulerian model for the atomization of a liquid jet. *Atom. Sprays* **11**, 619–642 (2001)



Influence of Particle Anisotropy and Motility on Preferential Concentration in Turbulence

Cristian Marchioli^{1,2(✉)}, Harshit Bhatia¹, and Diego Dotto¹

¹ DPIA, University of Udine, 33100 Udine, Italy
marchioli@uniud.it

² International Center of Mechanical Sciences, 33100 Udine, Italy

Abstract. The simplest numerical framework to study turbulent particle dispersion assumes that particles can be modeled as point-like spheres brought about by the flow. In spite of its simplicity, this framework has led to significant advancements in the study of particle-turbulence interactions. In this paper we examine how particle dispersion in dilute turbulent suspensions changes when particles are non-spherical (elongated) and may actively move within the fluid (motile). In particular, we show how elongation and motility add to particle inertia to modulate preferential concentration. Results for particles suspended in wall-bounded turbulence are presented to highlight effects on wall accumulation and segregation, which represent the macroscopic manifestation of preferential concentration.

Keywords: Preferential concentration · Non-sphericity · Motility

1 Introduction

Particle transport in turbulent flows is fundamental to science and technology. Examples of open scientific issues include emissions reduction in combustion, rheological characterization of fibrous particle suspension, plankton population dynamics and convection of pollutants in the atmosphere. From a physical standpoint, whichever the flow geometry, particle dynamics is controlled by turbulent flow structures whose timescale is comparable to the particle Stokes number, defined as $St = \tau_p/\tau_f$ where τ_p is the characteristic relaxation time of the particle and τ_f is the characteristic time of the flow. Previous works focusing on turbulent dispersed flows in channels, pipes and jets (see [1, 22] and references therein) show a strong correlation between coherent wall structures, local particle segregation and subsequent deposition and re-entrainment, the Stokes number being the scaling parameter. The reader is referred to [22] for an extensive review of these processes, how they are generated by particle-turbulence interactions at the particle scale and how they can be investigated by means of point-particle Euler-Lagrange simulations when particles are, in size, smaller than the Kolmogorov length scale of the flow. Here, we just provide a representative view of

particle dynamics and distribution in a turbulent boundary layer, resulting from local microscopic particle-turbulence interactions in the dilute regime. Figure 1(a) shows a cross-sectional view of the instantaneous particle distribution in turbulent channel flow, obtained from point-particle direct numerical simulations in the absence of gravitational settling and assuming that particle dynamics is governed by the drag force only. The shear Reynolds number is $Re_\tau = 300$, based on the half channel height, and spherical particles with Stokes number $St = 30$ are considered. Particles appear non-homogeneously distributed across the channel, and tend to cluster. From these clusters, particles are transported to the wall, and accumulate in specific “reservoirs” where concentration build-up occurs. Particles tend to stay long times in these accumulation regions, classified by a streamwise velocity lower than the mean [20], so that eventually particle concentration increases near the wall. To quantify near-wall accumulation, in Fig. 1(b) we show the particle concentration, C/C_0 (namely, the number of particles counted per unit fluid volume, normalised by its initial value C_0), as a function of the non dimensional distance from the wall, z^+ . Superscript + rep-

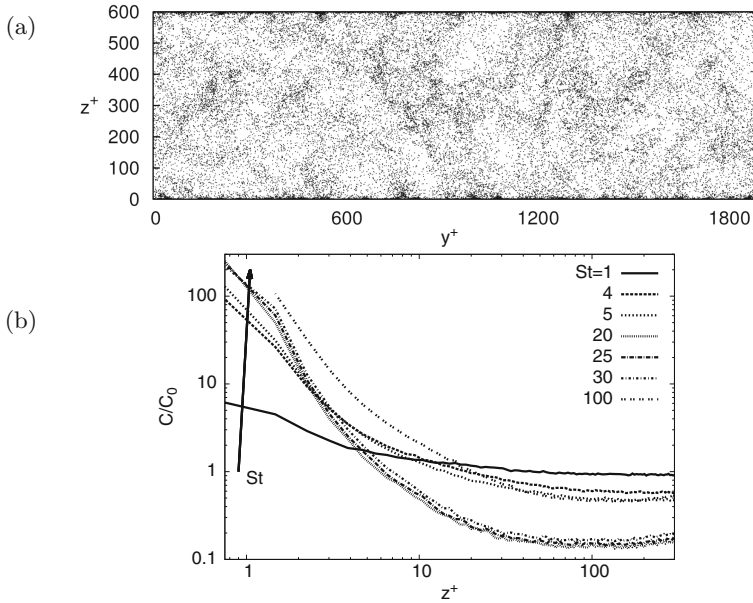


Fig. 1. Instantaneous distribution and wall accumulation of inertial particles in turbulent channel flow ($Re_\tau = 300$). Panels: (a) $St = 30$ particle position in the cross-flow plane; (b) particle concentration in the wall-normal direction, z^+ . Concentration is computed as follows: (1) the flow domain is divided into N_s wall-parallel fluid slabs of variable thickness, $\Delta z^+(s)$ (using hyperbolic-tangent binning with stretching factor $\gamma = 1.7$); (2) the number $N_{p,s}$ of particles with center of mass located in the s^{th} slab at each time step is counted; (3) the number density $C = N_{p,s}/V_s$ is computed, with V_s the volume of the s^{th} slab. The normalized concentration is obtained dividing C by its initial value C_0 .

resents wall units, defined in Sect. 2. Details on the calculation of C/C_0 can be found in [15]. The concentration profile corresponding to the $St = 30$ particle distribution of Fig. 1(a) is shown together with the profiles of additional particle sets, characterized by Stokes numbers ranging from 1 (relatively low inertia) to 100 (relatively high inertia). All concentration profiles develop a maximum well into the viscous sublayer, and the peak of C/C_0 increases monotonically with St , namely with particle inertia. This behaviour can be viewed as the outcome of the turbulence inhomogeneity [21].

Figure 1 provides an at-a-glance rendering of preferential concentration effects in a simplified and well-controlled situation in which these phenomena are due solely to particle inertia. Inertia introduces a time lag (the relaxation time, τ_p) in the particle response to the fluid velocity fluctuations. This leads to a deviation of particle trajectory with respect to pure tracers, which follow exactly the fluid streamlines. The ability to depart from fluid streamlines generates small-scale clustering and wall accumulation phenomena, explaining the fundamental physical mechanism by which a dilute suspension of inertial particles cannot be fully mixed by turbulence. In this paper, we investigate preferential concentration effects in more complex situations, characterized either by multiple sources of particle dispersion modulation, as in the case of heavy non-spherical particles, or by non-inertial effects, as in the case of motile particles that exploit their self-propelling capability to escape fluid streamlines. In both cases, we focus our discussion on dilute suspensions of point-wise particles and we exploit an Eulerian-Lagrangian approach based on direct numerical simulations of turbulence to examine statistically preferential concentration.

2 Methodology

The carrier fluid is Newtonian (with dynamic viscosity μ and kinematic viscosity ν) and incompressible (with density ρ). The fluid motion is governed by the following dimensionless mass and momentum conservation equations:

$$\nabla \cdot \mathbf{u} = 0; \quad \dot{\mathbf{u}} + (\mathbf{u} \cdot \nabla)\mathbf{u} = -\nabla p + Re_\tau^{-1}\nabla^2\mathbf{u} \quad (1)$$

where $\mathbf{u} = (u_x, u_y, u_z)$ is the fluid velocity, $\dot{\mathbf{u}}$ its time derivative, p is the fluid pressure, and $Re_\tau = hu_\tau/\nu$ is the shear Reynolds number, with h the channel half-height, and $u_\tau = \sqrt{\tau_w/\rho}$ the wall-friction velocity based on the wall shear stress τ_w . The flow is driven by a constant mean pressure gradient and is unaffected by the presence of the particles (one-way coupling). We performed direct numerical simulation of Eq. (1), considering both closed channel flow (for the spherical and elongated particles) and open channel flow (for the motile particles). Regardless of the flow configuration, periodic boundary conditions were imposed in the streamwise (x) and spanwise (y) directions. In the wall-normal/vertical direction (z), no-slip conditions at both walls were imposed in the closed channel configuration, whereas a free-slip condition was imposed at the free surface in the open channel configuration. Equations (1) are discretized using a pseudo-spectral method based on transforming variables into the wavenumber

space, through a Fourier representation in x and y , and a Chebyshev representation in z . A two-level explicit Adams-Bashforth scheme for the non-linear terms and an implicit Crank-Nicolson method for the viscous terms are employed for the time advancement. The convective non-linear terms are first computed in the physical space and then transformed in the wavenumber space using a de-aliasing procedure based on the 2/3-rule; derivatives are evaluated in the wavenumber space to maintain spectral accuracy [15].

Spherical particles with density $\rho_p \gg \rho$ are injected into the flow at concentration low enough to consider dilute system conditions (particle-particle interactions are neglected). Particles are assumed to be pointwise, rigid and heavy, so that the most significant force acting on them is Stokes drag. To keep the simulation setting as simplified as possible, thus allowing direct comparison among the different types of inertial particles considered in this paper, the effect of gravity has also been neglected. With the above assumptions the following Lagrangian equation for the particle velocity is obtained [17]:

$$\dot{\mathbf{u}}_p = -0,75 (C_D/d_p) (\rho/\rho_p) |\mathbf{u}_p - \mathbf{u}_{f@p}| (\mathbf{u}_p - \mathbf{u}_{f@p}), \quad (2)$$

with $\mathbf{u}_p = \dot{\mathbf{x}}_p$ the translational particle velocity, $\dot{\mathbf{u}}_p$ its time derivative, $\mathbf{u}_{f@p}$ the fluid velocity at the particle location, d_p the particle diameter, $C_D = 24Re_p^{-1}(1 + 0.15Re_p^{0.687})$ the drag coefficient, and $Re_p = d_p|\mathbf{u}_p - \mathbf{u}_{f@p}|/\nu$ the particle Reynolds number. For the present simulations, several particle sets were considered, characterized by different values of the relaxation time $\tau_p = \rho_p d_p^2 / 18\mu$, which is made dimensionless using wall variables and the Stokes number for each particle set is obtained as $St = \tau_p / \tau_f$ where $\tau_f = \nu / u_\tau^2$ is the characteristic flow time scale.

Elongated particles (also injected in a dilute flow, and referred to as fibers hereinafter) are modelled as pointwise rigid prolate spheroids with semi-major axis b , semi-minor axis a and aspect ratio $\lambda = b/a$. Translation and rotation are governed by the following equations:

$$m_p \dot{\mathbf{u}}_p = \mathbf{F}_D, \quad (\mathbf{I} \cdot \dot{\boldsymbol{\omega}}') + \boldsymbol{\omega}' \times (\mathbf{I} \cdot \boldsymbol{\omega}') = \mathbf{M}', \quad (3)$$

where $m_p = 4\pi a^3 \lambda \rho_p / 3$ is fiber mass. In Eq. (3), \mathbf{F}_D is the drag force acting on the fiber formulated in the *inertial* frame of reference $\mathbf{x} = \langle x, y, z \rangle$, \mathbf{I} is the moment of inertia tensor, $\boldsymbol{\omega}'$ is the angular velocity of the fiber and \mathbf{M}' is the Jeffery torque [6]. Both $\boldsymbol{\omega}'$ and \mathbf{M}' are formulated in the *particle* frame of reference $\mathbf{x}' = \langle x', y', z' \rangle$ with origin at the fiber center of mass and axes x' , y' and z' aligned with the principal directions of inertia. In the point-particle limit, the surrounding flow can be considered Stokesian and the drag force \mathbf{F}_D can be expressed as [2]:

$$\mathbf{F}_D = \mu \mathbf{R} \mathbf{K}' \mathbf{R}^T \cdot (\mathbf{u}_{f@p} - \mathbf{u}_p) = \mu \mathbf{K} \cdot \Delta \mathbf{u} \quad (4)$$

where \mathbf{R} is the orthogonal transformation matrix which relates the same vector in the two above-mentioned frames through the linear transformation $\mathbf{x} = \mathbf{R} \mathbf{x}'$ (\mathbf{R}^T being its transpose), \mathbf{K}' is the resistance tensor in the particle frame, and

$\Delta \mathbf{u} = \mathbf{u}_{f@p} - \mathbf{u}_p$ is the relative velocity between the fluid and the fiber at the center of mass of the fiber. Equation (4) is valid for a spheroid with arbitrary shape under creeping flow conditions, namely small fiber Reynolds number, $Re_p = 2a |\Delta \mathbf{u}| / \nu$. This condition is met for all fibers except the longest ones (see [23] for a more detailed discussion on the validity of the small- Re_p assumption for spheroids). The particle Stokes number is defined as [14]:

$$St = 4/3 (\rho_p / \rho_f) (a^+)^2 \lambda f(\lambda), \quad f(\lambda) = \ln(\lambda + \sqrt{\lambda^2 - 1}) / 6\sqrt{\lambda^2 - 1}, \quad (5)$$

where superscript + indicates wall units, obtained using u_τ and ν ($a^+ = au_\tau / \nu$).

Motile particles (referred to as swimmers hereinafter) are modelled as massless pointwise sphere with position \mathbf{x}_p evolving in time according to:

$$\dot{\mathbf{x}}_p(t) = \mathbf{u}_{f@p}(\mathbf{x}_p) + v_s \mathbf{p}, \quad (6)$$

where v_s is the (constant) swimming speed, and the unit vector \mathbf{p} defines the spatial orientation of the swimmer. Vector \mathbf{p} evolves in time according to the response of the swimmer to the biasing torques acting upon it: The viscous torque caused by shear, which rotates the body according to the local velocity gradients, and the gyrotactic torque arising from bottom heaviness, which tends to align the swimmer along the vertical direction \mathbf{k} [19]. The orientation rate is computed as:

$$\dot{\mathbf{p}} = (2\mathcal{B})^{-1} [\mathbf{k} - (\mathbf{k} \cdot \mathbf{p})\mathbf{p}] + \omega_{f@p} \wedge \mathbf{p} \quad (7)$$

with \mathbf{k} the unit vector pointing upward in the vertical direction, $\omega_{f@p}$ the fluid vorticity at the swimmer's position, and \mathcal{B} the characteristic time a perturbed gyrotactic swimmer takes to re-orient vertically when $\omega_{f@p} = 0$. The first term on the rhs of Eq. (7) represents the tendency of a swimmer to remain aligned with the vertical direction due to bottom-heaviness, while the second term represents the tendency of fluid vorticity to overturn the swimmer through a viscous torque. The key parameters in Eqs. (6) and (7) are the stability number $\Psi = \frac{1}{2\mathcal{B}} \frac{\nu}{u_\tau^2}$, which parameterises the importance of vortical overturning with respect to directional swimming, and the swimming number $\Phi = v_s / u_\tau$. As done for the inertial particles, swimmers are tracked assuming dilute flow conditions and using a point-particle approach, justified by the sub-Kolmogorov size typical of aquatic micro-organisms.

The statistics presented in this paper are relative to a turbulent Poiseuille channel flow. For the spherical and elongated particles, the shear Reynolds number is $Re_\tau = 300$, corresponding to a bulk Reynolds number $Re = u_0 h / \nu = 4200$, with $u_0 \simeq 3.3 \text{ m/s}$ (resp. $u_0 \simeq 0.21 \text{ m/s}$) the bulk velocity in the case of gas-solid flow (resp. liquid-solid flow). For the swimmers, values of Re_τ from 170 to 1020 were considered in order to explore Re_τ effects on vertical migration dynamics. In all simulations, and regardless of the specific value of Re_τ , the domain size is $L_x \times L_y \times L_z = 4\pi h \times 2\pi h \times 2h$ in the streamwise, spanwise and wall normal/vertical directions, respectively. The grids used to discretize this domain are given in Table 1. Lagrangian tracking of inertial particles was performed considering both spherical particles with Stokes numbers ranging from $St = 1$

to $St = 100$, and fibers with Stokes numbers $St = 5$ and $St = 30$ and aspect ratio $\lambda = 3, 10, 50$ (the case $\lambda = 1$ was also considered, to allow comparison with spherical particles). The simulation parameters for the different particle sets are provided in Tables 2 and 3, respectively. To simulate the motion of the swimmers, we fixed $\Phi = 0.048$, corresponding to a dimensional swimming velocity $v_s = 100 \mu\text{m}/\text{s}$ typical of *Chlamydomonas augustae* [4], and varied the stability number ($\Psi_H = 1.13, \Psi_I = 0.113, \Psi_L = 0.0113$), corresponding to $\mathcal{B} = 0.054, 0.54$ and 5.4 s , respectively: These values fall within the typical range of motile phytoplankton species [4].

Table 1. Simulation parameters for the flow field.

Flow configuration	Shear Reynolds number, Re_τ	Grid points $N_x \times N_y \times N_z$	Shear velocity u_τ [m s^{-1}]	Bulk Reynolds number, Re_b
Closed channel	300	$256 \times 256 \times 257$	0.2355	4200
Open channel	170	$128 \times 128 \times 129$	0.006	1400
	510	$256 \times 256 \times 257$	0.018	4300
	1020	$512 \times 512 \times 513$	0.036	8600

Table 2. Spherical particles simulation parameters (closed channel flow, $Re_\tau = 300$). V_s^+ is the dimensionless terminal velocity of the particle in still fluid.

St	τ_p (s)	d_p^+	d_p (μm)	$V_s^+ = g^+ \cdot St$	$Re_p^+ = V_s^+ \cdot d_p^+ / \nu^+$
1	$0.283 \cdot 10^{-3}$	0.153	10.2	0.0118	0.00275
4	$1.132 \cdot 10^{-3}$	0.306	20.4	0.0472	0.01444
5	$1.415 \cdot 10^{-3}$	0.342	22.8	0.0590	0.02018
20	$5.660 \cdot 10^{-3}$	0.684	45.6	0.2358	0.16129
25	$7.075 \cdot 10^{-3}$	0.765	51.0	0.2948	0.22552
100	$28.30 \cdot 10^{-3}$	1.530	102.0	1.1792	1.80418

Table 3. Elongated particles simulation parameters (closed channel flow, $Re_\tau = 300$).

St	Shape	λ	ρ_p/ρ_f	ρ_p	$2b^+$	$2b$ (μm)	-	St	Shape	λ	ρ_p/ρ_f	ρ_p	$2b^+$	$2b$ (μm)
5	Sphere	1	173.6	225.7	0.72	96.07	-	30	Sphere	1	1041.7	1354.2	0.72	96.07
5	Ellipsoid	3	92.9	120.8	2.16	287.9	-	30	Ellipsoid	3	557.1	724.2	2.16	287.9
		10	57.7	75	7.2	960.1	-			10	346.3	450.2	7.2	960.1
		50	37.7	49	36	4800	-			50	226.2	294	36	4800

For each tracked set, $N_p = 10^6$ particles/swimmers were injected into the flow with random position, random orientation and velocity equal to the fluid velocity at the release position. The equations of motion were solved using a 4th order Runge-Kutta scheme with a time step equal to that of the fluid. The fluid velocity and vorticity at the instantaneous particle location were obtained through interpolation based on 6th-order Lagrange polynomials. Periodic boundary conditions were imposed on particles in both streamwise and spanwise directions, whereas elastic reflection and conservation of angular momentum were applied when a particle touched the wall (or the free surface, in the case of the microswimmers). Elastic reflection was chosen since it is the most conservative assumption when measuring preferential concentration in a turbulent boundary layer. A more detailed discussion on the modelling issues associated to particle-wall collisions, not included here for sake of brevity, can be found in [16, 23].

3 Results and Discussion

We discuss the effect on preferential concentration introduced by two properties that provide particles with the ability to escape fluid streamlines: Particle shape (elongation, in particular, which adds to inertia in our problem) and particle motility (which leads to particle non-homogeneous distribution even without inertia). Statistics presented in this section were computed starting at time $t^+ = 1000$ upon particle injection, and gathered for a span $\Delta t^+ = 2000$, unless otherwise indicated.

Effect of Elongation on Preferential Concentration

Figure 2 shows the instantaneous distribution of the $St = 30$ fibers with $\lambda = 10$ (taken here as reference for the visualization) in the center region (panel a)

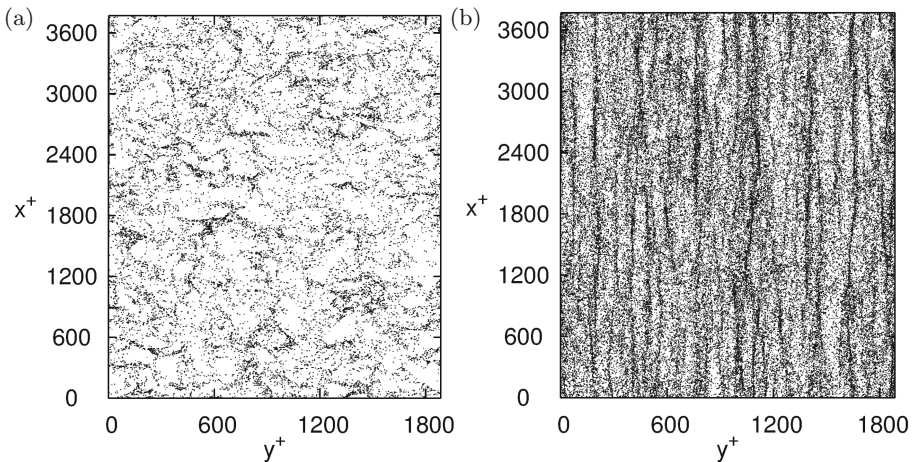


Fig. 2. Spatial distribution of $St = 30$ fibers with $\lambda = 10$ in closed channel flow at $Re_\tau = 300$. Panels: (a) Channel center; (b) Near-wall region.

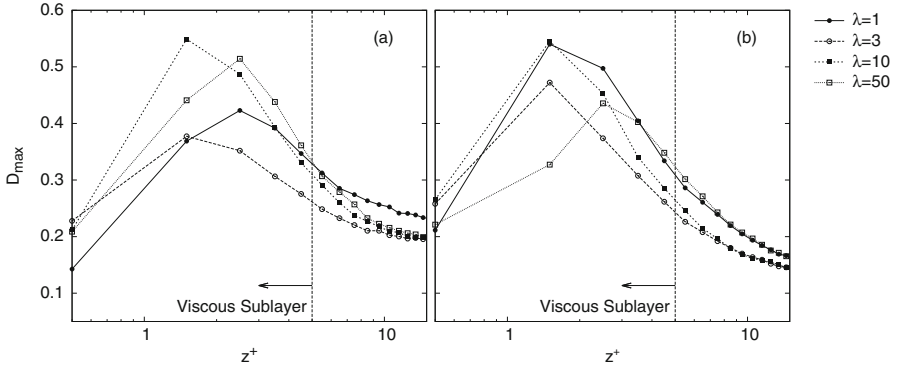


Fig. 3. Segregation parameter, D_{max} , along the wall-normal direction for inertial elongated fibers in closed channel flow at $Re_\tau = 300$. Panels: (a) $St = 5$; (b) $St = 30$.

and in the near-wall region (panel b) of the channel. Similar distributions are observed for the other sets (not shown). In the channel center, fibers cluster into groups leaving empty regions that have the same location for all fiber sets. This indicates that, in spite of the strong mathematical coupling between rotational and translational equations due to the dependency of the resistance tensor on the orientation [13], macroscopic fiber distributions are unaffected by elongation and depend only on inertia. Near the wall, fibers segregate into elongated streaks that correlate with regions of low-speed fluid velocity, but do not exhibit a strong preferential orientation in the streamwise direction. To examine in a more quantitative way the relative tendency of fibers to segregate in a turbulent flow, we computed the deviation from randomness, $D \equiv (\sigma - \sigma_{Poisson}) / \mu$ [5], where σ is the standard deviation for the measured number density distribution, $\sigma_{Poisson}$ is the standard deviation for a Poisson distribution (i.e. a purely random distribution of the same number of particles), and μ is the mean particle number density. $D = 0$ corresponds to a random distribution, $D < 0$ corresponds to a uniform distribution, $D > 0$ indicates segregation (larger values of D correspond to stronger segregation). The value calculated for D depends on the size of the cell volume Ω_{cell} used for the calculation. This dependency can be partially overcome by computing the number density distribution for several values of Ω_{cell} and keeping only the largest value of D [20], indicated as D_{max} in the following. In Fig. 3, we show the behavior of D_{max} as a function of the wall-normal coordinate, z^+ , for all cases considered in the (λ, St) -space. Profiles are averaged both in space, over the homogeneous directions, and in time, over the last 200 time units of the simulations. Segregation reaches a maximum inside the viscous sublayer ($z^+ < 5$), suggesting that such build-up is driven by inertia. Indeed, the larger values of D_{max} are obtained for the $St = 5$ and $St = 30$ fibers, which exhibit the highest tendency to undergo low-speed streak segregation. Small values are obtained for the $St = 1$ fibers, which exhibit the lowest tendency to undergo low-speed streak segregation (not shown), in agreement

with previous findings [14]. Once in the viscous sublayer, however, elongation becomes important in determining the location and the magnitude of maximum segregation. Changes in the aspect ratio produce non-monotonic modifications and cross-overs between profiles indicating that, locally, the influence of wall turbulence on fibers is strongly affected by λ and not only by St .

The results in Fig. 3 indicate the presence of a specific parameter range in which inertia combines with elongation to give rise to a non-trivial behaviour eventually leading to significant quantitative changes in near-wall dispersion. These will be analyzed next by means of concentration statistics. Figure 4 shows the instantaneous concentration profiles, computed as in [14], for both $St = 5$ fibers (panel a) and $St = 30$ fibers (bottom panel). The most evident changes occur in the very near-wall region, within few wall units from the wall: each profile develops a peak of concentration which is always found within the closest fluid slab considered for fiber counting. The peak value of C/C_0 differs depending on the aspect ratio: Compared to the spherical particles (black circles) with the same Stokes number, we observe a sharp increase of fiber accumulation already at $\lambda = 3$ for $St = 5$, followed by a decrease for longer fibers. Figure 4(b) suggests that this effect fades away for the shortest fibers ($\lambda < 10$ in our simulations) as fiber inertia increases. We remind that, for a given value of St , the mass of a fiber increases with its elongation so longer fibers have higher inertia. Therefore, the modification of the statistics that we observe when we increase the aspect ratio is due to a change in particle shape and is both direct and indirect (through increased inertia). Outside the viscous sublayer, variations are less evident and, again, the elongation of the fiber does not seem to play an important role. Overall, the results just discussed indicate that the fiber responsiveness to segregation and preferential concentration induced by the flow is strongly (and directly) correlated to the fiber aspect ratio mostly in the viscous sublayer, where particle anisotropy due to non-sphericity adds to flow anisotropy and the combined effects of shape and inertia lead to a quantitatively different build-up of fibers.

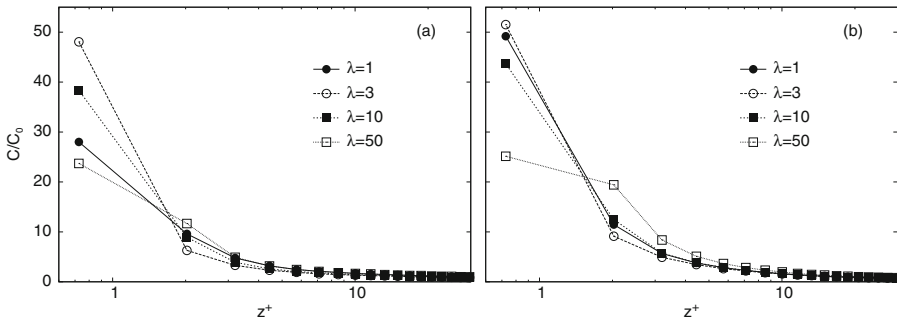


Fig. 4. Fiber concentration in the wall-normal direction (closed channel flow, $Re_\tau = 300$). Panels: (a) $St = 5$; (b) $St = 30$. Concentration was computed as explained in Fig. 1.

Effect of Motility on Preferential Concentration

A physical problem in which preferential concentration is observed in the absence of inertia is provided by the rising of gyrotactic micro-swimmers in free-surface turbulence. This phenomenon has been investigated recently [10,11,16], with the aim of elucidating the importance of the swimmer's vertical stability on its ability to move through turbulent vortices and reach the sub-surface layers of the flow. Turbulent flow structures near the free surface have been widely investigated [7,18]. Within the range of Re_τ investigated here, surface structures are generated and sustained by bursting phenomena that are continuously produced by wall shear turbulence inside the buffer layer. Bursts emanate from the bottom of the channel and produce upwelling motions of fluid that are advected toward the free surface. Near the surface, turbulence is restructured due to damping of vertical fluctuations: upwellings appear as sources for the surface-parallel fluid velocity and alternate to sinks associated with fluid downdrafts from the surface to the bulk. This phenomenology has been long recognized to produce flow with properties that differ from those typical of 2D incompressible turbulence [9]. To characterize the surface topology, we use the surface divergence $\nabla_{2D} = \frac{\partial u_f}{\partial x} + \frac{\partial v_f}{\partial y} = -\frac{\partial w_f}{\partial z}$. In open channel flow, ∇_{2D} does not vanish and swimmers located on the free surface probe a compressible 2D system [3], where velocity sources are regions of local flow expansion ($\nabla_{2D} > 0$) generated by upwellings and velocity sinks are regions of local compression ($\nabla_{2D} < 0$) due to downwellings. Figure 5 provides a qualitative characterization of swimmer clustering on the free surface by correlating the instantaneous swimmer distribution with the colormap of ∇_{2D} . Due to gyrotaxis, swimmers can not retreat from the free surface by simply following flow motions: They can only leave velocity sources (red areas in Fig. 5) and collect into velocity sinks (blue areas in Fig. 5), where they organize themselves in clusters that are stretched by the fluid to form filamentary structures. Formation of clusters with fractal mass distribution has been observed previously for the case of Lagrangian tracers in surface flow turbulence without mean shear [3,8], with wind-induced shear [16], and for the case of floaters in free-surface turbulence [11].

Another feature of swimmer dynamics that is clearly highlighted in Fig. 5, is the different number of cells that have reached the surface at the time instant of the visualizations. Swimmers with low gyrotaxis (low stability number Ψ_L , panel a), are out-numbered by swimmers with high gyrotaxis (high stability number Ψ_H , panel b). To quantify this qualitative observation, in Fig. 6(a) we show the wall-normal concentration profiles computed at the same time of Fig. 5 ($t^+ = 10^4$), comparing results at varying gyrotaxis. Concentration builds up within a thin layer just below the surface. The maximum value of concentration is reached right at the surface, and increases monotonically with gyrotaxis. In the bulk of the flow, the distribution of the swimmers remains uniform whereas the bottom wall is depleted of cells, indicating a continuous migration towards the free-surface. This process can be further analyzed considering the time behaviour of the number of swimmers that have reached the surface, represented by the solid line in Figs. 6(b)–(d), and normalized by the total number of swimmers

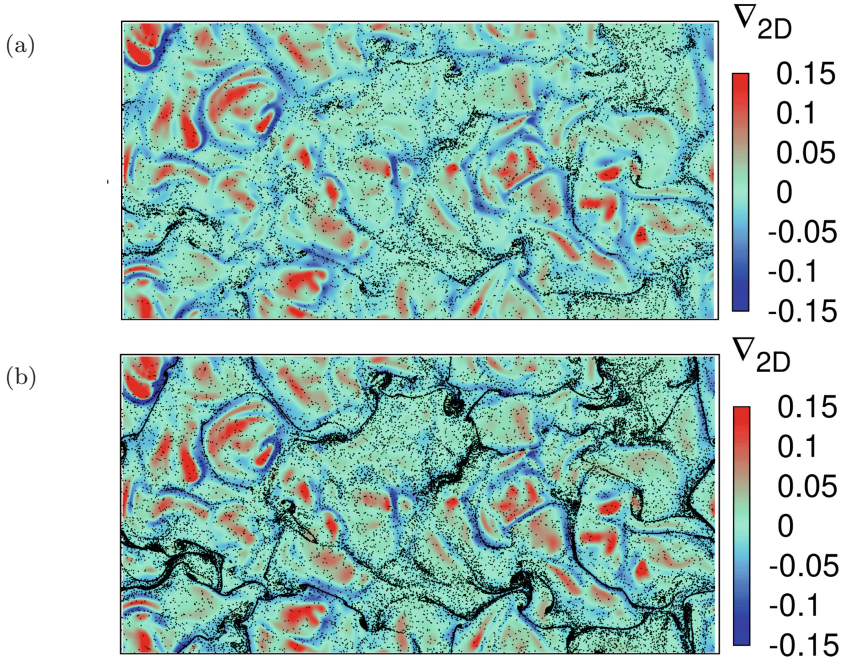


Fig. 5. Top view of micro-swimmers distribution on the free surface ($Re_\tau = 510$, $t^+ = 10^4$). Flow is from left to right. Panels: (a) Low gyrotaxis, Ψ_L ; (b) High gyrotaxis, Ψ_H .

tracked in the simulations. More precisely, these figures show the number of swimmers trapped in a monitor fluid slab $0.01 < z^+ < 0.5$ just below the free-surface, chosen in order to minimise the effect of the elastic rebound condition imposed at the upper boundary of the flow domain. In addition, the dashed and dotted curves in each figure represent the fraction of swimmers located in regions of the monitor fluid slab characterized by negative and positive values of the surface divergence, respectively. In agreement with the qualitative observations drawn from Fig. 5, the number of swimmers sampling $\nabla_{2D} < 0$ in downwelling regions is always much higher than the number of swimmers sampling $\nabla_{2D} > 0$ in upwelling regions. Within the time window of the simulations, n/N reaches a steady state only for swimmers with low gyrotaxis, Ψ_L , and only $5 \sim 6\%$ of the swimmers are able to reach the surface. For the cases of intermediate and high gyrotaxis, n/N increases steadily (up to roughly 70% for the Ψ_I swimmers and roughly 80% for the Ψ_H swimmers), and provides the source for continuous accumulation into filamentary clusters within downwellings.

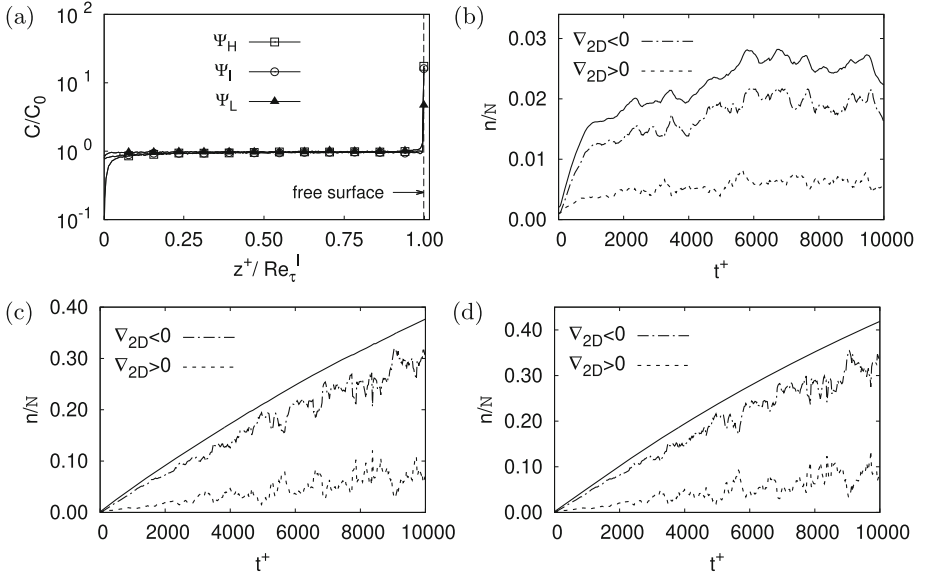


Fig. 6. Surfacing and accumulation of gyrotactic micro-swimmers ($Re_\tau = 510$). Panels: (a) Wall-normal concentration at varying gyrotaxis; (b), (c), (d) Evolution of the number of swimmers reaching the sub-surface layer $0.1 < z^+ < 0.5$ for low, intermediate and high gyrotaxis. The relative contributions due to swimmers in downwellings ($\nabla_{2D} < 0$, dash-dotted lines) and upwellings ($\nabla_{2D} > 0$, dashed lines) are also shown.

4 Conclusions

We have examined two instances of turbulent dispersed flow in which preferential concentration phenomena are not determined solely by particle inertia, and we have tried to highlight the differences introduced by the presence of shape effects or motility effects. The physical problems investigated all refer to one-way coupled flows, and therefore the results discussed in this paper are valid only for dilute particle suspensions. Our results show that, when shape effects add to inertial effects, significant quantitative modifications to particle segregation into clusters and to particle accumulation near solid boundaries occur. Such quantitative changes are, in general, not monotonically dependent on the increase of particle elongation and appear difficult to model within numerical approaches that are not based on direct numerical simulations of turbulence. In particular, it would be useful to include shape effects in subgrid closure models for predicting preferential concentration via Large-Eddy simulations [12]. However, present results suggest that this may be a very challenging task. We also show that preferential concentration can be observed in the absence of inertia, by considering particles that can propel themselves within the fluid. In this case, preferential

concentration is associated to two-dimensional clustering at a free surface, where the degree of segregation can be “tuned” by modulating the vertical stability of directional swimming.

References

1. Balachandar, S., Eaton, J.K.: Turbulent dispersed multiphase flow. *Annu. Rev. Fluid Mech.* **42**, 111–133 (2010)
2. Brenner, H.: The Stokes resistance of an arbitrary particle. *Chem. Eng. Sci.* **18**, 1–25 (1963)
3. Cressman, J.R., Davoudi, J., Goldburg, W.I., Schumacher, J.: Eulerian and Lagrangian studies in surface flow turbulence. *New J. Phys.* **6**, 53 (2004)
4. Durham, W.M., Climent, E., Barry, W.M., De Lillo, F., Boffetta, G., Cencini, M., Stocker, R.: Turbulence drives microscale patches of motile phytoplankton. *Nat. Commun.* **4**, 2148 (2013)
5. Fessler, J.R., Kulick, J.D., Eaton, J.K.: Preferential concentration of heavy particles in a turbulent channel flow. *Phys. Fluids* **6**, 3742–3749 (1994)
6. Jeffery, G.B.: The motion of ellipsoidal particles immersed in a viscous fluid. *Proc. Roy. Soc.* **102**, 161–179 (1922)
7. Kermani, A., Khakpour, H.R., Shen, L., Igusa, T.: Statistics of surface-renewal of passive scalars in free-surface turbulence. *J. Fluid Mech.* **678**, 379 (2011)
8. Larkin, J., Bandi, M.M., Pumir, A., Goldburg, W.I.: Power-law distributions of particle concentration in free-surface flows. *Phys. Rev. E* **80**, 066301 (2009)
9. Lovecchio, S., Zonta, F., Soldati, A.: Upscale energy transfer and flow topology in free surface turbulence. *Phys. Rev. E* **91**, 033010 (2015)
10. Lovecchio, S., Zonta, F., Soldati, A.: Influence of thermal stratification on the surfacing and clustering of floaters in free surface turbulence. *Adv. Water Res.* **72**, 22–31 (2014)
11. Lovecchio, S., Marchioli, C., Soldati, A.: Time persistence of floating particle clusters in free-surface turbulence. *Phys. Rev. E* **88**, 033003 (2013)
12. Marchioli, C.: Large-eddy simulation of turbulent dispersed flows: a review of modelling approaches. *Acta Mech.* **228**, 738–768 (2017)
13. Marchioli, C., Zhao, L., Andersson, H.I.: On the relative rotational motion between rigid fibers and fluid in turbulent channel flow. *Phys. Fluids* **28**, 013301 (2016)
14. Marchioli, C., Fantoni, M., Soldati, A.: Orientation, distribution and deposition of elongated, inertial fibers in turbulent channel flow. *Phys. Fluids* **22**, 033301 (2010)
15. Marchioli, C., et al.: Statistics of particle dispersion in direct numerical simulations of wall-bounded turbulence: results of an international collaborative benchmark test. *Int. J. Multiphase Flow* **34**, 879–893 (2008)
16. Mashayekhpour, M., Marchioli, C., Lovecchio, S., Nemati Lay, E., Soldati, A.: Wind effect on gyrotactic micro-organism surfacing in free-surface turbulence. *Adv. Water Resour.* **129**, 328–337 (2019)
17. Maxey, M., Riley, J.: Equation of motion for a small rigid sphere in a nonuniform flow. *Phys. Fluids* **26**, 883–889 (1983)
18. Nagaosa, R., Handler, R.A.: Statistical analysis of coherent vortices near a free surface in a fully developed turbulence. *Phys. Fluids* **15**, 375–394 (2003)
19. Pedley, T.J., Kessler, J.O.: Hydrodynamic phenomena in suspensions of swimming microorganisms. *Annu. Rev. Fluid Mech.* **24**, 313–358 (1992)

20. Picciotto, M., Marchioli, C., Soldati, A.: Characterization of near-wall accumulation regions for particles in turbulent boundary layers. *Phys. Fluids* **17**, 098101 (2005)
21. Reeks, M.W.: The transport of discrete particles in inhomogeneous turbulence. *J. Aerosol Sci.* **310**, 729–739 (1983)
22. Soldati, A., Marchioli, C.: Physics and modelling of turbulent particle deposition and entrainment. *Int. J. Multiphase Flow* **35**, 827 (2009)
23. Zhao, L., Marchioli, C., Andersson, H.I.: Slip velocity of rigid fibers in turbulent channel flow. *Phys. Fluids* **26**, 063302 (2014)



Reference Solutions and URANS Model Characterization for Turbulent Forced Convection Around Heated Square Cylinders

Xavier Nicolas¹(✉) , Hua Sun¹, and Yannick Sommerer²

¹ Université Paris Est Marne-la-Vallée, MSME UMR 8208 CNRS, 5 Bd Descartes, 77454 Marne-la-Vallée Cedex 2, France

Xavier.Nicolas@u-pem.fr

² Airbus, 316 Route de Bayonne, 31060 Toulouse Cedex 09, France

Abstract. Reference solutions for the turbulent forced convection of air around heated square cylinders at high Reynolds numbers ($Re \geq 10^4$) are set-up from a bibliographical synthesis of about twenty experiments. These reference solutions concern the flow dynamics and heat transfer. We particularly focus on the local Nusselt number around the obstacle. These solutions are used to identify the URANS models that are the most adequate to reproduce the flow physics and heat transfer in this configuration. Different versions of the k - ϵ and k - ω models are tested. The k - ω SST model is shown to be the most accurate to evaluate the flow dynamics and heat transfer: its accuracy is equivalent to that obtained by 3D LES and high performance computing.

Keywords: Heated square cylinder · Turbulent forced convection · URANS simulations · Bibliographical synthesis · Experimental reference solution

1 Introduction

In many industrial applications, an accurate prediction of the local convective heat transfer in the turbulent forced convection around heated bluff bodies is crucial. For instance, in the nacelle compartment of aeronautical engines, the equipment like valves, electrical harnesses, pumps or ducts is submitted to large heat fluxes in such a way that it must often be air-cooled to never exceed a maximum allowable temperature [1]. To optimize the cooling systems, accurate enough numerical simulations must be carried out. If correctly optimized and validated, URANS (Unsteady Reynolds Averaged Navier-Stokes) simulations can be preferred to LES to model a long period of a transient flow such as a complete flight mission for example. The objective of this communication is to define if an accurate prediction of the flow dynamics and heat transfer around heated

bluff bodies is possible from URANS simulations and to test and characterize different k - ϵ and k - ω models [2, 3].

In that aim, a 2D test case representative of the main physics and features encountered in this context is chosen. It is the ERCOFTAC benchmark proposed by Lyn, Rodi et al. [4–6] of an air flow around a square cylinder, placed transversally at mid-height of a channel, at Reynolds number $Re = 22,000$, but considering that the cylinder is heated. A large experimental and numerical database of the flow dynamics for this test case or for similar configurations is available in the literature. There is also a thermal database thanks to the experiments around heated square cylinders [7–10]. Thus, to characterize the different URANS models used in the present paper and enable comparisons between experiments and simulations, reference solutions for the global characteristics of the flow dynamics and heat transfer have been first set-up from a bibliographical review of about twenty experiments.

The outline of the paper is the following. The flow dynamics is presented in Sect. 2, the synthesis of the bibliographical review in Sect. 3 and the used URANS models, flow configuration and numerical methods in Sect. 4. The URANS results are then compared with the experimental reference results and discussed. The global quantities and statistics describing the flow dynamics and heat transfer are analyzed in Sect. 5, for four variants of the k - ϵ and k - ω models. The local profiles around the square cylinder, computed with the k - ω SST model, are analyzed in Sect. 6. Conclusions are given in Sect. 7.

2 Flow Dynamics of the Selected Test Case

Figure 1 sums up in a simplified way the main patterns observed in the turbulent air flow around a square obstacle at $Re = U_\infty D/\nu \geq 10^4$, with D the length of the obstacle edge and U_∞ the free stream velocity. In Fig. 1(left), the blue lines more or less correspond to the stream lines of the instantaneous phase averaged flow. Two shear layers symmetrically separate from the top and bottom leading edges. A Kelvin-Helmholtz (KH) instability intermittently develops in these shear layers [11–13] with, between them and the top and bottom faces of the square cylinder, two recirculations, very unstable over time, with a reverse flow near the wall. The shear layers do not reattach on the side walls, but eventually on the rear face. They flaps above and behind the trailing edges and they roll up as the Karman instability develops. The vortical structures associated with this instability are continuously and quasi periodically generated in the wake, while the KH vortical structures appear intermittently in the shear layers [12, 13]. The frequencies associated with the two instabilities are clearly separated in the Fourier spectra of the velocity or pressure time signals: the Strouhal number $St = fD/U_\infty$ of the Karman vortex shedding is approximately equal to 0.13 while it varies between 1 and 10 for the KH instability. In the near wake behind the obstacle, the turbulent intensity is very high and the instantaneous flow is complicated to describe. On the other hand, the time averaged flow is simple (Fig. 1(right)): it is steady and symmetrical through the horizontal axis; the two

separated shear layers are still present with two recirculations between them and the side walls; lastly, in the near wake, there are two steady contrarotative vortices with a reverse flow on the horizontal axis.

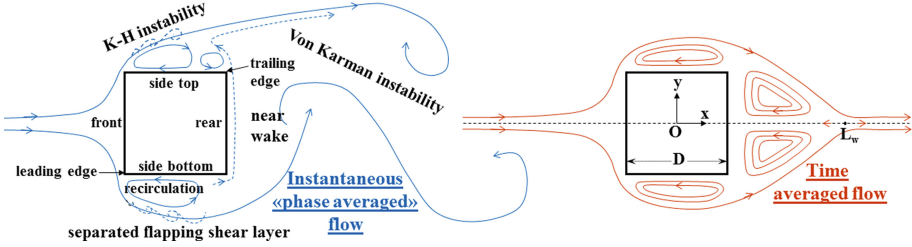


Fig. 1. Schematic representation of the instantaneous phase averaged and time averaged flow around a square cylinder at high Reynolds number.

3 Bibliographical Review for Reference Solution Setting-Up

Several quantities are quasi systematically measured to characterize the global dynamics of the just described flow. Their average values, with their dispersion margins, are compiled in Table 1. They result from a synthesis of 17 experiments ([4–6, 11, 12, 14–20] among others), not detailed in the present paper. The first reported quantity is the dimensionless wake length, L_w/D , where L_w is the length from the square center to the point where the averaged horizontal velocity, \bar{u} , vanishes (cf. Fig. 1(right)). $St = fD/U_\infty$ is the Strouhal number with f the frequency of the vortex shedding. \bar{C}_d , C'_d and C'_l are the time averaged drag coefficient, the RMS of the drag coefficient and the RMS of the lift coefficient respectively. $\bar{C}_{p,b} = 2(\bar{p} - p_\infty)/(\rho_\infty U_\infty^2)$ is the time averaged base pressure coefficient, where \bar{p} is the time averaged pressure on the rear face of the square cylinder; p_∞ and ρ_∞ are the free stream pressure and density respectively.

Table 1. Global flow characteristics around a square cylinder at $Re \geq 10^4$ resulting from the synthesis [21] and the present one. {BEC} = blockage effect corrected values.

Reference	Methods	$Re \times 10^{-3}$	I %	L_w/D	St	\bar{C}_d	C'_d	C'_l	$-\bar{C}_{p,b}$ {BEC}	D/H%
Sohankar 2006 [21]	LES& exp. synthesis	5–5000	0–2		0.13 ± 0.01	2.15 ± 0.15	0.18 ± 0.05	1.3 ± 0.3		~6
Present reference values	Synthesis from 17 experim.	10–200	0–2 4.4–6.5 10–14	1.4 ± 0.1 1.4 ± 0.1 1.4 ± 0.1	.13±.008 .13 ± .008 .13 ± .008	2.15 ± 0.1 1.9 ± 0.1 1.6 ± 0.1	.2±.03 .2 ± .03 .2 ± .03	1.2±0.2 1.1 ± 0.2 0.65 ± 0.25	1.5{1.4} ± 0.1 1.3{1.2} ± 0.1 0.9{0.8} ± 0.2	5–7.5

It is well known that these quantities and the flow structure do not depend on Re for 10^4 to $2 \times 10^4 \leq Re \leq 5 \times 10^6$ [21]. On the other hand, they may depend

on the inlet turbulence intensity, I , and the blockage effect, D/H , due to the presence of the cylinder in a finite size channel. When I increases, the inside and outside of the separated shear layers are more linked (the shear layers thicken); therefore the fluctuations of the lift force (C'_l) decrease, the base pressure $\overline{C}_{p,b}$ increases and the drag force (\overline{C}'_d) decreases [14,16,19]. Note however that C'_d and St are very few influenced by I .

The blockage effect, D/H , modifies the mean velocity at the obstacle level and the hydrodynamic forces exerted on it. However, when $D/H < 10\%$, its influence on the global quantities of Table 1 is weak comparing with I influence: the variations due to D/H are generally smaller than 10% but can reach 15% on $\overline{C}_{p,b}$, the quantity the most influenced by D/H . The blockage effect is a classical issue of closed wind tunnels, overcome by appropriate corrections of the results [22]. In the next to last column of Table 1, both the blockage effect corrected and uncorrected values of $\overline{C}_{p,b}$ are mentioned, with the corrected value into braces. The reference solutions resulting from our bibliographical review are given in the last row of Table 1, with their dispersion margin. As discussed above, they possibly depend on I and D/H . In the next to last line, they are compared with the reference solutions established by Sohankar [21]. These reference solutions agree well, with smaller dispersion margins for the present ones because LES results are not included in our analysis, contrary to [21].

Table 2. Experimental correlations of \overline{Nu} around a heated square cylinder at $Re > 10^4$ and \overline{Nu} values at $Re = 22,000$. In the last line: reference solutions for \overline{Nu} at $Re = 22,000$. In all the experiments, flows are smooth: $I < 0.6\%$. HT = heat transfer; HMTA = heat and mass transfer analogy; correl. = correlation; I&I = interpolation and integration of \overline{Nu} or \overline{Sh} profiles at $Re = 22,000$.

Reference	Metrology; plotted profiles	D/H %	Method and used fig. nb in the refer.	$Re \times 10^{-3}$	Nu_f front	Nu_s side or top-bottom	Nu_r rear	Nu_t total
Igarashi (1985) [7]	HT; \overline{Nu} profiles	3.8-7.3	correlation correl. value I&I of fig.4a	5.6-56 22 22	92.6	95.4-98.7	136.9	0.14Re ^{0.66} 102.8 105.9
Igarashi (1986) [8]	HT; \overline{C}_p , \overline{Nu} prof.	3.8-7.3	correlation correl. value	11-56 22	0.640Re ^{1/2} 94.9	0.131Re ^{2/3} 102.9	0.180Re ^{2/3} 141.3	0.14Re ^{2/3} 109.9
Tsutsui et al (2001) [9]	HT; \overline{C}_p , \overline{Nu} prof.	5	I&I of fig.10	22	90.5	102.1-100.6	136.1	107.3
Yoo et al. (2003) [10]	HMTA; \overline{Sh} prof.	10	correl of fig.5 correl. value I&I of fig.3c	11.25-37.5 22 22	2.197Re ^{0.386} 104.2 109.3	0.392Re ^{0.55} 95.9 106.5-100.4	.572Re ^{0.545} 133.1 139.5	107.3 113.9
\overline{Nu} reference values from the above exp.				22	100±10	101±6	137±5	108±6

Table 2 compiles experimental results on the averaged Nusselt numbers \overline{Nu} around a heated square cylinder at $Re \geq 10^4$ [7–9], with experiments on mass transfer, using naphthalene sublimation in air flows around square cylinders [10].

Indeed, using Colburn relation and heat and mass transfer analogy, the average Sherwood number \overline{Sh} is shown to be related to \overline{Nu} by $\overline{Nu}/\overline{Sh} = (Pr/Sc)^{1/3}$. That provides $\overline{Nu} = 0.6778\overline{Sh}$ at Prandtl number $Pr = 0.71$ and Schmidt number $Sc = 2.28$ for the diffusion of naphthalene vapor into air at ambient conditions [23]. The values of the front, side, rear and total average Nusselt numbers (noted \overline{Nu}_f , \overline{Nu}_s , \overline{Nu}_r and \overline{Nu}_t respectively) at $Re = 22,000$ are given in Table 2. They are obtained either directly from the experimental correlations or from interpolations and integrations of the experimental profiles of the Nusselt or Sherwood numbers at other Reynolds numbers. Reference solutions with their dispersion margins for \overline{Nu}_f , \overline{Nu}_s , \overline{Nu}_r and \overline{Nu}_t at $Re = 22,000$ are then established from these interpolated results and given in the last line of Table 2. They will be used below to validate the URANS simulations.

4 URANS Models, Flow Configuration and Numerical Methods

The turbulent vortex shedding behind a square cylinder is a typical example of large-scale coherent structures developing in a turbulent shear flow. The modelling of this flow type was addressed by Reynolds and Hussain [24,25]. They proposed a double or a triple decomposition of all the quantities, f , characterizing these flows, in order to separately describe their mean (time-averaged) contribution \overline{f} , their periodic contribution \tilde{f} (the coherent fluctuations around the mean), their turbulent contribution f' , and the interactions between \overline{f} , \tilde{f} and f' . Thus a time signal in this flow type can be decomposed as follows:

$$f(M, t) = \overline{f}(M) + \tilde{f}(M, t) + f'(M, t) \quad (1)$$

$$f(M, t) = \langle f(M, t) \rangle + f'(M, t) \quad (2)$$

where $\langle f(M, t) \rangle$ is the phase average obtained by averaging over a large ensemble of observations of $f(M, t)$ at the same phase of the flow with respect to a reference oscillator. As explained in [25], the phase averaging process rejects the background turbulence and extracts only the organized motions from the total signal. In the case of the turbulent vortex shedding behind a square cylinder, it is observed that the coherent contributions $\langle f \rangle$ or \tilde{f} are quasi periodic and quasi two-dimensional in the plane (O, x, y) transverse to the cylinder axis, and they are characterized by much larger space and time scales than those of the three-dimensional turbulence, f' . This explains the success of the URANS models for such flow configurations.

In the present study, the RNG and Realizable $k-\epsilon$ models and the standard and low Re versions of the $k-\omega$ SST model are tested in their basic forms (without changing the constants of the models) using the CFD software Ansys/Fluent. The Boussinesq hypothesis is used to relate the Reynolds stresses to the mean velocity gradients and the turbulent heat fluxes to the mean temperature gradients, with a turbulent Prandtl number $Pr_t = 0.85$. We refer to [2,3] and the Ansys/Fluent documentation [26] for more details.

The 2D flow configuration of the present simulations is presented on Fig. 2. It is similar to the 2D plane (O, x, y) in the 3D LES study performed by Boileau et al. (2013) [27]. An incompressible air flow, with the physical properties $\rho = 1.1774 \text{ kg/m}^3$, $\mu = 1.983 \times 10^{-5} \text{ kg/m.s}$, $k = 2.851072 \times 10^{-2} \text{ W/m.K}$ and $C_p = 1006.43 \text{ J/kg.K}$, is imposed at the inlet of a rectangular channel, with a uniform horizontal velocity $U_\infty = 9.2632 \text{ m/s}$ and temperature $T_\infty = 300 \text{ K}$, and with a turbulence intensity $I = 2\%$. This air flow encounters a non-slipping square cylinder of diameter $D = 4 \text{ cm}$, heated at $T_{cyl} = 330 \text{ K}$. Thus $Re = \rho U_\infty D / \mu = 22,000$ and $Pr = \mu C_p / k = 0.7$. The channel is limited by two horizontal slipping boundaries located at $6.5D$ from the top and bottom faces of the cylinder. A zero-gradient boundary condition is applied at the channel outlet located at $15D$ downstream the cylinder rear face. The reference frame (O, x, y) is at the square center with (Ox) and (Oy) the horizontal and vertical axes respectively.

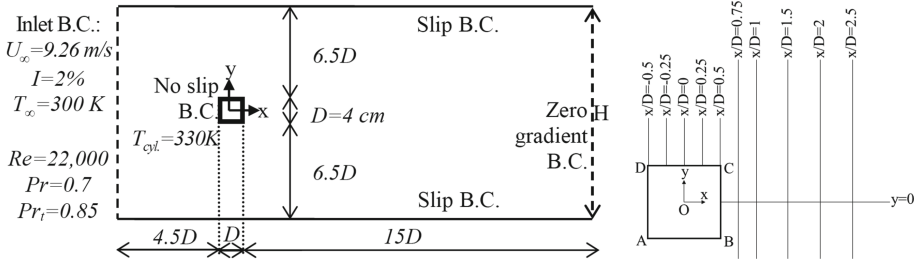


Fig. 2. Flow configuration and boundary conditions (B.C.) (left). Lines and coordinates of the lines used for profile plots around the square cylinder (right).

The 2D incompressible URANS equations are solved with ANSYS/Fluent v17.2 [26] by a collocated finite volume method using a 2nd order time implicit scheme and a 2nd order Quick scheme in space. The SIMPLE algorithm is used for the velocity/pressure coupling and $\Delta t = 10^{-4} \text{ s}$ for all the simulations. Since the period of the Von Karman vortices is $\tau = 0.0332 \text{ s}$ for a Strouhal number $St = D/(\tau U_\infty) = 0.13$, one period is equal to 332 time steps and $\Delta t_{adim} = U_\infty \Delta t / D = 0.023$; this was checked to provide time converged solutions. To get well converged statistics, the time integration duration is between 2 and 6 s , which corresponds to 60τ to 200τ .

To analyze the grid sensitivity of the solutions, five non uniform Cartesian grids refined close to the cylinder were used. The mesh total size $N_x \times N_y$ varies from $N_x \times N_y = 188 \times 110$ for the coarsest grid (that has 20×20 uniform cells around the square cylinder with $5 < \bar{y}^+ < 30$ to 50) to $N_x \times N_y = 435 \times 310$ for the finest grid (that has 140×140 uniform cells around the square cylinder with $0 < \bar{y}^+ < 5$ to 10). The different mesh sizes used are designated by the cell number around the square cylinder (e.g. 140×140). The total cell number $N_x \times N_y$ is indicated in Table 3. For the finest grid 140×140 , the first grid point close to the wall is located in the viscous sublayer because $\bar{y}^+ < 5$ (except on

the front face where $\bar{y}^+ < 10$). For the coarsest grid 20×20 , the first grid point is mainly located in the buffer layer because $5 < \bar{y}^+ < 32$.

5 Analysis of the Global Quantities and Statistics

The global quantities and statistics, characteristic of the flow and heat transfer around a square cylinder, are presented in Table 3 for the tested URANS models

Table 3. Flow and heat transfer global characteristics obtained from URANS simulations at $Re = 22,000$ and $I = 2\%$. Comparison with the reference solutions of Tables 1 and 2 and [21] (two last lines). The values in italics fit the reference ranges and the bold values in the yellow boxes are in a 10% accuracy from the references (20% accuracy for C'_d and $\overline{C}_{p,b}$, or in [21] range for C'_l).

URANS Re= 22,000	$N_x \times N_y$ (around square cyl)	L_w/D	St	\bar{C}_d	C'_d	C'_l	$\overline{-C}_{p,b}$ {BEC}	\overline{Nu}_r front	\overline{Nu}_s side or top-bot.	\overline{Nu}_r rear	\overline{Nu}_t total	
k- ω SST	188×110 (20×20)	1.12	<i>0.138</i>	<i>2.240</i> ± 0.005	<i>0.207</i> ± 0.001	1.42 ± 0.02	1.163	70.8	72.4 72.2	105.0	80.1 ± 3.0	
	290×190 (60×60)	1.13	<i>0.132</i>	<i>2.215</i> ± 0.005	<i>0.239</i> ± 0.005	1.47 ± 0.01	1.192	120.1	<i>95.3</i> <i>95.5</i>	120.8	<i>108.0</i> ± 3.8	
	365×250 (100×100)	1.26	<i>0.132</i>	<i>2.220</i> ± 0.005	0.280 ± 0.01	1.54 ± 0.02	1.189	136.5	<i>98.5</i> <i>98.2</i>	143.5	<i>119.2</i> ± 6	
	435×310 (140×140)	<i>1.325</i>	<i>0.122</i>	<i>2.220</i> ± 0.005	0.325 ± 0.01	1.57 ± 0.02	1.197	135.9	<i>96.7</i> <i>97.0</i>	148.0	<i>119.4</i> ± 7.6	
k- ω SST low Re	188×110 (20×20)	1.24	<i>0.138</i>	<i>2.225</i> ± 0.005	0.234 ± 0.001	<i>1.337</i> ± 0.005	1.143	70.9	69.7 69.5	105.2	78.9 ± 3.9	
	290×190 (60×60)	<i>1.39</i>	<i>0.139</i>	<i>2.220</i> ± 0.001	0.287 ± 0.001	<i>1.405</i> ± 0.01	1.159	119.1	84.3 84.5	118.6	<i>101.7</i> ± 4.9	
	365×250 (100×100)	<i>1.52</i>	<i>0.129</i>	<i>2.25</i> ± 0.01	0.37 ± 0.02	1.45 ± 0.02	1.170	132.6	85.9 85.9	<i>138.4</i>	<i>110.7</i> ± 7.3	
	435×310 (140×140)	1.54	0.142	2.39 ± 0.01	0.59 ± 0.01	1.69 ± 0.01	1.222	130.3	88.9 89.0	151.5	<i>114.9</i> ± 7.3	
k- ϵ RNG	188×110 (20×20)	2.15	<i>0.134</i>	1.908	0.0081	0.567 ± 0.001	0.839	119.8	87.8 87.9	85.5	95.2 ± 0.2	
	290×190 (60×60)	1.64	<i>0.132</i>	2.041	0.0277	0.959 ± 0.001	0.972	125.9	88.0 88.0	91.1	98.2 ± 0.3	
	365×250 (100×100)	1.58	<i>0.128</i>	<i>2.050</i> ± 0.001	0.0328 ± 0.0001	<i>1.048</i> ± 0.02	0.993	141.6	<i>90.7</i> <i>90.6</i>	95.1	104.5 ± 0.8	
	435×310 (140×140)	1.69	0.063	2.040 ± 0.001	0.0291 ± 0.0001	0.956 ± 0.001	0.983	143.3	91.2 91.2	93.6	104.8 ± 0.8	
k- ϵ realiz- able	188×110 (20×20)	1.98	0.147	1.949 ± 0.0001	0.0180 ± 0.0001	± 0.634 ± 0.0001	0.926	83.8	71.2 71.2	85.3	77.9 ± 0.25	
	290×190 (60×60)	<i>1.38</i>	<i>0.135</i>	<i>2.190</i> ± 0.0001	0.0377 ± 0.0001	± 1.333 ± 0.001	1.146	121.6	75.2 75.3	89.9	90.5 ± 0.09	
	365×250 (100×100)	<i>1.38</i>	<i>0.135</i>	<i>2.190</i> ± 0.0001	0.0377 ± 0.0001	± 1.333 ± 0.001	1.146	134.3	77.4 77.5	90.1	94.8 ± 0.8	
	435×310 (140×140)	<i>1.33</i>	<i>0.126</i>	<i>2.210</i> ± 0.0001	0.0560 ± 0.0001	± 1.538 ± 0.001	1.182	133.1	79.4 79.4	84.1	94.0 ± 0.8	
Sohankar [21]			0.13	2.15	0.18	1.3						
$5 \cdot 10^3 < Re < 5 \cdot 10^6$			± 0.01	± 0.15	± 0.05	± 0.3						
Present refer. values			1.4	0.13	2.15	0.20	1.2	{1.4}	100	101	137	108
$10^4 < Re < 2 \cdot 10^5, 0 < I < 2\%$			± 0.1	± 0.008	± 0.1	± 0.03	± 0.2	± 0.1	± 10	± 6	± 5	± 6

at $Re = 22,000$ and $I = 2\%$. The results of the $k-\epsilon$ and $k-\omega$ standard models are not presented because they are less good than with the improved versions and they are grid dependent. The reference solutions established in Tables 1 and 2 from the experimental results at $0 < I \leq 2\%$ are reminded in the last line of Table 3. The URANS values in italics in Table 3 are in the experimental reference ranges and the bold values in the yellow boxes are in a 10% accuracy from the references for L_w/D , St , $\overline{C_d}$ and the \overline{Nu} values, in a 20% accuracy for C'_d and $\overline{C_{p,b}}$, and in the Sohankar [21] reference range for C'_l . Larger accuracy ranges are used for C'_d , $\overline{C_{p,b}}$ and C'_l because they are harder to reproduce by URANS simulations. A first glance at Table 3 indicates that St and $\overline{C_d}$ are not pertinent criteria to qualify the URANS models: they are indeed not discriminant enough since nearly all the models are able to reproduce the St and $\overline{C_d}$ reference values. On the other hand, L_w/D , C'_d , $\overline{C_{p,b}}$, the averaged Nusselt number on each face, $\overline{Nu_f}$, $\overline{Nu_s}$, $\overline{Nu_r}$, and, to a lesser extent, C'_l and the averaged total Nusselt number $\overline{Nu_t}$, are quite hard to reproduce: very few values of these quantities are in italics in Table 3.

It appears that the $k-\epsilon$ RNG model does not well reproduce the experimental results, except St , $\overline{C_d}$, and $\overline{Nu_t}$. The result quality also depends on the grid size: only the mesh of 100×100 cells on the cylinder provides good enough results. The $k-\epsilon$ realizable model presents better results than the RNG version for the flow dynamics (except C'_d). However, it provides poor values of the Nusselt numbers. The best tested URANS model is $k-\omega$ SST because it allows recovering most of the experimental results whatever the grid size used. The exceptions are for the averaged Nusselt numbers that can be hard to obtain with the coarser grids (20×20 cells around the cylinder) and, on the front face, where $\overline{Nu_f}$ is over-estimated and strongly grid dependent. Finally, a low Re version of the $k-\omega$ SST model has been tested, in which the turbulent viscosity is damped by a damping function in the low Re regions. It does not improve the basic $k-\omega$ SST model.

6 Analysis of Thermal and Dynamical Profiles Around the Cylinder

Since the $k-\omega$ SST model is clearly the best among the tested models to mimic the global dynamical and thermal behaviors of the flow, we investigate now its ability to reproduce the local behaviors around the square cylinder. The lines used to plot the field and wall profiles around the square cylinder are drawn on Fig. 2(right). Comparisons of these profiles with experimental and LES results are analyzed below. The main used LES results are extracted from Boileau et al. (2013) [27] in which a high performance 3D simulation with heat transfer was carried out on an unstructured mesh of 12.6 million cells, with $y^+ < 2$ on most of the square cylinder surface.

On Fig. 3, longitudinal profiles of the time-averaged streamwise velocity component, \overline{u} , and time-averaged total kinetic energy, $\overline{k_{tot}}$, along the symmetry axis $y=0$ in the cylinder wake (see Fig. 2(right)) are presented. The profiles from the $k-\omega$ SST simulations are compared with experimental and LES results. On

Fig. 3(left), the $k-\omega$ SST profiles of \bar{u}/U_∞ along $y=0$ agree very well with the experimental profiles [5, 18, 20] in the near wake, for $x/D \leq 2.5$. In this zone, the $k-\omega$ SST profiles converge towards the experimental results with the grid refinement. The agreement of the LES profile [27] is a bit less good in this zone since the recirculation length predicted by LES is approximately equal to $L_w/D \approx 1$ while the experiments give $L_w/D \approx 1.4$. On the other hand, in the far wake, for $x/D > 3$, LES is able to predict the very slow velocity recovery observed experimentally in [5, 20]. This slow velocity recovery is due to the presence of the large turbulent eddies of the Von-Karman alley. A faster velocity recovery is observed in Durão et al. experiments [18] because both the background turbulence intensity ($I = 6\%$) and the blockage effect ($D/H = 12.8$) are much larger than in [5, 20] where $I < 3\%$ and $D/H \leq 7$: indeed the turbulent dissipation and the flow confinement both promote the large eddy disintegration and the velocity recovery. The URANS simulations also present this behavior on the largest grids because the turbulent dissipation is promoted in this case. But if the grid is refined (see the $k-\omega$ SST case 140×140), the URANS profiles better agree with the experiments.

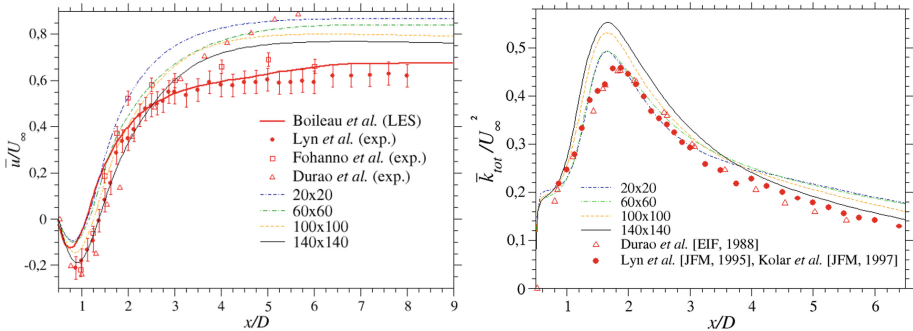


Fig. 3. Longitudinal profiles of the time-averaged streamwise velocity component and time-averaged total kinetic energy in the cylinder wake along $y=0$ (see Fig. 2 right). Comparison of the $k-\omega$ SST results with experimental [5, 6, 18, 20] and LES [27] results.

The fluctuations in the wake are depicted on Fig. 3(right) through the profiles of the time averaged total kinetic energy, \bar{k}_{tot} . In the URANS simulations, it is defined as the sum of the turbulent and coherent (or quasi-periodic) kinetic energies:

$$\bar{k}_{tot}(M) = \overline{\langle k \rangle}(M) + \bar{k}(M) \quad (3)$$

with the time-averaged coherent kinetic energy defined as:

$$\overline{\langle k \rangle}(M) = \frac{1}{2} \left(\overline{RMS^2(\langle u \rangle(M, t))} + \overline{RMS^2(\langle v \rangle(M, t))} \right) \quad (4)$$

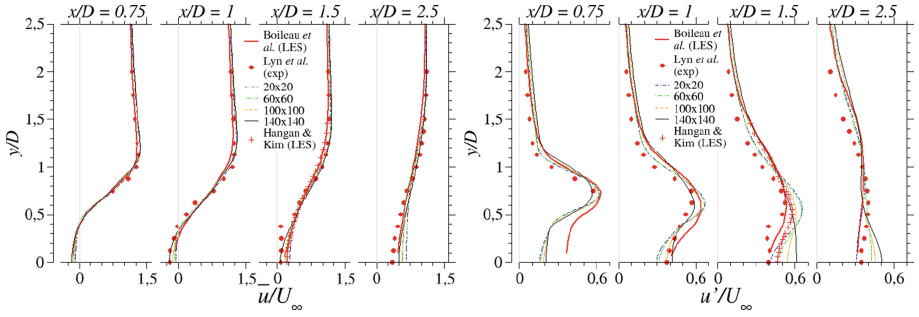


Fig. 4. Transverse profiles of the time-averaged (left) and fluctuating/RMS (right) streamwise velocity component in the cylinder top wake. Comparison with experiments [5] and LES [27, 28].

and $\bar{k}(M)$ the time-averaged turbulent kinetic energy. In the experiments, \bar{k}_{tot} is directly computed from the measured time signals of the velocity components as:

$$\bar{k}_{tot}(M) = \frac{1}{2} \left(\overline{RMS^2(u(M, t))} + \overline{RMS^2(v(M, t))} \right) \quad (5)$$

In Fig. 1(right), the $k-\omega$ SST profiles of \bar{k}_{tot} are compared with the experimental results from [5, 6, 18]. It appears that the $k-\omega$ SST profiles overestimate \bar{k}_{tot} compared to the experiments, particularly around $x/D = 2$. This could then explain the faster velocity recovery already observed in Fig. 3(left), the total fluctuations (turbulent and coherent) promoting the break-up of the large eddies.

The transverse/vertical profiles of the time-averaged and fluctuating/RMS streamwise velocity components, obtained from the $k-\omega$ SST simulations on four different grids, are plotted on Figs. 4 and 5. On Fig. 4, the profiles are located in the top near wake of the cylinder, for $0.75 \leq x/D \leq 2.5$ and $0 \leq y/D \leq 2.5$. On Fig. 5, they are located above the top surface of the cylinder along the vertical lines $x/D = -0.5$ to 0.5 drawn on Fig. 2(right). They are compared with experiments [4, 5] and LES [27, 28]. Globally, all these profiles are in good agreement with the experiments. Furthermore, the $k-\omega$ SST solutions are as accurate as the LES solutions when comparing with the experiments. The URANS averaged streamwise velocity profiles, $\bar{u}(y)$, perfectly agree with the experimental and LES results, particularly with the finest grid 140×140 , both above the cylinder (Fig. 5) and in its wake (Fig. 4). A good enough agreement is also observed for the averaged transverse velocity profiles $\bar{v}(y)$ (not shown) except in the near wake for $x/D \leq 1$ where the main discrepancies are observed. As for the velocity fluctuation profiles, $u'(y)$ (and $v'(y)$; not shown), the $k-\omega$ SST simulations seem to slightly overestimate the experimental values, at least for $y/D > 0.7$.

On Fig. 5, it is very satisfying to observe that the $k-\omega$ SST model is able to capture the complex flow physics above the cylinder. The flow separation at the leading edge of the bluff body, the thickness of the shear layer, the backflow with

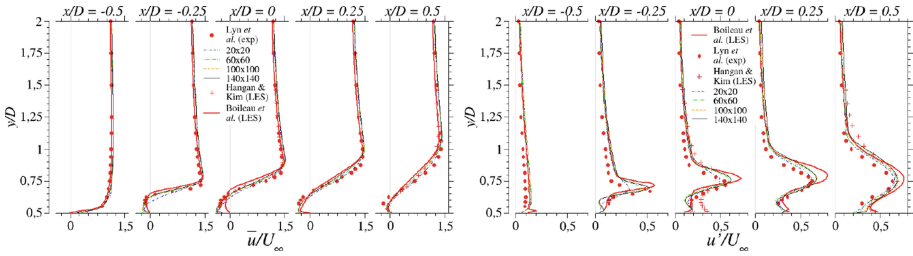


Fig. 5. Same as Fig. 4 for the cylinder top face and comparison with experiments [4].

a negative velocity in the recirculation below the separated shear layer are well reproduced by this URANS model (see $\bar{u}(y)$ on the left of Fig. 5). Moreover the intensity of the velocity fluctuations in the flapping shear layer are well captured, sometimes better than with the LES (see $u'(y)$ on the right of Fig. 5).

The wall profiles of the time-averaged pressure coefficient, $\overline{C_p}$, and Nusselt number, \overline{Nu} , around the cylinder surface are considered on Fig. 6. On the left, the $\overline{C_p}$ profiles on the front and rear faces and on the trailing edges of the horizontal faces (closed to the points B and C) are in a fairly good agreement with the experimental data [15, 17] and the recent DNS [13]. However discrepancies are observed on the top and bottom plates close to the leading edge (close to points A and D): the $\overline{C_p}$ values are underestimated by the $k-\omega$ SST model in this zone. These inaccuracies are maybe due to a too poor spatial resolution in these critical zones, where high speeds and boundary layer separations are observed (the y^+ values, not shown here, are maximum at points A and D). For the LES [27], an opposite agreement is observed: the maximum discrepancies with the experimental data are on the trailing edges of the horizontal faces and on the rear face.

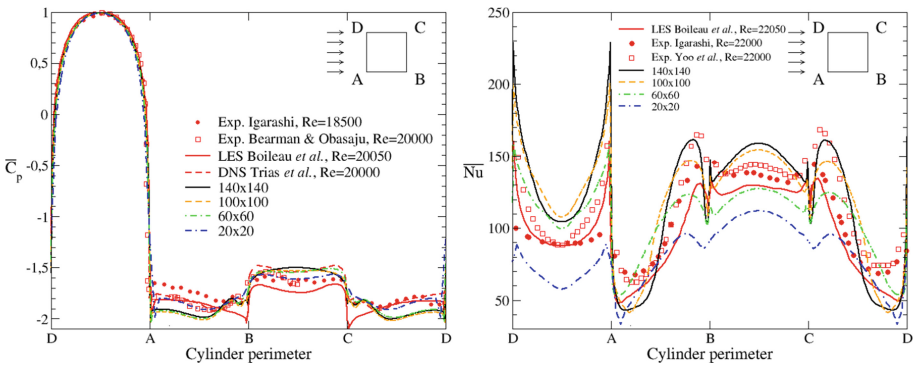


Fig. 6. Profiles of the time-averaged pressure coefficient (left) and Nusselt number (right) around the cylinder surface. Comparisons with experiments [7, 10, 15, 17], LES [27] and DNS [13].

The time-averaged Nusselt number is plotted on Fig. 6(right). The $k\text{-}\omega$ SST profiles are compared to the LES [27] and experimental solutions [7, 8, 10]. As the Nusselt profiles of these experiments are not measured at $Re = 22,000$, the \overline{Nu} experimental profiles of Fig. 6(right) are interpolated from the \overline{Nu} profiles plotted in [7, 8, 10] at other Re values. We have used the \overline{Nu} profiles at the closest Re values from 22,000 and the interpolation laws as a function of Re established in these references, whose equations are reported in Table 2 for each cylinder face. Table 2 has shown that the maximum averaged heat transfer around a square cylinder is located on the rear face. Figure 6(right) more precisely indicates that the maximum Nusselt numbers are located on the front face close to the angles (due to higher velocities at points A and D) and at the trailing edges of the horizontal faces (due to the flapping shear layers on the rear face [4] and the high level of the velocity fluctuations in the near wake of the cylinder; see Figs. 4(right) and 5(right)). When the grids are refined from 20×20 to 140×140 cells around the cylinder, the $k\text{-}\omega$ SST \overline{Nu} solutions seem to converge, at least on the front and rear faces (a variation is still present on the horizontal faces below the separated shear layer). Once again, the discrepancy between the URANS solution on the finest grid and the two experimental solutions [7, 10] is equivalent to the discrepancy between LES [27] and experiments, except on the front face where the $k\text{-}\omega$ SST solutions overestimate by 20% the experimental values.

7 Conclusions

The turbulent forced convection at high Reynolds number ($Re \geq 10^4$) around a square cylinder is a very interesting test case to qualify turbulence models because it contains very rich flow features: laminar/turbulent transition, flow separation, backward recirculation, turbulent wake flow with vortex shedding and heat transfer around the obstacle. In the first part of the paper, reference quantities describing the main flow and heat transfer characteristics of this test case have been set-up from a synthesis of around twenty distinct experiments. The flow characteristics concern the wake length, the Strouhal number and the time-averaged and RMS of the drag, lift and pressure coefficients. Furthermore a reference solution for the time-averaged wall Nusselt number on each cylinder face is built for the first time.

From the results of the various $k\text{-}\epsilon$ and $k\text{-}\omega$ models tested, it has been shown that the Strouhal number, the averaged drag coefficient and the RMS of the lift coefficient, which are usually used criteria to qualify numerical models, are in fact not selective enough to distinct between the appropriate and the non-pertinent models. On the other hand, quantities like the wake length, the RMS of the drag coefficient and the averaged Nusselt number on each face are hardly predictable.

Among the URANS models tested, it has been shown that the $k\text{-}\omega$ SST model is the most relevant to predict the flow dynamics and heat transfer in the present flow configuration, whatever the grid sizes for wall Reynolds numbers such as $y^+ < 20$. The $k\text{-}\epsilon$ type models provide unsatisfactory results for the present test

case, particularly for heat transfer. The low Re version of the $k-\omega$ SST model does not improve it.

An analysis of the averaged and fluctuating velocity profiles around the square cylinder and the wall profiles of the averaged pressure coefficients and Nusselt number has been carried out, with numerous comparisons with LES and experimental results. Compared with the experiments, the $k-\omega$ SST results are shown to be as accurate as the LES results [27], but for a much smaller computational cost, compatible with industrial applications. We have indeed evaluated the ratio of the LES CPU time in [27] to the present URANS CPU time: it varies between one and two magnitude orders according to the grid sizes.

To conclude, this paper proves that the $k-\omega$ SST model can be an excellent model for simple industrial flow configurations such as the present one, in particular when a sort of scale separation is present between the space and time scales of the largest eddies (here the von-Karman vortices) and those of the turbulence. However one cannot conclude that the $k-\omega$ SST model will be pertinent in more complex flow geometries, in particular when several characteristic frequencies of the flow will interact, like in the interaction between a wake flow and a free jet flow for instance.

Acknowledgments. Asmaa Ait Daraou and Salmane Merzouki are gratefully acknowledged for their contribution to the present work.

References

1. Sommerer, Y., Couton, D., Plourde, F.: Dissipative equipment thermal integration in powerplant compartment: experimental and numerical evaluation of heat transfer coefficient. In: Proceedings of the ASME Turbo Expo Conference, GT2014-25255, Düsseldorf, Germany (2014)
2. Wilcox, D.C.: Turbulence Modelling for CFD, 2nd edn. DCW Industries Inc., La Canada (1993)
3. Vieser, W., Esch, T., Menter, F.: Heat transfer predictions using advanced two-equation turbulence models, CFX Validation Report, CFX-VAL10/0602, pp. 1–65 (2002)
4. Lyn, D.A., Rodi, W.: The flapping shear layer formed by flow separation from the forward corner of a square cylinder. *J. Fluid Mech.* **267**, 353–376 (1994)
5. Lyn, D.A., Einav, S., Rodi, W., Park, J.-H.: A laser-Doppler velocimetry study of ensemble-averaged characteristics of the turbulent near wake of a square cylinder. *J. Fluid Mech.* **304**, 285–399 (1995)
6. Kolar, V., Lyn, D.A., Rodi, W.: Ensemble-averaged measurements in the turbulent near wake of two side-by-side square cylinders. *J. Fluid Mech.* **346**, 201–237 (1997)
7. Igarashi, T.: Heat transfer from a square prism to air stream. *Int. J. Heat Mass Trans.* **28**, 175–181 (1985)
8. Igarashi, T.: Local heat transfer from a square prism to air stream. *Int. J. Heat Mass Transf.* **29**, 777–784 (1986)
9. Tsutsui, T., Igarashi, T., Nakamura, H.: Drag reduction and heat transfer enhancement of a square prism. *JSME Int. J. Ser. B* **44**, 575–583 (2001)
10. Yoo, S.Y., Park, J.H., Chung, C.H., Chung, M.K.: An experimental study on heat/mass transfer from a rectangular cylinder. *J. Heat Transf.* **125**, 1163–1169 (2003)

11. Minguez, M., Brun, C., Pasquetti, R., Serre, E.: Experimental and high-order LES analysis of the flow in near-wall region of a square cylinder. *Int. J. Heat Fluid Flow* **32**, 558–566 (2011)
12. Brun, C., Aubrun, S., Goossens, T., Ravier, P.: Coherent structures and their frequency signature in separated shear layer on the sides of a square cylinder. *Flow Turbul. Combust.* **81**, 97–114 (2008)
13. Trias, F.X., Gorobets, A., Oliva, A.: Turbulent flow around a square cylinder at Reynolds number 22,000: a DNS study. *Comput. Fluids* **123**, 87–98 (2015)
14. Lee, B.E.: Effect of turbulence on the surface pressure field of a square prism. *J. Fluid Mech.* **69**, 263–282 (1975)
15. Bearman, P.W., Obasaju, E.D.: An experimental study of pressure fluctuations on fixed and oscillating square section cylinders. *J. Fluid Mech.* **119**, 297–321 (1982)
16. Nakamura, Y., Ohya, Y.: The effects of turbulence on the mean flow past two-dimensional rectangular cylinders. *J. Fluid Mech.* **149**, 255–273 (1984)
17. Igarashi, T.: Characteristics of the flow around rectangular cylinders (the case of the angle of attack 0 deg). *Bull. JSME* **28**, 1690–1696 (1985)
18. Durão, D.F.G., Heitor, M.V., Pereira, J.C.F.: Measurements of turbulent and periodic flows around a square cross section cylinder. *Exp. Fluids* **6**, 298–304 (1988)
19. Tamura, T., Miyagi, T.: The effect of turbulence on aerodynamic forces on a square cylinder with various corner shapes. *J. Wind Eng. Ind. Aerodyn.* **83**, 135–145 (1999)
20. Fohanno, S., Martinuzzi, R.J.: A phase-averaged analysis of droplet dispersion in the wake of a square cylinder in a uniform stream. *J. Fluids Eng.* **126**, 110–119 (2004)
21. Sohankar, A.: Flow over a bluff body from moderate to high Reynolds numbers using large eddy simulation. *Comput. Fluids* **35**, 1154–1168 (2006)
22. Maskell, E.C.: A theory of the blockage effects on bluff bodies and stalled wings in a closed wind tunnel, Reports and Memoranda n3400, Aeronautical Research Council (1963)
23. Chen, P.-H., Miao, J.-M., Jian, C.-S.: Novel technique for investigating the temperature effect on the diffusion coefficient of naphthalene into air. *Rev. Sci. Instrum.* **67**, 2831–2836 (1996)
24. Reynolds, W.C., Hussain, A.K.M.F.: The mechanics of an organized wave in turbulent shear flow. Part 3. Theoretical models and comparisons with experiments. *J. Fluid Mech.* **54**, 263–288 (1972)
25. Hussain, A.K.M.F.: Coherent structures - reality and myth. *Phys. Fluids* **26**, 2816–2850 (1983)
26. ANSYS Fluent Theory Guide, Release 17.2. Ansys Inc. Canonsburg (2016)
27. Boileau, M., Duchaine, F., Jouhaud, J.-C., Sommerer, Y.: Large-eddy simulation of heat transfer around a square cylinder using unstructured grids. *AIAA J.* **51**(2), 372–385 (2013)
28. Hangan, H., Kim, J.: Aerodynamic slot-control for 2D square prisms. *J. Wind Eng. Ind. Aero.* **91**, 1847–1857 (2003)



A Convergence Study of the One-Fluid Formulation in a Phase Inversion Application at Moderate Reynolds and Weber Numbers

Taraneh Sayadi¹(✉), Stéphane Zaleski¹, Stéphane Popinet¹, Vincent Le Chenadec², and Stéphane Vincent²

¹ Institut Jean le Rond d'Alembert, Sorbonne Université,
4 Place Jussieu, 75252 Paris, France

taraneh.sayadi@upmc.fr

² Laboratoire de Modélisation et Simulation Multi Échelle,
Université Paris-Est Marne-la-Vallée,
5 Boulevard Descartes, 77420 Champs-sur-Marne, France

Abstract. As a consequence of the remarkable advances in computational sciences realized over the past decades, complex physical processes can now be simulated. To insure fidelity and accuracy, precise convergence criteria must be satisfied. While efforts have been dedicated towards the validation of the computational tools specialized in two-phase flows, there remains a number of open questions. One of them is whether numerical solvers build upon the one-fluid formulation are able to converge integral quantities. This includes enstrophy, to which the boundary layers that develop in the interface vicinity contribute the most. A subsequent question is whether the lack of convergence of the aforementioned quantity affects lower order statistics, chief among them the surface area density. The presented work examines these questions in the context of the phase inversion configuration [1, 2]. Moderate Reynolds and Weber numbers are selected so as to guarantee proper resolution of the single-phase flow. The simulations are performed using Basilisk, a recently developed tree-based software using adaptive meshes.

Keywords: CFD · Multiphase flows · Convergence study

1 Introduction

As a consequence of the remarkable advances in computational sciences realized over the past decades, complex physical processes can now be simulated with an astonishing degree of fidelity and accuracy. In the case of two-phase flows in particular, simulation and modeling have evolved from simplistic or back-of-the-envelope estimates (integral balance, analytical analysis) to peta-scale and soon exa-scale computing applications, generating unprecedented amounts of information.

However, an increase in problem size does not necessarily correspond to an improvement in fidelity and predictability, since precise convergence criteria must be satisfied. While such properties are well-established in the computational methods employed in the single-phase community, the same can not be said for its two-phase counterpart, since the presence of the interface and related artifacts prohibits the use of the same analysis. The inability to perform such analysis is the main source of the discrepancies observed in direct numerical simulation (DNS) of multi-scale two-phase flows, where flow statistics fail to converge under mesh refinement (total enstrophy, for example [2]). In the past three decades, a series of efforts have been dedicated to physical validation of computational tools devoted to multi-phase flows. These studies range from interface tracking algorithm with analytical velocity fields, to comparison of Navier-Stokes simulations to available experiments and analytical solutions, or validation versus linear stability theory [3]. However, in most of these cases the topology of the interface is kept simple and the variation of only one multiphase flow characteristic, such as, oscillation modes of a free surface, coalescence of two drops, etc. is considered. Therefore, the details of the interaction between the interface and the underlying unsteady and usually turbulent flow, characteristic of most relevant environmental and industrial applications, remains unexplored.

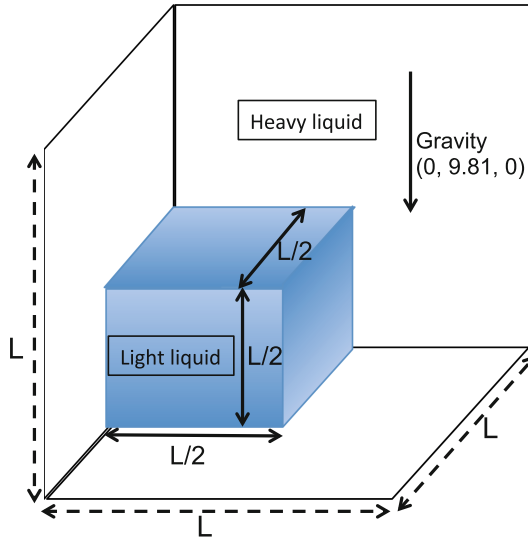


Fig. 1. A sketch of the phase inversion problem in a closed box. L denotes the size of the computational domain.

A reference problem, similar to the homogenous isotropic turbulence [4], adapted to multiphase flow configurations, would provide a benchmark for assessing features such as accuracy and convergence of the underlying solvers in a more rigorous fashion. Osmar *et al.* [2] introduced the phase inversion of an oil droplet

into a heavier fluid inside a box, shown in Fig. 1 and studied previously by [1, 5, 6], as a possible candidate, since it satisfies the following necessary criteria: (i) The initial condition is geometrically simple. (ii) The final steady-state solution is well known and is described by a horizontal plane with all the light fluid on the top. (iii) The problem showcases features similar to multi-scale multi-phase flows, as encountered in real motions, such as, large interfacial scales interacting with small dispersed droplets. The first two points are necessary in order to lift restrictions on the grid generation requirements and the numerical methods implemented for simulating the underlying flow. The set-up also allows an extensive parametric study by changing the density or viscosity ratios at the interface as well as the surface tension coefficient, resulting in various regimes: laminar, turbulent, strongly dispersed flows, as well as, large drop topologies. From a numerical point of view, physical parameters can also be defined such that a numerical convergence study is realizable for a DNS configuration, where time and spatial scales of both the flow and the interface are resolved.

This set-up is therefore chosen here to assess the performance of an open source code, Basilisk [7]. The objective of this study is to first investigate the convergence of the code in various Reynolds and Weber number regimes and to also establish whether the underlying Navier-Stokes solver together with the interface tracking technique can provide consistent solutions of this problem.

The manuscript is organized as follows. The governing equations are presented in Sect. 2. Section 3 briefly explains the numerical implementation of the underlying equations in Basilisk. The computational domain is presented in Sect. 4, where the specifications of various cases studied in this work are also described. The results are then discussed in Sect. 5. Finally, Sect. 6 presents the summary and conclusions of this work.

2 Governing Equations

The flow is governed by Navier-Stokes equations for a mixture of two immiscible fluids. The interface position is defined by a Heaviside function \mathcal{H} that takes the value of one in the reference phase and zero in the other [8]. The evolution of \mathcal{H} is given by

$$\frac{\partial \mathcal{H}}{\partial t} + \mathbf{u} \cdot \nabla \mathcal{H} = 0, \quad (1)$$

where \mathbf{u} denotes the velocity vector. The continuity and momentum equation in each phase i (for the purpose of this study $i = 1, 2$) reads as

$$\nabla \cdot \mathbf{u} = 0, \quad (2)$$

$$\rho \left(\frac{\partial \mathbf{u}}{\partial t} + (\mathbf{u} \cdot \nabla) \mathbf{u} \right) = -\nabla P + \rho \mathbf{g} + \nabla \cdot (\mu (\nabla \mathbf{u} + \nabla^T \mathbf{u})), \quad (3)$$

where P represents the pressure, \mathbf{g} the gravity vector, ρ the density, and μ the dynamic viscosity. Term $()^T$ denotes the transpose operator. In the one fluid formulation, each variable is weighted by the respective volume fraction and

then added to obtain evolution equations for the various averaged quantities. What remains is to account for the relation between the velocity and pressure, established by mass and momentum balances across a differentially thin interface located at x_I . In the absence of mass transfer, the velocity across the interface is continuous $u_1(x_I) = u_2(x_I)$, and the Laplace equation gives the pressure jump at the interface as

$$p_1 - p_2 = \sigma \kappa, \quad (4)$$

where, σ denotes the surface tension coefficient, and κ the curvature of the interface. Applying these conditions for the region containing an interface, the momentum equation can be represented for averaged quantities as [9]

$$\rho \left(\frac{\partial \mathbf{u}}{\partial t} + (\mathbf{u} \cdot \nabla) \mathbf{u} \right) = -\nabla P + \rho \mathbf{g} + \nabla \cdot (\mu (\nabla \mathbf{u} + \nabla^T \mathbf{u})) + \sigma \kappa n_i \delta_i. \quad (5)$$

In the above equation, n_i is the vector normal to the interface and δ_i a Dirac function indicating the location of the interface.

3 Numerical Treatment

An open-source numerical solver, Basilisk [7], is used to carryout the simulations. The basis for the numerical scheme, employed in this solver, is the incompressible adaptive Navier-Stokes solver Gerris [10, 11], which uses an octree for spatial discretization. This fine-scale adaptivity was proven invaluable [12], specifically in case of multiphase flows, where it is desirable to refine on and along interfaces. The interfaces itself is implicitly represented using an extension of the piece-wise linear geometric volume of fluid (VOF) treatment for adaptive meshes [12]. The resulting treatment allows full adaptivity along the interface while keeping all the other advantages of the VOF method, such as, arbitrary interface topology and topological changes, good mass conservation properties and sharp interface description. The basis for the advection of the volume fraction is the direction-split scheme originally implemented by DeBar [13] and re-implemented by others [14, 15], resulting in a scheme which is generally identical to the Eulerian-implicit-explicit scheme described by Rider and Kothe [14]. Volume fluxes are then estimated using the geometry of the reconstructed interface [13, 16]. This geometrical approach is efficient and simple to implement for Cartesian discretization elements. Finally, surface tension is calculated using a novel generalized height-function (HF) method for low resolutions, which ensures consistent second-order convergence of the curvature estimates across all resolutions [12], which is made applicable to octree grids by using the virtual regular Cartesian stencils method.

4 Computational Domain

The non-dimensional numbers governing the dynamics of this problem are the Reynolds (Re), and the Weber (We) numbers defined below;

$$\text{Re} = \frac{\rho_1 L U_g}{\mu_1}, \text{ and } \text{We} = \frac{\rho_1 L U_g^2}{\sigma}, \quad (6)$$

where $U_g = [(\rho_2 - \rho_1)/\rho_1 \times \sqrt{Hg/2}]$ is defined according to the density variations at the interface and the buoyancy forces. The related dimensionless numbers of the various cases visited in this study are given in Table 1.

Table 1. The parameters of the three cases discussed in this study.

	ρ_1 ($kg \cdot m^{-3}$)	μ_1 ($Pa \cdot s$)	ρ_2 ($kg \cdot m^{-3}$)	μ_2 ($Pa \cdot s$)	Surface tension, σ ($N \cdot m^{-1}$)	Gravity, g	L m	Re	We
Case 1	1000	0.1107	900	0.1107	0.0613	9.81	0.1	200	80
Case 2	1000	0.0111	900	0.0111	0.0153	9.81	0.1	2000	320
Case 3	1000	0.1107	900	0.1107	0.0153	9.81	0.1	200	320

In order to ensure that the various scales, present in the flow, are properly resolved throughout the convergence study, moderate Re and We numbers are selected in all the cases. For simplicity, slip boundary conditions are enforced at all the edges of the computational domain.

5 Results

The main objective of this study, as mentioned previously, is to verify whether in such low Reynolds and Weber number regimes convergence is achieved using the underlying numerical solver (Basilisk). Since this solver uses adaptive meshes, the grid-spacing is set by fixing the maximum refinement level permitted by the code *a priori*, and thus determining the maximum resolution. Henceforth all grids are reported using the maximum resolution, captured by the maximum level. Various quantities are considered in order to establish convergence, amongst which are kinetic energy and the evolution of enstrophy in fluid 1 using the following equation,

$$E = \int_{\Omega} C \cdot \frac{1}{2} \omega^2 dV, \quad (7)$$

where C is the characteristic function of phase one, with $C = 1$. Previous studies show that enstrophy is the most sensitive, as far as convergence is concerned, and therefore is selected as the measure of convergence in this study.

Figure 2 shows the evolution of kinetic energy and enstrophy for various level of refinement, applied to case 1 with the lowest Re and We numbers. As expected, kinetic energy is converged, while the same can not be said for enstrophy. Examining Fig. 2(b) suggest that for $0.8 < t < 1.3$ the evolution of enstrophy for various levels shows different behaviors, while for the remaining times convergence is achieved. These two limits, $t = 0.8$ and $t = 1.3$, are identified as cases A and B in the figure and the position of the interface for these two cases are shown in Figs. 2(c) and 2(d). These figures also show the grid refinement around the interface. Case A coincides with the time where the interface reaches the upper boundary, causing the breakup of the sheet. Case B, on the other hand,

coincides with the time where the sheet breakup is complete and the location of the interface with respect to the boundary does not change within the time frame of interest. Therefore, the lack of convergence could be attributed either to the sheet breakup or the interaction of the fluid with the upper boundary. Before examining these possibilities, the variation of the enstrophy is examined for increasing Reynolds and Weber numbers, in order to establish the influence of these parameters on the convergence of the solution.

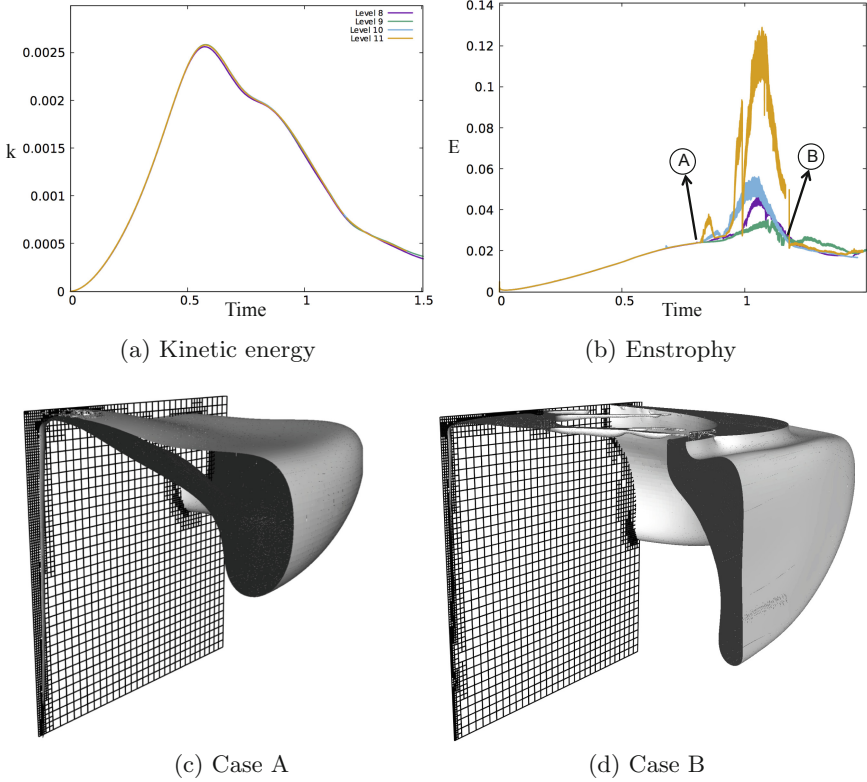


Fig. 2. Temporal evolution of kinetic energy and enstrophy, as well as, the position of interfaces for Cases A and B. The results are shown for $Re = 200$ and $We = 80$. —, 256^3 ; —, 512^3 ; —, 1024^3 ; —, 2048^3 .

Two cases are considered for further analysis: (i) a case where the value of both Reynolds and Weber numbers are increased compared to the original case (Fig. 2), and (ii) a case where only the value of the Weber number is increased and the Reynolds number is kept the same as the original case. The evolution and convergence of enstrophy for both cases is shown in Fig. 3. Comparison of the evolution of enstrophy profiles to the original case, Fig. 2(b), shows that the rapid oscillation in the enstrophy profile for the smaller grid resolutions is

boundary. In order to reach this limit the thickness of the film is chosen as $L_0 = L/4$. Figure 4(b) shows that when the rising interface reaches the layer of thin film on the top of the box, the convergence in the enstrophy is lost. However when the film is fully reconnected at $t \approx 1.2$, the prediction of the evolution of enstrophy agrees across all resolutions and convergence is established. Therefore, although the nature of boundary conditions is different than that of the original case, enstrophy seems to behave similarly, suggesting that the sheet breakup, and not the nature of the boundary condition, might be responsible for the lack of convergence in the enstrophy profile.

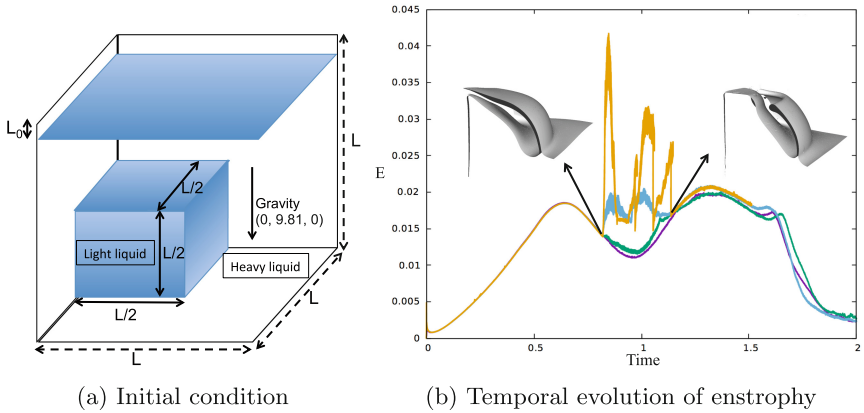


Fig. 4. A case with a thin film at the upper boundary. —, 256^3 ; —, 512^2 ; —, 1024^3 ; —, 2048^3 .

In order to examine the nature of the breakup as the sheet hits the upper boundary, the interface distribution of the lowest and highest grid resolutions, for the original case, are compared. Figure 5 shows the interface at the moment of breakup in the two cases. The comparison shows that the sheet breaks by forming small ligaments the size of the grid resolution. As the grid resolution changes, so do the structures that are formed during the breakup process, which can potentially effect the integral quantities such as the enstrophy. What remains to be established, is whether the numerical method through the alignment of the grid is affecting this process, or there exists a physical explanation. The answer to these questions are left as a topic of future research.

In order to establish whether the sheet breakup is responsible for the loss of convergence, the evolution of the enstrophy profile will be calculated over a modified domain, for case 1. The modified domain is defined such that the region which includes the sheet breakup is excluded when evaluating the desired integral quantity. As a first attempt, the integral is evaluated over the entire region $0 \leq z \leq (11 \times L_0)/12$, where z denotes the vertical axis. Figure 6 shows the evolution of the kinetic energy and enstrophy for this subdomain. Both profiles converge,

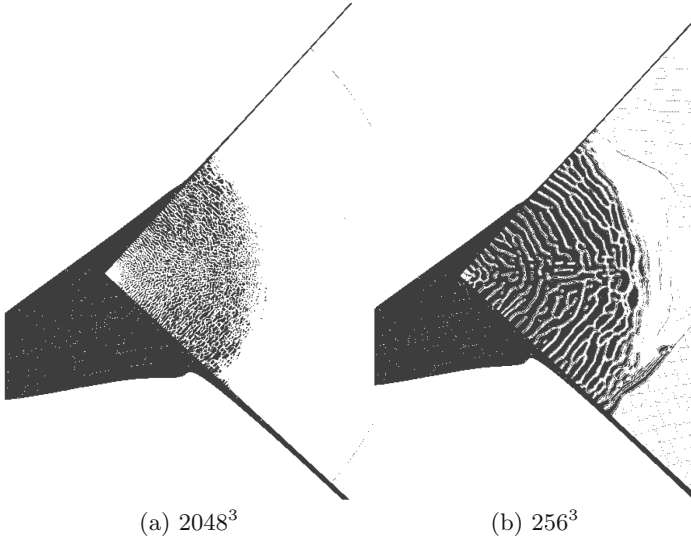


Fig. 5. The structure of the breakup as the interface reaches the upper boundary.

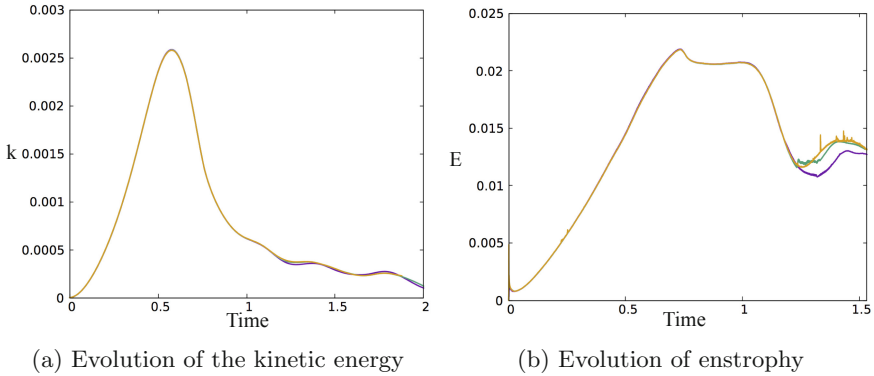


Fig. 6. Evolution of integral quantities for a subdomain, excluding the sheet breakup, for $Re = 200$ and $We = 80$. —, 256^3 ; —, 512^2 ; —, 1024^3 ; —, 2048^3 .

even after the interaction of the interface with the upper boundary, confirming the hypothesis that the sheet breakup at the top boundary is responsible for the lack of convergence in the integral quantities, and in particular, the enstrophy profile.

6 Summary and Conclusions

In this study a phase inversion problem [2] is used as a reference test case to investigate the convergence of an open source code “Basilisk” [7]. In order to

establish convergence, various integral quantities are considered, in particular, enstrophy, which has been shown to be the most sensitive as far as the convergence criteria is concerned. Therefore, most results throughout the study are presented using this integral quantity. The results show that even for moderate Re and We numbers, the convergence is lost as the interface reaches the upper boundary of the computational domain. Examining the interface topology as it reaches the upper boundary, it was shown, that it breaks by creating thin ligaments the size of the grid resolution. As the grid resolution increases, the width of these ligaments decrease, resulting in the lack of convergence in the quantity of interest. Increasing Re and We numbers has little effect on the convergence property at the time of breakup. By removing the region including the sheet breakup when calculating the integral quantity of interest, it was established that, convergence is achieved within the subdomain, suggesting that the existing sheet breakup is responsible for the loss of convergence. This hypothesis was also confirmed by replacing the slip boundary condition with a thin film of the lighter fluid and altering the interface/boundary interaction. The modified setup shows clearly, that throughout the region where the sheet breaks and reconnects the convergence is lost, and afterwards all grids arrive to a convergent solution again. This conclusion motivates further studies in the break up process of a liquid sheet, in order to establish whether the lack of convergence is due to the numerical treatment of the interface, or whether it is a consequence of a physical phenomenon.

References

1. Vincent, S., Caltagirone, J.P., Jamet, J.: Test case no.15: phase inversion in a closed box (pn, pe). *Multiphase Sci. Technol.* **6**, 101–104 (2004)
2. Osmar, L., Vincent, S., Caltagirone, J.P., Estivaleres, J. L., Auguste, F., Magnaudet, J., Menard, T., Berlemont, A., Aniszewski, W., Ling, Y., Zaleski, S.: Interface tracking methods applied to phase separation. In: 4th Joint US-European Fluids Engineering Division Summer Meeting collocated with the ASME 2014 12th International Conference on Nanochannels, Microchannels, and Minichannels. ASME, Chicago (2014)
3. Various Authors: Test-cases for interface tracking methods (2003). <http://test.interface.free.fr/>
4. Orszag, S.A., Patterson, G.S.: Numerical simulation of three-dimensional homogeneous isotropic turbulence. *Phys. Rev. Lett.* **28**, 76–79 (1972)
5. Vincent, S., Lacanette, D., Larocque, J., Toutant, A., Lubin, P., Sagaut, P.: Direct numerical simulation of phase separation and a priori two-phase LES filtering. *Comput. Fluids* **37**, 898–906 (2008)
6. Larocque, J., Vincent, S., Lubin, P., Lacanette, D., Caltagirone, J.P.: Parametric study of LES subgrid terms in a turbulent phase separation flow. *Int. J. Heat Fluid Flow* **31**, 536–544 (2010)
7. Popinet, S.: Basilisk. Basilisk Software (2014). <http://basilisk.fr/>
8. Tryggvason, G., Scardovelli, R., Zaleski, S.: *Direct Numerical Simulations of Gas-Liquid Multiphase Flows*. Cambridge University Press, Cambridge (2011)
9. Brackbill, J., Kothe, D.B., Zemach, C.: A continuum method for modeling surface tension. *J Comp. Phys.* **100**(2), 335–354 (1992)

10. Popinet, S.: Gerris: a tree-based adaptive solver for the incompressible Euler equations in complex geometries. *J. Comput. Phys.* **190**, 572–600 (2003)
11. Popinet, S.: The gerris flow solver (2007). <http://gfs.sf.net>
12. Popinet, S.: An accurate adaptive solver for surface-tension-driven interfacial flows. *J. Comput. Phys.* **228**, 5838–66 (2009)
13. DeBar, R.: Fundamentals of the KRAKEN code, Technical report, UCID-17366, California Univ., Livermore (USA), Lawrence Livermore Lab. (1974)
14. Rider, W., Kothe, D.: Reconstructing volume tracking. *J. Comput. Phys.* **141**(2), 112–152 (1998)
15. Rudman, M.: Volume-tracking methods for interfacial flows calculations. *Int. J. Numer. Methods Fluids* **24**(7), 671–691 (1997)
16. Li, J.: Calcul d'interface affine par morceaux. *Compt. Rendus l'acad. Sci. Série II Mécanique Phys. Chimie Astron.* **320**(8), 391–396 (1995)



Finite-Volume Filtering in Large-Eddy Simulations Using a Minimum-Dissipation Model

Roel Verstappen^(✉)

Bernoulli Institute for Mathematics, Computer Science and Artificial Intelligence,
University of Groningen, Groningen, The Netherlands
r.w.c.p.verstappen@rug.nl

Abstract. Large-eddy simulation (LES) seeks to predict the dynamics of the larger eddies in turbulent flow by applying a spatial filter to the Navier-Stokes equations and by modeling the unclosed terms resulting from the convective non-linearity. Thus the (explicit) calculation of all small-scale turbulence can be avoided. This paper is about LES-models that truncate the small scales of motion for which numerical resolution is not available by making sure that they do not get energy from the larger, resolved, eddies. To identify the resolved eddies, we apply Schumann's filter to the (incompressible) Navier-Stokes equations, that is the turbulent velocity field is filtered as in a finite-volume method. The spatial discretization effectively act as a filter; hence we define the resolved eddies for a finite-volume discretization. The interpolation rule for approximating the convective flux through the faces of the finite volumes determines the smallest resolved length scale δ . The resolved length δ is twice as large as the grid spacing h for an usual interpolation rule. Thus, the resolved scales are defined with the help of box filter having diameter $\delta = 2h$. The closure model is to be chosen such that the solution of the resulting LES-equations is confined to length scales that have at least the size δ . This condition is worked out with the help of Poincaré's inequality to determine the amount of dissipation that is to be generated by the closure model in order to counterbalance the nonlinear production of too small, unresolved scales. The procedure is applied to an eddy-viscosity model using a uniform mesh.

Keywords: Large-eddy simulation · Scale truncation · Filter length

1 Large-Eddy Simulation

The Navier-Stokes (NS) equations provide a model for turbulent flow. In the absence of compressibility ($\nabla \cdot u = 0$), the NS-equations are

$$\partial_t u + \nabla \cdot (u \otimes u) - \nu \nabla \cdot \nabla u + \nabla p = 0, \quad (1)$$

where u denotes the fluid velocity, p stands for the pressure and ν is the viscosity. The entire spectrum - ranging from the scales where the flow is driven to

the smallest, dissipative scales - is to be resolved numerically when turbulence is computed from the NS-equations. The available computing power is often inadequate to resolve the small scales where the dissipation takes place. In that case, the NS-equations do not provide a tractable model. Therefore, finding a coarse-grained description is one of the main challenges to turbulence research. A most promising methodology for that is large-eddy simulation [1].

Large-eddy simulation (LES) seeks to predict the dynamics of spatially filtered turbulent flows. To that end, a spatial filter is applied to the NS-equations:

$$\partial_t \bar{u} + \nabla \cdot (\bar{u} \otimes \bar{u}) - \nu \nabla \cdot \nabla \bar{u} + \nabla \bar{p} = \nabla \cdot (\bar{u} \otimes \bar{u} - \overline{u \otimes u}) \quad (2)$$

where the filter is denoted by a bar, i.e., \bar{u} denotes the filtered velocity field, and \bar{p} stands for the filtered pressure. Here it may be stressed that it is assumed that the filter commutes with spatial differential operators. The right-hand side represents the effects of the residual scales on the ‘larger eddies’. To remove the explicit dependence on the residual scales of motion, the commutator of $u \otimes u$ and the filter is replaced by a closure model. This yields

$$\partial_t v + \nabla \cdot (v \otimes v) - \nu \nabla \cdot \nabla v + \nabla \pi = -\nabla \cdot \tau(v) \quad (3)$$

where the variable name is changed from \bar{u} to v (and \bar{p} to π) to stress that the solution of (3) differs from \bar{u} , because the closure model τ is not exact [2].

2 Filter Length of a Finite-Volume Discretization

When the LES-equations are discretized in space, the low-pass characteristics of the discrete operators effectively act as a filter too. This numerical filter will inevitably interact with the filter that is explicitly applied to the Navier-Stokes equations. To try to distinguish these filters, we apply Schumann’s filter to the NS-equations [3]. That is, as in a finite-volume method we take

$$\bar{u} = \frac{1}{|\Omega_h|} \int_{\Omega_h} u(x, t) dx,$$

where Ω_h denotes a cell of the computational mesh. To start, we consider an one-dimensional uniform mesh with spacing h . Schumann’s filter is then given by

$$\bar{u}_i = \frac{1}{h} \int_{x_i-h/2}^{x_i+h/2} u(\xi, t) d\xi \quad (4)$$

Like in a finite-volume method, the conservation of momentum is described by

$$h \frac{d\bar{u}_i}{dt} + u_{i+1/2}^2 - u_{i-1/2}^2 = \dots \quad (5)$$

where $u_{i+1/2}$ denotes the velocity at $x_{i+1/2}$, that is exactly midway between the grid points x_i and x_{i+1} . The dots in Eq. (5) stand for the linear (diffusive) contributions to the conservation law. These contributions are omitted because

they are not important here. The core problem is that the velocities $u_{i+1/2}$ at the faces of the control volume (here in 1D) are to be expressed in terms of the box-filtered velocities \bar{u}_i . To make that connection, we introduce a second filter with filter length δ :

$$\tilde{u}_{i+1/2} = \frac{1}{\delta} \int_{x_{i+1/2}-\delta/2}^{x_{i+1/2}+\delta/2} u(\xi, t) d\xi \quad (6)$$

Note that this filter is half a grid cell shifted relative to the original filter. Now by choosing $\delta = 2h$, we obtain the key relation

$$\tilde{u}_{i+1/2} = \frac{1}{2} (\bar{u}_i + \bar{u}_{i+1}) \quad (7)$$

This equation does not contain any error! Thus the conservation law (5) can also be written as

$$h \frac{d\bar{u}_i}{dt} + \tilde{u}_{i+1/2}^2 - \tilde{u}_{i-1/2}^2 = -\sigma_{i+1/2} + \sigma_{i-1/2} + \dots \quad (8)$$

where $\sigma_{i+1/2} = \tilde{u}_{i+1/2}^2 - u_{i+1/2}^2$. According to Eq. (7), the left-hand side depends on the spatially filtered velocities \bar{u}_{i-1} , \bar{u}_i and \bar{u}_{i+1} . In the conventional finite-volume method, Eq. (7) is viewed as the interpolation rule for the fluxes - the interpolation rule is then given by $u_{i+1/2} \approx \tilde{u}_{i+1/2}$. Consequently, the right-hand side of (8) represents the interpolation error. If, however, Eq. (8) is seen as a closure problem, then the problem reads: express $\sigma_{i+1/2}$ in terms of the box-filtered velocity $\tilde{u}_{i+1/2}$. So from that point of view, (the effect) of the residual of the δ -filter is to be modeled to close (8). These different points of view illustrate the entanglement of the discretization (here: interpolation) error and the closure model.

We take $\delta = 2h$ and consider two neighboring ‘volumes’, say $[x_{i-1/2}, x_{i+1/2}]$ and $[x_{i+1/2}, x_{i+3/2}]$. The two corresponding momentum equations (Eq. (8) for \bar{u}_i as well as for \bar{u}_{i+1}) can be added together using Eq. (7). Thus, we get

$$\delta \frac{d\tilde{u}}{dt} \Big|_{i+1/2} + \tilde{u}_{i+3/2}^2 - \tilde{u}_{i-1/2}^2 = -\sigma_{i+3/2} + \sigma_{i-1/2} + \dots$$

A finite-difference approximation with stepsize $\delta = 2h$ induces a spatial filter too. Indeed,

$$\frac{\phi_{i+3/2} - \phi_{i-1/2}}{\delta} = \frac{1}{\delta} \int_{x_{i-1/2}}^{x_{i+3/2}} \frac{\partial \phi}{\partial x}(\xi) d\xi = \frac{\widetilde{\partial \phi}}{\partial x} \Big|_{i+1/2}$$

Hence by combining the two equations above, we obtain

$$\partial_t \tilde{u} + \widetilde{\partial_x \tilde{u}^2} = \partial_x (\widetilde{\tilde{u}^2 - u^2}) + \dots \quad (9)$$

Once again, it may be stressed that the above momentum equation is exact: it does not contain any error yet. The nonlinear term in the left-hand side is usually

not filtered; hence to put it the standard LES-form, we add the residual of $\partial_x \tilde{u}^2$ to both the left- and right-hand side. This yields the common LES-template wherein the filter length equals $\delta = 2h$ (i.e., is given by the interpolation filter):

$$\partial_t \tilde{u} + \partial_x \tilde{u}^2 = \partial_x (\tilde{u}^2 - \widetilde{u^2}) + \dots \quad (10)$$

So, in a finite-volume setting, we need to model the effects of all scales smaller than $\delta = 2h$, and not just the subgrid contributions. Indeed, the finite-volume template (8) can be closed by modeling the effect of the residue of the interpolation filter (6). If we view the finite-volume method in this way, we should be borne in mind that the closure condition is to be imposed at the scale $\delta = 2h$ which is determined by the interpolation rule. It may be remarked here that the highest frequency that can be represented on the grid (the mode that equals $+1$ in the even grid points and -1 in the odd grid points) lies in the kernel of the interpolation operator; hence that mode is invisible and therefore it's effect need be modeled.

So far, we have only considered one spatial dimension. The above reasoning can simply be extended to more dimensions. Indeed, also in two or three dimensions we need to interpolate the velocities to the faces of the control volumes and the interpolation filter has width $2h$.

3 Separation of Scales

The very essence of large-eddy simulation is that the (explicit) calculation of all small-scale turbulence - for which numerical resolution is not available - is avoided. This sets a condition to the closure model [4–7]. To determine this condition, we consider an arbitrary part of the flow domain with diameter δ . With the aid of the associated box filter,

$$\tilde{v} = \frac{1}{|\Omega_\delta|} \int_{\Omega_\delta} v(x, t) dx, \quad (11)$$

the undesirable small scales in the LES-field v are defined by $v' = v - \tilde{v}$.

We make use of the Poincaré-Wirtinger inequality to develop a scale-separation condition, see also [4–6]. This inequality states that there exists a constant C_δ depending only on the domain Ω_δ such that

$$\int_{\Omega_\delta} |v - \tilde{v}|^2 dx \leq C_\delta \int_{\Omega_\delta} |\nabla v|^2 dx \quad (12)$$

That is, the $L^2(\Omega_\delta)$ norm of the residual field v' is bounded by a constant (independent of v) times the $L^2(\Omega_\delta)$ norm of ∇v . Payne and Weinberger [8] have shown that the Poincaré constant is given by $C_\delta = (\delta/\pi)^2$ for convex (bounded, Lipschitz) domains Ω_δ . This is the best possible estimate in terms of the diameter alone.

The Poincaré inequality provides an upper bound for the energy of the unwanted subfilter scales of motion. Note that if we take the closure model such that $\int_{\Omega_\delta} |\nabla v|^2 dx = 0$ for all times, then $\int_{\Omega_\delta} |v'|^2 dx = 0$.

4 Counterbalancing the Production of Too Small Scales

Equation (12) shows that the energy of the too small scales can be bounded by $L^2(\Omega_\delta)$ norm of the velocity gradient ∇v . According to Eq. (3), this L^2 -norm is governed by

$$\begin{aligned} \frac{d}{dt} \int_{\Omega_\delta} \frac{1}{2} |\nabla v|^2 dx &= \int_{\Omega_\delta} \nabla \cdot (\nu \nabla \cdot \nabla v) : \nabla dx \\ &\quad - \int_{\Omega_\delta} \nabla \nabla \cdot (\tau + (v \otimes v) + \pi I) : \nabla v dx \end{aligned} \quad (13)$$

Here it may be remarked that we use the common notation $a : b = \sum_{ij} a_{ij} b_{ij}$. The second line of the right-hand side above represents the nonlinear production as a result of the pressure, convection and the modeled eddy-dissipation, respectively. Equation (13) shows that

$$\frac{d}{dt} \int_{\Omega_\delta} \frac{1}{2} |\nabla v|^2 dx = -\nu \int_{\Omega_\delta} \nabla \cdot \nabla v : \nabla \cdot \nabla v dx \leq 0 \quad (14)$$

provided the closure model τ is chosen such that

$$\int_{\Omega_\delta} \nabla \nabla \cdot (\tau + (v \otimes v) + \pi I) : \nabla v dx = \int_{\partial\Omega_\delta} \nu \nabla v : \partial_n \nabla v ds \quad (15)$$

It goes without saying that we have to initialize the velocity field such that $v' = 0$ at $t = 0$. Then, v is constant in Ω_δ ; hence $\nabla v = 0$ in Ω_δ . Thus, we have $\int_{\Omega_\delta} |\nabla v|^2 dx = 0$ at $t = 0$. If Eq. (14) is supplied with this initial condition we obtain $\int_{\Omega_\delta} |\nabla v|^2 dx = 0$ for all times $t \geq 0$. Now by applying Poincaré's inequality (12) we arrive at $\int_{\Omega_\delta} |v'|^2 dx = 0$. So, in conclusion, Eq. (15) ensures that all scales of size smaller than δ are insignificant, and hence need not be computed. Stated otherwise, if Eq. (15) is satisfied, the closure model τ counterbalances the nonlinear production of small, unresolved scales of motion in a large-eddy simulation of turbulence.

To elaborate on this truncation condition, we use Cayley-Hamilton's theorem. For incompressible flows, Cayley-Hamilton states that $\nabla v^3 - Q \nabla v + R I = 0$, where the second and third invariant of the velocity-gradient tensor are given by $Q(v) = \frac{1}{2} \nabla v : \nabla v$ and $R(v) = -\frac{1}{3} \nabla v \nabla v : \nabla v = -\det \nabla v$, respectively. The convective contribution to the left-hand side of Eq. (15) can be written in terms of these invariants. Indeed, since $\partial_k v_k = 0$, we have

$$\begin{aligned} &\int_{\Omega_\delta} \partial_i \partial_k (v_k v_j) \partial_i v_j dx \\ &= \int_{\Omega_\delta} \partial_i v_k \partial_k v_j \partial_i v_j + \frac{1}{2} \partial_k \left(v_k (\partial_i v_j)^2 \right) dx \\ &\quad - \int_{\Omega_\delta} 3R(v) dx + \int_{\partial\Omega_\delta} Q(v) v \cdot n ds \end{aligned}$$

where n is the outward-pointing normal vector to the boundary $\partial\Omega_\delta$ of Ω_δ and $n_i = n_i/\delta_i$. It may be noted that the Einstein summation convention applies here, i.e., the above formula represents a summation over the terms indexed by i , j and k . In the sequel we will implicitly use Einstein's notation too.

In conclusion, the nonlinear contributions to the evolution of the $L^2(\Omega_\delta)$ norm of ∇v are balanced by the closure model if

$$\begin{aligned} \int_{\Omega_\delta} \nabla \nabla \cdot (\tau + \pi I) : \nabla v \, dx &= 3 \int_{\Omega_\delta} R(v) \, dx \\ &- \int_{\partial\Omega_\delta} (Q(v) v \cdot n + \nu \partial_n Q) \, ds \end{aligned} \quad (16)$$

This condition ensures that the dissipation provided by the closure model τ is sufficient to damp the production of any scales of size smaller than δ . Thus the model confines the LES-solution to scales having at least length δ . It may be noted that the surface integral in Eq. (16) consists of two parts. The first part represents the convective flux of Q through the boundary of the box; the negative sign occurs because the normal is taken in the outward direction. The second part represents the viscous diffusion of Q through the boundary of the box Ω_δ . The volume integral describes the production of Q ; note: R provides a measure for the production.

5 Eddy Viscosity

The eddy-viscosity model is the most widely used model. For that reason, we consider it here. That is, we adopt the template

$$\tau(v) - \frac{1}{3} \text{tr}(\tau) I = -2\nu_t S(v) \quad (17)$$

where ν_t denotes the eddy viscosity and $S(v)$ is the symmetric part of the velocity gradient, $S(v) = \frac{1}{2}(\nabla v + \nabla v^*)$. As usual, the factor -2 is introduced in Eq. (17). Moreover only the deviatoric component of the closure tensor is described here, because the divergence of the volumetric, isotropic component $\frac{1}{3} \text{tr}(\tau) I$ can be incorporated into the pressure gradient; see Eq. (3). The classical Smagorinsky model reads $\nu_t = C_S^2 \delta^2 \sqrt{4q}$, where C_S is the Smagorinsky constant and $q = \frac{1}{2} S$: S is the second invariant of S .

The scale-truncation condition can be used to determine the eddy-viscosity in Eq. (17). By substituting the eddy-viscosity model into (16), we obtain the following expression for the eddy viscosity

$$\begin{aligned} - \int_{\Omega_\delta} \nabla \nabla \cdot \nu_t \nabla v : \nabla v \, dx &= 3 \int_{\Omega_\delta} R(v) \, dx \\ &- \int_{\partial\Omega_\delta} (Q(v) v \cdot n + \nu \partial_n Q) \, ds \end{aligned} \quad (18)$$

where we neglected the contribution of the pressure, since we only consider the deviatoric component of the closure model. The left-hand side represents the eddy-dissipation of scales that are too small to be resolved, the volume integral over R represents the production of these scales, and the surface integrals in the right-hand side describe their convective and diffusive transport. Now if we assume that the dissipation balances the production, then there is no net production; so there is nothing to be transported. Therefore we omit the contribution of the transport terms here. Furthermore, we assume that the eddy-viscosity consists of large scales only; hence, ν_t is taken constant in Ω_δ . Under these assumptions, Eq. (18) simplifies to

$$-\nu_t \int_{\Omega_\delta} \nabla \nabla \cdot \nabla v : \nabla v \, dx = 3 \int_{\Omega_\delta} R(v) \, dx$$

If we divide this equation by the $L^2(\Omega_\delta)$ -norm of the scaled velocity gradient ∇v , we get

$$\nu_t \text{Ray}(-\nabla \cdot \nabla, \nabla v) = \frac{3 \int_{\Omega_\delta} R(v) \, dx}{2 \int_{\Omega_\delta} Q(v) \, dx} \quad (19)$$

where the Rayleigh quotient is defined by

$$\text{Ray}(-\nabla \cdot \nabla, \nabla v) = \frac{\int_{\Omega_\delta} -\nabla \cdot \nabla \nabla v : \nabla v \, dx}{\int_{\Omega_\delta} \nabla v : \nabla v \, dx} \quad (20)$$

The eddy viscosity ν_t depends on the (scaled) velocity-gradient via Q and R as well as on the Rayleigh quotient of the (negative) Laplacian $-\nabla \cdot \nabla$ in the direction of ∇v . The physical dimension of the right-hand side in (19) is 1/time; the Rayleigh quotient in Eq. (20) has dimension 1/length². So in this set-up, the ratio of the invariants $Q(v)$ and $R(v)$ defines the time that is necessary to construct an eddy-viscosity, and the Rayleigh quotient provides the length.

Unfortunately, calculating the Rayleigh quotient numerically is not a great option, because a direct numerical computation yields a proper approximation of the spectrum of the Laplacian (and thus of the Rayleigh quotient) only if the filter length is taken much larger than the grid width, which means in practice that the cost of the simulation becomes too high. To work around this we first note that the Rayleigh quotient scales with $1/\delta^2$; hence, it can be approximated by $(c/\delta)^2$, where c denotes a constant; details to follow. In this way we arrive at

$$\nu_t = \frac{3\delta^2}{2c^2} \frac{\int_{\Omega_\delta} R(v) \, dx_+}{\int_{\Omega_\delta} Q(v) \, dx} \quad (21)$$

where the index ‘+’ denotes the positive part, i.e., $f_+ = \max\{0, f\}$. Thus, negative values are clipped (see also [9]).

Next, we bound the Rayleigh quotient on basis of the smallest eigenvalue of the (negative) Laplacian on Ω_δ . In a numerical simulation, the value of the constant c depends on the discretization of the convective derivative, see [10]. The Rayleigh quotient of $-\nabla \cdot \nabla$ (in the direction of ∇v) can be bounded from

below with the help of the smallest eigenvalue of the discretization of $-\nabla \cdot \nabla$ on Ω_δ . On an uniform 1D mesh the smallest eigenvalue of a second-order central discretization of the second derivative on an interval of length δ is equal to $4/\delta^2$. The associated eigenmode is $-1 \ 0 \ +1 \ 0 \ -1$, i.e., the amplitude is zero in the odd grid points and oscillates between -1 and $+1$ in the even grid point. Note: $\delta = 2h$. It may be noted this will be the dominant mode if the closure model functions well, since then all other modes, smaller scales of motion, are effectively dampened by the closure model. Likewise, in 3D, the largest eigenvalue of a second-order central discretization of the Laplacian on Ω_δ is equal to $12/\delta^2$; hence $c^2 = 12$ in that case. For this choice of the discretization (and mesh) the eddy viscosity is given by

$$\nu_t = \frac{\delta^2}{8} \frac{\int_{\Omega_\delta} R(v) dx_+}{\int_{\Omega_\delta} Q(v) dx} \quad (22)$$

To calculate the eddy viscosity from this expression, the invariants $R(v)$ and $Q(v)$ are to be computed from the (scaled) discrete velocity gradient, where the gradient is discretized as in the convective term. Furthermore, the integrals over the filter box Ω_δ are to be approximated with the help of a quadrature rule, the trapezoidal rule or the midpoint rule, for example.

6 Results

The eddy-viscosity model given by Eq. (22) yields $\nu_t = 0$ in any part Ω_δ of the flow where $R = 0$ (no production of scales $< \delta$). It goes without saying that the performance of the eddy-viscosity model has to be investigated for many cases. As a first step it was tested for an isotropic turbulent flow by means of a comparison with a direct numerical simulation (DNS). The computational grid used for the large-eddy simulation consists of 64^3 points. Figure 1 shows the results of 3 large-eddy simulations. As can be seen in Fig. 1 the LES using the eddy-viscosity model (22) with $\delta = h$ does not dissipate the energy sufficiently: the tail of the energy spectrum is too high. Taking $\delta = 2h$ gives much better results. The dynamic Smagorinsky model is a bit more dissipative in his case, that is damps the small-scales too much. This example confirms that $\delta = 2h$ is the right choice for the eddy-viscosity model (22).

Next, the eddy-viscosity model (22) is evaluated for the numerical simulation of a turbulent channel flow by means of a comparison with a direct numerical simulation (DNS). The results are compared to the DNS data of Moser *et al.* at $\text{Re}_\tau = 590$ [11]. In fact, we should compare the LES-solution \tilde{v} to the filtered DNS-solution \tilde{u} . Yet, since the filtered DNS-solution is not given by Moser *et al.* we will compare v directly to u . The dimensions of the channel are taken identical to those of the DNS of Moser *et al.* The computational grid used for the large-eddy simulation consists of 64^3 points. The DNS was performed on a $384 \times 257 \times 384$ grid, i.e., the DNS uses about 144 times more grid points than the present LES. As can be seen in Fig. 2 both the mean velocity and the root-mean-square of the fluctuating velocity are in good agreement with the DNS.

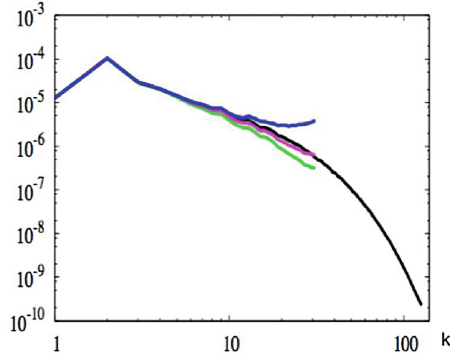


Fig. 1. Energy spectrum of an isotropic turbulent flow. The spectrum that extend beyond $k = 100$ corresponds to a DNS. The other three spectra represents results of large-eddy simulations. The upper curve corresponds to the eddy-viscosity model (22) with $\delta = h$; the lower curve shows the result of a LES using the dynamic Smagorinsky model for comparison, the middle curve corresponds to (22) with $\delta = 2h$.

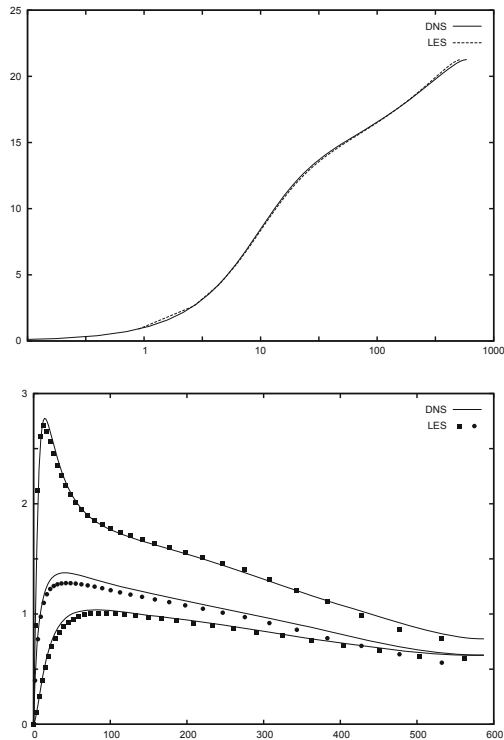


Fig. 2. The upper figure shows the mean velocity (in wall coordinates) obtained with the help of the 64^3 LES and the DNS [11]. The lower figure displays the rms of the fluctuating velocities; here the upper and lower curve represents the stream-wise and wall-normal component, respectively.

Here, it may be remarked that 64^3 simulations without a LES-model predict a wall friction that differs about 10% from the DNS.

7 Conclusions

We discussed closure models for large-eddy simulation of incompressible turbulent flows. In particular, we considered minimum-dissipation models which ensure that the closure model provides sufficient dissipation to counteract the production of any (small) scales for which numerical resolution is not available. When the LES-equations are discretized in space, the low-pass characteristics of the discrete operators effectively act as a filter too. In this paper we focussed on a finite-volume discretization technique. For such a discretization method the resolved scales are defined with the help of interpolation rule for approximating the convective fluxes through the faces of control volumes. Consequently, in a finite-volume setting, we need to model the effects of all scales smaller than $\delta = 2h$, where h denotes the mesh width. We used Poincaré's inequality to truncate the nonlinear dynamics at the scale δ set by the interpolation rule.

References

1. Sagaut, P.: Large Eddy Simulation for Incompressible Flows. Springer, Berlin (2001)
2. Guermond, J.L., Oden, J.T., Prudhomme, S.: Mathematical perspectives on large eddy simulation models for turbulent flows. *J. Math. Fluid Mech.* **6**, 194–248 (2004)
3. Schumann, U.: Subgrid scale model for finite difference simulations of turbulent flows in plane channels and annuli. *J. Comp. Phys.* **18**, 376–404 (1975)
4. Verstappen, R.: When does eddy viscosity damp subfilter scales sufficiently? *J. Sci. Computing* **49**, 94–110 (2011)
5. Rozema, W., Bae, H.J., Moin, P., Verstappen, R.: Minimum-dissipation models for large-eddy simulation. *Physics of Fluids* **27**, 085107 (2015)
6. Verstappen, R.: How much eddy dissipation is needed to counterbalance the nonlinear production of small, unresolved scales in a large-eddy simulation of turbulence? *Computers & Fluids* **176**, 276–284 (2018)
7. Rozema, W., Verstappen, R.W.C.P., Kok, J.C., Veldman, A.E.P.: Low-dissipation simulation methods and models for turbulent subsonic flow. *Arch. Comp. Meth. Engng.* **27**, 299–330 (2020)
8. Payne, L.E., Weinberger, H.F.: An optimal Poincaré inequality for convex domains. *Arch. Rat. Mech. Anal.* **5**, 286–292 (1960)
9. Germano, M., Piomeli, U., Moin, P., Cabot, W.: A dynamic subgrid-scale eddy viscosity model. *Physics of Fluids A* **8**, 1760–1765 (1991)
10. Verstappen, R.W.C.P., Rozema, W., Bae, H.J.: Numerical scale separation in large-eddy simulation. In: *Proceedings 2014 Summer Program, Center for Turbulence, Stanford, USA* (2014)
11. Moser, R.D., Kim, J., Mansour, N.N.: Direct numerical simulation of turbulent channel flow up to $Re_\tau=590$. *Phys. Fluids* **11**, 943–945 (1999)

Contributed Papers



Simulation of a Particulate Flow in 3D Using Volume Penalization Methods

Philippe Angot¹, Léa Batteux²(✉), Jacques Laminie², and Pascal Pouillet²

¹ Université d'Aix-Marseille, 13007 Marseille, France

² Université des Antilles, Campus de Fouillole, Pointe-à-Pitre 97157, Guadeloupe
lea.batteux@univ-antilles.fr

Abstract. We are concerned with modelling a particulate flow in a three-dimensional domain. The particles are assumed to be rigid, allowing us to describe their motion using the Newton laws. As we aim to take into account complex shapes for the solid inclusions, we adopt volume penalization methods. Those methods allow us to extend the fluid problem inside the solid domain by assimilating the particle as a porous medium. The homogeneous fluid flow is governed by the incompressible Navier-Stokes equations. The whole problem is solved with a projection-correction method using finite volumes and a staggered mesh to ensure the inf-sup condition for the stability. Regarding the transport of the particles, a marker-based front tracking method is used for the fluid-solid interface, as well as a collision strategy. Both penalization methods are studied and compared in the context of particulate flows.

Keywords: Fluid-structure interactions · Fictitious domain · Penalization

1 Introduction

We are interested in the modelling of fluid-solid systems where we consider rigid solid inclusions in an incompressible viscous fluid flow in a three-dimensional domain. Such problems led to a wide panel of methods to attempt to model and reproduce faithfully the fluid-solid interactions observed in real life problems. Depending on the needs, different degrees of coupling between the fluid and the particles may be applied. In what follows we will resort to a strong coupling to make evident the influence of the solid inclusions on the fluid. Using an Eulerian formulation for the fluid flow, we extend the fluid problem inside the solid domain as defined by the fictitious domain methods. Given the assumptions on the particles we require a rigidity constraint on the solid domain. Among the most famous methods in this field, the works of Glowinsky et al. [1] which resort to Lagrange multipliers for the constraint, and volume penalty methods [2, 3]. The latter idea is based on porous laws and will be considered in our model.

The computational tests have been performed using the server of the Centre Commun de Calcul Intensif (C3I) of Université des Antilles.

Let us introduce our physical domain Ω along with its boundary Γ , containing the fluid domain $\Omega_f(t)$ and N particles $\Omega_s^i(t)$ such that $\cup_{i=1}^N \Omega_s^i(t) = \Omega_s(t)$ defines the solid domain. Therefore we have $\Omega_f(t) = \Omega \setminus \overline{\Omega_s(t)}$. Given the assumptions, we will work with the incompressible Navier-Stokes equations to govern the fluid flow,

$$\left\{ \begin{array}{ll} \rho \left(\frac{\partial \mathbf{v}}{\partial t} + (\mathbf{v} \cdot \nabla) \mathbf{v} \right) - 2 \nabla \cdot (\mu \mathbf{D}(\mathbf{v})) + \nabla p = \mathbf{f} & \text{in } \mathbb{R}^+ \times \Omega_f(t) \\ \nabla \cdot \mathbf{v} = 0 & \text{in } \mathbb{R}^+ \times \Omega_f(t) \\ \mathbf{v}(0, \mathbf{x}) = \mathbf{v}_0 & \text{in } \mathbb{R}^+ \times \Omega_f(0) \\ \mathbf{v}(t, \mathbf{x}) = \mathbf{v}_\Gamma & \text{on } \mathbb{R}^+ \times \Gamma \\ \mathbf{v}(t, \mathbf{x}) = \mathbf{V}_i(t) + \boldsymbol{\omega}_i(t) \times \mathbf{r}_i(t, \mathbf{x}) & \text{on } \mathbb{R}^+ \times \partial \Omega_s^i(t) \end{array} \right.$$

with the fluid velocity \mathbf{v} and pressure p as the unknowns. The fluid here is defined by its density ρ and dynamic viscosity μ . The term $\mathbf{D}(\mathbf{v})$ in the momentum equation refers to the tensor of deformation rate of the fluid, and we have: $\mathbf{D}(\mathbf{v}) = \frac{1}{2}(\nabla \mathbf{v} + (\nabla \mathbf{v})^T)$. The last relation defines the no-slip condition; it closes the boundary conditions on Ω_f and enables the coupling with the solid domain. It states that the fluid velocity and the solid velocity are equal on the fluid–solid interface. Finally, as the particles are assumed to be rigid, their motion can be described using the translational and rotational velocities $(\mathbf{V}_i, \boldsymbol{\omega}_i)$ of their respective center of mass \mathbf{X}_i . As such we can define the rigid velocity field $\mathbf{v}_s(t, \mathbf{x})$ in $\Omega_s(t)$: $\forall \mathbf{x} \in \Omega_s(t), \exists (\mathbf{V}_i(t), \boldsymbol{\omega}_i(t)), \mathbf{v}_s(t) = \mathbf{V}_i(t) + \boldsymbol{\omega}_i(t) \times \mathbf{r}_i(t, \mathbf{x})$ where $\mathbf{r}_i(t, \mathbf{x}) = \mathbf{x} - \mathbf{X}_i(t)$. In addition we have for each particle that,

$$\left\{ \begin{array}{l} M_i \frac{d\mathbf{V}_i}{\delta t} = \int_{\Omega_s^i(t)} \rho_s \mathbf{f}_i(t, \mathbf{x}) dx + \int_{\partial \Omega_s^i} \boldsymbol{\sigma}(\mathbf{v}, p) \cdot \mathbf{n} dS \\ \frac{d(J_i(t) \boldsymbol{\omega}_i)}{\delta t} = \int_{\Omega_s^i(t)} \rho_s \mathbf{r}_i(t, \mathbf{x}) \times \mathbf{f}_i(t, \mathbf{x}) dx + \int_{\partial \Omega_s^i} \mathbf{r}_i(t, \mathbf{x}) \times (\boldsymbol{\sigma}(\mathbf{v}, p) \cdot \mathbf{n}) dS \end{array} \right.$$

Here the particle is subjected to the exterior force \mathbf{f}_i . The coupling with the fluid exists within the surface integrals, as they involve $\boldsymbol{\sigma}(\mathbf{v}, p) = (-p\mathbf{I} + 2\mu\mathbf{D}(\mathbf{v}))$, the surface stress tensor of the incompressible fluid. The surface integral applied to the translational (resp. rotational) acceleration will be denoted \mathbf{F}_i (resp. \mathbf{T}_i). We also define the density, mass and inertia tensor (ρ_s, M_i, J_i) of the particle i .

So as to prevent the use of time–dependent spatial meshes, we resort to fictitious domain methods to extend the fluid problem inside the solid domain. In our case we will be using and comparing the L2–penalty and the H1–penalty methods, which consist in penalizing specific quantities in the fluid problem. Convergence estimates can be found in [2, 4] for fixed obstacles. Notably, the L2–penalty has a convergence rate of $\mathcal{O}(\eta^{1/2})$ in the fluid in regard to the penalization parameter η whereas the H1–penalty has a convergence rate of $\mathcal{O}(\eta)$.

1.1 The Darcy or L2-Penalty

We penalize the velocity itself by introducing a perturbation term to the momentum equation in order to extend the problem inside the solid domain:

$$\begin{cases} \rho\left(\frac{\partial \mathbf{v}}{\partial t} + (\mathbf{v} \cdot \nabla)\mathbf{v}\right) - 2\nabla \cdot (\mu D(\mathbf{v})) + \nabla p + \frac{\mu}{\eta} \mathbf{1}_{\Omega_s}(\mathbf{v} - \mathbf{v}_s) = \mathbf{f} & \text{in } \mathbb{R}^+ \times \Omega \\ \nabla \cdot \mathbf{v} = 0 & \text{in } \mathbb{R}^+ \times \Omega \end{cases}$$

The parameter η roughly describes the permeability of the solid domain, which is now considered as a porous medium. The latter will be taken as small as possible, in order to obtain the no-slip condition on $\partial\Omega_s$ in a weak sense with fixed point iterations regarding the convergence of \mathbf{v}_s .

Following the introduction, the system of equations above is coupled to the Newton laws for the transport of the solid domain. Owing to the modified momentum equation, we can consider for the fluid contributions on the particle $\Omega_s^i(t)$:

$$\begin{aligned} \mathbf{F}_i &= \lim_{\eta \rightarrow 0} \frac{\mu}{\eta} \int_{\Omega_s^i(t)} (\mathbf{v} - \mathbf{v}_s) dx + \rho \int_{\Omega_s^i(t)} \frac{d\mathbf{v}}{dt} dx \\ \mathbf{T}_i &= \lim_{\eta \rightarrow 0} \frac{\mu}{\eta} \int_{\Omega_s^i(t)} \mathbf{r}_i(t, \mathbf{x}) \times (\mathbf{v} - \mathbf{v}_s) dx + \rho \int_{\Omega_s^i(t)} \mathbf{r}_i(t, \mathbf{x}) \times \frac{d\mathbf{v}}{dt} dx \end{aligned}$$

Using these definitions, one deals with volume integrals, favoring greatly their computation in the context of fictitious domain methods.

1.2 The Viscous or H1-Penalty

We constraint the extended fluid velocity by penalizing its tensor of deformation rate $D(\mathbf{v})$ inside the solid domain, in the momentum equation. To achieve this we resort to a multiphase flow representation of the problem, using the non-homogeneous incompressible Navier-Stokes equations with variable viscosity,

$$\begin{cases} \frac{\partial \rho}{\partial t} + (\mathbf{v} \cdot \nabla)\rho = 0 & \text{in } \mathbb{R}^+ \times \Omega \\ \frac{\partial(\rho \mathbf{v})}{\partial t} + \nabla \cdot (\rho \mathbf{v} \otimes \mathbf{v}) - 2\nabla \cdot (\mu(\rho)D(\mathbf{v})) + \nabla p = \mathbf{f} & \text{in } \mathbb{R}^+ \times \Omega \\ \nabla \cdot \mathbf{v} = 0 & \text{in } \mathbb{R}^+ \times \Omega \end{cases}$$

along with inflow boundary conditions for ρ on $\{\mathbf{x} \in \Gamma, (\mathbf{v}(t, \mathbf{x}) \cdot \mathbf{n}(\mathbf{x})) < 0\}$ as well as initial conditions. Consequently we have introduced the transport equation of the two-valued density $\rho(t, \mathbf{x}) \geq \underline{\rho} > 0$, which will carry out the transport of the particles rather than the Newton laws. Similarly, we have for the viscosity: $\mu_f \leq \mu(\rho) \leq \mu_s$. The solid viscosity μ_s will be taken as great as possible to

enforce the penalization of the tensor $\mathbf{D}(\mathbf{v})$. We aim that way to tend towards $\|\mathbf{D}(\mathbf{v})\|_{\mathbf{L}^2(\Omega_s(t))} = 0$. With this property we can go back to a rigid motion velocity field in $\Omega_s(t)$ for an accurate representation of the rigid behaviour of the particles.

2 Numerical Method to Solve the Problem

In the present section we describe time and spatial discretization schemes applied to the penalized problems, followed by the strategies regarding the fluid–structure coupling. We resort to the incremental projection scheme [5, 6] adapted to both penalty methods to solve the extended problem in Ω . Using the Hodge–Helmholtz decomposition of a given vector in $\mathbf{L}^2(\Omega)$, we are able to decouple the computation of the velocity and pressure. In a first sub-step we account for the viscous terms to determine a predicted velocity, followed by a second sub-step where we enforce the incompressibility constraint to obtain the pressure and corrected velocity. For the discretization of the derivatives, we use a BDF2 formulation for the time derivative of the velocity and a Richardson extrapolation for the non—linear inertia term. Thereafter we complete the projection scheme with the transport of the solid domain. For the Darcy penalty, we use an implicit scheme of the Newton laws in regards to the particle velocities.

Resorting to an advection scheme of the phase field of the particles for the viscous penalty could render difficult the localisation of the fluid–solid interface. Instead we carry out the transport of markers defined on the surface of the particles using Runge–Kutta schemes [7]. We require at least $N_{df} = 6$ markers for each particle, N_{df} being the degree of freedom for a 3–dimensional rigid solid. Using the no–slip condition, we end up with at most an overdetermined system given by the rigid–body equations valued on each marker.

As we aim to simulate a large collection of particles we need to adopt a fitting strategy to account for the potential collisions between particles or the boundaries of the computational domain. One can resort to repulsive forces using the given position and orientation of the particle. In our case we will couple the fluid–solid scheme above with the method introduced in [8]. In the latter reference we break down a particle in sub–spheres in such a way that we can define the particle as the union of the convex hulls of two neighbouring sub–spheres (Fig. 1). Using an Uzawa algorithm, the predicted velocities of all sub–spheres are projected on a set of admissible velocities.

Regarding the spatial discretizations, finite volumes and a staggered mesh have been chosen. We define the fields for the penalty quantities $(\rho, \mu, \mathbf{1}_{\Omega_s})$ on the velocity grids. To compute those fields on the cells where the fluid–solid interface is located, we adopt an averaging method.

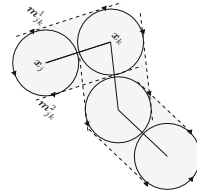


Fig. 1. Defining the markers for a particle in 2D

3 Validation Tests and Comparisons

3.1 Dropping a Ball in a Viscous Fluid

For a first test we drop a rigid heavy sphere in a viscous fluid and observe it attaining its terminal velocity according to the principle that the drag force exerted on the particle by the fluid as well as buoyancy balances the gravity applied to the sphere. We define the fluid using the density $\rho_f = 1$ and viscosity $\mu_f = 0.01$. The sphere with radius $r = 0.05$ and density $\rho_s = 5$ is falling in the rectangular domain $[0, 1] \times [0, 1] \times [0, 3]$ to which we applied channel-flow boundary conditions. The gravity constant applied to the ball is $g = 98.1$. We take for the penalty parameters $\mu_s = 10^4$ and $1/\eta = 10^7$. For the time step we will be using $\delta t = 0.001$. The spatial step h is such that $h = \max_{i=x,y,z} h_i = 1/50$. The initial position for the ball is $(0.5, 0.5, 1)$ (Figs. 2 and 3).

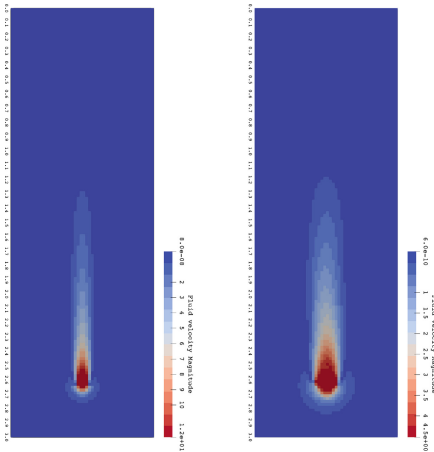


Fig. 2. Fluid velocity magnitude for the L2-penalty (left) and H1-penalty (right) when $Z(t) = 2.617$

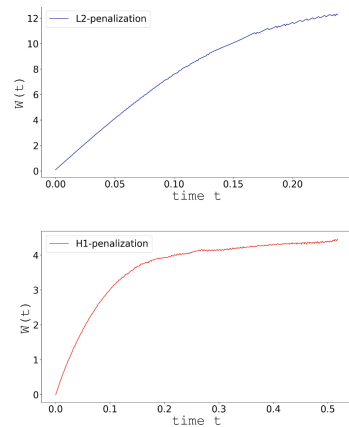


Fig. 3. W -component of the translational velocity reaching a terminal velocity of the for the L2-penalty (above) and H1-penalty (bottom)

In both cases the velocity of the particle keeps a straight trajectory and reaches a terminal velocity, which is a first satisfying result. However the terminal velocities while being within the same order ($4L.T^{-1}$ against $12L.T^{-1}$) still differ. We can also observe a diffusion around the sphere constrained with the H1/viscous penalty. This could be explained by the fact that no specific treatment regarding the interface is used when computing the viscous part of the momentum equation of the penalized problem. Meanwhile the Darcy penalty probably requires corrections regarding the physical parameters and external forces to obtain a coherent coupling between the Newton laws and the fluid problem.

3.2 A Rigid Rod in a Lid-Driven Cavity

To demonstrate the marker strategy with a non-spherical particle, we place a rigid rod in the domain $\Omega = [0, 1]^3$ with the boundary conditions of a lid-driven cavity problem. On the side $\{(x, y, z) \in \Gamma, z = 1\}$ of Ω we set $\mathbf{u}(t, \mathbf{x}) = 1$. The rigid rod is defined with the density $\rho_s = 0.8$, a length $l = 0.1$ and width $w = 0.02$. For the fluid we use $\mu_f = 1.0$. We neglect the gravity and leave the boundary conditions to establish the flow. We use the spatial step $h = 1/70$ and the same time step as the previous test. We take $\mu_s = 10^4$ to penalize the solid (Fig. 4).

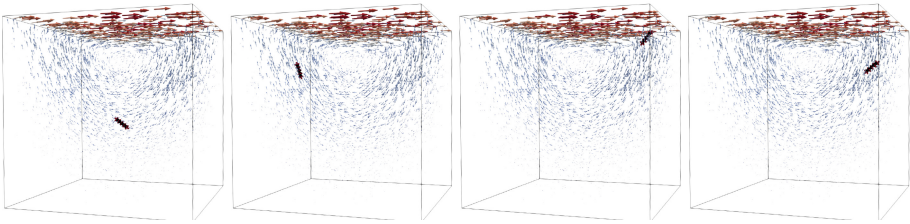


Fig. 4. State of the problem at times $t = 2.25$, $t = 4$, $t = 6.0$, $t = 6.75$

Despite the rather coarse mesh and the thin rod used in this test, the particle properly follows the flow and rotates appropriately, while remaining rigid. The markers seem to handle correctly the decomposition of a complex particle using sub-spheres from the collision strategy.

4 Concluding Remarks

We were able to study and compare the L2-penalty and the H1-penalty methods in the context of particulate flows. As far as we know, comparative studies between those two methods do not exist for such situations. Therefore, this work can be considered as a novel short progress in this direction. The numerical tests were overall satisfying and allowed us to take a step further in validating our code. However more work is required regarding the calibration of the Darcy penalty problem and the sharpness of the interface with the viscous-penalized problem to help with the comparison of the methods and the global observations.

References

1. Glowinski, R., Pan, T.-W., Hesla, T.I., Joseph, D.D.: A distributed Lagrange multiplier/fictitious domain method for particulate flows. *Int. J. Multiph. Flow* **25**, 755–794 (1999)
2. Angot, P., Bruneau, C.-H., Fabrie, P.: A penalization method to take into account obstacles in incompressible viscous flows. *Numer. Math.* **81**, 497–520 (1999)

3. Khadra, K., Angot, P., Parneix, S., Caltagirone, J.-P.: Fictitious domain approach for numerical modelling of Navier-Stokes equations. *Int. J. Numer. Methods Fluids* **34**, 651–684 (2000)
4. Carbou, G., Fabrie, P.: Boundary layer for a penalization method for viscous incompressible flow. *Int. Adv. Differ. Equ.* **8**(12), 1453–1480 (2003)
5. Guermond, J.L., Mineev, P., Shen, J.: An overview of projection methods for incompressible flows. *Comput. Methods Appl. Mech. Eng.* **195**, 6011–6045 (2006)
6. F evri ere, C., Laminie, J., Pouillet, P., Angot, P.: On the penalty-projection method for the Navier-Stokes equations with the MAC mesh. *J. Comput. Appl. Math.* **226**, 228–245 (2009)
7. Angot, P., Caltagirone, J.-P., Fabrie, P.: A kinematic vector penalty-projection method for incompressible flow with variable density. *Comptes Rendus Math ematique* **354**(11), 1124–1131 (2016)
8. Faure, S., Martin, S., Maury, B., Takahashi, T.: Towards the simulation of dense suspensions: a numerical tool. *ESAIM Proc.* **28**, 55–79 (2009)



Simulation of a Confined Turbulent Round Jet at Moderate Reynolds Number

Georges Halim Atallah^{1,2}(✉), Emmanuel Belut¹, Sullivan Lechêne¹,
Benoît Trouette², and Stéphane Vincent²

¹ INRS, French National Research and Safety Institute for the Prevention of Occupational Accidents and Diseases, Lab. Aeraulic Engineering, Vandœuvre, France
georges.halimatallah@inrs.fr

² Laboratoire Modélisation et Simulation Multi Echelle, MSME UMR 8208, CNRS, UPEC, UPEM, Université Paris-Est, 77454 Marne-la-Vallée, France
georges.halimatallah@u-pem.fr

Abstract. The objective of this study is to numerically simulate the turbulent flow of a confined round jet at moderate Reynolds number, which is representative, in a first step, of an available experiment characterizing a problem of pollutant transport in a confined medium.

Keywords: Confined round jet · Moderate Reynolds number · Comparison between DNS and experiments · LES

1 Introduction

In numerous scientific research areas, particularly in chemistry, operators are very often required to handle materials that could be volatile and could probably be inhaled. Depending on the materials being studied, the gases generated can be toxic and therefore present a real danger to the operator's health in case of inhalation. Laboratory fume cupboards are devices that are supposed to ensure the protection of the operator. Their ability to contain pollutant gases is vulnerable to turbulent phenomena and aeraulic perturbations, which are themselves induced by drafts or moving objects. When a laboratory fume cupboard is disturbed, the pollutant gas, instead of being confined inside the device, leaks because of the induced turbulent flow. In order to simulate the pollutant transport process when the device is submitted to disturbances, we first propose to design a small-scale experimental model involving the same physical phenomena. This is an experiment describing the transport of pollutant injected into a confined enclosure through a round turbulent jet that allows to collect experimental data of time average velocity, kinetic energy and mean age air profile [2,4] so that numerical simulations can be validated against experimental measurements and statistics. In the present work, we only focus on flow characteristics and more particularly on the turbulent aspect of the carrier flow motion.

2 Confined Turbulent Round Jet at Moderate Reynolds Number

2.1 Experimental Setup

Air is injected into a rectangular enclosure containing the same fluid at rest through a circular inlet (round jet) at a flow rate of $40 \text{ L} \cdot \text{min}^{-1}$ and exits through an open circular outlet at atmospheric pressure. The diameter of the inlet injector is $D = 0.04 \text{ m}$, so that the Reynolds number based on the injector diameter $\text{Re} = 1500$. The flow rate is sufficiently high so that the flow degenerates into turbulence [1]. Airflow velocity profiles were measured by Laser Doppler Anemometry in the central plane ($y = 0 \text{ m}$) in several cross-sections located at $x = 0.1, 0.3, 0.5$ and 0.7 m in the streamwise x -direction [2].

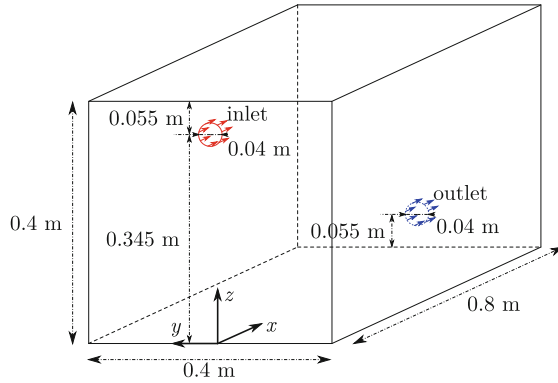


Fig. 1. Geometric description of the confined air injection in a cavity with cylindrical inlet and outlet.

2.2 Model and Numerical Methods

All developments are investigated with the home made code Fugu, developed in the TCM team of MSME lab. We performed numerical simulation of an airflow assumed to be incompressible and isothermal using a finite volume method on an irregular and staggered Cartesian grid governed by the following set of equations:

$$\nabla \cdot \mathbf{u} = 0, \quad (1a)$$

$$\rho \left(\frac{\partial \mathbf{u}}{\partial t} + \nabla \cdot (\mathbf{u} \otimes \mathbf{u}) \right) = -\nabla p + \nabla \cdot [(\mu + \mu_{\text{sgs}}) (\nabla \mathbf{u} + (\nabla \mathbf{u})^T)], \quad (1b)$$

where \mathbf{u} is the velocity vector, p is the pressure, $\rho = 1.2250 \text{ kg} \cdot \text{m}^{-3}$ is the density and $\mu = 1.7894 \cdot 10^{-5} \text{ Pa} \cdot \text{s}$ is the dynamic viscosity of the fluid. When a

turbulence model is considered, a turbulent viscosity μ_{sgs} is incorporated through an eddy viscosity model in the motion equations. In the present work, gravity effects are neglected. Boundary conditions for \mathbf{u} are no-slip condition for all walls and zero gradient at the outlet for the normal component. Imposing a velocity profile such as the one of the experience requires taking into account a number of factors that are difficult to simulate. In practice, the injector nozzle is never really designed with perfect geometry and therefore has imperfections. They can then cause instabilities that directly affect the potential core area (near-field) of the jet. Thus, a simple flat velocity profile such that $u^{\text{inlet}} = \mu\text{Re}/\rho D$ is imposed at the inlet and only intermediate and far fields region of the jet are investigated and compared to experiments in the present work. A centered scheme is used to discretize the advection term and viscous terms whereas time integration is carried out with a second order Gear scheme. Pressure is obtained by using a time-splitting approach for handling pressure-velocity coupling. A scalar projection method is considered here [3]. These schemes are combined with the preconditioned MILU-BICGSTAB II solver to build a solution of Eqs. (1a–1b).

A mesh convergence study was first performed with direct numerical simulation (DNS) to assess if the obtained numerical solutions reproduce the behavior of experimental data. The mesh convergence study was performed with mesh sizes of $\{n_x, n_y, n_z\} = \{128, 64, 64\}$, $\{192, 96, 96\}$ and $\{256, 128, 128\}$. For each case, the mesh is refined with 400, 900 and 1600 cells respectively along the jet inlet cross section. It was observed that a simple regular mesh size generates too much dissipation for the same number of cells, which inhibits the ability to capture a degeneration to turbulence. This is why we chose to use a refined irregular mesh in the jet inlet cross section to capture the effects of turbulence. The time step is defined as $\Delta t = \text{CFL} \times h_{\text{min}}$ with $\text{CFL} = 0.5$ and h_{min} is the length of the smallest cell. The flow was also simulated with Large Eddy Simulation (LES) models on the coarsest mesh size. The idea is to measure the capability of LES to provide a suitable solution on a too coarse mesh for tackling with DNS.

2.3 Large Eddy Simulation (LES) Turbulence Modeling

Our LES simulations were performed with a variety of classical LES models [6]. The first is an eddy viscosity model based on the mixed scale approach, which is a combination of the Smagorinsky and the Turbulent Kinetic Energy (TKE) models. The subgrid-scale viscosity is classically evaluated by the following formula:

$$\nu_{\text{sgs}} = C_m \bar{\Delta}^{1+\alpha} (2\bar{S}_{ij}\bar{S}_{ij})^{\alpha/2} (q_c^2)^{(1-\alpha)/2}, \quad (2)$$

with $C_m = C_s^{2\alpha} C_{\text{TKE}}^{1-\alpha}$, $\bar{\Delta} = (\Delta x \Delta y \Delta z)^{1/3}$, \bar{S}_{ij} is the resolved strain rate tensor, q_c is the subgrid-scale kinetic energy. In our implementation, $\alpha \in [0, 1]$ is a weighting coefficient ($\alpha = 0$ gives the TKE model, $\alpha = 1$ gives the Smagorinsky model). In our approach, α is taken equal to 0.5 for the mixed scale model. C_s and C_{TKE} are the constant of the Smagorinsky and TKE models and are taken

equal to 0.18 and 0.2 respectively. In the motion equations, $\mu_{\text{sgs}} = \rho\nu_{\text{sgs}}$ is then added to the molecular dynamic viscosity as shown in Eq. (1b).

The other one is the Wall Adapting Local Eddy-viscosity (WALE) model [6]. Its known advantage is that it allows to reproduce a good asymptotic behaviour near solid walls for wall bounded flows. The subgrid-scale viscosity is define as:

$$\nu_{\text{sgs}} = (C_w \overline{\Delta})^2 \frac{(\overline{S}_{ij}^d \overline{S}_{ij}^d)^{3/2}}{(\overline{S}_{ij} \overline{S}_{ij})^{5/2} + (\overline{S}_{ij}^d \overline{S}_{ij}^d)^{5/4}}, \quad (3)$$

with $C_w = 0.75$ and $\overline{S}_{ij}^d = \overline{S}_{ik} \overline{S}_{kj} + \overline{\Omega}_{ik} \overline{\Omega}_{kj} - \frac{1}{3} (\overline{S}_{mn} \overline{S}_{mn} - \overline{\Omega}_{mn} \overline{\Omega}_{mn}) \delta_{ij}$. $\overline{\Omega}_{ij}$ is the resolved rotation tensor and δ_{ij} is the Kronecker delta.

3 Results and Discussion

Direct Numerical Simulation. When possible, DNS is the simplest model for turbulence and also the more accurate to investigate on a numerical point of view. Its main drawback is the requirement of solving all the time and space scales of the flow, which is generally impossible as soon as the Reynolds number is high. In our experiment of turbulent round jet, the Reynolds number is moderate, so it is reasonable to try to simulate the problem with DNS. If we succeed, a reference simulation will be available, which could be degenerated in terms of mesh or time step in order to try to simulate faster the same problem with LES models.

After thirty seconds of physical time corresponding to an established jet motion, average fields are then calculated over thirty seconds of physical time, ensuring a converged behavior of these average fields. As shown in Fig. 2, outside the jet area ($z \leq 0.3$ m), we can observe a little influence of the mesh size. In these zones, the flow is mainly laminar and all grids capture the correct motion. Inside the jet ($z > 0.3$ m), numerical solutions on all meshes globally reproduces the average velocity intensities. However, refining the grids allows to converge simulation results to those of the experiments, which is a nice feature of the Fugu code. Note that the fact that the maximum velocities are not at the same height z is explained by the fact that the imposed velocity profile is spatially constant in the injector, which is not the case in the experiment [2].

The DNS gives results in fairly good agreement with those of the experiments, but the computation cost is far too high on the finer mesh, even with the MPI parallel implementation that we considered (512 processors). An important point is to be able to carry out this kind of simulation with mesh sizes of the order of the coarsest grid presented here ($128 \times 64 \times 64$ cells). Therefore, in the next section, LES simulations with models presented in Sect. 2.3 were performed on the coarsest mesh.

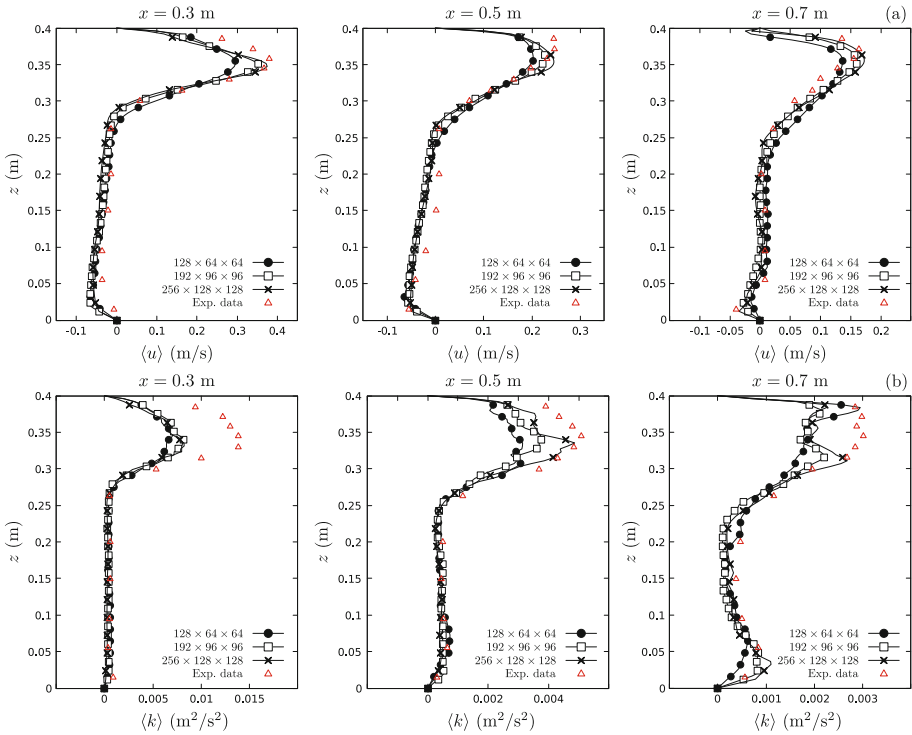


Fig. 2. Measured and computed (a) mean velocity profiles and (b) mean turbulent kinetic energy at the central plane $y = 0$ m and $x = 0.3, 0.5$ and 0.7 m. Comparison between DNS simulations (without explicit LES model) and experiments [2].

Large Eddy Simulation. In order to reach such results as in DNS on fine mesh at a lower cost, simulations were performed on the coarsest mesh using LES models with the same numerical setup as in DNS. A first observation is that the three Smagorinsky, TKE and mixed scale models maintain the jet in a laminar state and inhibit the transition to turbulence. However, the WALE model provides a better behaviour than the others despite the fact that the laminar-turbulent transition occurs farther than it occurs in DNS. This leads to an overestimation of velocity intensities as shown in Fig. 3.

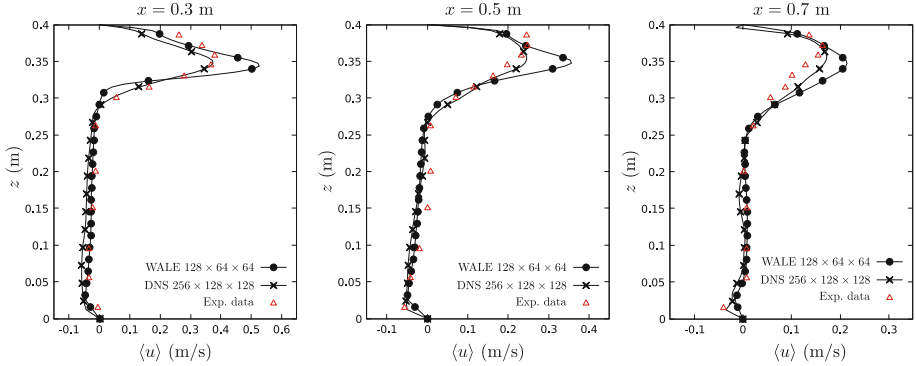


Fig. 3. Comparison between computed mean velocity at the central plane $y = 0$ m and $x = 0.3, 0.5$ and 0.7 m with LES WALE model and DNS on $256 \times 128 \times 128$ mesh size.

4 Concluding Remarks

The dynamics of a cylindrical jet at moderate Reynolds number of 1500 has been simulated with DNS and LES turbulence approaches. The results of the DNS compare favorably to those provided by the experiments. LES conducted on the coarsest DNS grid are not able to recover the correct experimental jet dynamics. The main reason that we have identified, by changing all physical and numerical parameters of the simulations, is that the results are very sensitive to inlet jet profile of mean velocity (for the DNS) and also to the fluctuating (or subgrid component) of the velocity, that is not considered in the present work. Future improvements of our LES simulations will be to impose synthetic turbulent unsteady inlet jet conditions [5] in order to feed simulations with realistic subgrid scale fluctuations of the velocity.

Acknowledgements. The authors are grateful for access to the computational facilities of the French CINES (National computing center for higher education) and CCRT (National computing center of CEA) under project number A0032B06115.

References

1. Abdel-Rahman, A.: A review of effects of initial and boundary conditions on turbulent jets. *WSEAS Trans. Fluid Mech.* **4**(5), 257–275 (2010)
2. Belut, E., Christophe, T.: A new experimental dataset to validate CFD models of airborne nanoparticles agglomeration. In: *Proceedings of the 9th International Conference on Multiphase Flow*, Firenze, Italy (2016)
3. Goda, K.: A multistep technique with implicit difference schemes for calculating two- or three-dimensional cavity flows. *J. Comput. Phys.* **30**(1), 76–95 (1979)
4. Guichard, R., Belut, E.: Simulation of airborne nanoparticles transport, deposition and aggregation: experimental validation of a CFD-QMOM approach. *J. Aerosol Sci.* **104**, 16–31 (2017)

5. Klein, M., Sadiki, A., Janicka, J.: A digital filter based generation of inflow data for spatially developing direct numerical or large eddy simulations. *J. Comput. Phys.* **186**(2), 652–665 (2003)
6. Sagaut, P., Meneveau, C.: *Large Eddy Simulation for Incompressible Flows: An Introduction*. Scientific Computation. Springer, Heidelberg (2006)



Effect of Very-Large-Scale Motions on One- and Two-Point Statistics in Turbulent Pipe Flow Investigated by Direct Numerical Simulations

Christian Bauer^{1,2}(✉) and Claus Wagner^{1,2}

¹ Institute of Aerodynamics and Flow Technology, German Aerospace Center, Göttingen, Germany

christian.bauer@dlr.de

² Institute of Thermodynamics and Fluid Mechanics, Technische Universität Ilmenau, Ilmenau, Germany

Abstract. Very-large-scale motions appear in the bulk region of turbulent pipe flow. They become increasingly energetic with the Reynolds number and interact with the near-wall turbulence. These structures appear either in the shape of positive (high-speed) or negative (low-speed) streamwise velocity fluctuation. The impact of the sign of the structures on the pipe flow turbulence is analysed in this study by means of conditionally averaged one- and two-point statistics, using data from direct numerical simulations of turbulent pipe flow in a flow domain of length $L = 42R$ and friction Reynolds numbers of $180 \leq Re_\tau \leq 1500$. Conditionally averaged two-point velocity correlations reveal that low-speed motions are longer and more energetic than their high-speed counterparts. The latter are predominately responsible for the Reynolds number dependency of turbulence statistics in the vicinity of the wall, which is in good agreement with observations of the so-called amplitude modulation in wall-bounded turbulence.

Keywords: Turbulent pipe flow · DNS · VLSM

1 Introduction

Very long coherent regions of energetic streamwise velocity fluctuations, also referred to as very-large-scale motions (VLSM), play an important role in high Reynolds number wall-bounded turbulence, since they carry a substantial fraction of turbulent energy [2, 6]. Although the maximum energy content of VLSM is located in the outer flow region, they penetrate deep into the buffer layer. The interaction of the large- and very-large-scale outer flow motions with the near-wall coherent structures and their impact on high-order turbulence statistics has recently been discussed by Bauer et al. [1]. Due to this interaction, logarithmic Reynolds number dependencies of different statistical moments of the

velocity distribution were found and reported. In the current study, the different contributions of high- and low-speed VLSM to one- and two-point statistics are investigated in more detail. Therefore, conditionally averaged statistics are computed from the DNS data used in Bauer et al. [1] and subsequently analyzed.

2 Numerical Methodology

The incompressible Navier-Stokes equations in their dimensionless form

$$\frac{\partial \mathbf{u}}{\partial t} + \mathbf{u} \cdot \nabla \mathbf{u} + \nabla p = \frac{1}{Re_\tau} \nabla^2 \mathbf{u}, \quad (1)$$

$$\nabla \cdot \mathbf{u} = 0, \quad (2)$$

are integrated in time using a leapfrog-Euler scheme, after being discretised by means of a fourth-order finite volume method. The governing equations as well as all quantities presented below are normalised in viscous units, i.e. the friction Reynolds number $Re_\tau = u_\tau R / \nu$, based on friction velocity, pipe radius and kinematic viscosity, and the viscous length $\delta_\nu = \nu / u_\tau$. The flow geometry is a smooth annular pipe with length L and radius R . Table 1 lists the different considered cases for which DNS were performed in Bauer et al. [1].

Table 1. Turbulent pipe flow simulation cases. N_z , N_φ and N_r are the number of grid points with respect to the axial, azimuthal and radial direction, respectively. Δz^+ , streamwise grid spacing; $R^+ \Delta \varphi$, azimuthal grid spacing at the wall; Δr_{min}^+ and Δr_{max}^+ , minimal and maximal radial grid spacing, respectively. All grid spacings normalised by wall units.

Case	Re_τ	L/R	N_z	N_φ	N_r	Δz^+	$R^+ \Delta \varphi$	Δr_{min}^+	Δr_{max}^+
<i>P180</i>	180	42	1536	256	84	4.9	4.4	0.31	4.4
<i>P360</i>	360	42	3072	512	128	4.9	4.4	0.39	4.4
<i>P720</i>	720	42	4608	1024	222	6.6	4.4	0.49	6.6
<i>P1500</i>	1500	42	8192	2048	408	7.7	4.6	0.49	7.8

Statistical quantities are computed as follows

$$\langle u \rangle(r) = \frac{1}{L} \frac{1}{2\pi r} \frac{1}{\Delta t} \int_{t=t_0}^{t_0+\Delta t} \int_{z=0}^L \int_{\varphi=0}^{2\pi} u(z, \varphi, r, t) r d\varphi dz dt, \quad (3)$$

where angle brackets indicate averaging in both homogeneous directions and time with Δt being the averaging interval in time.

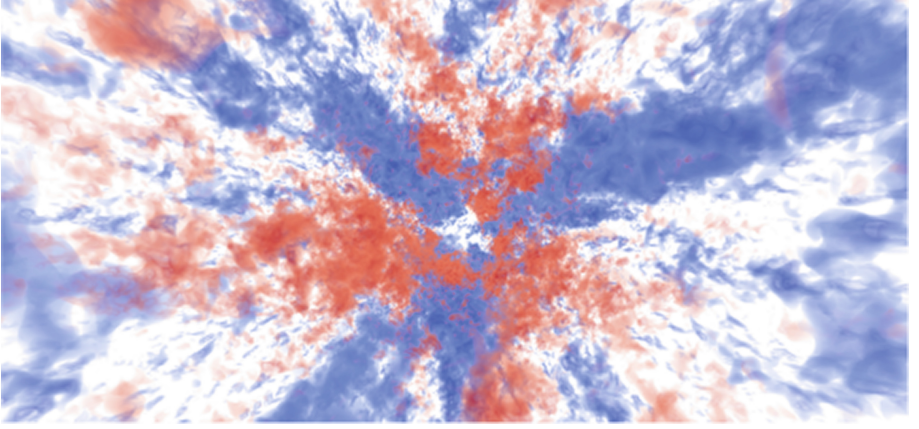


Fig. 1. Iso-volumes of the streamwise velocity fluctuation $u_z'^+$ inside the pipe. Red (blue) structures exhibit values ranging from $+(-)3$ to $+(-)5$.

3 Results

Instantaneously, VLSM can be visualised by means of iso-volumes of the streamwise velocity fluctuation u_z' shown in Fig. 1. The statistical counterpart of these turbulent coherent structures are iso-contours of the streamwise two-point velocity correlation

$$R_{zz}(\Delta z, \Delta \varphi, r_0 + \Delta r) = \frac{\langle u_z'(0, 0, r_0) u_z'(\Delta z, \Delta \varphi, r_0 + \Delta r) \rangle}{\langle u_z'(0, 0, r_0) u_z'(0, 0, r_0) \rangle}, \quad (4)$$

where Δz , $\Delta \varphi$ and Δr are the axial, azimuthal and radial separation lengths, respectively, and r_0 is the reference point. Iso-contours of the streamwise three-dimensional two-point velocity correlation with $R_{zz} = +(-)0.1$ are depicted in Fig. 2 for the different considered Reynolds numbers. The reference point of the velocity correlations is located at $r_0 = 0.6R$. For the lowest Reynolds number, $Re_\tau = 180$ (Fig. 2 (a)), the footprint of near-wall velocity streaks—located at a wall distance of $y^+ \approx 15$ —is visible in the form of near-wall tails of the iso-contours. With increasing Reynolds number these structures become less pronounced, since they scale in viscous units. VLSM, on the contrary, appear at Reynolds numbers around $Re_\tau \approx 720$ and become increasingly energetic and clearly visible through the iso-contours shown in Fig. 2 (d). VLSM appear as either high- or low-speed motions [3]. The latter are of larger streamwise extent than the former, as the iso-contours of the conditionally averaged streamwise velocity correlations depicted in Fig. 3 show. The logarithmic Reynolds number dependency of statistical moments of the velocity distribution up to the fourth is related to the interaction of the large- and very-large outer scale motions with the near-wall turbulence [1]. In order to determine the effect of high- and low-speed motions separately, the variance and skewness of the streamwise velocity distribution are computed conditionally for regions of positive and negative

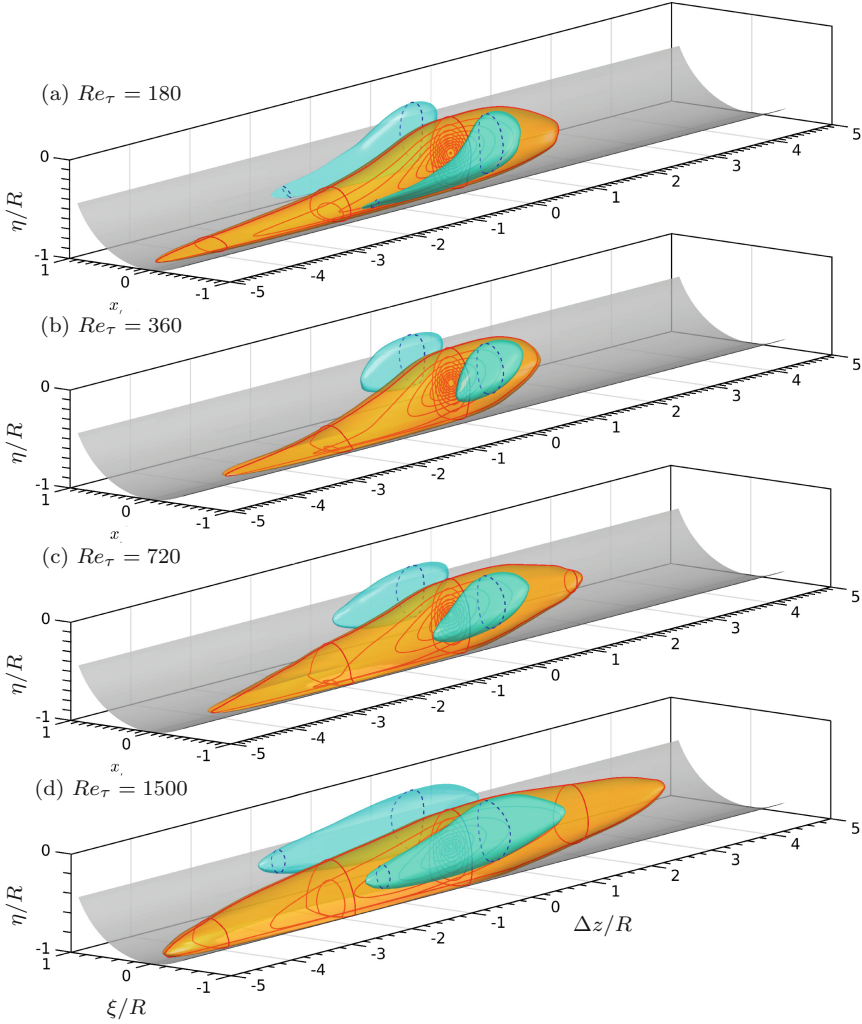


Fig. 2. Iso-surfaces and contours of the three-dimensional two-point velocity correlation of the streamwise velocity component $R_{zz}(\Delta z, \varphi, r_0 + \Delta r)$ as a function of the axial, azimuthal and radial separation lengths. Reference point of the correlation at $r_0 = 0.6R$. Cartesian cross-sectional coordinates $\xi = (r_0 + \Delta r)\sin(\Delta\varphi)$, $\eta = (r_0 + \Delta r)\cos(\Delta\varphi)$. (a) $Re_\tau = 180$, (b) $Re_\tau = 360$, (c) $Re_\tau = 720$, (d) $Re_\tau = 1500$. The orange (cyan) iso-surfaces exhibit values of $+(-)0.1$. Iso-contours values range from $+(-)0.1$ to $+(-)1$, increment of 0.1 .

velocity fluctuations. The results are shown in Fig. 4 for both variance (a) and skewness (b) for regions of positive (solid lines) and negative (dashed lines) streamwise velocity fluctuations. For both quantities the profiles for high-speed

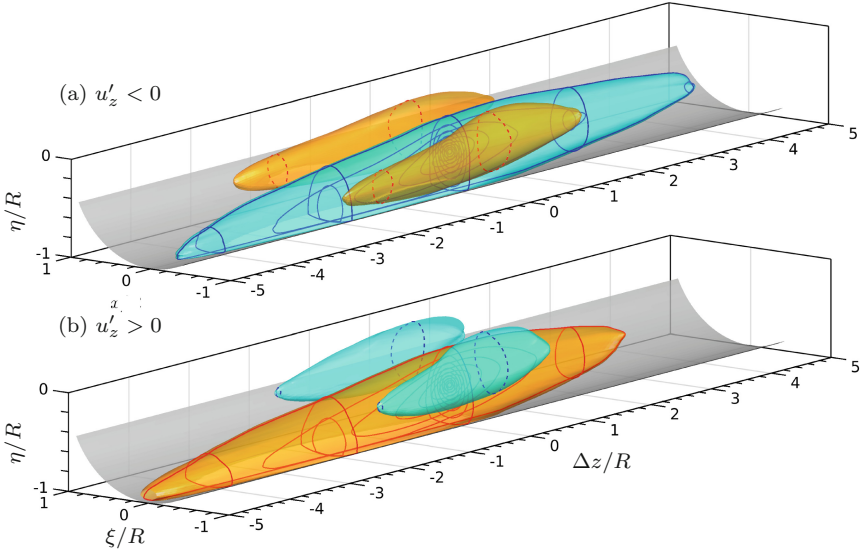


Fig. 3. Iso-surfaces and contours of the conditionally averaged three-dimensional two-point velocity correlation of the streamwise velocity component $R_{zz}(\Delta z, \varphi, r_0 + \Delta r)$ depicted as in Fig. 2. (a) Condition $u'_z < 0$, cyan (orange) iso-surfaces exhibit values of $+(-)0.1$. (b) Condition $u'_z > 0$, orange (cyan) iso-surfaces exhibit values of $+(-)0.1$. $Re_\tau = 1500$.

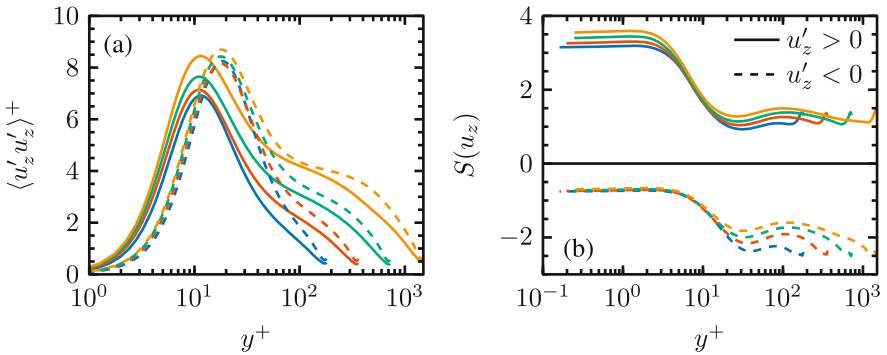


Fig. 4. Variance $\langle u'_z u'_z \rangle^+$ (a) and Skewness $S(u_z)$ (b) of the streamwise velocity distribution. Conditionally averaged for regions of positive (solid lines) and negative (dashed lines) streamwise velocity fluctuations. —, $Re_\tau = 180$; —, $Re_\tau = 360$; —, $Re_\tau = 720$; —, $Re_\tau = 1500$.

regions reflect a significantly stronger dependency on the Reynolds number in the vicinity of the wall as the ones for low-speed regions. This means that the modulation of the small scales in the vicinity of the wall is primarily caused by

high-speed outer flow motions, which is in good agreement with observations of the amplitude modulation in turbulent boundary layer flows [4, 5].

4 Conclusion

Observations from DNS data of turbulent pipe flow show that high- and low-speed VLSM appearing in the outer layer of the flow, interact differently with the near-wall turbulence. High-speed motions modulate the small-scale motions in the vicinity of the wall considerably more than their low-speed counterparts, which can be seen in the analysis of conditionally averaged turbulence statistics. This is consistent with the general observations of sweeps and ejections in wall-bounded turbulence. High-speed fluid is predominately moving towards the wall (sweep), whereas low-speed fluid is ejected away from the wall. Since the small scales near the wall are modulated by the large scales in the outer flow, it is plausible that this modulation is related to high-speed motions and, thus, to the sweeps.


Acknowledgements. Computing resources on SuperMUC provided by Leibniz Supercomputing Centre (LRZ) under grant *pr62zu* and proof-reading by Annika Köhne are gratefully acknowledged.

References

1. Bauer, C., Feldmann, D., Wagner, C.: On the convergence and scaling of high-order statistical moments in turbulent pipe flow using direct numerical simulations. *Phys. Fluids* **29**, 125105 (2017)
2. Kim, K.C., Adrian, R.J.: Very large-scale motion in the outer layer. *Phys. Fluids* **11**(2), 417–422 (1999)
3. Lee, J., Ahn, J., Sung, H.J.: Comparison of large- and very-large-scale motions in turbulent pipe and channel flows. *Phys. Fluids* **27**, 025101 (2015)
4. Mathis, R., Hutchings, N., Marusic, I.: Large-scale amplitude modulation of the small-scale structures in turbulent boundary layers. *J. Fluid Mech.* **628**, 311–317 (2009)
5. Mathis, R., Marusic, I., Hutchings, N., Sreenivasan, K.R.: The relationship between the velocity skewness and the amplitude modulation of the small scale by the large scale in turbulent boundary layers. *Phys. Fluids* **23**, 121702 (2011)
6. Smits, A.J., McKeon, B.J., Marusic, I.: High-Reynolds number wall turbulence. *Annu. Rev. Fluid Mech.* **43**(1), 353–375 (2011)



Large Eddy Simulation of Turbulent Heat Transfer in Pipe Flows of Temperature Dependent Power-Law Fluids

Paulin Sourou Ganmbode¹, Meryem Ould-Rouiss¹(✉), Xavier Nicolas¹, and Paolo Orlandi²

¹ Université Paris Est Marne-la-Vallée, MSME UMR 8208 CNRS,
5 Bd Descartes, 77454 Marne-la-Vallée Cedex 2, France
{Meryem.ould-rouiss,Xavier.Nicolas}@u-pem.fr

² Dipartimento di Ingegneria Meccanica e Aerospaziale, Università La Sapienza,
Roma, Italy

Abstract. Heat transfer in turbulent forced convection of power-law fluids, in a heated horizontal pipe at isoflux conditions, is analyzed by large eddy simulations (LES), with an extended Smagorinsky model. A temperature dependent fluid is studied at various Pearson numbers ($0 \leq Pn \leq 5$), for two power law indices ($n = 0.75$ and 1), at Reynolds and Prandtl numbers $Re_s = 4000$ and $Pr_s = 1$. The LES predictions are validated through comparisons with the literature at $Pn = 0$. They allow a better understanding of the physical mechanisms involved in the non-Newtonian temperature dependent fluid flows: with increasing Pn , the relative viscosity is reduced close to the wall and enhanced towards the pipe center, reducing the turbulent fluctuations and heat transfer in the bulk and, as a consequence, the friction factor and Nusselt number.

Keywords: LES · Non-Newtonian · Temperature dependent power-law fluids · Turbulence · Pipe flow · Heat transfer

1 Introduction

Turbulent flows of non-Newtonian fluids are encountered in a wide range of engineering applications such as flows through ducts, pumps, turbines and heat exchangers, in the petroleum, chemical and food industries. When the Reynolds number is sufficiently large, large eddy simulation provides an effective tool to predict the effect of the flow parameters on the turbulent fields. Otha and Miyashita [1] developed a turbulence model that can reproduce DNS results in non-Newtonian fluid flows. They performed LES with a Smagorinsky model, extended according to their DNS results. They showed that this model can more accurately predict the velocity of turbulent flows, for fluids described by Casson's and power-law models, than the standard Smagorinsky model. Gnamboe et al. [2] used this extended Smagorinsky model to predict the turbulent pipe flow

of power law fluids, for various flow indices ($0.5 \leq n \leq 1.4$), Reynolds numbers ($4000 \leq Re_s \leq 12000$) and Prandtl numbers ($1 \leq Pr_s \leq 100$).

LES studies of heat transfer in a turbulent pipe flow of a non-Newtonian fluid are scarce. Some theoretical and experimental [4, 5] works focused on the turbulent heat transfer in pipe flows of non-Newtonian fluids for a constant viscosity case. Studies accounting for the temperature dependent viscosity observed in applications are even more scarce.

The objective of this work is to numerically investigate by LES, with an extended Smagorinsky model, turbulent heat transfer in the fully developed pipe flow of a temperature dependent power law fluid at $n = 0.75$ and 1 , $Re_s = 4000$, and $Pr_s = 1$, for $0 \leq Pn \leq 5$, where the Pearson number, Pn , is the dimensionless number measuring the temperature effect on the consistency of a non-Newtonian fluid. The aim is to gain more insights into such complex fluid flows whose viscosity is a function of both the temperature and the shear rate.

2 Governing Equations and Numerical Procedure

The present study deals with the fully developed turbulent flow and heat transfer of power law fluids in pipes whose wall is heated at a constant heat flux ϕ_w . The filtered non-Newtonian equations are made dimensionless using the centerline axial velocity of the analytical fully developed laminar profile, $U_{cl} = (3n + 1)U_b/(n + 1)$, the pipe radius, R , and the reference temperature, $T_{ref} = \phi_w R/\lambda$, for the velocity, length and temperature scales respectively, where U_b is the bulk velocity and λ the fluid thermal conductivity. The filtered equations (with the continuity eq. $\partial \bar{u}_i/\partial x_i = 0$) read:

$$\frac{\partial \bar{u}_j}{\partial t} + \frac{\partial \bar{u}_i \bar{u}_j}{\partial x_i} = \frac{\partial \bar{P}}{\partial x_j} + \frac{1}{Re_s} \frac{\partial}{\partial x_i} \left[\gamma^{n-1} e^{Pn \Theta} \left(\frac{\partial \bar{u}_i}{\partial x_j} + \frac{\partial \bar{u}_j}{\partial x_i} \right) \right] + \frac{\partial \bar{\tau}_{ij}}{\partial x_i} \quad (1)$$

$$\frac{\partial \bar{\Theta}}{\partial t} + \frac{\partial}{\partial x_j} \left(\bar{u}_j \bar{\Theta} - \bar{\tau}_{\theta j} \right) - \bar{u}_z \frac{d}{dz} \langle T_w \rangle = \frac{1}{Re_s Pr_s} \frac{\partial^2 \bar{\Theta}}{\partial x_k \partial x_k} \quad (2)$$

where $\Theta = (\langle T_w \rangle (z) - T(r, \theta, z, t))/T_{ref}$ is the dimensionless temperature, T_w is the wall temperature and $\langle \rangle$ is an average in time and in the periodic directions. The subgrid heat flux tensor is defined by $\tau_{\theta j} = -\alpha_t (\partial \Theta / \partial x_j)$, with $\alpha_t = \nu_t / Pr_t$ the turbulent thermal diffusivity linked to the turbulent viscosity, ν_t , by the turbulent Prandtl number, Pr_t , which is constant for a given flow index n . Preliminary LES carried out with the dynamical Smagorinsky model [2] resulted in the following estimates: for $n = 1$, $Pr_t = 0.7$ and for $n = 0.75$, $Pr_t = 1.5$. The Reynolds and Prandtl numbers of the simulations are defined as $Re_s = \rho U_{cl}^{2-n} R^n / K_0$ and $Pr_s = K_0 / \rho \alpha R^{n-1} U_{cl}^{n-1}$. The apparent viscosity η of the fluid is modeled by a power-law: $\eta = K \gamma^{n-1}$, where $K = K_0 \exp[Pn(\Theta - \Theta_b)]$, with K_0 the consistency at the bulk temperature T_b , $Pn = b T_{ref}$ the Pearson number and b the parameter of the thermo-dependence. $\gamma = (S_{ij} S_{ij})^{1/2}$ is the shear rate, with the strain rate tensor $S_{ij} = (u_{i,j} + u_{j,i})/2$. The subgrid stress tensor is equal to $\bar{\tau}_{ij} = -2\nu_t \bar{S}_{ij}$. In the non-Newtonian Smagorinsky model [1], $\nu_t = C_s f_s (f_\eta \Delta)^2 \bar{S}_{ij}$,

where f_s is the van Driest wall damping function and $f_\eta = \eta/\eta_w$ the correction function for the change in viscosity.

An in-house finite difference code is used to solve the above LES model in a 3D cylindrical domain of axial length $L_z = 20R$ so that the largest thermal structures are well captured. Periodic boundary conditions (BC) and a uniform grid are used in θ and z directions. No slip BC and a non-uniform grid refined close to the wall are used in the radial direction. The mesh size is $N_\theta \times N_r \times N_z = 65^3$. More details on the non-Newtonian Smagorinsky model, numerical methods, simulation parameters and validations are given in [2].

3 Results and Discussion

3.1 Mean Velocity and RMS Profiles

The mean streamwise velocity profiles, $U^+ = U/U_\tau$, scaled by the friction velocity $U_\tau = (\overline{\tau_w}/\rho)^{1/2}$, are depicted in Fig. 1 left, for $Re_s = 4000$, $Pn = 0$ and $Pr_s = 1$, as a function of the wall distance $y^+ = \rho U_\tau (r - R)/\eta_w$ with $\eta_w = (K\gamma^{n-1})_w$ the viscosity at the wall. These profiles are in satisfactory agreement with the DNS results by Rudman et al. [3] for $n = 0.75$, and with the well-known universal law for $n = 1$. The profiles of the root mean square (RMS) of the velocity fluctuations also agree well with the DNS data [3], Fig. 1 right. Since, for the shear thinning fluid ($n = 0.75$), the apparent viscosity is smaller close to the wall and larger in the bulk than with a Newtonian fluid ($n = 1$), the mean velocity is expected to be larger and the RMS to be smaller in the flow core (for $y^+ > 20$) for $n = 0.75$.

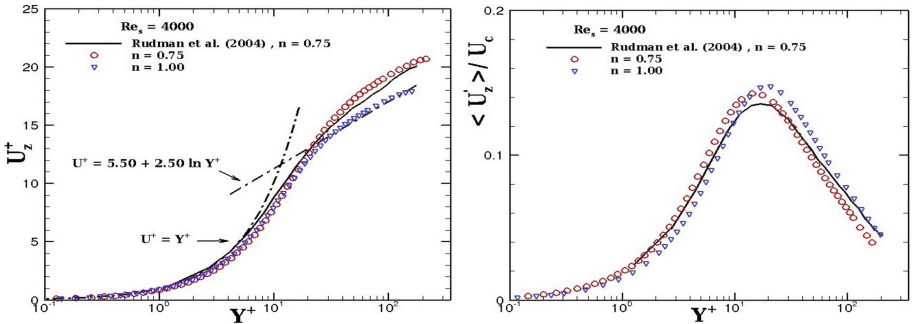


Fig. 1. Effect of n on the axial velocity (left) and on the RMS of U'_z (right) at $Pn = 0$.

For the Newtonian fluid ($n = 1$), the viscosity is constant when $Pn = 0$ because $\eta = K_0$. In accordance with the experiments [4,5], for a $n < 1$, the viscosity $\eta = K\gamma^{n-1}$ increases towards the duct center with increasing Pn (see Fig. 2 left, for $n = 0.75$). This is due to the decreasing shear rate γ and the increasing consistency $K = K_0 \exp[Pn(\Theta - \Theta_b)]$ towards the center. Indeed, $Pn > 0$ and, when the duct wall is heated, $\Theta - \Theta_b = T_b - T$ is negative close to

the wall but positive in the core region. The fluid becomes more rigid towards the pipe center and leads to a monotonous decrease of all the velocity fluctuations (normal and parallel to the wall) when Pn increases (see Fig. 2 right for U'_z). Note that all the fluctuations are damped towards the pipe center for $Pn \geq 3$.

On the other hand, a non-monotonous evolution of the mean axial velocity with increasing Pn is observed in the log-region at $n = 0.75$ (Fig. 3 left) and $n = 1$ (not shown). This behavior is correlated with the non-monotonous evolution of the mean wall shear stress $\overline{\tau}_w = K\overline{\gamma}_w$ or friction factor $f = 2\overline{\tau}_w/\rho\overline{U}^2$ (Fig. 3 right): f decreases and the flow accelerates when Pn increases from 0 to 2 and f increases and the flow decelerates when Pn increases from 2 to 5. This is due to the competition, in the wall boundary layer, between the decreasing consistency due to heating and the increasing shear rate when Pn increases.

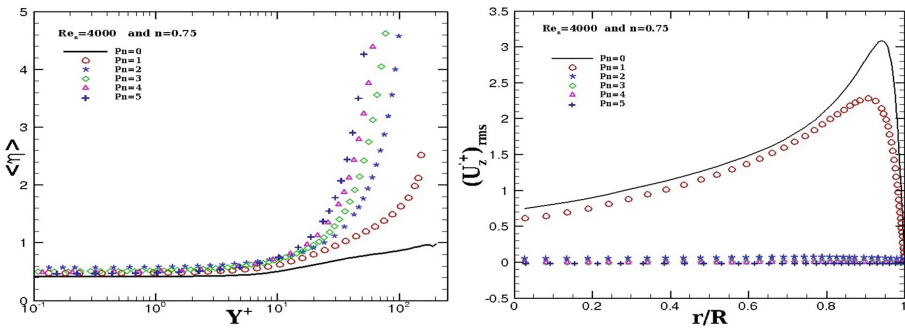


Fig. 2. Effect of Pn on the mean viscosity (left) and on the RMS of U_z (right).

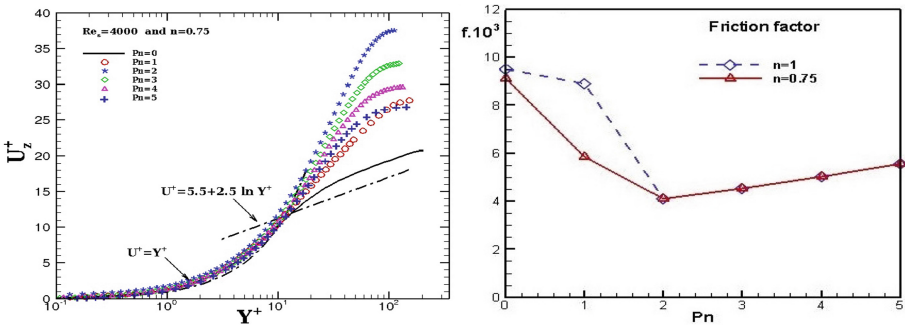


Fig. 3. Effect of Pn on the axial velocity (left) and on the friction factor (right).

3.2 Temperature, RMS and Turbulent Heat Fluxes

As already seen above, due to the strong increase of the apparent viscosity in the bulk flow when Pn increases, the velocity and temperature fluctuations decrease from $Pn = 0$ to 2 and almost vanish beyond (Fig. 4 left). As a consequence, with increasing Pn , the turbulent wall-normal heat flux undergoes a noticeable reduction (Fig. 4 right): it is strong at $Pn = 0$, twice smaller at $Pn = 1$ and nearly zero beyond due to the simultaneous decrease of the fluctuating radial velocity and temperature. The same behavior is observed for the axial turbulent heat flux $\langle U'_z \Theta' \rangle$ (not shown here).

To help interpreting Fig. 5 left, remind that $\Theta - \Theta_b = T_b - T$ is negative close to the wall and positive in the core region. Therefore the Θ -increase corresponds to a reduction of T . Thus Fig. 5 left shows that the fluid is the hottest and the most T -homogenous at $Pn = 0$, thanks to the strong turbulent radial heat flux which controls heat transfer (Fig. 4 right). When Pn increases from 0 to 2, T significantly decreases towards the pipe center due to the decrease of the turbulent radial heat flux and the smaller residence time of the fluid particles in the channel because of the fluid acceleration (Fig. 3 left). As a consequence the average Nusselt number, $Nu = hD/k$, strongly decreases from $Pn = 0$ to 2 (Fig. 5 right). When Pn increases from 2 to 5, the flow decelerates and heat transfer is controlled by the mean axial convection because the turbulent radial heat flux nearly vanishes: the residence time increases and the fluid is more heated by radial molecular diffusion (Fig. 5 left); thus, Nu is small and nearly constant (Fig. 5 right). The similar behavior of f and Nu in Figs. 3 and 5 (right) also indicate a clear analogy between the momentum and heat transfer for each fluid.

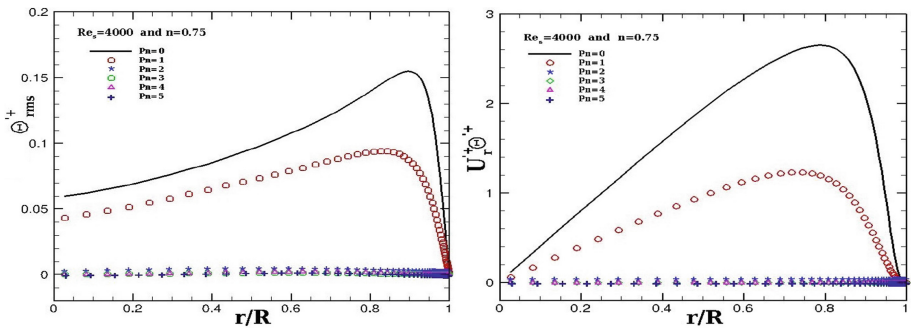


Fig. 4. Effect of Pn on the RMS of Θ' (left) and on the radial heat flux (right).

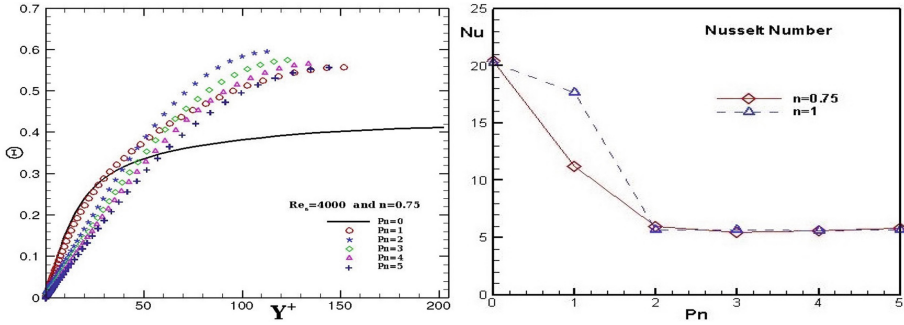


Fig. 5. Effect of Pn on the temperature (left) and on the Nusselt number (right).

3.3 Visualizations

To show the effects of Pn and n on the flow, the resolved axial velocity fluctuations are presented in Fig. 6, in the full cylindrical plane (θ, z) at $y^+ \simeq 15$. For the Newtonian fluid ($n = 1$), with increasing Pn , the turbulent structures are less random and the streaks are larger indicating a less developed turbulence. For the shear-thinning fluid ($n = 0.75$), the number of streaks is reduced compared with $n = 1$ and much longer streaks appear, particularly at $Pn = 1$. This suggests a reduction of the turbulence and, as a consequence, of the heat transfer, more pronounced at $n = 0.75$ than at $n = 1$ due the augmentation of the viscosity towards the pipe center. Clearly these visualizations and the f and Nu behaviors in Figs. 3 and 5 indicate a structural change in the flow for $Pn \geq 1$.

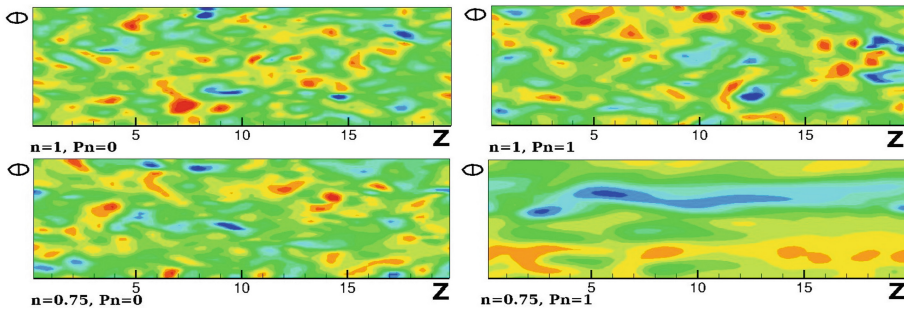


Fig. 6. 2D field of the resolved axial velocity fluctuations in the plane (θ, z) at $y^+ \simeq 15$.

4 Conclusions

This study is the first contribution that uses LES, with an extended Smagorinsky model, to simulate turbulent flows and heat transfer of temperature dependent power-law fluids in pipes, under isoflux conditions. These LES enable to analyze

these complex fluid flows with shear rate and temperature dependent viscosity. The Pearson number effect on the flow and thermal fields is in depth studied. For the non-temperature dependent viscosity case ($Pn = 0$), the axial velocity profiles for the shear-thinning and Newtonian fluids, as well as the friction factors and Nusselt numbers, are in reasonably good agreement with the findings of the literature. With increasing Pn (temperature dependent viscosity case), the mean viscosity is enhanced towards the pipe center. As a consequence, the RMS of the temperature Θ^+ , similarly to the RMS of U_z , is reduced when approaching the pipe center, and the Nusselt number undergoes a significant reduction when Pn increases. From $Pn = 0$ to 2, this leads to a decrease of the turbulent radial heat flux, acceleration of the flow and temperature reduction in the log-region.

References

1. Ohta, T., Miyashita, M.: DNS and LES with extended Smagorinsky model for wall turbulence in non-Newtonian fluids. *J. Non-Newton. Fluid Mech.* **206**, 29–39 (2014)
2. Gnambode, P.S., Orlandi, P., Ould-Rouiss, M., Nicolas, X.: Large-eddy simulation of turbulent pipe flow of power-law fluids. *Int. J. Heat Fluid Flow* **54**, 196–210 (2015)
3. Rudman, M., Blackburn, H.M., Graham, L.J.W., Pullum, L.: Turbulent pipe flow of shear-thinning fluids. *J. Non-Newton. Fluid Mech.* **118**, 33–48 (2004)
4. Peixinho, J.: Contribution expérimentale à l'étude de la convection thermique laminaire, transitoire et turbulente pour un fluide à seuil en écoulement dans une conduite, PhD thesis, Univ. Nancy 1, France (2004)
5. Nguyen, V.T., Lebouché, M.: Etude numérique de l'écoulement d'un fluide non-newtonien thermodépendant entre plaques parallèles. *C.R.A.S. Méc.* **333**, 365–369 (2005)



The Flow Around a Surface Combatant at 10° Static Drift: Assessment of Turbulence Models

Emmanuel Guilmineau^(✉), Michel Visonneau, and Ginevra Rubino

Centrale Nantes, LHEEA, CNRS UMR 6598, 1 rue de la Noë, BP 92101,
44321 Nantes Cedex 3, France

Emmanuel.Guilmineau@ec-nantes.fr

Abstract. This paper presents a computational study of the flow around the DTMB 5415 at 10° static drift. Two RANS (Reynolds Averaged Navier-Stokes) turbulence models, as the isotropic $k-\omega$ SST and the non linear anisotropic EARSM (Explicit Algebraic Reynolds Stress Model) and one hybrid RANS-LES model, the DES (Detached Eddy Simulation) based on the $k-\omega$, are used with the flow solver ISIS-CFD. All numerical results are compared to experimental data. The numerical results show that the DES model is the one turbulence model that able to predict correctly the behavior of the flow in the core of the SDTV (Sonar Dome Tip Vortex), and particularly the high level of the turbulence kinetic energy.

Keywords: Turbulence models · DTMB 5415 · Static drift

1 Introduction

For ship design, environmental aspects and signature characteristics, it is important to understand the three-dimensional flow around a ship and in the wake of the hull under straight ahead or static drift conditions. For this geometry and these conditions, the flow is dominated by the onset of longitudinal vortices progressing in the close vicinity of the hull. With a Reynolds Averaged Navier-Stokes (RANS) approaches, using an Explicit Algebraic Reynolds Stress Model (EARSM) or Reynolds Stress Transport Model (RSTM), the averaged iso-wakes or longitudinal vorticity were in agreement with the measurements [1, 6]. However, for two hulls, the Japanese Bulk Carrier (JBC) and the David Taylor Model Basin (DTMB) 5415, the level of the turbulent kinetic energy (TKE) predicted with a RANS turbulence model is underestimated compared to the experimental data. For the JBC, a Large Eddy Simulation predict a high level of TKE [8].

The geometry used in this study is the DTMB 5415, see Fig. 1, which has a length between the perpendiculars $L_{PP} = 3.048$ m. The draught of the ship is $T = 0.248$ m and the hull is fixed. The model is a bare hull except the bilge keels. The Reynolds number, based on the length L_{PP} and the towing velocity $U = 1.531$ m/s, is $Re = 4.65 \times 10^6$ and the Froude number is $Fr = 0.28$.



Fig. 1. Geometry of DTMB 5415.

In this study, the ship has a drift angle $\beta = 10^\circ$ and all flow measurements have been performed by IIHR [10] which provides tomographic PIV information at several stations. Due to the static drift, the flow is asymmetric about the hull centerline as the hull is oriented obliquely to the incoming flow. The main vortices are the sonar dome tip vortex (SDTV), the bilge keel tip vortex (BKTV) and the aft-body keel vortex (ABKV). In the following of the paper, the comparisons will examine SDTV.

2 ISIS-CFD at Glance

ISIS-CFD, developed by the Ecole Centrale de Nantes and CNRS and available as a part of the FINE/Marine computing suite, is an incompressible Unsteady Reynolds-Averaged Navier-Stokes (URANS) method. The solver is based on the finite volume method to build the spatial discretization of the transport equations. The unstructured discretization is face-based, which means that cells with an arbitrary number of arbitrarily shaped faces are accepted. A second order backward difference scheme is used to discretize time. The solver can simulate both steady and unsteady flows. The velocity field is obtained from the momentum conservation equations and the pressure field is extracted from the mass equation constraint, or continuity equation, transformed into a pressure equation. In the case of turbulent flows, transport equations for the variables in the turbulence model are added to the discretization.

The solver features sophisticated turbulence models: apart from the classical two-equation $k-\varepsilon$ and $k-\omega$ models, the anisotropic two-equation Explicit Algebraic Reynolds Stress Model (EARSM), as well as Reynolds Stress Transport Models, are available [2,3]. All these are RANS models. One hybrid RANS-LES method used is the Detached Eddy Simulation (DES), based on the $k-\omega$ model [7]. Recently, some modifications of this formulation proposed by Griskevich et al. [4] includes recalibrated empirical constants in the shielding function and a simplification of the original Spalart-Allmaras-based formulation. This new model is called Improved Delayed Detached Eddy Simulation (IDDES). These hybrid RANS-LES models have been validated on automotive flows characterized by large separations [5].

Free surface flow is simulated with a multi-phase flow approach: the water surface is captured with a conservation equation for the volume fraction of water, discretized with specific compressive interface-capturing scheme [9].

3 Results

The mesh is generated by HexpressTM, an automatic unstructured mesh generator. A first refinement box including the hull with a cell size of 10 mm in each direction is used. Two other boxes, one including the sonar dome until $X/L_{PP} = 1.0$ and the other including the windward bilge keel until $X/L_{PP} = 1.0$, are used. For these two boxes, the cell size is $\Delta x = 1.5$ mm and $\Delta y = \Delta z = 0.7$ mm. Finally, a last box covering the sonar dome until $X/L_{PP} = 0.6$ is used with the cell size $\Delta x = 0.75$ mm and $\Delta y = \Delta z = 0.35$ mm. The final mesh contains 162.6 million cells.

Figure 2 presents a comparison of the axial velocity in a plane located at $X/L_{PP} = 0.4$. In this slice, only the SDTV vortex is visible. The comparison of the vortex size with the different turbulence models is similar and in agreement with the experimental data.

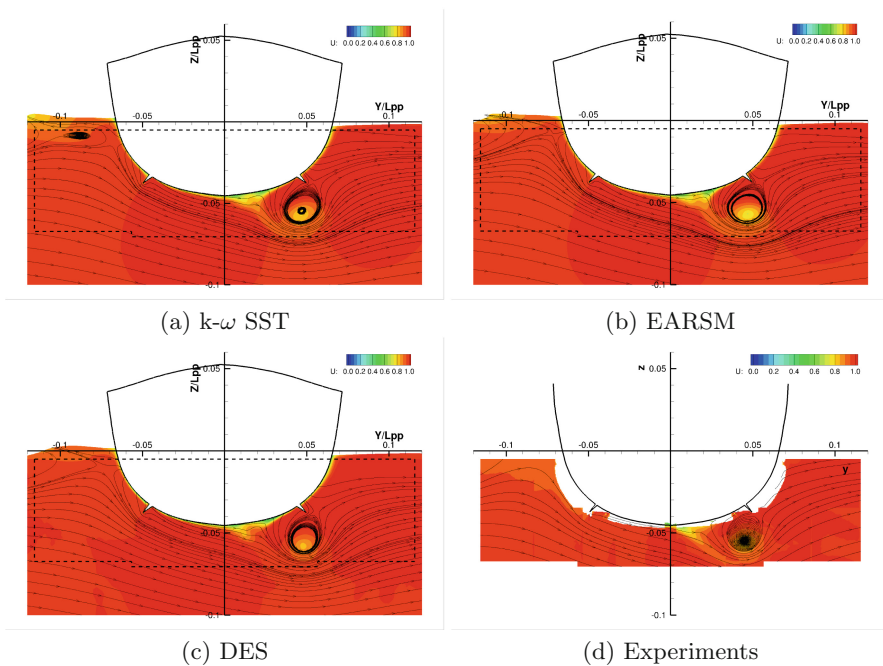


Fig. 2. Comparison of the axial velocity at $X/L_{PP} = 0.4$.

For the same slice, it is possible to plot the turbulence kinetic energy, see Fig. 3. In the experiments, a maximum of TKE is observed in the core of the vortex while with the RANS turbulence models, a minimum of TKE is predicted. Only the hybrid RANS-LES model predicts this high level of TKE in the core of the vortex.

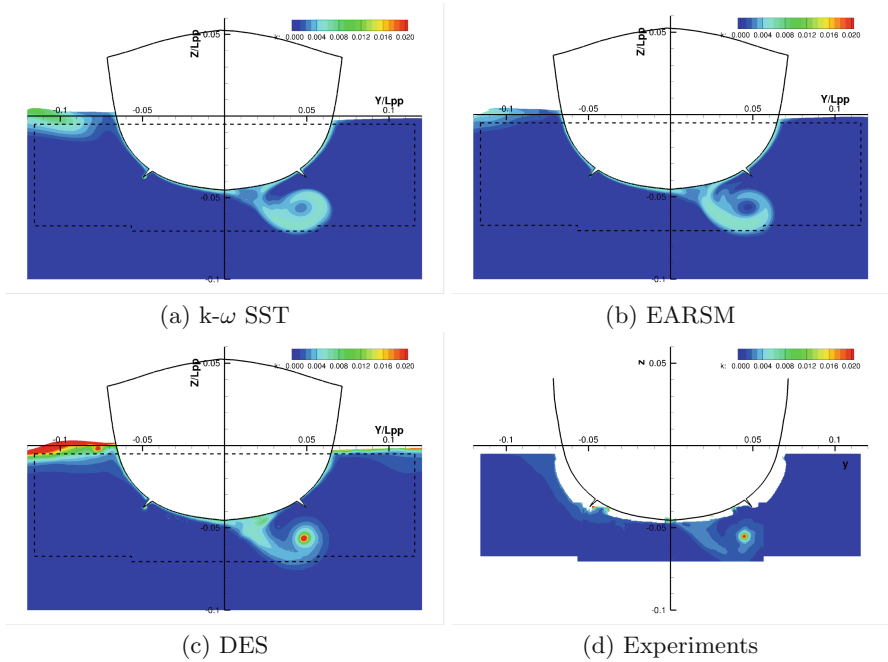


Fig. 3. Comparison of the turbulent kinetic energy at $X/L_{PP} = 0.4$.

With the help of several slices, it is possible to plot the longitudinal evolution in the core of SDTV and BKTV, see Fig. 4 which presents the position of the vortex core, the axial velocity and TKE. The positions of SDTV and BKTV are very well predicted by all numerical simulations. For the axial velocity, the velocity predicted with the EARSM turbulence model is not in agreement with the experimental data. Indeed, in the numerical simulation, a decrease of the velocity is predicted until $X/L_{PP} = 0.8$ while in the experiments, the velocity increases until $X/L_{PP} = 0.6$ and then decreases slightly. With the $k-\omega$ SST turbulence model, the velocity is constant until $X/L_{PP} = 0.6$ and then increases. The DES model is the only one that is able to predict the correct behavior of the velocity in the core of SDTV. For the turbulence kinetic energy, the RANS models predict a decrease when we move along the hull. However, in the experiments, the level of TKE is constant in the core and the hybrid RANS-LES model is able to predict this behavior.

This high level of turbulent kinetic energy is due to a population of ring vortices, see Fig. 5 which shows the core of the SDTV vortex obtained with the hybrid RANS-LES model, that comes from the periodic shedding at the trailing edge of the sonar dome. These vortices are driven in a global rotation motion around the axis of the SDTV and then create a high level of resolved fluctuations in its core. So, the high level of k in the core is not due to vortex meandering.

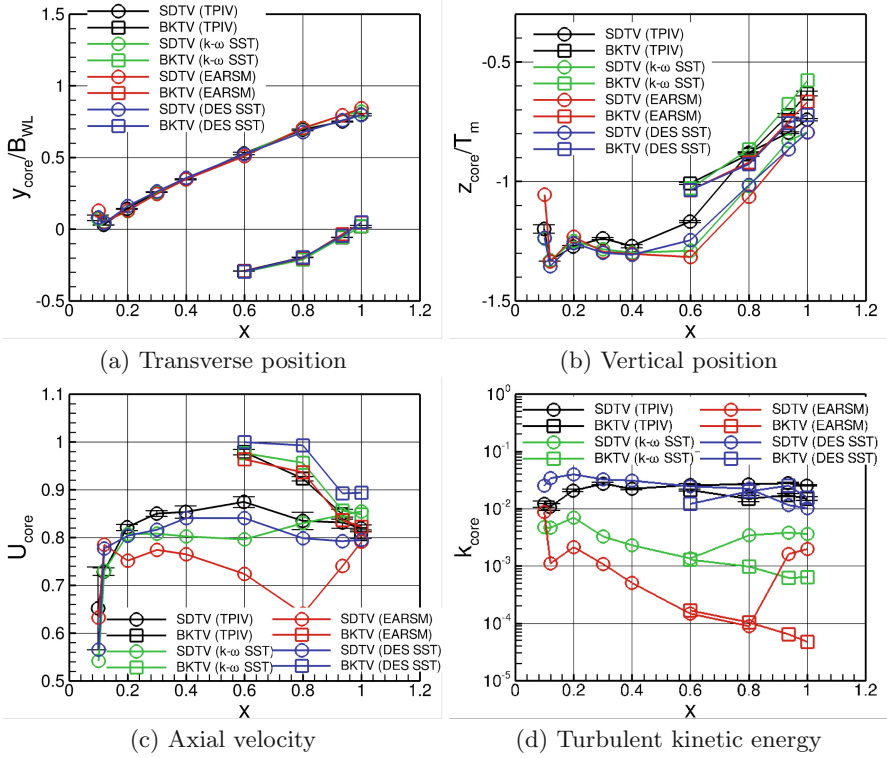


Fig. 4. Longitudinal evolution in the core of SDTV.

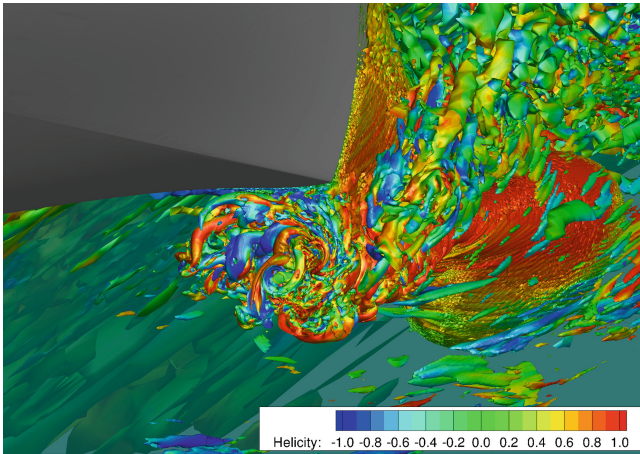


Fig. 5. View of an iso-surface of non-dimensional Q ($Q^* = 50$) around the SDTV vortex.

4 Conclusions

In this paper, an investigation of RANS and hybrid RANS-LES models for the flow simulation around a DTMB 5415 at 10° static drift has been conducted. This numerical study has been carried out with the flow solver ISIS-CFD. It has been shown that the use of the hybrid RANS-LES model offers an advantage over RANS models, particularly in terms of the turbulence kinetic energy in the core of the vortex. This high level of turbulent kinetic energy prediction is due to a vortex shedding on the trailing edge of the sonar dome.


Acknowledgments. This work was granted access to the HPC resources of CINES under the location A0022A00129 and A0042A00129 made by GENCI (Grand Equipement National de Calcul Intensif).

References

1. Tokyo 2015: A workshop on CFD in ship hydrodynamics. <http://www.t2015.nmri.go.jp/>
2. Deng, G.B., Visonneau, M.: Comparison of explicit algebraic stress models and second-order turbulence closures for steady flow around ships. In: 7th Symposium on Numerical Ship Hydrodynamics, pp. 4.4–1–15, Nantes (July 1999)
3. Duvigneau, R., Visonneau, M., Deng, G.B.: On the role played by turbulence closures in hull ship optimization at model and full scale. *J. Mar. Sci. Technol.* **8**, 11–25 (2003)
4. Gritskevich, M.S., Garbaruk, A.V., Schütze, J., Menter, F.R.: Development of DDES and IDDES formulations for the $k-\omega$ shear stress transport model. *Flow Turbul. Combust.* **88**, 431–449 (2012)
5. Guilmineau, E., Deng, G.B., Leroyer, A., Queutey, P., Visonneau, M., Wackers, J.: Assessment of hybrid RANS-LES formulations for flow simulation around the Ahmed body. *Comput. Fluids* (2017). <https://doi.org/10.1016/j.compfluid.2017.05.005>
6. Larsson, L., Stern, F., Visonneau, M. (eds.): *Numerical Ship Hydrodynamics - An Assessment of the Gothenburg 2010 Workshop*. Springer, Netherlands (2014)
7. Menter, F.R., Kuntz, M., Langtry, R.: Ten years of industrial experience with the SST turbulence model. In: Hanjalić, K., Nagano, Y., Tummers, M. (eds.) *Turbulence, Heat and Mass Transfer 4*, vol. 19, pp. 339–352. Begell House, Inc. (2003)
8. Nishikawa, N.: Application of fully resolved large eddy simulation to Japan bulk carrier with an energy saving device. In: *Tokyo 2015 Workshop on CFD in Ship Hydrodynamics*, Tokyo, Japan (2015)
9. Queutey, P., Visonneau, M.: An interface capturing method for free-surface hydrodynamic flows. *Comput. Fluids* **36**, 1481–1510 (2007)
10. Yoon, H., Gui, L., Bhushan, S., Stern, F.: Tomographic PIV measurements for a surface combatant at straight ahead and static drift conditions. In: *30th Symposium on Naval Hydrodynamics*, Hobart, Tasmania, Australia (2014)



Experiments and Large Eddy Simulations on Particle Interaction with a Turbulent Air Jet Impacting a Wall

Syphax Ikardouchene^{1,2}, Xavier Nicolas¹ , Stéphane Delaby²,
and Meryem Ould-Rouiss¹

¹ Université Paris Est Marne-la-Vallée, MSME UMR 8208 CNRS,
5 Bd Descartes, 77454 Marne-la-Vallée Cedex 2, France
Xavier.Nicolas@u-pem.fr

² CSTB, 24 rue Joseph Fourier, 38400 Saint-Martin-d'Hères, France

Abstract. Experiments and large eddy simulations are carried out to study the interaction of spherical particles with a turbulent air jet impacting a wall. The context is that of the dynamical air curtains used to separate a contaminated ambiance with passive or inertial particles from a clean ambiance. In the present study, the jet and particle Reynolds numbers and the jet and turbulence Stokes numbers are respectively equal to $Re_j = 13500$, $0.7 \leq Re_p \leq 3.5$, $0.02 \leq St_j \leq 0.35$ and $0.1 \leq St_t \leq 1$: they mainly concern passive particles. The rate of the particles that cross the air jet is analyzed according to the particle size, for two particle injection heights. A non-monotonic passing rate of the particles through the jet with respect to the particle size is observed in the experiments.

Keywords: Impacting plane jet · Air curtain · Particle/jet interaction · Passive particles · Experiments · LES

1 Introduction

Plane air jets are widely used in industry and cover a large range of applications: cooling and wiping of liquid films by plane turbulent jets [1], spread reduction of fumes and gaseous pollutants in tunnel fires [2] etc. In our case, a plane air jet is used for the separation of two clean and polluted atmospheres by inertial and passive (non-inertial) particles. The purpose of this work is to define if large eddy simulations (LES) allow qualitatively and quantitatively reproducing the interaction between particles and a turbulent vertical air jet. In that aim, an experimental apparatus and a numerical tool based on the coupling of LES and a Lagrangian model for the particle transport have been developed. The studied configuration is that of an air jet impacting a wall (similar to that of experiments [3] and LES [4]) and crossed by particles. The objective is to study the jet dynamics without particle and, then, to inject particles towards the jet, to measure their passage rate through the jet and to compare it with that of the LES.

2 Analysis of the Impinging Plane Air Jet, Without Particle

2.1 Experimental Facility and Method

In order to characterize impacting plane air jets, we designed the experimental device of Fig. 1. A vertical plane air jet is generated by a centrifugal fan that blows air through a divergent and convergent channel, then through a rectangular nozzle of section width $e = 3\text{ mm}$ in x -direction and depth $d_z = 200\text{ mm}$ in z -direction. The nozzle aspect ratio $d_z/e = 66$ ensures that the flow is statistically two-dimensional and free from the side wall effects when taking measurements in the central plane ($z = 0$) of the jet. The nozzle outlet is located in the middle of the top wall of a horizontal rectangular channel of height $H = 3\text{ cm}$, depth $d_z = 200\text{ mm}$ and length $L_x = 60\text{ cm}$ in x -direction (30 cm on each side of the jet). The jet average velocity at nozzle outlet is $U_j = 65\text{ m/s}$. The jet Reynolds number $Re = U_j e/\nu = 13500$ and the opening ratio $H/e = 10$ are fixed in all the study. The analysis of the velocity field is carried out by particle image velocimetry (PIV), by seeding with oil particle tracers directly at the fan level and using a Nd-Yag laser (65 mJ, 15 Hz) and a fast camera (FS EO 4M-32).

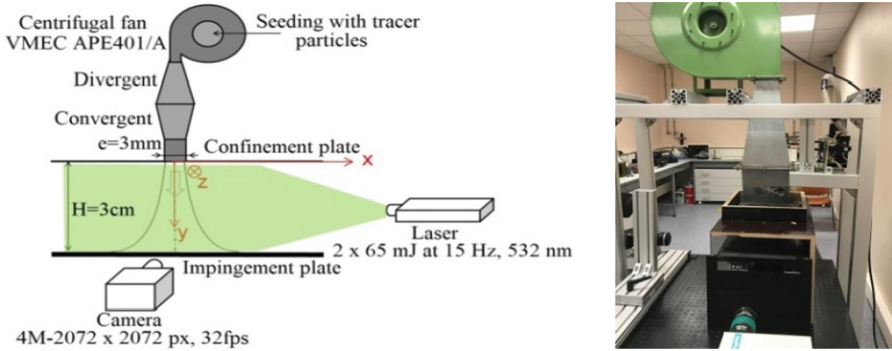


Fig. 1. Sketch and photography of the experimental facility.

2.2 Flow Configuration, LES Model and Numerical Methods

The LES are performed with the CFD code Ansys/Fluent v18.2 using the WALE model for the sub-grid effects. The filtered Navier-Stokes equations are solved by a finite volume method with a second order bounded central scheme, a second order time implicit scheme and PISO algorithm. The numerical configuration is close to that of the experiments. The computational domain size is $L_x \times L_y(H) \times L_z = 243 \times 30 \times 18.84\text{ mm}^3$ in the horizontal, vertical and depth directions respectively (Fig. 2 left). The vertical plane jet is injected into the

domain by a nozzle of section $L_z \times e = 18.84 \times 3 \text{ mm}^2$ located in the center of the upper horizontal wall. The experimental velocity profile measured in [3] at the outlet of the nozzle and taken up in the LES [4] is interpolated and imposed as inlet boundary conditions (B.C.) in our simulations with the average velocity $U_j = 65 \text{ m/s}$. Turbulent fluctuations in the inlet velocity profiles are generated, with a turbulent intensity $I = 2\%$, by a «spectral synthesizer». No slip B.C. are imposed on the horizontal walls and periodic B.C. on the front and back faces. The depth $L_z/e = 2\pi$ is chosen so that the time signals are decorrelated in z -direction [4]. The air jet impacts the lower wall and horizontally flows out through the left and right vertical openings considered at atmospheric pressure. A non-uniform Cartesian mesh of size $N_x \times N_y \times N_z = 236 \times 150 \times 64$ cells ($y_{max}^+ < 5.6$) is used (Fig. 2 right). It is uniform in z -direction. The time step is $\Delta t = 10^{-6} \text{ s}$ such that $CFL_{L_{max}} = (U \Delta t / \Delta x)_{max} = 7$. The time duration for the statistics is 0.02 s.

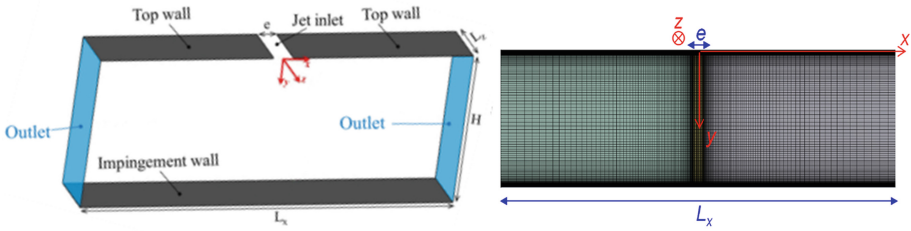


Fig. 2. Sketch of the computational domain (left) and mesh in the $(x-y)$ plane (right).

2.3 Result Discussion for an Air Jet Without Particle

Figure 3 shows average and rms velocity profiles obtained by the present PIV and LES, compared with experimental [3, 5] and LES [4] results. Other validations were carried out by comparing various vertical and transverse profiles of the time averages and rms of the velocity components and pressure, the Reynolds stresses, the half width of the jet and the spectral analysis of time signals. All these results are in good agreement with the results published in the reference literature (see [6] for more details about the validations).

3 Analysis of the Jet/Particles Interaction

3.1 Experimental Facility and Particle Generation (Spinning Disk)

To generate particles, the spinning disk method is used (Fig. 4 right). The principle is the fragmentation and dispersion of oil droplets under the centrifugal force of a rotating disk. The edge of this disk is placed at 1 cm from the jet

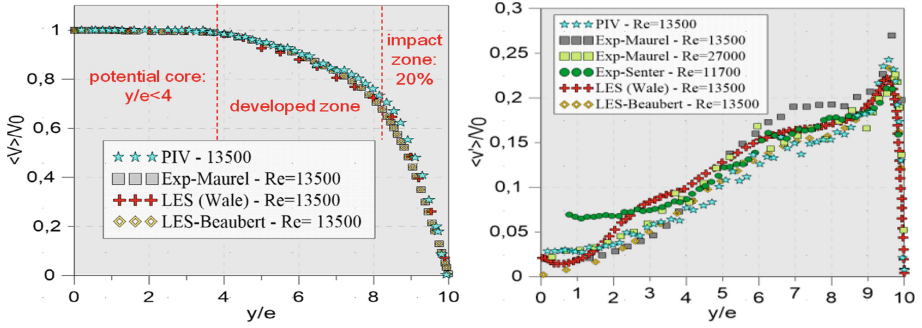


Fig. 3. Mean velocity magnitude (left) and vertical velocity rms (right) along jet axis.

axis and its tangential speed is $V_t = R\omega = 38 \text{ m/s}$ with $R = 1.6 \text{ cm}$. Figures 4 and 5 show that the presence of the rotating disk does not perturb the air jet flow. The oil mass flow rate for particle generation is $\dot{m} = 0.2 \text{ g/min}$ and the generated particle diameter is $0.3 \leq d_p \leq 7 \mu\text{m}$. The particle total concentrations, $C_{p,l}$ and $C_{p,r}$, and size distribution are locally measured on the two sides of the jet, at $x = \pm 20 \text{ cm}$, by an optical particle counter (COP-GRIMM; Fig. 4 left). $C_{p,l}$ is measured on the left side (opposite side of the rotating disk with respect to the jet) and $C_{p,r}$ on the right side (on the side of the rotating disk). We have checked that these concentrations are quasi homogeneous in all the channel section at this distance. The particle passing rate through the jet, defined by $PPR = \frac{C_{p,l}}{C_{p,l} + C_{p,r}}$, is computed from the average values of the concentrations measured during a ten minute particle injection in the presence of the jet, for two positions of the rotating disk: at $y = 7 \text{ mm}$ (jet potential cone level) and $y = 17 \text{ mm}$ (jet developed zone; Fig. 3 left). Since, the optical counter can measure the diameter d_p of each particle, the PPR can also be measured for each class of particle size.

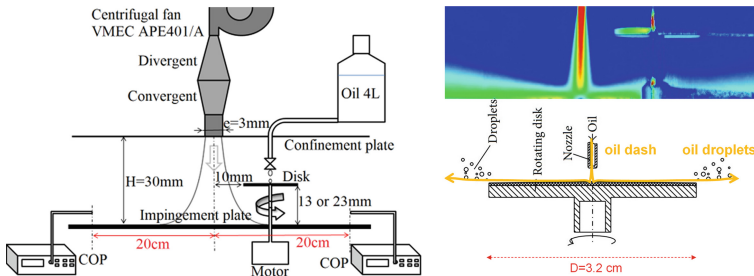


Fig. 4. Experimental facility for the jet/particle interaction study (left). Spinning disk principle and PIV field of the mean velocity magnitude with the rotating disk (right).

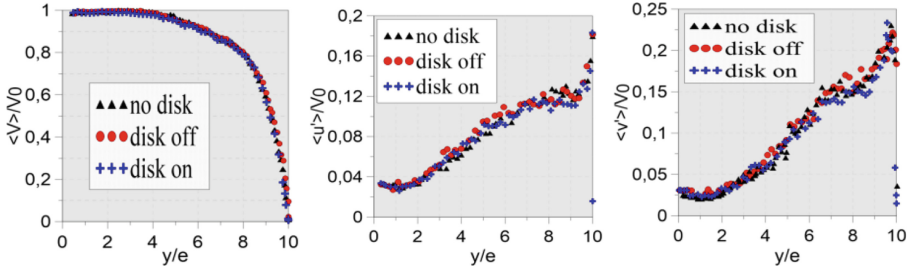


Fig. 5. Profiles of the mean vertical velocity (left) and rms of the horizontal (center) and vertical (right) velocities along the jet axis, with and without the disk in rotation.

3.2 Configuration and Parameters of the Jet/Particle Simulations

A Lagrangian model expressing the balance between the inertial, drag and gravity forces is used for the transport of the oil droplets considered as spheres. In this model, the particle relaxation time $t_p = \frac{\rho_p d_p^2}{18\mu} \frac{24}{C_D Re_p}$ and the drag coefficient $C_D = a_1 + \frac{a_2}{Re_p} + \frac{a_3}{Re_p^2}$ ($a_i = cst$) are function of $Re_p = \frac{\rho d_p |u_p - u|}{\mu}$, the particle Reynolds number. A “stochastic tracking model” is also activated in Ansys/Fluent to take into account the turbulent dispersion of the particles (see [7] for more details). Since the largest particle volume fraction was estimated around 10^{-3} in the spinning disk neighborhood at the end of the injection period, a two-way-coupling model was used in the simulations. Furthermore, $t_s = e/(2u_p)$ being the characteristic time of the particles to go through the half of the jet thickness and t_κ being the Kolmogorov time scale, the jet and turbulence Stokes numbers are estimated to vary in the ranges $0.02 \leq St_j = t_p/t_s \leq 0.35$ and $0.1 \leq St_t = t_p/t_\kappa \leq 1$ (to 7, locally), when d_p varies between 1 and $5\mu\text{m}$. Therefore the particles are mainly passive, that is with little inertial effects.

The injection and boundary conditions for the particles are presented on Fig. 6 (left). Around 1 million of spherical particles of the same diameter ($d_p = 1, 3$ or $5\mu\text{m}$) and density $\rho_p = 920\text{kg/m}^3$ are injected in the domain from a thin surface of depth \times height = $18.8 \times 1\text{mm}^2$, located at $x = 10\text{mm}$ from the air jet median plane and at $y = 7$ or 17mm from the top wall. They are injected during 2 ms, with a horizontal velocity $u_p = -10\text{m/s}$ and mass flow rate $\dot{m} = 0.3\text{g/min}$. Their trajectories are followed during 5 ms for the injection at $y = 7\text{mm}$ and during 50 ms at $y = 17\text{mm}$. The particles are reflected on the top wall and on the bottom wall in front of the air jet nozzle, but they are trapped on the rest of the bottom wall. Due to the simulation cost, the *PPR* is only computed for the injection at $y = 17\text{mm}$: it is the proportion of particles of the same diameter that have passed through the jet median plane ($x=0$) at $t = 50\text{ms}$. The total user time of these simulations is around two months on 20-cores of recent high-performance computing workstations.

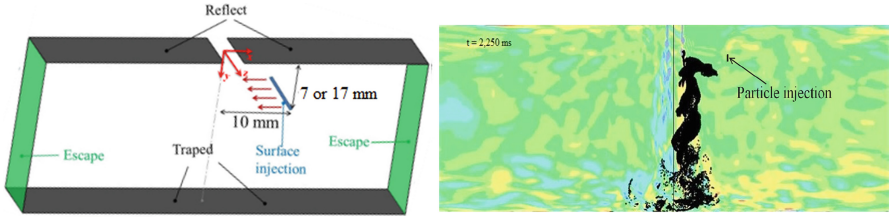


Fig. 6. Simulation domain with the injection line and the particle B.C. (left). Vorticity contours and $3\ \mu\text{m}$ -particle location (black points) in the vertical median plane at $z = 0$, at $t = 2.25\ \text{ms}$, for the particles injected at $y = 7\ \text{mm}$ from the top wall (right).

3.3 Result Discussion for an Air Jet with Particle Injection

Figure 6 (right) shows the particle/vorticity interaction, for $d_p = 3\ \mu\text{m}$ and the injection position at $y = 7\ \text{mm}$, just after the injection period, at $t = 2.25\ \text{ms}$. The particles are driven by Kelvin Helmholtz rolls that are partially responsible for the passage of the particles through the jet, mainly in the impact zone (see also [4]). Note that, due to the presence of two large vortices on both sides of the jet (not shown here; see [6] for more details), the evacuated particles towards the channel outlets can be taken back to the jet by these vortices, for $t > 10\ \text{ms}$. This explains why the *PPR* is measured at $t = 50\ \text{ms}$ in the simulations.

The experimental time evolution of the particle concentration $C_{p,l}$ is shown on Fig. 7 (left) for three different tests. There are four distinct phases in this graph which correspond to the time variation of $C_{p,l}$: (1) in the environment (before particle injection) in order to subtract it from the following measurements; (2) with particle injection but without air jet; (3) with particle injection and with air jet (it is therefore the concentration of particles passing through the jet); (4) after stopping the particle generation. One can see that the repeatability of the measurements is ensured and a decrease in the particle concentration is observed in the presence of the jet.

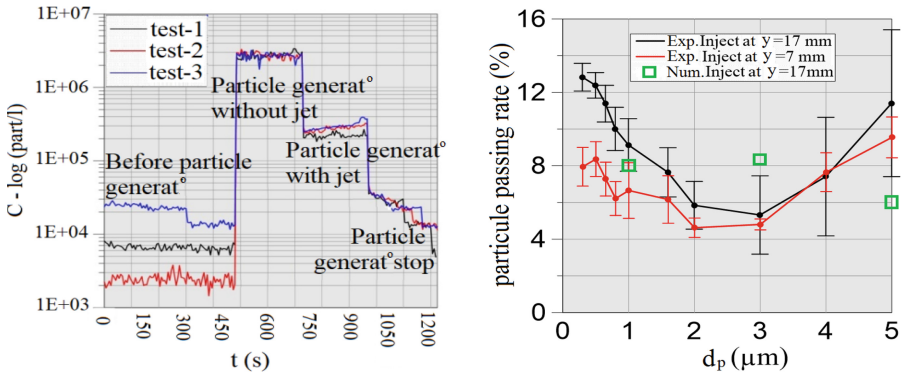


Fig. 7. Time evolution of the particle concentration $C_{p,l}$ (left). Passing rate of the particles through the jet with respect to the particle diameter (right).

Figure 7 (right) presents the PPR evolution, for each class of particle size, with respect to d_p , for the two positions of the rotating disk in the experiments and at $y = 17$ mm for the simulations. The experimental PPR values are similar for the two injection locations, except at $d_p < 1 \mu\text{m}$. As already noted above, this can be partly explained by the presence of the two large vortices on both sides of the jet that “recycle” the particles [6]. For the injection at 17 mm, the experimental and numerical PPR values are in a relatively good agreement when the standard deviations of the experimental results are taken into account. However a non-monotonic PPR evolution with d_p is clearly visible in the experiments but is not reproduced by LES. In the experiments, the larger value of the PPR for the smallest d_p could be due to the turbulent dispersion of the smallest particles while its increase for the largest d_p could be due to inertial effects relatively to the turbulence scale ($St_{t,max} = 7$ for $d_p = 5 \mu\text{m}$). This small-scale phenomenon is filtered by LES and likely not taken into account in the numerical model. Another explanation could be the coalescence (resp., the break-up) of the oil droplets, increasing then the PPR of the biggest (resp., smallest) particles.

4 Conclusions

In the first part of this study, an analysis of the air jet dynamics without particles has been performed with PIV and LES simulations. The comparison of the results has shown that the Wale LES model is appropriate to simulate a turbulent air jet impacting a wall. In the second part, the interactions between this air jet and spherical particles of different diameters was investigated by the two approaches. The method of particle generation by a spinning disk has appeared to be a very interesting method because it does not perturb the jet. The experiments have enabled to set up reference results to validate simulations with particle/jet interaction because no experiment exists in the literature for this configuration. The LES have enabled a better understanding of the particle/jet interactions, in particular the interactions with the Kelvin-Helmholtz rolls. A non-monotonic passing rate of the particles through the jet with respect to the particle size has been experimentally observed. This paper is a presentation of the first results of this study but new results and deeper analyses are in progress.

Acknowledgments. This study is part of the CAPTEUR project supported by ANR and PIA via COMUE UPE and Isite FUTURE (contract no. ANR-16-IDEX-0003).

References

1. Lacanette, D., Vincent, S., Arquis, E.: A numerical experiment on the interaction between a film and a turbulent jet. *Comptes Rendus Mécanique* **333**, 343–349 (2005)
2. Guyonnaud, L., Sollic, C., Dufresne de Virel, M., Rey, C.: Design of air curtains used for area confinement in tunnels. *Exp. Fluids* **28**(4), 377–384 (2000)
3. Maurel, S., Sollic, C.: A turbulent plane jet impinging nearby and far from a flat plate. *Exp. Fluids* **31**(6), 687–696 (2001)

4. Beaubert, F., Viazzo, S.: Large eddy simulation of plane turbulent impinging jets at moderate Reynolds numbers. *Int. J. Heat Fluid Flow* **24**, 512–519 (2003)
5. Senter, J.: Analyse expérimentale et numérique des écoulements et des transferts de chaleur convectifs produits par un jet plan impactant une plaque plane mobile. Ph.D. thesis, Univ. de Nantes (2006)
6. Ikardouchene, S.: Analyses expérimentale et numérique de l'interaction de particules avec un jet d'air plan impactant une surface. Application au confinement particulaire. Ph.D. thesis, Univ. Paris Est (2019)
7. ANSYS Fluent Theory Guide, Release 17.2. Ansys Inc., Canonsburg (2016)



A Review of Geometrical Interface Properties for 3D Front-Tracking Methods

Désir-André Koffi Bi^(✉), Mathilde Tavares, Éric Chénier,
and Stéphane Vincent

Univ. Gustave Eiffel, CNRS, MSME UMR 8208, 77454 Marne-la-Vallée, France
`desir-andre.koffibi@u-pem.fr`

Abstract. Modeling and simulating multiphase flows still remain an exciting and stimulating scientific challenge. Many approaches were developed to describe the topological evolution of the interface. This paper remains in the domain of the Front-Tracking method [8, 10], in which, in addition to the use of an Eulerian mesh to solve the Navier-Stokes equations, a Lagrangian interfacial mesh of surface elements (triangles in 3D) explicitly describes the evolution of the interface. Whatever the method used, getting the interfacial capillary, mass or energy transfers is crucial for the study of multiphase flows. A comparison is done between different techniques [7, 10] used to get the geometrical properties of the 3D front-tracking objects, such as the surface tension forces, mean curvatures and normal vectors, which are essential for the modeling and understanding of multiphase flows.

Keywords: Front-tracking · Multiphase flow · Surface tension · Curvature

1 Introduction

The numerical simulation and modeling of multiphase flows have been of great interest these last two decades. It has a wide range of involvements in our daily life, whether in chemical engineering, material design, energy field or propelling, with boiling crisis, combustion in motors, atomization, surface coating, to cite but a few. Different approaches are used to take into account the surface tension forces. In the Direct Numerical Simulation (DNS) of multiphase flows, unstructured meshes are usually used for discretization [2]. Each phase is resolved independently, and the junction at the interface is satisfied through jump conditions [3], including the surface tension forces. In the case of the One-Fluid model, contrary to the previous one, a structured mesh is often used to solve the conservation equations in the entire domain. The surface tension forces \mathbf{F}_{st} are included in the Navier-Stokes equations. One way to estimate them is using the Continuum Surface Force (CSF) proposed by Brackbill *et al.* [1]. But

whatever the method employed, the mean curvature κ and the unit normal vector \mathbf{n} must be accurately evaluated, for they are essential geometrical properties for the study of multiphase flows and interfacial transfers. In the case of 3D front-tracking methods, four approximations are presented and compared to get those surfaces properties.

2 Geometrical Interface Properties

Four approaches to get the geometrical properties of the interface, namely the mean curvature κ and the unit normal vector \mathbf{n} , are shown below, knowing the triangular interface mesh (vertices positions and mesh connectivity). They can be gathered into two groups.

2.1 The Meyer et al. Approach

The Meyer approach is based on a discrete formulation of the Laplace-Beltrami operator [7]. The curvature and the normal vector are obtained through a linear combination of the \mathcal{N}_i edges sharing the same vertex \mathbf{x}_i .

$$\mathbf{K}(\mathbf{x}_i) = \frac{1}{2\mathcal{A}_{mixed}} \sum_{j=1}^{\mathcal{N}_i} (\cot \alpha_{ij} + \cot \beta_{ij})(\mathbf{x}_i - \mathbf{x}_j) = 2\kappa\mathbf{n} \quad (1)$$

where α_{ij} and β_{ij} are the angles facing the edge $[\mathbf{x}_i\mathbf{x}_j]$, and \mathbf{K} is the Laplace-Beltrami operator, which is basically a Laplacian acting on the surface (see Fig. 1b). Two variants can be differentiated based on the construction of the area \mathcal{A}_{mixed} : the Standard Meyer Method [7] and the Barycentric Meyer Method [4]. In both cases, when the triangle is acute, the Voronoi area is used. If the triangle is obtuse, either the middle of the edge opposite to the obtuse angle (Standard Meyer Method), or the centroid (Barycentric Meyer Method) is employed to construct \mathcal{A}_{mixed} .

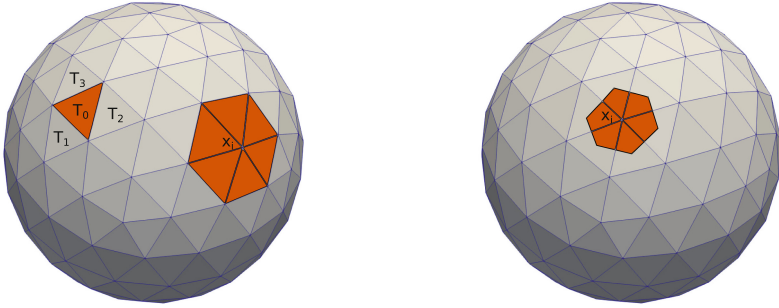
2.2 The Frenet Approach

The Frenet approach is used in the works by Shin and Juric [8], as well as in those by Tryggvason *et al.* [10]. Evaluated on an element (line in 2D and triangle in 3D), it can be called Frenet Element Method. The average surface tension force is:

$$\bar{\mathbf{f}} = \frac{\sigma}{S} \int_S \kappa \mathbf{n} dS = \frac{\sigma}{S} \oint_{\partial S} \mathbf{t} \wedge \mathbf{n} dl \quad (2)$$

with \wedge the cross product, S the area of the element, ∂S its perimeter, \mathbf{t} and \mathbf{n} the unit tangent and normal vectors at the edge. The average force is approximated by:

$$\bar{\mathbf{f}} \approx \frac{\sigma}{S} \sum_{i=1}^3 (\mathbf{t}_{0i} \wedge \mathbf{n}_{0i}) L_{0i} \quad (3)$$



(a) Frenet element and vertex stencils

(b) Standard Meyer stencil

Fig. 1. Areas on which are applied the average force for the frenet element and vertex methods (a) and the Standard Meyer method (b).

where \bullet_{0i} refers to the parameters at the edge shared by elements T_0 and T_i . For an analytical surface, it is simple to get the tangent and the normal vector at the edge. This is more problematic for the approximated surface. To mimic the continuous formulation in the 3D discrete case, the normal vector to the edge shared by the elements T_0 and T_1 is approximated by:

$$\mathbf{n}_{01} = \frac{S_1 \mathbf{n}_0 + S_0 \mathbf{n}_1}{\|S_1 \mathbf{n}_0 + S_0 \mathbf{n}_1\|} \tag{4}$$

Instead of computing the mean values of the curvature and normal vector on the element, an average value centered around a vertex \mathbf{x}_i can be preferred, the so called Frenet Vertex Method. The resulting surface tension force, constructed on the elements sharing the same vertex \mathbf{x}_i , consists in a linear combination of the average force on each element, using the Frenet Element Method:

$$\mathbf{F}(\mathbf{x}_i) = \sum_{j=1}^{\mathcal{N}_i} S_j \bar{\mathbf{f}}_j \quad \text{and} \quad \bar{\kappa \mathbf{n}} = \frac{\mathbf{F}(\mathbf{x}_i)}{\sigma \sum_{j=1}^{\mathcal{N}_i} S_j} \tag{5}$$

3 Simulations and Results

The aforementioned methods are compared and their accuracy estimated on an analytical surface [6], where the exact curvature and normal vector are computed [5]. The following analytical surface is considered (see Fig. 2):

$$f(u, v) = \sin(5u) \sin(5v) \quad \text{with} \quad (u, v) \in \left[-\frac{\pi}{5}, \frac{\pi}{5}\right] \times \left[-\frac{\pi}{5}, \frac{\pi}{5}\right] \tag{6}$$

Its discrete approximation results in a projection of a planar mesh, for which the size and the shape of the elements are controlled. Let $\mathbf{x} = (x_1, x_2, 0)$ be a vertex of an initial planar mesh of equilateral triangles, the edges size of which

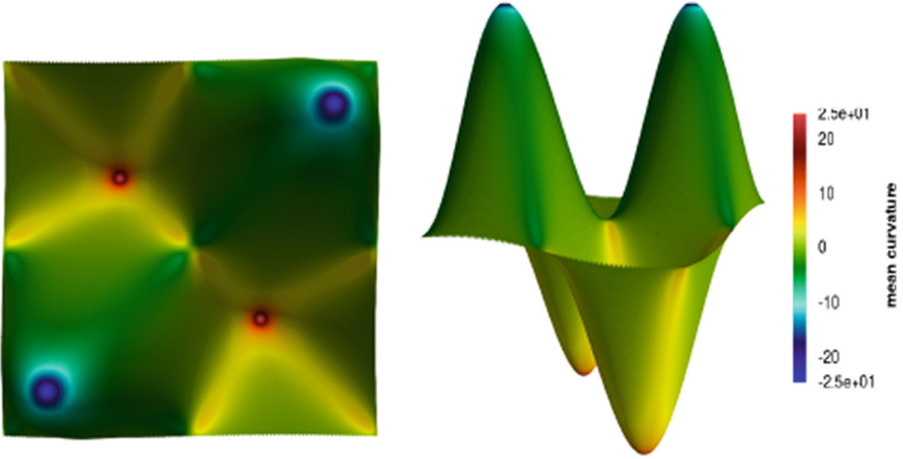


Fig. 2. Top view (left) and side view (right) of the mean curvature κ for the analytical surface $f(u, v)$ (Eq. 6).

is d . From this initial planar mesh, random disturbances are introduced: $\tilde{\mathbf{x}} = \mathbf{x} + r \times p \times d \times (\cos 2\pi\theta, \sin 2\pi\theta, 0)$, where p is the maximum magnitude of the perturbation ($0 \leq p < 0.5$), and (r, θ) is a couple of random numbers drawn from a standard uniform distribution. To evaluate the accuracy of the approximations, the following measure is defined:

$$\text{Err}_2^{\text{rel}}(\bullet) = \sqrt{\frac{\sum_{j=1}^N \|\bullet_j - \bullet_j^{\text{ref}}\|^2}{\sum_{j=1}^N \|\bullet_j^{\text{ref}}\|^2}} \quad (7)$$

where $\|\bullet\|$ is the absolute-value for a scalar number, or the Euclidean norm for a vector, N denotes the number of vertices (Meyer approach and Frenet Vertex Method) or elements (Frenet Element Method). The notation \bullet_j^{ref} stands for the average force direction $\mathbf{n}_j^{\text{ref}}$ or intensity κ_j^{ref} on the surface \mathcal{S} , which corresponds to, either the element j , or the stencil surrounding the vertex \mathbf{x}_j :

$$\mathbf{n}_j^{\text{ref}} = \frac{\bar{\mathbf{F}}}{\|\bar{\mathbf{F}}\|}, \quad \kappa_j^{\text{ref}} = \frac{\|\bar{\mathbf{F}}\|}{\sigma}, \quad \text{with } \bar{\mathbf{F}} = \frac{\sigma}{S} \int_{\mathcal{S}} \kappa \mathbf{n} ds \quad (8)$$

The convergence of the approximation is studied as a function of the dimensionless mesh size $d \times \max_j(\kappa_j^{\text{ref}})$, which represents the size of the triangles used for describing the maximum curvature. First, no perturbation is applied on the planar equilateral mesh ($p = 0$). The numerical errors reported in Table 1 indicate that the best methods which stand out are the Standard Meyer Method,

Table 1. Comparative and convergence study on κ , $p = 0$

$d \times \max(\kappa)$	Std Meyer		Bar Meyer		Frenet vertex		Frenet element	
	$\text{Err}_2^{\text{rel}}(\kappa)$	<i>Order</i>	$\text{Err}_2^{\text{rel}}(\kappa)$	<i>Order</i>	$\text{Err}_2^{\text{rel}}(\kappa)$	<i>Order</i>	$\text{Err}_2^{\text{rel}}(\kappa)$	<i>Order</i>
7.80E-01	2.04E-02		3.27E-02		1.98E-02		9.95E-02	
3.90E-01	6.20E-03	1.72	1.86E-02	0.81	7.20E-03	1.46	5.33E-02	0.90
1.95E-01	1.82E-03	1.77	1.42E-02	0.39	3.05E-03	1.24	2.72E-02	0.97
9.75E-02	5.38E-04	1.76	9.04E-03	0.66	1.13E-03	1.43	1.42E-02	0.94
4.87E-02	1.65E-04	1.71	6.75E-03	0.42	5.36E-04	1.08	7.22E-03	0.97
2.44E-02	5.31E-05	1.63	4.68E-03	0.53	2.07E-04	1.37	3.61E-03	1.00

Table 2. Comparative and convergence study on κ , $p = 0.05$

$d \times \max(\kappa)$	Std Meyer		Bar Meyer		Frenet vertex		Frenet element	
	$\text{Err}_2^{\text{rel}}(\kappa)$	<i>Order</i>	$\text{Err}_2^{\text{rel}}(\kappa)$	<i>Order</i>	$\text{Err}_2^{\text{rel}}(\kappa)$	<i>Order</i>	$\text{Err}_2^{\text{rel}}(\kappa)$	<i>Order</i>
7.80E-01	2.38E-02		3.39E-02		2.04E-02		1.02E-01	
3.90E-01	1.39E-02	0.78	2.34E-02	0.54	8.99E-03	1.18	5.90E-02	0.79
1.95E-01	1.24E-02	0.16	2.05E-02	0.19	5.90E-03	0.61	3.77E-02	0.65
9.75E-02	1.24E-02	0.00	2.00E-02	0.04	5.48E-03	0.11	3.03E-02	0.31
4.87E-02	1.24E-02	0.00	1.98E-02	0.01	5.44E-03	0.01	2.80E-02	0.11
2.44E-02	1.24E-02	0.00	1.98E-02	0.00	5.42E-03	0.00	2.74E-02	0.03

Table 3. Comparative and convergence study on \mathbf{n} , $p = 0.2$

$d \times \max(\kappa)$	Std Meyer		Bar Meyer		Frenet vertex		Frenet element	
	$\text{Err}_2^{\text{rel}}(\mathbf{n})$	<i>Order</i>	$\text{Err}_2^{\text{rel}}(\mathbf{n})$	<i>Order</i>	$\text{Err}_2^{\text{rel}}(\mathbf{n})$	<i>Order</i>	$\text{Err}_2^{\text{rel}}(\mathbf{n})$	<i>Order</i>
7.80E-01	1.23E-01		1.23E-01		1.56E-01		8.78E-02	
3.90E-01	5.23E-02	1.23	5.23E-02	1.23	6.39E-02	1.29	5.46E-02	0.69
1.95E-01	1.41E-02	1.90	1.40E-02	1.90	1.11E-02	2.52	2.72E-02	1.00
9.75E-02	3.93E-03	1.84	3.89E-03	1.85	2.83E-03	1.97	1.32E-02	1.04
4.87E-02	1.12E-03	1.82	1.08E-03	1.85	1.20E-03	1.24	6.75E-03	0.97
2.44E-02	3.53E-04	1.66	3.30E-04	1.71	5.08E-04	1.24	3.37E-03	1.00

followed by the Frenet Vertex one. From now on, random perturbations are introduced in the aforementioned planar mesh, and 100 simulations are performed to get the mean statistical values. As shown in Table 2 for small disturbances ($p = 0.05$), all methods saturate when refining the mesh. This saturation is all the more high as the magnitude p of the perturbations increases. Indeed, for $p = 0.2$ and $d \times \max_j(\kappa_j^{\text{ref}}) = 2.44 \times 10^{-2}$, the relative curvature errors for the Standard Meyer and the Frenet Vertex Methods are 4 times larger, with respectively $\text{Err}_2^{\text{rel}}(\kappa) = 4.96 \times 10^{-2}$ and $\text{Err}_2^{\text{rel}}(\kappa) = 2.35 \times 10^{-2}$. Concerning the normal vector approximation \mathbf{n} , even for large perturbations ($p = 0.2$), the methods converge, with at least a 1st order accuracy (Table 3). However, despite the

convergence of the unit normal vector, the saturation of the curvature prevents the convergence of the surface tension force.

4 Remarks and Conclusion

Getting the surface tension force, the mean curvature and the normal vector at the interface of multiphase flows is not as straightforward as in 2D, where the usual methods give good results, both in terms of errors and accuracy [9]. The tests conducted in this paper show that, without random perturbation, the Standard Meyer and the Frenet Vertex Methods stand out and have a good accuracy. It is worth to point out that, after projection onto the surface, the triangles are not equilateral anymore. However, the surface mesh still varies smoothly, since the analytical function is regular enough. In contrast, the addition of disturbances definitely breaks this regularity, preventing the convergence of the curvature (and the surface tension force). In the framework of multiphase flows approximated by 3D front-tracking methods, the mesh quality is difficult to manage because of the complexity of the dynamics. Therefore, despite relatively small errors, applying the different methods is questionable due to their lack of convergence.

References

1. Brackbill, J., Kothe, D., Zemach, C.: A continuum method for modeling surface tension. *J. Comput. Phys.* **100**(2), 335–354 (1992)
2. Compere, G., Marchandise, E., Remacle, J.F.: Transient adaptivity applied to two-phase incompressible flows. *J. Comput. Phys.* **227**(3), 1923–1942 (2008)
3. Delhaye, J.: Jump conditions and entropy sources in two-phase systems. Local instant formulation. *Int. J. Multiph. Flow* **1**(3), 395–409 (1974)
4. Essadki, M.: Contribution to a unified Eulerian modeling of fuel injection: from dense liquid to polydisperse evaporating spray. Ph.D. thesis, Universite Paris-Saclay (2018)
5. Goldman, R.: Curvature formulas for implicit curves and surfaces. *Comput. Aided Geometr. Design* **22**, 632–658 (2005)
6. Li, X., Xu, G., Zhang, Y.J.: Localized discrete laplacebeltrami operator over triangular mesh. *Comput. Aided Geometr. Design* **39**, 67–82 (2015)
7. Meyer, M., Desbrun, M., Schroder, P., Barr, A.H.: Discrete differential-geometry operators for triangulated 2-manifolds. In: Hege, H.C., Polthier, K. (eds.) *Visualization and Mathematics III*, pp. 35–57. Springer, Heidelberg (2003)
8. Shin, S., Juric, D.: Modeling three-dimensional multiphase flow using a level contour reconstruction method for front tracking without connectivity. *J. Comput. Phys.* **180**(2), 427–470 (2002)
9. Tavares, M., Koffi-Bi, D.A., Chénier, E., Vincent, S.: A second order conservative front-tracking method with an original marker advection method based on jump relations. *Commun. Comput. Phys.* (2020, to be published)
10. Tryggvason, G., Scardovelli, R., Zaleski, S.: *Direct Numerical Simulations of Gas-Liquid Multiphase Flows*, 1st edn. Cambridge University Press, Cambridge (2011)



Soft-Sphere DEM Simulation of Coarse Particles Transported by a Fully Developed Turbulent Gas Vertical Channel Flow

Ainur Nigmatova¹, Yann Dufresne², Enrica Masi¹(✉), Vincent Moureau², and Olivier Simonin¹

¹ Institut de Mécanique des Fluides de Toulouse (IMFT),
Université de Toulouse, CNRS, Toulouse, France
ainur.nigmatova@toulouse-inp.fr, enrica.masi@imft.fr
² CORIA UMR 6614 CNRS – INSA, Université de Rouen,
76801 Saint-Etienne du Rouvray, France

Abstract. The main focus of the present study is to evaluate the accuracy of the soft-sphere method to represent the particle-particle and the particle-wall collision effect in dilute rapid particulate flow. At this aim, 3D soft-sphere Discrete Element Method (DEM) simulation results are presented for frictionless elastic and inelastic particles, for different sizes and mean solid volume fractions, transported in a fully developed vertical channel flow. The effect on particle statistics of the friction during particle-wall collisions is analyzed. Profiles of time-averaged quantities are assessed and well agree with simulation results available from the literature, obtained by using the hard-sphere model.

Keywords: Gas-particles flows · Discrete element method · Soft-sphere model

1 Introduction

Understanding the dynamics of turbulent gas–particle flows has great importance for the successful design and optimization of many industrial applications, such as fluidized beds, dust collectors, cyclone separators. These systems involve many complex mechanisms, which are often coupled and interacting with each other. In the past decades, the focus was mainly on the complexity of the interaction between particles and gas-phase turbulence [1, 15] and the effect of particle–particle and particle–wall collisions [13, 14].

Gas turbulence has a predominant effect on particle diffusion for small particles. In this case, the influence of the solid-solid interactions is less important, because their dynamics is controlled by the fluid motion. However, in the case of large particles, the distance they need to respond to the fluid flow is larger than the characteristic dimension of the confinement, and the effect of the flow

turbulence may be neglected. Their motion is considerably influenced by the solid-solid collision process in confined flows. In this work, the inertial particles motion in a steady and imposed fluid flow is studied.

Due to the discrete nature of the particles, the numerical simulation of the particle motion is performed in a Lagrangian framework by Discrete Element Method (DEM). Such an approach can be coupled with different models resolving the fluid phase, depending on the characteristic length scales of the fluid and particles.

An accurate resolution of particle-particle and particle-wall interactions is necessary to describe properly the whole gas-particles flow dynamics. For this reason, the objective of the present work is twofold. The first objective is to study the influence of particles properties (particle size, concentration, restitution coefficient, etc.) on the velocity statistics in vertical channel flows using the DEM simulation. For modeling the solid-solid interaction, DEM uses two approaches, the hard-sphere [3] and the soft-sphere models [5]. The soft-sphere model has computational advantages in simulating dense suspensions with multiple particle-particle contacts, while the hard-sphere model is better suited to dilute regimes. Indeed, the soft-sphere models makes it possible to address multiple collisions which occur in dense regimes, allowing particles to deform slightly at the contact point. The hard-sphere approach assumes instead that no deformation occurs during the instantaneous collision between the two solid bodies. In this work, the soft-sphere model is used, since this can treat both low and high particle number densities, and it can handle multiple contacts. Thus, the second objective is to evaluate the accuracy of the soft-sphere model to reproduce the solid-solid collision effect in a rapid gas-particles flow with dilute suspension of massive particles, comparing with Lagrangian simulation results based on the hard-sphere model [7, 9, 10].

2 General Description

2.1 Flow Configuration

The proposed test case is a gas-particles vertical fully developed channel flow, studied early by [7, 9, 10]. The corresponding Reynolds number of the fully developed flow in the channel is about 42000. The computational domain is a rectangular box, with periodic boundary conditions in the spanwise (x) and streamwise directions (z) (see Fig. 1), while the y direction is normal to the walls. A monodisperse particle-laden fluid is introduced in the vertical direction z . The physical characteristics of the fluid are $\rho_f = 1.205 \text{ kg.m}^{-3}$, $\nu_f = 1.515 \times 10^{-5} \text{ m}^2.\text{s}^{-1}$. For the dispersed phase, two kinds of particle are studied: $d_p = 1.5 \text{ mm}$ and $\rho_p = 1032 \text{ kg.m}^{-3}$, or $d_p = 406 \text{ }\mu\text{m}$ and $\rho_p = 1038 \text{ kg.m}^{-3}$. These simulations are carried out for mean solid volume fractions $\langle \alpha_p \rangle$ varying between 10^{-3} and 10^{-2} . Low solid volume fractions and the large particle inertia make it possible to neglect the interactions between the fluid turbulence and the particles as well as the influence of the particles on the mean fluid flow. The Stokes number $St = \tau_p u_* / L_y$ for the present problem is about 200 and 2500 for smaller and

larger particles, respectively. Here, $\tau_p = \rho_p d_p^2 / 18\mu_f$ is the particle response time, u_* is the friction velocity and L_y is the channel width. According to the Stokes number values, it turns out that $St \gg 1$, then the particles are not affected by the turbulence of the fluid. The mean fluid velocity profile is determined from a preliminary single-phase $k - \epsilon$ computation (see Fig. 2) and fixed during all the simulations.

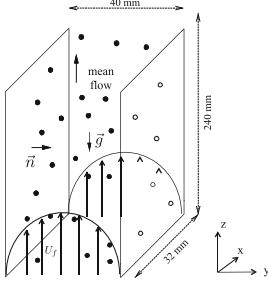


Fig. 1. Flow configuration.

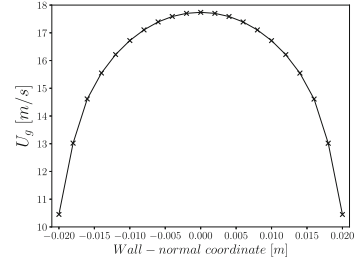


Fig. 2. Mean streamwise velocity.

2.2 Averaging of Physical Quantities

Thanks to the homogeneity of streamwise and spanwise directions, mean variables depend only on the wall-normal coordinate y . Therefore, the channel is divided into 40 slices for $d_p = 406 \mu\text{m}$, 15 slices for $d_p = 1.5 \text{ mm}$, parallel to the walls in y direction. Particles are associated with the slice in which their centres are located. The quantities are averaged spatially and temporally in each slices. The averaging operator will be written as $\langle \cdot \rangle$, $U_{p,i}$ and $u''_{p,i} = u_{p,i} - U_{p,i}$ indicate the mean velocity of the particles in the i -th direction and the velocity fluctuations, respectively. Second and third order moments are defined as following $\langle u''_{p,i} u''_{p,j} \rangle$ and $\langle u''_{p,i} u''_{p,j} u''_{p,m} \rangle$, respectively. For the sake of simplicity, the particle velocity components $(u_{p,1}, u_{p,2}, u_{p,3})$ will be written as (u, v, w) , the mean velocity components $(U_{p,1}, U_{p,2}, U_{p,3})$ will be noted as (U, V, W) , and the fluctuation components $(u''_{p,1}, u''_{p,2}, u''_{p,3})$ will be noted as (u'', v'', w'') . And $n_p = N_p/V_c$ is defined as the particle number density, computed in a slice of volume V_c containing N_p particles.

3 Particle Dynamics: Lagrangian Simulation

The Lagrangian solver for particle tracking runs in two successive steps. The first step takes into account the fluid and gravity effects, which make move the particles. Each particle is tracked in a Lagrangian fashion based on the DEM. The fluid entrains the particles, and their velocity is changed using a second-order explicit Runge-Kutta algorithm. Since, periodic boundary conditions for particles are considered in streamwise and spanwise directions, particles leaving the calculation domain will be relocated using the periodicity and rebound

conditions. For the fluid-particles interaction, the only drag is considered. The second step deals with the inter-particle and particle-wall collisions. To compute contact between solid bodies the soft-sphere model is employed. The solids are allowed to overlap with each other in a controlled manner. The collision is detected, when the distance between two particles and between a particle and a wall is less than the sum of their radii and the radius of the particle, respectively. The collision is computed in the mass-spring-dashpot system over a time step, that must be smaller than the time step for the fluid flow. In the soft-sphere model the choice of several numerical parameters is important to solve collisions properly. Particle rotation is not taken into account in our simulations. Each step will be detailed in the following sections.

3.1 The Equations of Motion

DEM simulations is the way to simulate particulate processes, tracking each particle and considering all particle-particle and particle-wall interactions. The motion of a single spherical particle p with mass m_p is deduced from Newton's second law

$$m_p \frac{d\mathbf{u}_p}{dt} = \mathbf{F}_{D,p} + \mathbf{F}_{G,p} + \mathbf{F}_{C,p} \text{ and } \frac{d\mathbf{x}_p}{dt} = \mathbf{u}_p \quad (1)$$

\mathbf{u}_p and \mathbf{x}_p are the particle velocity, and position, $\mathbf{F}_{D,p}$ is the drag force, $\mathbf{F}_{G,p}$ is the gravity force and $\mathbf{F}_{C,p}$ is the collision force exerted by the neighbouring solid bodies in contact. The total collision force $\mathbf{F}_{C,p}$ acting on a particle p is computed as the sum of all the forces exerted by the N_p particles and N_w walls in contact $\mathbf{F}_{C,p} = \sum_{b=1}^{N_p+N_w} \mathbf{f}_{q \rightarrow p}^{col}$. The drag force $\mathbf{F}_{D,p}$ acting on the particle p is written

$$\mathbf{F}_{D,p} = m_p \frac{\mathbf{u}_g - \mathbf{u}_p}{\tau_{gp}}, \quad \tau_{gp} = \frac{4}{3} \frac{\rho_p d_p}{\rho_g C_D |\mathbf{u}_g - \mathbf{u}_p|} \quad (2)$$

where C_D is the drag coefficient. According to the assumption, the only fluid-particle interaction force taken into account is the drag. The drag coefficient is based on the Schiller and Naumann correlation [12]. And the gravitational force is written as $\mathbf{F}_{G,p} = m_p \mathbf{g}$.

For each particle, the equation of motion Eq. 1 is solved at each time step. To integrate it properly, different characteristic times based on the different phenomena (gravity, drag) are defined. Therefore, several criteria must be verified on each particle to choose the smallest time step appropriated to the most limiting characteristic time. In dilute rapid particulate flow simulations, once the stationary state is reached, the limiting time step is that defined from collision parameters.

3.2 Collision Model

Particle-particle and particle-wall collisions are modeled using the soft-sphere approach [6] originally proposed by Cundall and Strack [5]. The particles are represented as a mass-spring-dashpot system (see Fig. 3). When the distance

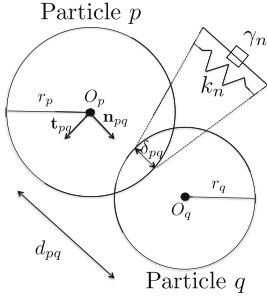


Fig. 3. Soft-sphere representation of two particles during collision.

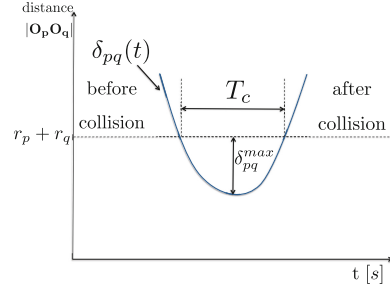


Fig. 4. Temporal evolution of the collision between two particles.

between particles p and q is less than the sum of their radii r_p and r_q , particle starts to collide and a collision force $\mathbf{f}_{q \rightarrow p}^{col}$ is generated. This force may be decomposed in normal and tangential components. $\mathbf{f}_{q \rightarrow p}^{col} = \mathbf{f}_{n,q \rightarrow p}^{col} + \mathbf{f}_{t,q \rightarrow p}^{col}$. The normal component is computed as

$$\mathbf{f}_{n,q \rightarrow p}^{col} = \begin{cases} -k_n \delta_{pq} \mathbf{n}_{pq} - 2\gamma_n M_{pq} \mathbf{u}_{pq,n}, & \text{if } \delta_{pq} > 0 \\ 0, & \text{else} \end{cases} \quad (3)$$

where k_n is the normal spring stiffness, \mathbf{n}_{pq} the normal unit vector, γ_n is the normal damping coefficient, and $\mathbf{u}_{pq,n}$ is the normal relative velocity. The term δ_{pq} is defined as the overlapping distance between two particles $\delta_{pq} = r_p + r_q - \|\mathbf{O}_p - \mathbf{O}_q\|$ and $M_{pq} = (\frac{1}{m_p} + \frac{1}{m_q})^{-1}$ is the effective mass of the $p - q$ binary system. The overlapping distance is considered only in the normal direction. The unit normal vector and the normal relative velocity between particles p and q are defined respectively as

$$\mathbf{n}_{pq} = \frac{\mathbf{x}_p - \mathbf{x}_q}{\|\mathbf{x}_p - \mathbf{x}_q\|}, \quad u_{pq,n} = ((\mathbf{u}_p - \mathbf{u}_q) \cdot \mathbf{n}_{pq}) \mathbf{n}_{pq} \quad (4)$$

where \mathbf{u}_p and \mathbf{u}_q are the p and q particle velocities, respectively. For the tangential component of the contact force a Coulomb-type friction law is retained $\mathbf{f}_{t,q \rightarrow p}^{col} = -\mu \|\mathbf{f}_{n,q \rightarrow p}^{col}\| \mathbf{t}_{pq}$ where μ is the dynamic friction coefficient.

3.3 Collision Parameters

The projection of the Eq. 1 on \mathbf{n}_{pq} gives the equation for δ_{pq} in the normal direction:

$$M_{pq} \ddot{\delta}_{pq} = -k_n \delta_{pq} - 2\gamma_n M_{pq} \dot{\delta}_{pq} \quad (5)$$

Equation 5 is the differential equation of the damped harmonic oscillator and its solution is

$$\delta_{pq}(t) = \frac{|u_{pq,n}^0|}{\sqrt{\omega_0^2 - \gamma_n^2}} \exp(-\gamma_n t) \sin(\sqrt{\omega_0^2 - \gamma_n^2} t) \quad (6)$$

with undamped angular frequency $\omega_0 = \sqrt{\frac{k_n}{M_{pq}}}$ and normal damping parameter $\gamma_n = \frac{-\ln e_n}{\sqrt{\pi^2 + \ln^2 e_n}} \omega_0$, where e_n is the normal restitution coefficient. It means that the overlap depends on the user-defined parameters k_n , e_n and the particle properties. The differentiation of Eq. 6 provides that $\dot{\delta}_{pq}(t = 0) = |u_{pq,n}^0|$. The contact during collision is solved over time and the duration of a contact can be determined as a time corresponding to the end of the collision $\delta_{pq}(t = T_c) = 0$ (see Fig. 4):

$$T_c = \frac{\pi}{\sqrt{\omega_0^2 - \gamma_n^2}} \quad (7)$$

Since, the particle phase is monodisperse, T_c has a unique value in the particulate system. The contact duration depends on ω_0 , γ_n , which depend on k_n , e_n and particle properties. It is essential to estimate the appropriate collision duration to perform simulations with appropriate particle time step.

3.4 Numerical Parameters

To ensure the numerical stability for the used numerical schemes and to treat the collision properly, the particle time step Δt_p must be small enough. For example, in the case of the hard-sphere model, according to [11], where the particle velocity after collision is defined analytically from the velocity before collision, the limiting condition is defined as $\Delta t_p < \theta d_p / \|\mathbf{u}_r\|$, with $\theta \approx 0.3$. The information needed to estimate this condition is the mean relative impact velocity $u_r = \|\mathbf{u}_r\|$, which can be estimated from the particles agitation $q_p^2 = 1/2(u'' + v'' + w'')$

$$u_r = \sqrt{\frac{8}{3\pi} q_p^2} \quad (8)$$

In our simulations based on the soft-sphere model, to estimate the time step, several conditions must be verified. First of all, Δt_p has to be smaller or equal than the fluid time step, which is estimated from the CFL condition for the fluid phase $CFL = \max_{i=1,3} |u_{f,i}| \Delta t_f / \Delta x_f$. To choose an appropriate value for Δt_p two conditions should be verified. The first condition $CFL_p = \Delta t_p \|\mathbf{u}_p\| / \Delta x_f$ for each particle is needed to ensure that a particle does not move more than few elements of the Eulerian mesh during a substep. The second condition is based on the fact that during a substep particles do not move more than $100 \cdot CFL_p^{col} \%$ of their diameter, where $CFL_p^{col} = \Delta t_p |u_{pq,n}^0| / d_p$. It means that this condition is necessary to control and limit the overlapping distance at the first impact. Another condition is that Δt_p must be inferior to the contact time T_c to limit the overlapping distance during the collisions and to reach a sufficient resolution for the time integration of the stiff collision term in Eq. 1 (see Fig. 4)

$$\Delta t_p < \frac{T_c}{N_c}. \quad (9)$$

N_c is the minimum number of steps during one contact. It is recommended in the literature to integrate a dry contact with Δt_p in the range $[T_c/50, T_c/15]$ [2], and following [8] in the gas-particles flow N_c should be greater than $N_c > 5$.

As discussed above, T_c depends on some parameters like k_n , e_n and particle properties. Then to predict the collision duration T_c , the appropriate value for k_n must be chosen for a given particle. Frequently used practice is to predict the appropriate value for k_n from the maximum value for the overlapping distance. The maximum overlap δ_{pq}^{max} is obtained from $\delta(t) = 0$

$$\frac{\delta_{pq}^{max}}{d_p} = \frac{|u_{pq,n}^0|}{\omega_0 d_p} \exp\left(-\frac{\gamma_n}{\sqrt{\omega_0^2 - \gamma_n^2}} \arcsin \frac{\sqrt{\omega_0^2 - \gamma_n^2}}{\omega_0}\right) \quad (10)$$

By using an estimate for the value of $u_{pq,n}^0$ and fixing the maximum overlap δ_{pq}^{max} , k_n can be obtained from Eq. 10. The only drawback of this approach is the lack of information concerning $u_{pq,n}^0$ before performing the simulations. In some references, it is recommended that the maximum overlapping δ_{pq}^{max} is less than 10% of the particle diameter [4], other references propose instead to keep its value less than 1% [8]. The resulting high value of k_n leads to a small particle time step, which is very limiting for the numerical simulation. The point is how should be evaluated the stiffness coefficient to have less constrained particle time step without significantly affecting the flow dynamics. It will be discussed in the next section.

4 Simulation Results and Discussions

DEM simulations of the vertical channel flow are here presented. They are used to study the influence of the particle properties on the velocity statistics and to evaluate the soft-sphere approach in rapid particulate flow. Numerical test cases and main parameters are presented in the Table 1. The value of relative velocity u_r for all cases is obtained from q_p^2 using Eq. 8.

Table 1. Numerical test cases.

Case	d_p	$\langle\alpha_p\rangle$	N_p	δ_{pq}^{max}/d_p	k_n	Δt_p	Δt_f	N_c	CFL_p	CFL_p^{col}	u_r
B	406 μm	1.2×10^{-3}	10520	0.05	3000 N/m	10^{-6} s	10^{-5} s	10	1.5	0.01	1.05 m/s
C	406 μm	4×10^{-3}	35067	0.05	3000 N/m	10^{-6} s	10^{-5} s	10	1.5	0.3	0.87 m/s
D	406 μm	1×10^{-2}	87668	0.05	3000 N/m	10^{-6} s	10^{-5} s	10	1.5	0.3	0.79 m/s
E	1.5 μm	4.1×10^{-3}	712	0.03	5000 N/m	4×10^{-5} s	2.5×10^{-5} s	10	1.5	0.01	0.61 m/s
F	1.5 mm	1.4×10^{-2}	2433	0.03	5000 N/m	4×10^{-5} s	2.5×10^{-5} s	10	1.5	0.3	0.56 m/s
G	1.5 mm	4.1×10^{-2}	7127	0.03	5000 N/m	4×10^{-5} s	2.5×10^{-5} s	10	1.5	0.3	0.53 m/s

Results for the mean particle streamwise velocity are shown by Fig. 5 (left panel). The fluid velocity is frozen and is the same for all studied cases (see Fig. 2). The left and middle panels of Fig. 5 correspond to the elastic frictionless cases for the inter-particle ($e_c = 1, \mu_c = 0$) and the particle-wall ($e_w = 1, \mu_w = 0$) collisions. Results show that, for all the cases, the mean particle velocity profile is flatter than that of the fluid (Fig. 2); this is due to the strong influence of transverse particle dispersion. Results also show that the mean particle velocity

is mostly dependent on the particle diameter, which in turn shows the strong influence of the drag. The mean particle number density demonstrates (see the middle panel of Fig. 5) that near-wall geometrical effects have a strong influence on the collisional characteristics and lead to an overcrowding of the particles, creating a mean force towards the wall [7, 9, 10]. Smaller particles ($d_p = 406 \mu\text{m}$) are more transported by the fluid than larger particles ($d_p = 1.5 \text{ mm}$) at the center of the channel. Larger particles are instead more concentrated at the near wall region than the small ones. The numerical simulations results based on the soft-sphere model are in excellent agreement with hard-sphere model simulations for both mean streamwise velocity and mean particle number density (see the left and middle panel of Fig. 5). Kinetic stress components (second-order particle velocity correlations) for the case $\langle \alpha_p \rangle = 1 \times 10^{-2}$ are presented by Fig. 5 (right panel) for two different set of particles-wall collision parameters ($e_w = 1, \mu_w = 0$ and $e_w = 0.94, \mu_w = 0.325$). The difference between the elastic frictionless case and the inelastic case with friction shows the strong sensitivity of the system to the boundary conditions for particles. Inelastic restitution $e_w < 1$ induces dissipation at the wall. When $\mu_w > 0$, it causes a friction effect at the wall characterized by a non-zero value of the shear stress $\langle u''v'' \rangle$. The friction effect involves a production of the vertical variance $\langle u''u'' \rangle$ by the velocity gradient term and, by collisional redistribution, an increase in $\langle v''v'' \rangle$ and $\langle w''w'' \rangle$. In the inelastic case with friction our results also fully agree with the simulations based on the hard-sphere model [10].

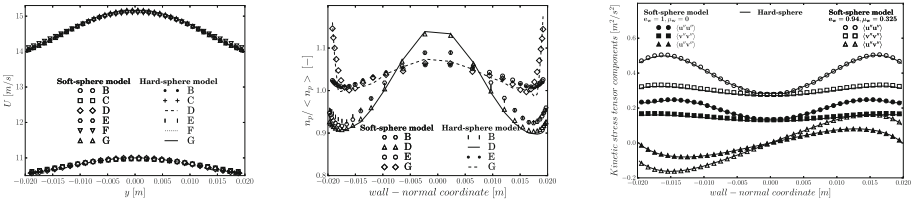


Fig. 5. Comparison between numerical simulations based on the soft-sphere and the hard-sphere model. Left: mean streamwise velocity, middle: mean particle number density, right: kinetic stress tensor components for the case D.

The stiffness coefficient sensitivity analysis is realized to evaluate the accuracy of the soft-sphere model. In order to ensure this, first, Eq. 10 can be bounded from above using $e_c \leq 1$ or $e_w \leq 1$

$$\frac{\delta_{pq}^{max}}{d_p} \leq \frac{|u_{pq,n}^0|}{d_p} \sqrt{\frac{M_{pq}}{k_n}} \leq \lambda, \quad 0 < \lambda \leq 0.01 \quad (11)$$

for the highest value of k_n . On the other hand, $|u_{pq,n}^0| \approx k \cdot u_r$ for $k \leq 2$. Then, Eq. 11 will be rewritten like

$$\frac{\delta_{pq}^{max}}{d_p} \leq \frac{u_r}{d_p} \sqrt{\frac{M_{pq}}{k_n}} \leq \frac{\lambda}{k}, \quad 0 < \lambda \leq 0.01 \quad (12)$$

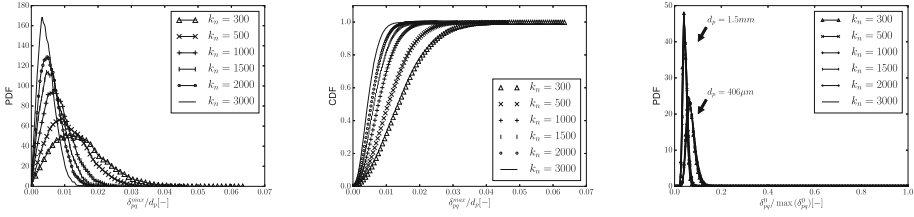


Fig. 6. Comparison for the different values of the stiffness coefficient. Left: probability density function (PDF) of the dimensionless maximum overlapping distance ($d_p = 406 \mu\text{m}$), middle: cumulative distribution function (CDF) of the dimensionless maximum overlapping distance ($d_p = 406 \mu\text{m}$), right: PDF of the first overlap weighted by $\max(\delta_{pq}^0)$

As shown by Fig. 6 (left panel), the maximum value of the overlap is strongly dependent on k_n (see Eq. 10). The higher k_n , the lower the mean value of δ_{pq}^{max}/d_p will be. But it is relevant to notice that even when k_n is low ($k_n = 300$), the percentage of the collisions which have the high overlapping is very small, as shown by cumulative distribution function (see the middle panel of Fig. 6). And its mean value corresponds more to the small overlapping. The high values of δ_{pq}^{max}/d_p occurring rarely do not affect the whole dynamics of the gas-particles flow as demonstrated by Fig. 7 for different quantities. This observation provides to weaken the conditions on δ_{pq}^{max}/d_p (Eq. 11).

Moreover, from Fig. 6 (right panel), it is observed that the first distance of the overlap δ_{pq}^0 does not depend on the stiffness coefficient value for different particle diameters, the first impact relative velocity u_r does not as well. This fact allows to identify the dimensionless parameter $\kappa_n = \frac{u_r}{d_p} \sqrt{\frac{M_{pq}}{k_n}}$ depending on u_r and to estimate the mean overlapping distance as

$$\frac{\delta_{pq}^{mean}}{d_p} \leq \kappa_n \leq \lambda^* \tag{13}$$

where λ^* takes values between (0, 0.05) less constraining for Δt_p . The dimensionless parameter κ_n provides the estimation of the mean overlapping knowing the value of the mean particles agitation and k_n for a given particle.

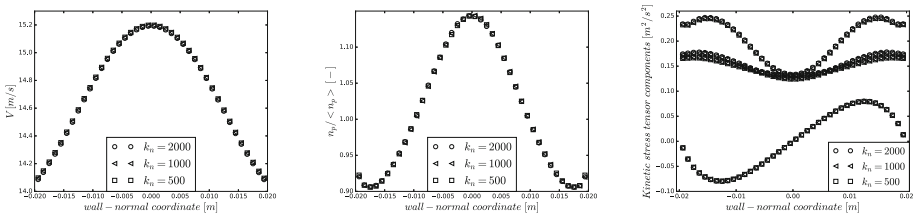


Fig. 7. Simulation results based on the soft-sphere model for different stiffness coefficients for the case D. Left: mean streamwise velocity, middle: mean particle number density, right: kinetic stress tensor components

5 Conclusion

Soft-sphere DEM simulations have been performed and numerical results analyzed for a vertical gas-particles channel flow. Simulations have been performed neglecting the influence of the fluid turbulence on the particle fluctuating motion and the modification of the fluid flow by the particles. Two types of particles have been studied, for various mean volume fractions. Results based on two approaches, the soft-sphere and the hard-sphere models, have been compared and validated quantitatively and qualitatively for different physical variables. Thereafter, a sensitivity analysis about the soft-sphere model parameters has been carried out to gain insight in the choice of the optimal ones to properly treat the solid-solid collision. It was found that a less restrictive model for the maximum overlapping distance can be defined as a function of the mean value of the impact variables without influencing the flow behaviour.

Acknowledgement. This work received funding from Agence nationale de la recherche (ANR) through the project MORE4LESS. It was granted access to the HPC resources of CINES supercomputing center under the allocations A0012B07345 and A0062B10864. CINES is gratefully acknowledged.

References

1. Berlemont, A., Simonin, O., Sommerfeld, M.: Validation of inter-particle collision models based on large eddy simulation. *ASME-PUBLICATIONS-FED* **228**, 359–370 (1995)
2. Bernard, M., Climent, E., Wachs, A.: Controlling the quality of two-way Euler/Lagrange numerical modeling of bubbling and spouted fluidized beds dynamics. *Ind. Eng. Chem. Res.* **56**, 368–386 (2016)
3. Campbell, C., Brennen, C.: Computer simulation of shear flows of granular material. *Stud. Appl. Mech.* **7**, 313–326 (1983)
4. Capecelatro, J., Desjardins, O.: An Euler-Lagrange strategy for simulating particle-laden flows. *J. Comput. Phys.* **238**, 1–31 (2013)
5. Cundall, P., Strack, O.: A discrete numerical model for granular assemblies. *Geotechnique* **29**, 47–65 (1979)
6. Dufresne, Y., Moureau, V., Masi, E., Simonin, O., Horwitz, J.: Simulation of a reactive fluidized bed reactor using CFD/DEM (Center for Turbulence Research Proceedings of the Summer Program) (2016)
7. Fede, P., Simonin, O.: Direct simulation Monte-Carlo predictions of coarse elastic particle statistics in fully developed turbulent channel flows: comparison with deterministic discrete particle simulation results and moment closure assumptions. *Int. J. Multiphase Flow* **108**, 25–41 (2018)
8. van der Hoef, M.A., Ye, M., van Sint Annaland, M., Andrews, A.T., Sundaresan, S., Kuipers, J.A.: Multiscale modeling of gas-fluidized beds. *Adv. Chem. Eng.* **31**, 65–149 (2006)
9. Sakiz, M., Simonin, O.: Continuum modelling and Lagrangian simulation of the turbulent transport of particle kinetic stresses in a vertical gas-solid channel flow. In: 3rd International Conference on Multiphase Flows, Lyon, France (1998)

10. Sakiz, M., Simonin, O.: Development and validation of continuum particle wall boundary conditions using Lagrangian simulation of a vertical gas-solid channel flow. ASME-PUBLICATIONS-FED **99** (1999)
11. Sakiz, M.: Simulation numérique Lagrangienne et modélisation eulérienne d'écoulements diphasiques gaz-particules en canal vertical. Ph.D. thesis, Marne-la-vallée, ENPC (1999)
12. Schiller, L., Naumann, A.: A drag coefficient correlation. Vdi Zeitung **77** (1935)
13. Sommerfeld, M.: Analysis of collision effects for turbulent gas-particle flow in a horizontal channel: part I. Particle transport. Int. J. Multiphase Flow **29**, 675–699 (2003)
14. Tanaka, T., Tsuji, Y.: Numerical simulation of gas solid two-phase flow in a vertical pipe on the effect of inter particle collision (1991)
15. Vreman, A.: Turbulence characteristics of particle-laden pipe flow. J. Fluid Mech. **584**, 235 (2007)



Rod-Bundle Thermalhydraulics Mixing Phenomena: 3D Analysis with Cathare-3 of ROSA-2/LSTF Experiment

Raphaël Préa^(✉) and Anouar Mekkas

CEA - Commissariat à l'Énergie Atomique et aux Énergies Alternatives,
DEN/DM2S/STMF - Service de Thermohydraulique et de Mécanique des Fluides,
Université Paris-Saclay, 91191 Gif-sur-Yvette, France
{raphael.prea,anouar.mekkas}@cea.fr

Abstract. CATHARE-3 is the new version of the French Thermal-hydraulic code for the safety analysis of nuclear reactors, its 3D module is mainly used to model the reactor vessel with a “porous” medium approach of two-fluid six equations model. Therefore, the balance equations are established using a double-averaged method: first, a time-average, and then, space-average. Optional terms can be added in momentum and energy balance equations to model turbulent diffusion and dispersion effects. These terms have an impact on core simulations at sub-channel scale. So, the CATHARE team have established models for these terms in rod bundle geometry and had validated them on various experiments. The presented simulations are a 3D modeling of the core of the ROSA-2/LSTF experiment using CATHARE-3 3-D module with a radial nodalization of one mesh per rod. A phase of core uncovering during which the rod temperatures in the dry zone increase is observed in an experimental test and experimental evolutions of rods and gas temperatures are compared with CATHARE-3 calculations with and without the turbulent terms.

Keywords: CATHARE-3 · Two-phase flow · Core-mixing · ROSA-2/LSTF

1 Introduction

First, in Sect. 2, this article presents the CATHARE-3 code and its 3-D Module, with its basic set of equations and its turbulence modeling. Then, in Sect. 3, an experimental test (ROSA-2 Test 3) made on the Large Scale Test Facility (LSTF) and its 3D modeling with the CATHARE-3 code are described. In the Sect. 4, CATHARE-3 calculations of LSTF core are analyzed and compared with the experimental evolutions.

2 The CATHARE Code and its 3D Module

CATHARE-3 is the new version of the French Thermal-hydraulic code for safety analysis of Pressurized Water Reactor (PWR) [8]. Its development has begun in 2006 as part of the NEPTUNE project launched by the CEA, EDF, FRAM-ATOME and IRSN in 2001 [9], in the continuity of the reference multi-concept CATHARE-2 [2]. The 3-D Module of CATHARE-2 has been validated to model both the whole reactor Pressure Vessel (PV) and some subcomponents like the core or the downcomer from the Small to Large Break (SB to LB) Loss-Of-Coolant-Accidents (LOCA) with a coarse meshing of about 1000 meshes for the whole PV. The 3D modeling abilities of CATHARE-3 have been improved compared to CATHARE-2 with:

- New numerical methods, which allow simulations with large number of 3D-cells,
- Non-conformal Multi-3D Modules modeling of the vessel (see [12]),
- Optional closure laws, modelling turbulence for sub-channel analysis,

The 3-D Module of CATHARE is based on a ‘‘porous’’ version of the two-fluid 6-equation model. To obtain this model, the local instantaneous two-phase balance equations are double-averaged: first time-averaged to filter the pseudo-aleatory variations of the flow variables due to turbulence and two-phase intermittence, and then space-averaged to account for the interactions of the flow with the internal solid structures. Thus, the complex and relatively small structures such as rod bundles, grids, guide tubes, are managed via a porous medium approach. The mass, momentum (one in each direction) and energy balance equations (Eq. 1 to 3) are written for each phase k (liquid or gas):

$$\phi \frac{\partial(\alpha_k \rho_k)}{\partial t} + \nabla \cdot (\phi \alpha_k \rho_k \mathbf{V}_k) = (-1)^k \phi \Gamma \quad (1)$$

$$\alpha_k \rho_k \left(\frac{\partial \mathbf{V}_k}{\partial t} + \mathbf{V}_k \cdot \nabla \mathbf{V}_k \right) + \alpha_k \nabla P = -(p_i + p_i^T) \nabla \alpha_k - (-1)^k \tau_i - \tau_{wk} \\ + \alpha_k \rho_k \mathbf{g} + \frac{1}{\phi} \nabla \cdot (\alpha_k \rho_k \mathbf{t}_k^T) \quad (2)$$

$$\phi \frac{\partial(\alpha_k \rho_k e_k)}{\partial t} + \nabla \cdot (\phi \alpha_k \rho_k e_k \mathbf{V}_k) = -P \left[\phi \frac{\partial \alpha_k}{\partial t} + \nabla \cdot (\phi \alpha_k \mathbf{V}_k) \right] + \phi q_{ke} \\ + \phi (-1)^k \Gamma H_k + S_c q_{wk} + \nabla \cdot (\alpha_k \rho_k \mathbf{q}_k^T) \quad (3)$$

In these equations, the main variables are the enthalpy H_k ; the volumic fraction α_k (with $\alpha_L + \alpha_G = 1$); the pressure P and the velocity \mathbf{V}_k . The density ρ_k is determined with an equation of state: $\rho_k = f(P, H_k)$ and the internal energy e_k is calculated with the enthalpy ($e_k = f(P, H_k)$). The porosity ϕ and the heating surface S_c are set by the user. The closure terms are the interfacial pressure p_i ; the interfacial friction τ_i ; the wall friction τ_{wk} with the phase k ; the interfacial heat transfers q_{ke} of the phase k with the interface; the wall heat flux q_{wk} to the phase k and Γ is the interfacial mass transfer: $\Gamma = (S_c q_{wi} - q_{ge} - q_{le}) / (H_G - H_L)$ with q_{wi} the wall-to-interface heat flux. The turbulent

dispersion of void p_i^T , the turbulent diffusion and dispersion of momentum \mathbf{t}_k^T and the turbulent diffusion and dispersion of energy \mathbf{q}_k^T are optional closure terms, they came out during the double (time and space) averaging process of the local convection terms:

$$\mathbf{t}_k^T = (\nu_{tk}^\phi + \nu_{dk}^\phi) \left[\nabla(\phi \mathbf{V}_k) + \nabla^T(\phi \mathbf{V}_k) - \frac{2}{3} \nabla(\phi \mathbf{V}_k) \mathbf{I} \right] \quad (4)$$

$$\mathbf{q}_k^T = (\alpha_{tk}^\phi \mathbf{I} + \mathbf{D}_{dk}^\phi) \phi \nabla e_k \quad (5)$$

In CATHARE-3, these two terms are modeled with algebraic models and no additional equation is solved. Two global coefficients are used in the code, modeling both turbulent diffusion and dispersion (or neglecting one of the two effects): the total macroscopic turbulent viscosity ($\nu_T^\phi = \nu_{tk}^\phi + \nu_{dk}^\phi$) and the thermal dispersive tensor component ($\mathbf{D}_T^\phi = \alpha_{tk}^\phi \mathbf{I} + \mathbf{D}_{dk}^\phi$).

A model for the spatial average of the turbulent kinetic energy $\langle k \rangle_f$ in a single phase flow in tubes or rod-bundle has been established [6]:

$$\langle k \rangle_f = c_p \mathbf{V}_k^2 Re^{-1/6} \quad (6)$$

With c_p a constant equal to 0.0367; \mathbf{V}_k the flow velocity and Re the Reynolds number based on the hydraulic diameter (D_H - set by the user): $Re = (\rho \mathbf{V} D_H) / \mu$.

Thus, correlations have been developed, fitted on experimental data [7, 13]:

$$\nu_T^\phi = A D_H \sqrt{\langle k \rangle_f} \quad (7)$$

$$\mathbf{D}_T^\phi = \frac{\nu_T^\phi}{Pr_T} = \frac{A D_H \sqrt{\langle k \rangle_f}}{Pr_T} \quad (8)$$

$$p_i^T = B \rho_L \mathbf{V}_L \sqrt{\langle k \rangle_f} \quad (9)$$

With $A = 0.5$, $B = 0.2$ and the macroscopic turbulent Prandtl number $Pr_T = 1$.

The turbulent diffusion and dispersion of momentum has been validated with the liquid adiabatic single phase tests on GRAZIELLA loop and the AGATE test section with partial grids. The turbulent diffusion and dispersion of energy has been validated with the PSBT Benchmark and the heated single phase (liquid) tests in the OMEGA-2 and GRAZIELLA loops. The void fraction dispersion has been validated with the PSBT Benchmark and the boiling tests on GRAZIELLA test section. It has to be emphasized that the momentum diffusive flux remains negligible in front of turbulent diffusion and dispersion of energy as long as the gradient of the mean velocity are small, which is often the case inside the core. The main conclusion which can be draw from this validation is that the calibration of the present simple algebraic models clearly depends on the type of grids (mixing vane or simple spacer) and on the distance between grids¹ [7].

¹ GRAZIELLA and OMEGA-2 test sections do not include mixing vane on spacer grids. On heated tests, A constant of the turbulent diffusion and dispersion of energy model (Eq. 8) must be divided by a factor 30 to obtain the right temperature gradients.

It must be noted that the current validation do not cover the single phase gas flow.

3 LSTF and the ROSA-2 Test 3

The OECD/NEA ROSA-2 Project [11] was performed to resolve key safety issues of PWR Thermal-hydraulics by means of LSTF experiments at the Japan Atomic Energy Agency (JAEA). LSTF is a full-pressure and full-height integral test facility using a full-height core (3.66m of heating length) composed of more than 1000 simulated fuel rods with 10 MW electrical power. The rods are regrouped in 24 assemblies and the radial power profile is divided in 3 zones (high, mean and low) with radial peaking factor of 1.51. Test 3 is a Hot-Leg SB-LOCA transient during which the primary circuit empties through the break and the core start to boiling (Fig. 1 - left). Then, a phase of core unrecovery is observed during about 250 seconds at a pressure around 7MPa. Liquid level drop down to half height in the core by boil-off and a core temperature excursion took place (Fig. 1 - center). As explained in [3]; because of the non-homogeneous radial power profile in the core, cross-flows are expected in the dry zone (Fig. 1 - right) with a ‘‘chimney effect’’ (steam cross-flows from the low power assemblies to the hot ones). These cross-flows have an impact on the maximum cladding temperature and may be influenced by turbulent effects (core spacers with mixing vanes, ...).

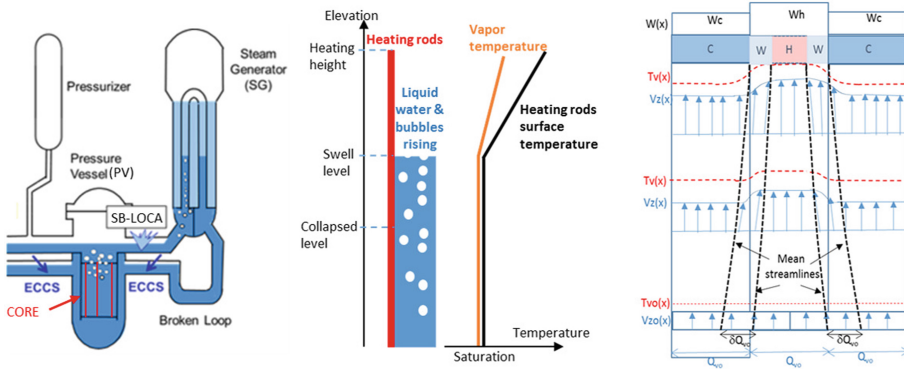


Fig. 1. Schemes of the ROSA-2/LSTF Test 3 transient phenomena with the system scale at the left [11]; the core scale at the center and the rod bundle scale in the dry zone at the right [3]

Experimental data package provide heating rods cladding temperature (localized at the center of the assemblies) and gas temperature (localized at the corner of the assemblies on non-heating rods) for 4 elevations of the dry zone. The observed maximum rod cladding temperature was about 500 °C.

The CATHARE-3 3D modeling of the LSTF core with a radial nodalization of one mesh per rod (and 48 axial meshes) is presented Fig. 2, only a quart (in a

radial plan) of the core is modeled. Indeed, the geometry and the radial power profile are symmetrical by quart (more exactly, by 1/8) and we have performed verification of the symmetrical behavior of the temperatures experimental evolutions when it was possible. At the top of the core, the imposed outlet condition is the evolution of the experimental pressure. At the bottom, an incoming liquid flow at saturation is imposed as limit condition and the flow rate is regulated during the simulation in order to have the experimental position of the collapsed level (obtained by ΔP measurements). Thermal structures (heating rod, non-heating rod, core barrel) are modeled and power is injected in the heating rods, following the power experimental evolution.

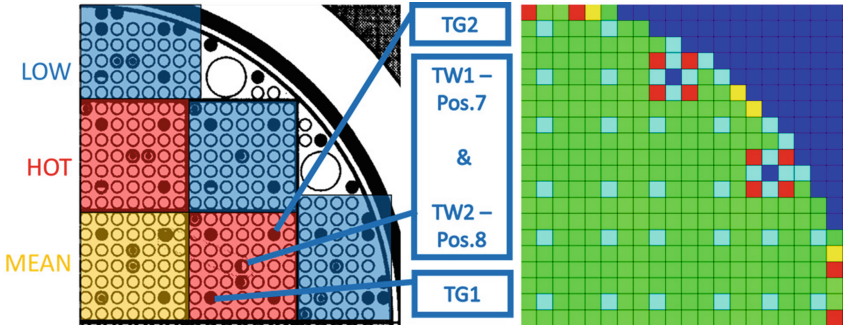


Fig. 2. Left, a scheme of the experimental core with the power level of each assemblies and the position of some experimental measurements, and right, the radial nodalization used in CATHARE-3 calculations with the porosity field

From the experimental evolutions of the cladding temperature, we can say that axial position of the swell level is the same for the all the core, even with the radial peaking factor. The wetted zone is thus characterized by a perfect or quasi-perfect radial mixing with cross-flows and there should be a uniform axial steam flux at the exit of the swell level all over the core. These experimental observations and deductions have also been observed on PERICLES-2D experiment [10] and are well predicted by CATHARE-3. As the main focus is the analysis of the dry zone, an adjustment on the interfacial friction τ_i has been made in the goal to have the correct start of the temperature rise in the calculations. Indeed, in the standard calculation, there is a little shift on the swell level².

4 Comparison Between CATHARE and LSTF

CATHARE-3 calculations have been done with and without the turbulent models (the turbulent diffusion and dispersion of momentum t_k^T and the turbulent

² Of about 15 seconds on the instant of start of increase which is equivalent to 10 cm on the swell level - this is lower than the experimental uncertainty of the collapsed level.

diffusion and dispersion of energy q_k^T , the turbulent dispersion of void p_i^T was not used). Figure 3 shows the radial field of gaz temperature in the dry zone without (left) and with (right) the turbulent models. The two calculations provides results quite similar, one can see some mixing layers at the border between the cold and the hot assemblies. Moreover, the cold steam from cold assemblies moves to hot assemblies: the expected “chimney effect” is observed in the calculations. Diffusion terms impact the radial transfers, indeed, there are smoothly radial profile for the steam temperature in the calculation with turbulent models. Moreover, in the channels without heating rod, radial transfers increase with turbulent models and the temperature is more homogeneous. One more information can be drawn from the radial field: the maximum temperature is not localized at the exact center of the hot assembly but there is a little offset due to the “chimney effect”.

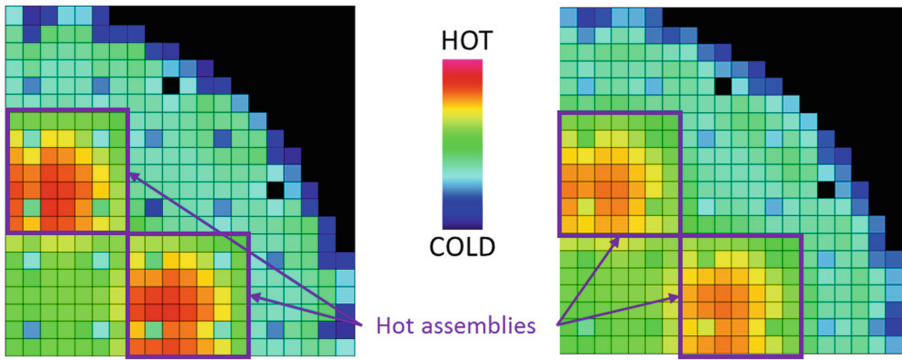


Fig. 3. Radial field of steam temperature in the dry zone without (left) and with (right) the turbulent models

The Fig. 4 shows comparison between experimental evolutions of the temperature and the temperature resulting from the CATHARE-3 calculations. The observed differences on experimental steam evolutions between TG1 (localized next to hot and mean assemblies - see Fig. 3) and TG2 (localized next to two cold assemblies - see Fig. 3) are due to the “chimney effect”. Indeed, TG2 position (or thermocouple) receive more cold steam than TG1 one. So, this is a direct experimental proof of this effect. In calculation, effect is more visible with diffusion terms but differences remains with the experimental evolutions. Concerning the maximum cladding temperature, the turbulent models have a very low impact and both CATHARE-3 calculations are quite good. But this is no experimental evolution of the steam temperature in the central part of the hot assembly which can be used to validate with precision the CATHARE-3 wall-to-steam heat flux correlation.

It must be noticed that the current turbulent models are not validated in single phase steam flow and this work is one of the first evaluation with

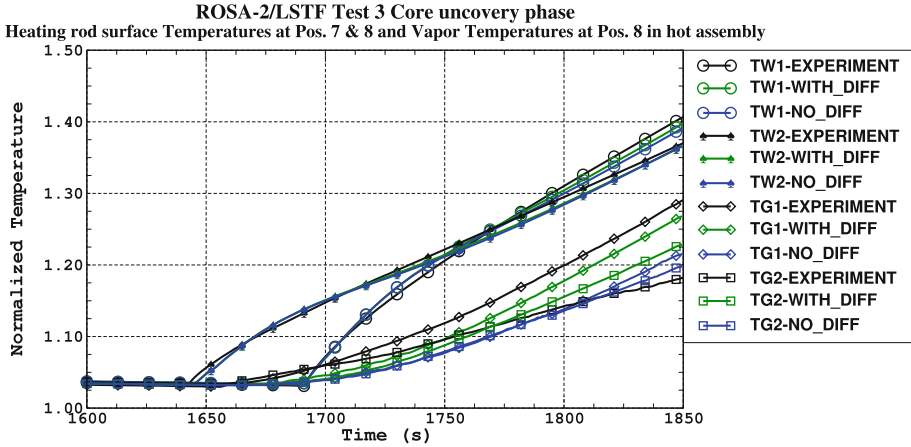


Fig. 4. The evolution of the temperature in the dry zone with the experimental curves (in black) and the results of CATHARE-3 calculations with (in blue) and without (in green) the turbulent models. The cladding temperature is drawn at two elevation in the core (position 7 with the circles and position 8 with the spades), localized at the center of the hot assembly. The steam temperature is drawn for two position at the elevation 7 of the hot assembly (TG1 with the diamonds and TG2 with the squares) - see Fig. 3 for the exact localization.

experimental comparisons of these models in such conditions. The experimental data on LSTF is not sufficient enough to calibrate and validate these models.

5 Conclusions

It has been shown that turbulent effects impact the radial transfers in the dry zone of the core and they have to be modeled in sub-channel analysis. But, improvements are needed for the turbulence models of CATHARE-3. So, the work on these models will be continued, with several way:

- Other rod-bundle experiments can be used, sub-channel calculations with turbulent models on PERICLES-2D experiment [10] have already been done with CATHARE-3 but without comparison with the experimental data [1],
- CFD simulations of turbulent non-axial flow in rod bundle [5] can also be used for model development with upscaling process,
- The experimental program METERO [4], which will be made in CEA, will provide information for the development and validation of turbulent diffusion and dispersion terms. METERO test section is two half PWR assemblies,

This modeling also shows the capabilities of CATHARE-3 to manage a large number of 3D-cells (about 15 000 useful) and to perform simulations comparable to the simulation of a whole PWR assembly at the subchannel scale.

References

1. Alku, T.: Modeling of turbulent effects in LOCA conditions with CATHARE-3. *Nucl. Eng. Des.* **321**, 258–265 (2017). <https://doi.org/10.1016/j.nucengdes.2016.10.050>
2. Antoni O., Geffraye G., Kadri D., Lavielle G., Rameau B., Ruby A.: CATHARE 2 V2.5.2: a single version for multi-applications. In: *Proceedings of 13th International Topical Meeting on Nuclear Reactor Thermal Hydraulics (NURETH-13)*, Kanazawa City, Japan (2009)
3. Bestion, D., Fillion, P., Gaillard, P., Valette, M.: 3D core thermalhydraulics phenomena in PWR SB-LOCAs and IB-LOCAs. In: *Proceedings of 17th International Topical Meeting on Nuclear Reactor Thermal Hydraulics (NURETH-17)*, Xi'an, China (2017)
4. Bestion, D., Fillion, P., Pr ea, R., Bernard-Michel, G.: Improved PWR LOCA simulations through refined core 3D simulations - an advanced 3D modelling and the associated METERO validation program. In: *Proceedings of 12th International Topical Meeting on Nuclear Reactor Thermal-Hydraulics, Operation and Safety (NUTHOS-12)*, Qingdao, China (2018)
5. Bieder, U., Scoliege, A., Feng, Q.: Turbulent non-axial flow in rod bundle. In: *Turbulence and Interaction 2015 - Notes on Numerical Fluid Mechanics and Multidisciplinary Design*, vol. 135, pp. 89–100 (2018). https://doi.org/10.1007/978-3-319-60387-2_8
6. Chandesris, M., Serre, G., Sagaut, P.: A macroscopic turbulence model for flow in porous media suited for channel, pipe and rod bundle flows. *Int. J. Heat Mass Transf.* **49**, 2739–2750 (2006). <https://doi.org/10.1016/j.ijheatmasstransfer.2005.12.013>
7. Chandesris, M., Mazoyer, M., Serre, G., Valette, M.: Rod bundle thermalhydraulics mixing phenomena: 3D analysis with CATHARE-3 of various experiments. In: *Proceedings of 13 th International Topical Meeting on Nuclear Reactor Thermal Hydraulics (NURETH-15)*, Pisa, Italy (2013)
8. Emonot, P., Souyri, A., Gandrille, J.L., Barr e, F.: CATHARE-3: a new system code for thermal-hydraulics in the context of the NEPTUNE project. *Nucl. Eng. Des.* **241**, 4476–4481 (2011). <https://doi.org/10.1016/j.nucengdes.2011.04.049>
9. Guelfi, A., Bestion, D., Boucker, M., Boudier, P., Fillion, P., Grandotto, M., Herard, J.M., Hervieu, E., Peturaud, P.: NEPTUNE: a new software platform for advanced reactor thermal hydraulics. *Nuclear Sci. Eng.* **156**, 281–324 (2007). <https://doi.org/10.13182/NSE05-98>
10. Morel, C., Bestion, D.: Validation of the CATHARE code against PERICLES 2D BOIL-UP tests. In: *Proceedings of 9th International Topical Meeting on Nuclear Reactor Thermal Hydraulics (NURETH-9)*, San Francisco, USA (1999)
11. OECD/NEA: Final Integration Report of the Rig-of-Safety Assessment (ROSA-2) Project (2009-2012), NEA/CSNI/R(2016)10 (2017). <https://www.oecd-nea.org/nsd/docs/2016/csni-r2016-10.pdf>
12. Pr ea, R., Figerou, V., Mekkas, A., Ruby, A.: CATHARE-3: a first computation of a 3-inch break loss-of-coolant accident using both Cartesian and cylindrical 3D meshes modelling of a PWR vessel. In: *Proceedings of 17 th International Topical Meeting on Nuclear Reactor Thermal Hydraulics (NURETH-17)*, Xi'an, China (2017). <https://hal-cea.archives-ouvertes.fr/cea-02434036>
13. Valette, M.: Analysis of Subchannel and Rod Bundle PSBT experiments with CATHARE-3. *Sci. Technol. Nuclear Installat.* **2012**, Article ID 123426 (2012). <https://doi.org/10.1155/2012/123426>



Sensitivity of Approximate Deconvolution Model Parameters in *a Posteriori* LES of Interfacial Turbulence

Mahdi Saeedipour¹(✉), Stéphane Vincent², and Stefan Pirker¹

¹ Department of Particulate Flow Modelling, Johannes Kepler University, 4040 Linz, Austria

{mahdi.saeedipour, stefan.pirker}@jku.at

² Laboratoire de Modélisation et Simulation Multi Echelle UMR CNRS 8208, Université Gustave Eiffel, 77454 Marne-La-Valle, France
stephane.vincent@univ-eiffel.fr

Abstract. The current state of the art of large eddy simulation of immiscible two-phase flows suffers from the lack of appropriate closure models for subgrid scale (SGS) contributions of interfacial physics. In this study, we extend the Approximate Deconvolution Model [1] to the two-phase LES with volume of fluid method (ADM-VOF) to account for all the SGS terms appearing in spatially-filtered governing equations of incompressible interfacial flows. Following the central concept of the ADM, the subgrid surface tension force and interfacial transport terms as well as the subgrid stress tensor are reconstructed by approximating the inverse of filter operation. Accordingly, the filtered Navier-Stokes equations as well as the filtered VOF equation are closed and solved using the two-phase finite volume solver in OpenFOAM. In our recent investigation [2], the ADM-VOF formulation is developed into details, and employed for an *a posteriori* LES on the phase inversion benchmark problem. In the present study, the sensitivity of the simulation results to the ADM parameters such as size and type of filter kernels as well as the approximation order of the inverse filter are investigated. The results clearly reveal the potentials of the structural approach of ADM-VOF for large eddy simulation of interfacial turbulence where functional SGS closures are almost impractical.

Keywords: Large eddy simulation · ADM-VOF · Structural subgrid model · Explicit filter

1 Introduction

Large eddy simulation of two-phase interfacial flows is still complicated due to the lack of a general conclusion on subgrid scale closure models. There are two basic families for modelling SGS terms in the filtered governing equations: functional and structural models [3]. The former are originally developed for

single-phase LES and rely on the turbulent energy cascade theory which might not be applicable in the context of multiphase flows. This makes the latter a crucial alternative for modelling the SGS terms with more physical complexities. Indeed, the structural models have a mathematical nature and can be established with no prior knowledge of the physics of the interactions between the resolved and subgrid scales. A well-known type of structural models is Approximate Deconvolution Model (ADM) [1] which originates from single-phase flow but has been paid attention to in the recent years for two-phase flows. In this structural method, an approximation of the unfiltered solution is obtained mathematically and can be used to close the SGS terms in the filtered equations while respecting the mathematical structure of the SGS terms. Our *a priori* study [4] have clearly shown that the ADM predicts the SGS contributions of stress tensor and interface dynamics in one-fluid formulation significantly more accurate than the conventionally-used functional LES models. We recently extended the ADM to the two-phase LES formulation by modelling all the subgrid terms appearing in the filtered Navier-Stokes and volume of fluid equations [2]. By employing this new approach (hereinafter called ADM-VOF), an *a posteriori* large eddy simulation was performed on the well-known benchmark problem of liquid-liquid phase inversion. A comparison with highly resolved (quasi-DNS) simulations has demonstrated the potentials of ADM-VOF in predicting the macroscopic characteristics of interfacial turbulence. However, many details on the ADM parameters remain to discuss. In the present study, the sensitivity of the *a posteriori* LES results to the ADM parameters such as size and type of filters as well as the level of deconvolution are investigated in detail.

2 Numerical Methodology

2.1 Description of ADM-VOF Approach

Turbulent interfacial flows can be described by the continuity and incompressible Navier-Stokes equations as well as the advection equation of interface capturing technique (in this study VOF method is employed). By applying a spatial filter operator \mathcal{G} to a flow quantity $\phi(\mathbf{x}, t)$, the filtered quantity reads:

$$\bar{\phi}(\mathbf{x}, t) = \mathcal{G} * \phi(\mathbf{x}, t) = \int_D \mathcal{G}(\mathbf{x} - \mathbf{x}') \phi(\mathbf{x}', t) d\mathbf{x}' \quad (1)$$

where $(\bar{\cdot})$ indicates the spatial non-weighted filtering. Therefore, the filtered governing equations are derived as follows:

$$\nabla \cdot \bar{\mathbf{U}} = 0 \quad (2a)$$

$$\begin{aligned} \frac{\partial(\bar{\rho}\bar{\mathbf{U}})}{\partial t} + \nabla \cdot (\bar{\rho}\bar{\mathbf{U}} \otimes \bar{\mathbf{U}}) = & -\nabla\bar{p} + \nabla \cdot (2\bar{\mu}\bar{D}) + \bar{\rho}\mathbf{g} + \bar{\mathbf{S}}_{\sigma} \\ & + \nabla \cdot (\tau_{\mu D} - \tau_{uu}) + \tau_{\sigma} - \tau_{tt} \end{aligned} \quad (2b)$$

$$\frac{\partial \bar{\alpha}}{\partial t} + \nabla \cdot (\bar{\alpha} \bar{\mathbf{U}}) = -\nabla \cdot \tau_{\alpha u} \quad (2c)$$

In this one-fluid formulation, \mathbf{U} is the mixture velocity vector shared with all phases. p is the pressure and \mathbf{D} is the rate of deformation tensor in the form of $\mathbf{D} = \frac{1}{2}(\nabla \mathbf{U} + \nabla^T \mathbf{U})$. The scalar function α is the volume fraction field which determines the physical properties of the flow as $\rho = \alpha \rho_1 + (1 - \alpha) \rho_2$ and $\mu = \alpha \mu_1 + (1 - \alpha) \mu_2$. The surface tension force is treated by the Continuous Surface Force (CSF) method [5] and reads $\mathbf{S}_\sigma = \sigma \kappa \hat{\mathbf{n}} \delta_s$, where σ is the surface tension coefficient and $\hat{\mathbf{n}}$ and κ are the interface normal vector and interface curvature, respectively. The subgrid terms on the RHS of the equations should be closed using SGS models. In the ADM the original unfiltered flow fields are recovered by approximating the inverse of filter kernel \mathcal{G} .

$$\phi(\mathbf{x}, t) = \mathcal{G}^{-1} * \bar{\phi}(\mathbf{x}, t) \quad (3)$$

If \mathcal{Q} is the deconvolution operator approximated by $\mathcal{Q} \approx \mathcal{G}^{-1}$, then the deconvoluted solution of flow quantity reads $\phi^*(\mathbf{x}, t) = \mathcal{Q} * \bar{\phi}(\mathbf{x}, t) \approx \phi(\mathbf{x}, t)$. According to [1], \mathcal{Q} can be approximated by an infinite series of filter operators such as $\phi^{*(\nu+1)} = \phi^{*(\nu)} + (\bar{\phi} - \mathcal{G} * \phi^{*(\nu)})$ with the initial condition $\phi^{*(0)} = \bar{\phi}$, that iterates until $\nu + 1$ reaches the intended \mathcal{N} . The *a priori* analysis in [4] reported that $\mathcal{N} = 7$ reveals the most accurate correlation with the DNS results. Using ADM, the important SGS terms are closed and implemented in C++ libraries of OpenFOAM [7] as presented in Table 1. It should be noted that the SGS terms $\tau_{\mu D}$ and τ_{tt} are not modelled due to their negligible subgrid contributions [4].

Table 1. The ADM-based closures for three SGS terms.

SGS term	ADM closure
τ_{uu}	$(\rho \bar{\mathbf{U}}^* \otimes \bar{\mathbf{U}}^* - \bar{\rho} \bar{\mathbf{U}}^* \otimes \bar{\mathbf{U}}^*)$
τ_σ	$\sigma (\kappa^* \nabla \alpha^* - \kappa^* \nabla \alpha^*)$
$\tau_{\alpha u}$	$(\alpha^* \bar{\mathbf{U}}^* - \bar{\alpha}^* \bar{\mathbf{U}}^*)$

It has to be noted that in the context of ADM an additional relaxation term is required in the momentum equation to reproduce the energy dissipation of the reconstructed scales in the subgrid [1]. In fact, the ADM reconstructs the flow information between the explicit and implicit (i.e. the grid) filtered scales of the LES. In this study, the relaxation term is accounted by a modified functional model that is a dynamic Smagorinsky in which the scales reconstructed by ADM are removed from the Germano identity [2]. The procedure of implementation of this term is explained in [6] and thus is not repeated here.

2.2 Explicit Filter Operation

It remains to discuss the explicit filter operations used to create the deconvoluted fields (ϕ^*) in ADM-VOF, where the discrete form of explicit filters are used as a

mathematical operator. A general formulation for the discrete box and Gaussian filters with second-order accuracy on a 3-point stencil reads [8]

$$\bar{\phi}_i = \frac{1}{24}\epsilon^2(\phi_{i-1} + \phi_{i+1}) + \frac{1}{12}(12 - \epsilon^2)\phi_i \quad (4)$$

where ϵ is the ratio of filter size to the grid size (i.e. $\epsilon = \Delta/\Delta x$). In the framework of OpenFOAM, the discrete form of second-order box and Gaussian filters are implemented under the name of `laplace` filter where it is possible to switch in between by setting the corresponding parameters [7]. We further extend this formulation to include fourth-order filters. Therefore, the general formulation for the explicit filter reads

$$\bar{\phi} = \phi + \frac{(\Delta x)^2}{C_1}\nabla^2\phi + a\frac{(\Delta x)^4}{C_2}\nabla^2\nabla^2\phi \quad (5)$$

where a switches between 0 and 1 for the 2^{nd} order and 4^{th} order filters, respectively. Also, C_1 and C_2 are user-input constants that control the filter size as presented in table 2. Although the box and Gaussian filters share similar formulation for second-order accuracy, their fourth-order forms are different from each other [8]. In this study, we focus on the Gaussian filters at different sizes and orders. For further numerical details we refer to [2].

Table 2. The user-input parameters for different filters used in this study.

Filter order	Filter size ratio (ϵ)	C_1	C_2
2^{nd} order	1	24	–
2^{nd} order	1.5	$\frac{32}{3}$	–
2^{nd} order	2	6	–
4^{th} order	1	24	1152

3 Results and Discussion

In order to investigate the sensitivity of ADM parameters, a two-dimensional phase inversion benchmark is simulated on a very fine structured grid of 2048^2 as the reference case. It represents a buoyancy-driven turbulent interfacial flow with several interfacial events such as coalescence and rupture as shown in Fig. 1. This benchmark is also used in [2] where the details of the simulation setup, numerical schemes, flow characteristics, and grid dependency are presented comprehensively. Two coarse grids of 256^2 and 512^2 are considered to perform the *a posteriori* simulation. We started the ADM-VOF simulations with the highest approximation order for the inverse filter and the filter to grid ratio of unity (i.e. $\mathcal{N} = 7$ and $\epsilon = 1$). Then, the ADM parameters varied in accordance with Table 1. Two macroscopic characteristics of the flow are considered for comparison: (i) the volume integral of enstrophy in heavier fluid ($E = \int_{\Omega} \frac{1}{2}(\nabla \times \mathbf{U})^2 dV$),

and (ii) total interfacial length ($\Lambda = \int_{\Omega} |\nabla \alpha| d\mathbf{V}$). The former is normalized by the maximum enstrophy in the reference case while the latter is normalized by its magnitude at the beginning of the process. The temporal evolution of E and Λ are plotted for two different grid sizes in Figs. 2 and 3. We further filtered the quasi-DNS results by the box filters of 8×8 and 4×4 to obtain the highly-resolved flow fields filtered by the corresponding grid of *a posteriori* simulations. For better comparison, the Λ from the quasi-DNS results is also plotted. The LES results demonstrate sensitivity to the ADM filter size depending on the grid size. On the much coarse grid of 256^2 , increasing ϵ results in slight improvement on the interfacial length with no noticeable influence on enstrophy. But, on the finer grid of 512^2 , the large ADM filter size results in a large overestimation of both E and Λ . Increasing the approximation order of the inverse filter improves the prediction of the maximum enstrophy and its decreasing rate especially on the grid of 512^2 .

The results further reveal that changing the filter type to fourth-order Gaussian can only improve the E in the latest stages of the process. Also, on the finer grid of 512^2 , it slightly corrects the overestimation of Λ compared to second-order filter. Given the computational overhead of high order filters, the second-order Gaussian filter seems accurate enough for the ADM-VOF simulations.

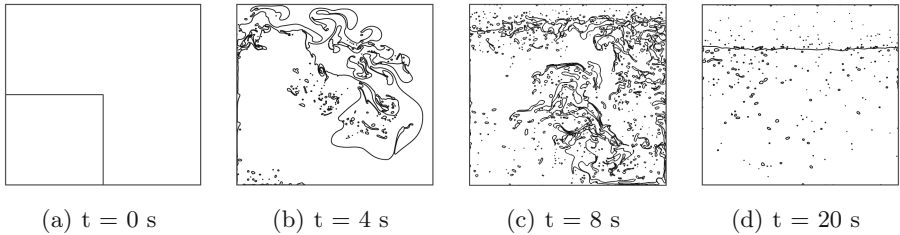


Fig. 1. The α iso-contour of 0.5 at different stages of phase inversion benchmark.

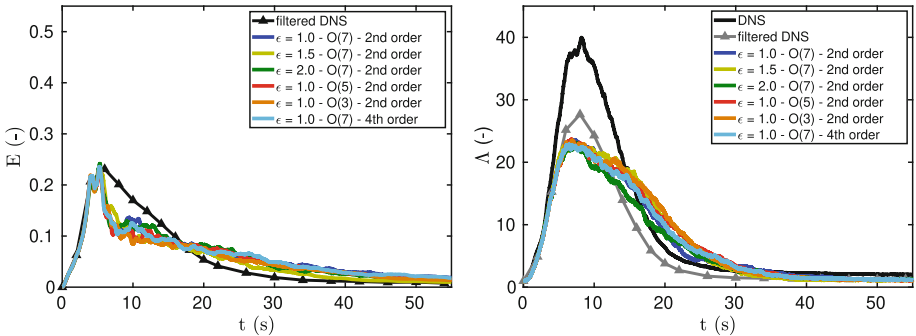


Fig. 2. Temporal evolution of normalized total enstrophy in heavier fluid (left) and total interfacial length (right) on the grid of 256^2 for different cases.

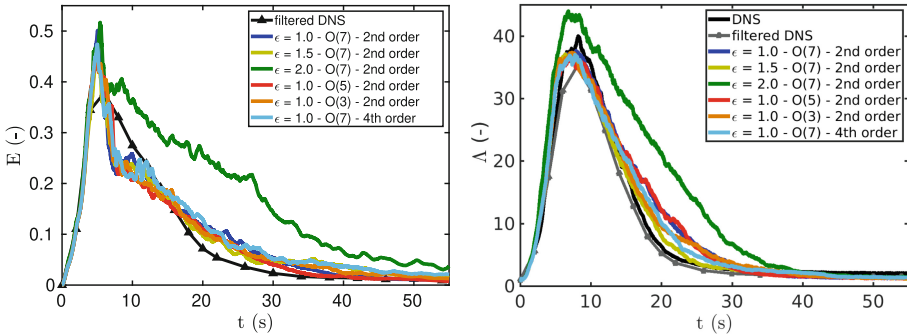


Fig. 3. Temporal evolution of normalized total enstrophy in heavier fluid (left) and total interfacial length (right) on the grid of 512^2 for different cases.

4 Conclusion

In the present study, a sensitivity analysis on the ADM-VOF method parameters in *a posteriori* LES of interfacial turbulence is presented. The size and type of explicit filters as well as the order of deconvolution are investigated. A general conclusion can be drawn that (i) the effect of filter size depends on the LES grid resolution, (ii) the approximation order of $\mathcal{N} = 7$ for the inverse filter gives the more accurate results and (iii) higher order Gaussian filters can only improve the results slightly. Investigation on effect of ADM relaxation term and *a priori* analysis of a 3D phase inversion flow with different filtering approaches remain for future studies.

Acknowledgments. The first author acknowledges the financial support from the K1-MET competence center for metallurgical research in Austria.

References

1. Stolz, S., Adams, N.A.: An approximate deconvolution procedure for large-eddy simulation. *Phys. Fluids* **11**, 1699–1701 (1999)
2. Saeedipour, M., Vincent, S., Pirker, S.: Large eddy simulation of turbulent interfacial flows using approximate deconvolution model. *Int. J. Multiph. Flow* **112**, 286–299 (2019)
3. Sagaut, P.: *Large Eddy Simulation for Incompressible Flows: An Introduction*, 3rd edn. Springer, Heidelberg (2006)
4. Vincent, S., Tavares, M., Fleau, S., Mimouni, S., Ould-Rouiss, M., Estivalèzes, J.-L.: A priori filtering and LES modeling of turbulent two-phase flows application to phase separation. *Comput. Fluids* **176**, 245–259 (2018)
5. Brackbill, J., Kothe, D., Zemach, C.: A continuum method for modeling surface tension. *J. Comput. Phys.* **100**, 335–354 (1992)

6. Germano, M., Piomelli, U., Moin, P., Cabot, H.C.: A dynamic subgrid-scale eddy viscosity model. *Phys. Fluids* **3**, 1760–1765 (1991)
7. The OpenFOAM Foundation. <http://www.OpenFOAM.org>
8. Sagaut, P., Grohens, R.: Discrete filters for large eddy simulation. *Int. J. Numer. Meth. Fluids* **31**, 1195–1220 (1999)



Time-Resolved High-Density Particle Tracking Velocimetry of Turbulent Rayleigh-Bénard Convection in a Cubic Sample

Daniel Schiepel¹ , Sebastian Herzog¹ , and Claus Wagner^{1,2}

¹ German Aerospace Center, Bunsenstr. 10, 37073 Göttingen, Germany
{daniel.schiepel,sebastian.herzog,claus.wagner}@dlr.de

² Technische Universität Ilmenau, Helmholtzring 1, 98684 Ilmenau, Germany
<http://www.dlr.de>

Abstract. A newly developed high-density particle tracking velocimetry (HD-PTV) technique is introduced and validated on a synthetic data set. Further, Lagrangian velocities in turbulent Rayleigh-Bénard Convection (RBC) are determined based on particle images measured in a cubic sample filled with water with a Prandtl number $Pr = 6.9$ and a Rayleigh number of $Ra = 1.0 \cdot 10^{10}$. It is shown that the new technique allows to resolve not only a three-dimensional (3D) large-scale circulation in a diagonal plane of the sample but also the secondary flow structures developing in the corners of the perpendicular plane.

1 Introduction

Turbulent thermal convection occurs frequently in nature, e.g. atmospheric flows, and in numerous technical applications, such as room or cabin ventilation. Measurements of the three-dimensional (3D) velocity and temperature fields are important since they determine the heat transport in thermal convection problems [1]. Measurements of all three velocity components are possible with the large-scale Tomographic Particle Image Velocimetry (Tomo-PIV). This was shown in [2] studying the large-scale flow structures developing in mixed convection and in turbulent Rayleigh-Bénard convection (RBC) [3]. The major drawback of the correlation-based Tomo-PIV approach is the limited spatial resolution of the obtained velocity fields. Hence, small-scale flow structures typically developing in turbulent flows in general and especially in the corners of cuboidal samples, cannot be resolved if large measurement volumes are considered. These smaller flow structures are however important since they are interacting with the well-known large-scale circulation (LSC) found in one diagonal plane of the samples.

In addition, previous Tomo-PIV studies [3] have shown that RBC in a cube is characterized by secondary structures, which develop in a plane perpendicular to the plane of the LSC. However, the additional smaller secondary structures

in the corners were not resolved by Tomo-PIV. However it was shown in [4] that small scale structures are better resolved with Particle Tracking Velocimetry (PTV) and high particle densities.

In this context, we developed a high-density Particle Tracking Velocimetry (HD-PTV) method which is validated on a synthetic data set below. Additionally, its capability to compute the Lagrangian trajectories of the aforementioned secondary structures in RBC is demonstrated using an experimental data set.

2 Experimental and Synthetic Setup

Turbulent RBC in water of Prandtl number $Pr = 6.9$ in a cubical sample with a side length of 500 mm enclosed by 10 mm thick glass walls is considered at a mean sample temperature of $\bar{T} = 21$ °C and a Rayleigh number of $Ra = 1.0 \cdot 10^{10}$. TiO_2 -coated neutrally buoyant latex particles are employed as flow tracers. The entire volume is illuminated using a high-power LED array. A time-resolved measurement is realized by separating two subsequent light-pulses with a time delay of $\Delta t = 0.35$ s. The scattered light from the tracer particles is recorded using 4 PCO-Pixelfly CCD-cameras. A detailed description of the time-resolved measurement and the experimental setup can be found in [3].

An additional synthetic data set is generated to be able to validate the trajectories provided by the HD-PTV method in comparison to the ground truth. The synthetic test case allows for the evaluation of five fundamental capabilities of the PTV algorithm: 3D particle movement, particles leaving the domain, contradicting movement of particle images, varying particles per pixel (ppp) densities and the impact of particle acceleration. The data set features three structures: A large rotating ring in the vertical plane, a smaller horizontal ring and a line intersecting both. The particles are distributed according to analytical functions. The two ring structures are based on a *sine* and *cosine* combination such that the large one orientates normal to the horizontal Z direction and the smaller one normal to the vertical Y direction while both are centered around zero. The particles move tangentially to the prescribed circle. The line has its source at $(X = -250$ mm, $Y = -250$ mm, $Z = -250$ mm) and the particles move until they reach the boundary at $(X = 250$ mm, $Y = 250$ mm, $Z = 250$ mm) and are reset to the position at the source. All particles are Gaussianly distributed around their central structure. An exemplary particle distribution is presented in Fig. 2a) with color coding according to the particle ID. In the context of thermal convection one parameter is of specific interest: the particle acceleration. The individual particle acceleration can be interpreted as the turbulent fluctuations modeled by random Gaussian factors, centered around one with a width of σ_V , which are applied to the velocity components of each particle. For each time step, the particles are projected to the four synthetic camera images using on Soloff-Polynomials [5] such that each particles covers 2×2 pixels. Various data sets, each containing 4000 time steps, with different particle numbers and σ_V are generated.

3 High-Density PTV

The process chain of the new HD-PTV approach is illustrated in Fig. 1. First, the volume is illuminated and the scattered light is recorded by four cameras. Each camera records two images at the two time steps t and $t + \Delta t$. The particle distribution in 3D space is determined using a modified version of the iterative particle reconstruction (IPR) [6], see Sect. 3.1. At high seeding densities, it is challenging to keep track of the position of the particles at the next time step. Thus, a prediction is needed to improve the assignment. Once, the motion of a particle i is known at $t + \Delta t$, a simple guess of its position at $t + 2\Delta t$ leads to $X_i(t + 2\Delta t, i) = X_i(t + \Delta t, i) + \Delta t \cdot V_i(t + \Delta t, i)$. Since this guessed position can vary greatly from the actual particle position, a reliable particle position predictor is mandatory for the below presented particle tracking.

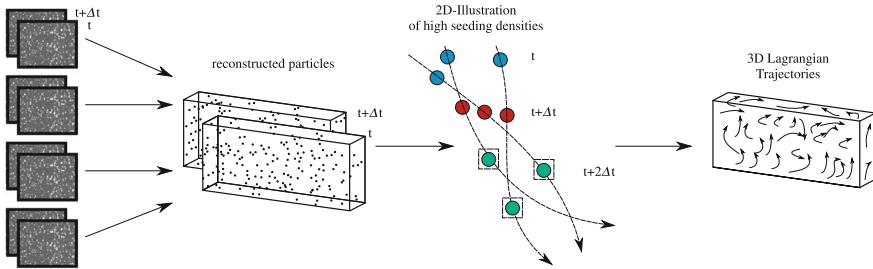


Fig. 1. Illustration of the HD-PTV software chain.

3.1 Three Dimensional Particle Tracking

First, the 3D particle reconstruction is performed using of a modified version of an iterative particle reconstruction [6] taking into account the imaging properties, shape and brightness, of the particles. The particle distribution in 3D space is determined using triangulation methods. The translation from 3D space to 2D images is performed with Soloff-Polynomials [5] determined from a volume self calibration. The projections are computed and compared to the recorded images. The position of any candidate in 3D space is corrected by varying it in every direction until the residual is converged. The remaining particle images are used to reconstruct additional particles in 3D space until all particle images are used.

The initialization step is performed for n_{init} time steps, typically 5 to 20 are sufficient. The particles are tracked by a track initialization using possible particle displacements computed from all neighboring particles and a median filter of the possible displacements to determine the most likely displacement. The exact association of a particle is determined using a regularization to compensate the uncertainty from the displacement. This step results in particle associations for the n_{init} time steps.

After the initialization, the particle associations are used for the particle tracking with a simplified Gaussian Mixture Model which increases the tracking accuracy considerably. It provides further a compact representation for each trajectory. Thus, there is no need for an individual treatment of every single snapshot of the particle distribution. The current particle positions and velocities are used to calculate a trajectory for the following time step, just by applying the velocity components to the position of the particle and regularizing the 3D particle in all three dimensions until the projection error to the images is minimal. This allows an accurate prediction of the particle position at the next time step while saving computational resources. All remaining particles from the camera images are added by employing the initialization step.

4 Synthetic Case

The synthetic case is designed to mimic the large scale circulations in the convection sample presented below. The flow velocities are typically small. Assuming a PCO Pixelfly camera operating at 3.3 Hz in rolling shutter mode, the average velocity is $\bar{V} = 16$ mm/s.

The reconstructed particle distribution for $\sigma_V = 0.10$ is shown in Fig. 2b). The particle positions are indicated using spheres and the reconstructed velocities from the last 10 time steps are attached as tails. The three large structures are clearly visible and the particle distribution is virtually identical with the ground truth in Fig. 2a). The average deviation of a reconstructed from an associated true particle is determined to an average L2 distance of $3.9 \cdot 10^{-4}$ mm thus proving the accuracy of the new technique.

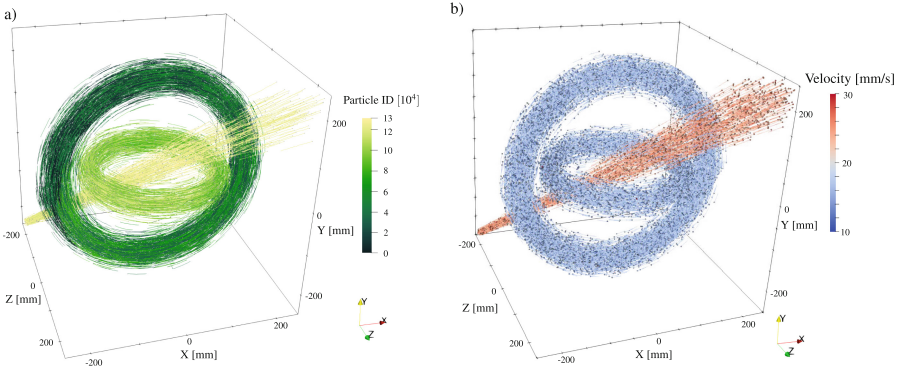


Fig. 2. a) Synthetic flow structures with the particle position indicated using spheres and the particle paths of the last 10 time step as tails with color coding according to the particle ID. b) the reconstructed flow structures with color coding according to the velocity magnitude for the tails. Both for 0.035 ppp and $\sigma_V = 0.10$.

Trajectories for different particle densities are obtained by altering the number of particles in the system and thus the particles per pixel (ppp) on the

synthetic camera images. In addition, the variance is increased in the range $\sigma_V = 0.00$ – 0.10 to simulate stronger velocity fluctuations. In Fig. 3, the obtained matched particles are plotted as a function of the total number of particles. All three curves start at a close to 100% efficiency and decrease with increasing number of particles. Further, large σ_V -values lead to lower efficiencies and the case with the highest σ_V (green curve) reflects the lowest percentage of matched particles. This is expected for higher velocity fluctuations since particles deviate more likely from the ideal path. Up to 0.052 ppp, the number of matched particles remains close to 100% and decreases for higher ppp values. However, 50% to 70% of matched particles are obtained for the highest density of 0.128 ppp. To conclude, for moderately high seeding densities up to 0.085 ppp, the HD-PTV method is viable for all investigated variances i.e. mimicked turbulent intensities.

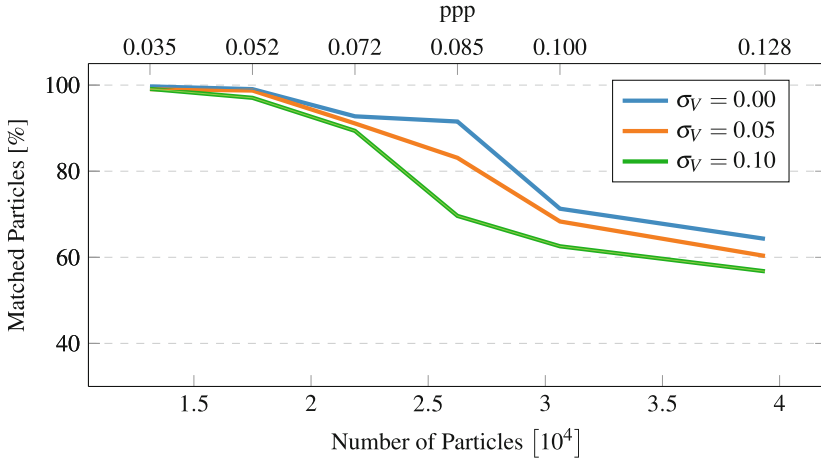


Fig. 3. Percentage of matched particles depending on the particle number for three different velocity variances $\sigma_V = 0.00$ – 0.10 .

5 Experimental Case

HD-PTV is employed to measure the flow structures developing in turbulent RBC from camera images with 0.062 ppp obtained in an RBC measurement. The particle positions and the associated Lagrangian trajectories are reconstructed to study the LSC and the developing secondary structures. In the considered time period, on average 5260 particles could be tracked and their velocities were deduced. The resulting particle paths are presented in Fig. 4a). In a diagonal subvolume of the sample, ranging from 30% to 70% of the diagonal length, the particle positions are highlighted as grey dots. The associated trajectories of the last 50 time steps are attached as tails. Only particles with a trajectory length of more than 25 time steps are shown. The particle paths are colored

according to the velocity magnitude. Especially the fast wall-parallel particle trajectories highlight the resolved LSC in the diagonal of the sample. Further, a maximum velocity magnitude of 18.9 mm/s could be obtained from the HD-PTV trajectories.

A close up view of a smaller structure located in the corner of the sample is shown in Fig. 4b). Even though the seeding density in the corner of the sample is reduced due to adhesion of the particles to the boundaries, this structure with a diameter of 40 mm (8% of the sample-filling LSC) and a velocity of 4.8 mm/s are successfully resolved with the presented HD-PTV technique.

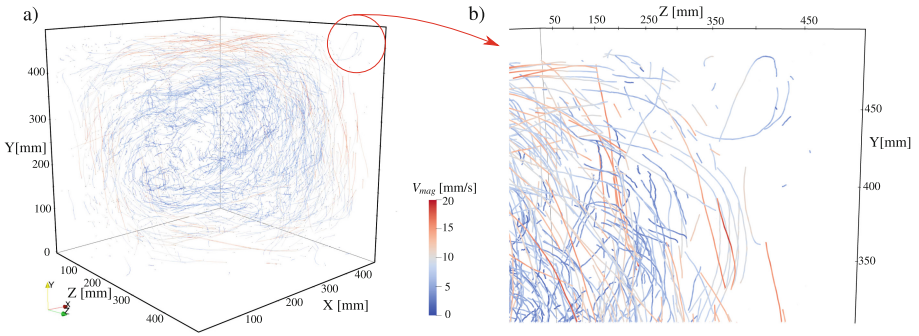


Fig. 4. a) Particle trajectories with an extension of more than 25 time steps in a diagonal subvolume of the sample. The particles are indicated using grey dots and the particle paths are color-coded according to the velocity magnitude. Close up view of the corner of the sample in b).

6 Conclusion

HD-PTV, a newly developed PTV technique for high seeding densities, was presented and validated using synthetic data sets to compare the reconstructed trajectories to the ground truth. For various particle images densities $0.035 < ppp < 0.128$ the reconstruction efficiency was measured for three different velocity variances in the range $0.00 < \sigma_V < 0.10$ mimicking an increase of the turbulence intensity. It is found that for moderately high seeding densities up to 0.085 ppp, the HD-PTV method reconstructs the Lagrangian particle trajectories for all σ_V with more than 70–90% matched particles.

Additionally, the particle trajectories of RBC in a cubic sample filled with water at $Pr = 6.9$ and $Ra = 1.0 \cdot 10^{10}$ were determined. It was shown that the new technique allows to resolve not only the LSC in a diagonal plane of the sample but also the secondary flow structures developing in the corners of the perpendicular plane.

References

1. Ahlers, G., Grossmann, S., Lohse, D.: Heat transfer and large scale dynamics in turbulent Rayleigh-Bénard convection. *Rev. Mod. Phys.* **81**, 503–537 (2009)
2. Kühn, M., Ehrenfried, K., Bosbach, J., Wagner, C.: Large-scale Tomo PIV using helium-filled soap bubbles. *Exp. Fluids* **50**, 929–948 (2011)
3. Schiepel, D., Bosbach, J., Wagner, C.: Tomographic particle image velocimetry of turbulent Rayleigh-Bénard convection in a cubic sample. *JFVIP* **20**(1–2), 3–23 (2013)
4. Schanz, D., Schröder, A., Gesemann, S., Michaelis, D., Wieneke, B.: Shake the box: a highly efficient and accurate tomographic particle tracking velocimetry (TOMO-PTV) method using prediction of particle positions. In: *PIV13*, Delft, The Netherlands (2013)
5. Soloff, S.M., Ronald, A., Liu, Z.C.: Distortion compensation for generalized stereoscopic particle image velocimetry. *Meas. Sci. Technol.* **8**(12), 1441–1454 (1997)
6. Wieneke, B.: Iterative reconstruction of volumetric particle distribution. *Meas. Sci. Technol.* **24**(2), 024008 (2013)



Sub-grid Deconvolution Approach for Filtered Two-Fluid Models and the Application to Fluidized Gas-Particle Suspensions

Simon Schneiderbauer^{1,2}(✉)  and Mahdi Saeedipour² 

¹ Christian Doppler Laboratory for Multi-Scale Modeling of Multiphase Processes, Johannes Kepler University, Altenbergerstr. 69, 4040 Linz, Austria

² Department of Particulate Flow Modeling, Johannes Kepler University, Altenbergerstr. 69, 4040 Linz, Austria
{simon.schneiderbauer,mahdi.saeedipour}@jku.at

Abstract. In our prior study [9], an a-priori analysis on the spatially-filtered two-fluid model (TFM) was presented for turbulent gas-solid flows, where the unresolved terms were modeled by an approximate deconvolution model (ADM). With such an approach, an approximation of the unfiltered solution is obtained by repeated filtering allowing the determination of the RSFS (resolved sub-filter scales) contribution of unclosed terms of the filtered equations directly. In the present study, this ADM-TFM approach is implemented in an a-posteriori manner for the coarse grid simulation of unbounded fluidization of Geldart type A particles. The ADM-TFM predictions of the domain averaged slip are in fairly good agreement with the fine grid reference case previously published in literature [3] and do not show a notable grid-dependency. Compared to TFM simulations using the same grid resolution, the ADM-TFM approach does only require marginally more computational resources but yields considerably better agreement with the fine grid data.

Keywords: Multiphase turbulence · Kinetic theory based two-fluid model (TFM) · Sub-grid closure · Structural turbulence model

1 Introduction

Turbulent (clustered) gas-solid flows emerge in a variety of industrial important processes. Important applications are fluidized beds. Especially, in the riser section of circulation fluidized beds (CFB), there are clusters and streamers of particles which are continuously formed and broken. In principle, Euler-Euler (i.e. two-fluid model, TFM) and Euler-Lagrange simulations are capable of predicting those heterogenous meso-scale structures [3]. However, to accurately predict the hydrodynamics of fluidized beds, the computational grid size for those simulation methods should be much smaller than the typical length scale of clusters.

To account for those small unresolved scales in coarse grid simulations, filtered two-fluid models (fTFM) have been developed ([9] and references therein). More recently, a different class of filtered (averaged) models employs the concepts of turbulence modeling to derive constitutive relations for unresolved terms [2, 7]. Particularly, recent turbulence models are of functional type and follow either the concept of RANS [2] or LES (large eddy simulation) [7].

In the past two decades, structural LES models [9, 11] have been successfully proposed as an alternative to the well established functional models [4] in single phase flows. The main advantage of structural models is the aim to reconstruct certain unresolved scales (resolved sub-filter scales, RSFS) by, for example, de-filtering [11] or Taylor series expansions [6]. Thus, these models can be established with no a-priori knowledge of the physics of the interactions between the resolved and sub-grid scales [6]. On the contrary, functional methods rely on the turbulent energy cascade [4], which might not be the case in turbulent multiphase flows. One of the most popular structural approaches is the approximate deconvolution model (ADM) originally proposed by Stolz and Adams [11]. Recently, the a-priori study of [9] has demonstrated that predictions of ADM are in fairly good agreement with the highly resolved TFM simulations of moderately dense gas-solid flows for various filter sizes and different particle sizes. However, an a-posteriori analysis of the applicability of ADM to the coarse grid simulation of (moderately dense) gas-solid flow involving clustering and bubbling (such as observed in risers and fluidized beds) is still missing.

In this paper, we apply ADM to fTFM to close the unresolved sub-grid terms. The results received from the ADM-TFM approach are discussed with respect to a highly resolved reference simulation in the case of unbounded fluidization.

2 Filtered Two-Fluid Model

In the case of coarse grids not all flow features are resolved by the TFM equations. Thus, balance equations for the meso-scale flow can be found by applying a spatial filter operation the TFM equations yielding their filtered counterpart [9]

$$\frac{\partial(1 - \bar{\phi})}{\partial t} + \frac{\partial}{\partial x_k} ((1 - \bar{\phi})\tilde{v}_k) = 0, \quad (1)$$

$$\frac{\partial(1 - \bar{\phi})\tilde{v}_i}{\partial t} + \frac{\partial}{\partial x_k} ((1 - \bar{\phi})\tilde{v}_i\tilde{v}_k) = \frac{1}{\rho_g} (\bar{f}_{gi} + \bar{f}_{gi}^R), \quad (2)$$

and

$$\frac{\partial \bar{\phi}}{\partial t} + \frac{\partial}{\partial x_k} (\bar{\phi}\tilde{u}_k) = 0, \quad (3)$$

$$\frac{\partial \bar{\phi}\tilde{u}_i}{\partial t} + \frac{\partial}{\partial x_k} (\bar{\phi}\tilde{u}_i\tilde{u}_k) = \frac{1}{\rho_s} (\bar{f}_{si} + \bar{f}_{si}^R), \quad (4)$$

where ϕ being the solids volume fraction, ρ_q the density of the gas phase ($q \equiv g$) and the solid phase ($q \equiv s$). v_i and u_i denote the i -th component of the gas and

solid phase velocities, respectively. In Eqs. (1) through (4) we employed Favre (phase) averages defined as $\tilde{v}_i = \overline{(1-\phi)v_i}/(1-\bar{\phi})$ and $\tilde{u}_i = \overline{\phi u_i}/\bar{\phi}$. Here, $\overline{(\cdot)}$ denotes a simple box filter with filter length Δ_{fi} [5,9]. The Reynolds-stress-like contribution stemming from the convective terms reads

$$\overline{f_{gi}^{\text{R}}} = -\frac{\partial}{\partial x_k} R_{g,ik}, \quad \overline{f_{si}^{\text{R}}} = -\frac{\partial}{\partial x_k} R_{s,ik}, \quad (5)$$

with

$$R_{g,ik} = \rho_g \left(\overline{(1-\phi)v_i v_k} - (1-\bar{\phi})\tilde{v}_i \tilde{v}_k \right), \quad R_{s,ik} = \rho_s \left(\overline{\phi u_i u_k} - \bar{\phi} \tilde{u}_i \tilde{u}_k \right). \quad (6)$$

It has to be further noted that whenever two identical indices appear in the same term, a summation over all values of the repeated index is implied. We use this convention throughout this paper. Furthermore, the remaining term, $\overline{f_{qi}}$, on the right hand side of Eqs. (2) and (4) is given by [9]

$$\begin{aligned} \overline{f_{gi}} &= -(1-\bar{\phi}) \frac{\partial \bar{p}}{\partial x_i} + \frac{\partial}{\partial x_k} (\mu_g (1-\bar{\phi}) \tilde{D}_{g,ik}) - \frac{\bar{\phi} \rho_s}{\bar{\tau}_p} (\tilde{v}_i - \tilde{u}_i + \tilde{u}_{d,i}) \\ &\quad + (1-\bar{\phi}) \rho_g g_i, \\ \overline{f_{si}} &= -\bar{\phi} \frac{\partial \bar{p}}{\partial x_i} - \frac{\partial}{\partial x_k} \overline{\Sigma_{ik}^{\text{fr}}} + \frac{\bar{\phi} \rho_s}{\bar{\tau}_p} (\tilde{v}_i - \tilde{u}_i + \tilde{u}_{d,i}) + \bar{\phi} \rho_s g_i. \end{aligned} \quad (7)$$

where p denotes the gas-phase pressure, ρ_q the density, Σ_{ik}^{fr} the frictional stress, $\bar{\tau}_p$ the particle relaxation time from Wen and Yu [13] evaluated from filtered quantities and g_i the standard acceleration due to gravity. Furthermore, μ_g is the gas-phase viscosity and $D_{g,ik} = (\partial v_i / \partial x_k + \partial v_k / \partial x_i) / 2$. Constitutive models employed for the particle-phase stress, Σ_{ik}^{fr} , can be found in tables 3 and 4 in our previous study [8].

It remains to discuss the drift velocity $\tilde{u}_{d,i}$, which is defined as [9]

$$\tilde{u}_{d,i} = \frac{\overline{\phi v_i}}{\bar{\phi}} - \tilde{v}_i. \quad (8)$$

Approximate Deconvolution Model: ADM-TFM

The filter operation (with filter G) is formally written as $\bar{g} = G \star g$. Thus, g may be reconstructed from the filtered quantities $g = G^{-1} \star \bar{g}$ and, therefore, the filtered drag force and the Reynolds-stress contribution may be computed directly from the reconstructed ϕ , u_i and v_i . However, in most interesting cases G is not invertible. Higher-order reconstruction of G^{-1} can be achieved by the iterative deconvolution method of van Cittert [1], where the unfiltered quantities can be derived by a series of successive filtering operations (G) applied to the filtered quantities with

$$g^{(k+1)} = g^{(k)} + \left(\bar{g} - G \star g^{(k)} \right) \quad (9)$$

with the initial condition $g^{(0)} = \bar{g}$. Equation (9) is iterated until $k + 1$ reaches the desired level of deconvolution, ν , and finally, $g^* = g^{(\nu)}$.

To reconstruct the contributions of the unresolved terms appearing on the right hand side of the filtered solid momentum equation, the approximate unfiltered velocities, u_i^* and v_i^* , and the approximate unfiltered volume fraction, ϕ^* , are substituted into Eqs. (6) and (7) yielding their modeled counterparts of R_{ik} and \bar{f}_{si} ; these are [9]

$$\begin{aligned} R_{g,ik}^{(m)} &= \rho_g \left(\overline{(1 - \phi^*)v_i^*v_k^*} - (1 - \bar{\phi}^*)\widetilde{v_i^*v_k^*} \right), \\ R_{s,ik}^{(m)} &= \rho_s \left(\overline{\phi^*u_i^*u_k^*} - \bar{\phi}^*\widetilde{u_i^*u_k^*} \right), \\ \bar{f}_{gi}^{(m)} &= -(1 - \bar{\phi})\frac{\partial \bar{p}}{\partial x_i} + \frac{\partial}{\partial x_k} (\mu_g(1 - \bar{\phi})\widetilde{D}_{g,ik}) - \frac{\bar{\phi}\rho_s}{\bar{\tau}_p} (\widetilde{v}_i - \widetilde{u}_i + \widetilde{u_{d,i}^*}) \\ &\quad + (1 - \bar{\phi})\rho_g g_i, \\ \bar{f}_{si}^{(m)} &= -\bar{\phi}\frac{\partial \bar{p}}{\partial x_i} - \frac{\partial}{\partial x_k} \overline{\Sigma_{ik}^{\text{fr}^*}} + \frac{\bar{\phi}\rho_s}{\bar{\tau}_p} (\widetilde{v}_i - \widetilde{u}_i + \widetilde{u_{d,i}^*}) + \bar{\phi}\rho_s g_i, \end{aligned} \quad (10)$$

with the drift velocity $\widetilde{u_{d,i}^*} = \frac{\phi^*v_i^*}{\bar{\phi}^*} - \frac{\overline{(1 - \phi^*)v_i^*}}{1 - \bar{\phi}^*}$.

Here, $\overline{\Sigma_{ik}^{\text{fr}^*}}$ indicates that the frictional stress contribution is evaluated from deconvoluted fields, where we employ the $\mu(I_s)$ -rheology [8]. Following our previous study [8], $\overline{\Sigma_{ik}^{\text{fr}^*}}$ solely gets active in regions with $\bar{\phi} > 0.5$. Finally, it has to be noted that for the terms in Eq. (10), which do not require closure such as $-\bar{\phi}\partial\bar{p}/\partial x_i$, no deconvolution is applied.

3 Case Setup

In this paper, we consider the unbounded fluidization of particles with a diameter of $d_s = 75 \mu\text{m}$ and a density of 1500 kg m^{-3} in a three-dimensional periodic domain. The size of the domain is the same as that of Fullmer and Hrenya [3], which is $L_x = L_y = 0.8 \text{ cm}$ in the horizontal directions and $L_z = 3.2 \text{ cm}$ in the vertical (streamwise) direction. A pressure gradient is applied to balance the weight of the suspension in the domain so that the mixture as a whole does not accelerate; this part is added as an extra source term in the momentum Eqs. (2) and (4). A uniform discretization is used for all simulations with a grid size between $666 \mu\text{m}$ and $800 \mu\text{m}$, which is 2.6 to 3.2 times coarser than the grid size required for grid size independent solutions using TFM [3] (more details are given in [3]).

The open-source CFD code OpenFOAM 5 (<https://openfoam.org>) was employed for numerical solution of the governing equations. Particularly, we modified the OpenFOAM solver *twoPhaseEulerFoam* to account for Eq. (10). Time advancement is achieved by a variable time-step procedure, where the time step is limited by a maximum Courant number of 0.25. Pressure-velocity

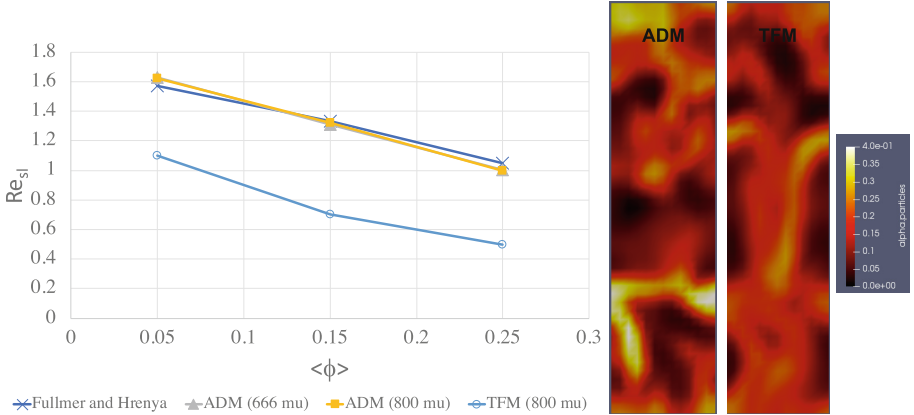


Fig. 1. Left: comparison of mean-slip Reynolds numbers, Re_{sl} , between TFM and ADM-TFM simulations for various mean solid volume fractions and grid spacings (\times : highly resolved TFM from [3]; \triangle , \square , \circ : present study). Right: snapshots of solid volume fraction.

coupling is based on the PIMPLE algorithm [12]. Similar to [3], the SuperBee flux-limiter was used for all variable extrapolation. For more details the reader is referred to [10].

4 Results and Discussion

In Fig. 1 the time averages of mean-slip Reynolds number, $Re_{sl} = \rho_g \tilde{u}_{sl} d_s / \mu_g$, received from ADM-TFM with $\nu = 7$ are compared with the published highly resolved TFM results of [3]. The agreement of the coarse grid ADM-TFM simulations with fine-grid TFM is excellent, where both show a decreasing mean slip velocity \tilde{u}_{sl} with increasing mean solid volume fraction. In contrast, neglecting the unresolved structures by using TFM with a coarse grid resolution yields a considerable underprediction of the mean slip velocity. This, in turn, implies that the gas-solid drag force is significantly overestimated. Furthermore, our results unveil that in this case (especially for higher solid concentrations) no distinct clusters form. In particular, these “blurred” structures are much more dilute than the more distinct clusters received from the ADM-TFM simulations (Fig. 1 right).

5 Conclusions

In this paper, we have assessed the ADM-TFM approach for closing the unresolved terms appearing in the filtered TFM-equations, where the approximate deconvolution model (ADM) originally stemming from the single-phase large eddy simulation was extended to the two-phase gas-solid flow in our previous

study [9]. The ADM-TFM approach has been applied to a coarse grid simulation of the unbounded fluidization of fine particles, where the coarse grid ADM-TFM simulations are in excellent agreement with fine-grid reference simulations published in literature [3]. To conclude, this study demonstrates that, in terms of agreement of Re_{sl} with the reference data, the presented ADM-TFM approach applies well to the coarse-grid simulation of fluidized gas-solid flows of fine particles. However, still the ADM-TFM approach has to be tested at even coarser grids.

Acknowledgements. The financial support by the Austrian Federal Ministry for Digital and Economic Affairs and the National Foundation for Research, Technology and Development is gratefully acknowledged. The author also wants to acknowledge the financial support from the K1MET center for metallurgical research in Austria (www.k1-met.com).

References

1. van Cittert, P.H.: Zum Einfluß der Spaltbreite auf die Intensitätsverteilung in Spektrallinien. II. Zeitschrift für Physik **69**(5–6), 298–308 (1931)
2. Fox, R.O.: On multiphase turbulence models for collisional fluid-particle flows. J. Fluid Mech. **742**, 368–424 (2014)
3. Fullmer, W.D., Hrenya, C.M.: Quantitative assessment of fine-grid kinetic-theory-based predictions of mean-slip in unbounded fluidization. AIChE J. **61**(1), 11–17 (2016)
4. Germano, M., Piomelli, U., Moin, P., Cabot, W.H.: A dynamic subgrid-scale eddy viscosity model. Phys. Fluids A **3**, 1760–1765 (1991)
5. Saeedipour, M., Vincent, S., Pirker, S.: Large eddy simulation of turbulent interfacial flows using approximate deconvolution model. Int. J. Multiph. Flow **112**, 286–299 (2019)
6. Sagaut, P.: Large Eddy Simulation for Incompressible Flows, 3rd edn. Springer, Heidelberg (2006)
7. Schneiderbauer, S.: A spatially-averaged two-fluid model for dense large-scale gas-solid flows. AIChE J. **63**(8), 3544–3562 (2017)
8. Schneiderbauer, S., Puttinger, S., Pirker, S.: Comparative analysis of subgrid drag modifications for dense gas-particle flows in bubbling fluidized beds. AIChE J. **59**(11), 4077–4099 (2013)
9. Schneiderbauer, S., Saeedipour, M.: Approximate deconvolution model for the simulation of turbulent gas-solid flows: an a-priori analysis. Phys. Fluids **30**(2), 023301 (2018)
10. Schneiderbauer, S., Saeedipour, M.: Numerical simulation of turbulent gas-solid flow using an approximate deconvolution model. Int. J. Multiph. Flow **114**, 287–302 (2019)
11. Stolz, S., Adams, N.A.: An approximate deconvolution procedure for large eddy simulation. Phys. Fluids **11**(7), 1699–1701 (1999)
12. The OpenFOAM Foundation: OpenFOAM v5 user guide (2018)
13. Wen, C.Y., Yu, Y.H.: Mechanics of fluidization. In: Chemical Engineering Progress Symposium Series, vol. 62, pp. 100–111 (1966)



A Front-Tracking Method for Multiphase Flows with a Sharp Interface Representation

Mathilde Tavares^(✉), Désir-André Koffi Bi, Eric Chénier,
and Stéphane Vincent

Université Paris-Est Marne-la-Vallée, Lab. Modélisation et Simulation Multi Echelle,
MSME, UMR 8208 CNRS 5 bd Descartes, 77454 Marne-la-Vallée, France
mathilde.tavares@u-pem.fr

Abstract. A front-tracking method is developed with specific algorithms for handling volume conservation and arbitrary shape interfaces. We propose a marker advection method which takes into account the jump relation in order to deal with the jump of the physical discontinuities at the interface for two-phase flow simulations. A comparison to different interface tracking approaches is carried out on a rising bubble test case in order to show the ability of our conservative front-tracking method to describe interfaces with high accuracy.

Keywords: Front-tracking · Velocity reconstruction based on jump relations · Multiphase flow · Volume conservation

1 Introduction

The understanding of the dynamics of multiphase flows remains challenging because of the complex physics they entail. A major difficulty in multiphase flow simulation is to capture simultaneously the smallest and the largest scales of the interface while describing accurately the topology changes of the flow and the interfacial characteristics such as capillary forces when small and large deformable interfaces interact in an unsteady flow motion.

The front-tracking approach is a class of method, where the front interface between two phases is represented by connected markers independent of the Cartesian grids used for the discretization of the Navier-Stokes equations. The computed interfacial source terms are transferred to the Cartesian fixed grid for the integration process. We present here an improvement of this method with the development of specific algorithms in order to obtain the most accurate advection of the interface as possible while keeping the volume constant after the interface advection step. A thoroughly description of this method is detailed in [5]. The front-tracking method presented here is based on the Tryggvason et al. work [1] for multiphase and isothermal flows. The interface is represented by a chain

of markers connected by segments and the connectivity between neighbouring elements is stored to compute the magnitude and the direction of the surface tension.

2 The Front-Tracking Method

2.1 Base Components of the Front-Tracking Method

Lagrangian Advection of the Interface Markers. The interface is advected by solving the following Lagrangian equation $\frac{d\bar{x}_m}{dt} = \bar{V}_m(t)$ with $\bar{V}_m(t)$ the Lagrangian velocity of the marker m at position \bar{x}_m . For the time integration, a second order Runge-Kutta scheme combined with a second order Adams-Bashforth extrapolation method is used.

To get the velocities at \bar{x}_m , different interpolation procedures can be investigated. The bilinear interpolation method [3] is quite common [3]. The Parabolic Edge Reconstruction Method (PERM) by Pope et al. [2] which consists in a divergence free approximation at the nodes and cell centers of the Eulerian velocity grids is also considered here for validation purposes.

Management of the Interface Elements Size. When the interface is highly stretched and deformed, inducing the appearance of regions with different marker densities, markers are locally inserted or suppressed in order to keep the instantaneous size of each interface element almost constant and maintain a good accuracy at each time step.

At $t^{(n)}$, if the size of an element is too large, the mesh is enriched. Similarly, the deletion of a too small element depends on its size but also on the dimensionless curvatures calculated at the markers in order to avoid the local deterioration of the interface shape.

2.2 Volume Conservation

As the interface is approximated by linear elements and advected by the velocity field, the front-tracking method cannot geometrically conserve the volume delimited by the connected elements for incompressible flows. To keep the volume constant, two specific algorithms have been developed in this work.

Homothetic Rescaling Method. The homothetic rescaling method is purely geometric and consists in performing a homothety of the markers position after the advection step with respect to the relation $\mathcal{V}^{(n+1)} = \mathcal{V}^{(n)}$ where $\mathcal{V}^{(n)}$ is the known volume at time $t^{(n)}$. For all markers of the front, the coordinate \bar{x}_m of the marker m is adjusted to satisfy the volume conservation as follows:

$$\bar{x}_m \leftarrow \bar{x}_O + k_{\bar{x}_O}(\bar{x}_m - \bar{x}_O) \quad (1)$$

where $k_{\bar{x}_O}$ is the homothety coefficient expressed by $k_{\bar{x}_O} = \sqrt{\frac{\mathcal{V}^{(n)}}{\mathcal{V}^{(n+1)}}}$ and \bar{x}_O the homothety centre. Even if the location of \bar{x}_O is free, its position plays an important role and a natural choice could be to identify \bar{x}_O at the centroid of the considered front-tracking surface.

Velocity Based Correction (VBC) Method. This method is based on the fluid flow characteristics namely the markers displacement over a time step. After the advection step, each marker m is slightly moved in the normal direction ($\bar{n}_m^{(n+1)}$) to the interface:

$$\bar{x}_m^{(n+1)} \leftarrow \bar{x}_m^{(n+1)} + k\bar{p}_m \quad (2)$$

with $\bar{p}_m \stackrel{\text{def}}{=} \left| (\bar{x}_m^{(n+1)} - \bar{x}_m^{(n)}) \cdot \bar{n}_m^{(n+1)} \right| \bar{n}_m^{(n+1)}$. The coefficient k is therefore solution of a second order polynomial (see [5]).

These two algorithms are investigated and compared in the rising bubble test case in the Sect. 4.

3 A Marker Advection Method Based on the Jump Relations at the Interface

The velocity reconstruction method we present in this section is based on the physical jump at the interface and has been developed to give a better representation of the velocity derivatives discontinuity at the interface. If we consider an incompressible and immiscible two fluid flow, labeled 1 and 2, separated by an interface Γ , of surface tension σ , we can write the jump relations at each point belonging to Γ :

$$\bar{v}_1 = \bar{v}_2 \quad (3)$$

$$\bar{n} \cdot (\bar{T}_1 - \bar{T}_2) \cdot \bar{n} = \sigma(\bar{\nabla} \cdot \bar{n}) \quad (4)$$

$$\bar{t} \cdot (\bar{T}_1 - \bar{T}_2) \cdot \bar{n} = (\bar{\nabla} \sigma) \cdot \bar{t} \quad (5)$$

with the velocity vector \bar{v} , the stress force applied by the fluid flow on both sides of the interface, $\bar{T} \equiv (-p\bar{I} + \mu(\bar{\nabla}\bar{v} + (\bar{\nabla}\bar{v})^t))$, \bar{n} the unit outward normal vector of the fluid domain 2 and \bar{t} the tangential unit vector. Thanks to these relations, the velocity of the interface mesh nodes \bar{V}_m is evaluated, but also the velocity gradients, at the marker m and finally, the interface is advected with the calculated velocities. This requires the development of specific algorithms presented briefly below.

Linear Approximation Function for the Velocity Components. The calculation of \bar{V}_m requires the construction of linear approximation functions for the velocity components in each of the two fluid domains. For example, we note $V_m^{x,1}$ the unknown horizontal velocity component of the fluid domain 1 at m with

coordinates \bar{x}_m . We construct a linear interpolation polynomial based on triangles using two other Eulerian grid nodes $n_2^{x,1}$ and $n_3^{x,1}$ of coordinates $\bar{x}_2^{x,1}$ and $\bar{x}_3^{x,1}$ and the related velocities are $v_2^{x,1}$ and $v_3^{x,1}$, to get a local continuous approximation $\tilde{v}^{x,1}(\bar{x})$. Then, the linear approximation of the horizontal component of the velocity is given by:

$$\tilde{v}^{x,1}(\bar{x}) = V_m^{x,1}\psi_m^{x,1}(\bar{x}) + v_2^{x,1}\psi_2^{x,1}(\bar{x}) + v_3^{x,1}\psi_3^{x,1}(\bar{x}) \quad (6)$$

where $\psi_\alpha^{x,1}(\bar{x})$ are the Lagrangian linear polynomials such that $\psi_\alpha^{x,1}(\bar{x}_\beta^{x,1}) = \delta_{\alpha,\beta}$, for $(\alpha, \beta) \in \{m, 2, 3\} \times \{m, 2, 3\}$, with the Kronecker delta $\delta_{\alpha,\beta} = 0$ if $\alpha \neq \beta$ and $\delta_{\alpha,\alpha} = 1$. The variables $v_k^{x,1}$, $k = 2, 3$, are the known horizontal velocities on the horizontal Eulerian grid and $V_m^{x,1}$ is the unknown horizontal velocity of the interface marker m for fluid 1.

Pressure Evaluation at the Interface Node. The pressures in the two fluid domains at any interface node m are approximated using the Eulerian nodes of the pressure grid. For fluid 1 for example, the pressures p_2^1 and p_3^1 at $n_2^{p,1}$ and $n_3^{p,1}$ which coordinates are $\bar{x}_2^{p,1}$ and $\bar{x}_3^{p,1}$, are used for the approximation. Then, the pressure p_m^1 at the marker m is equal to the interpolated pressure at the intersection point n_I^1 whose coordinate is \bar{x}_I^1 , located at the intersection between the straight line $\Delta = \{\bar{x}_m + \xi\bar{n}_m; \xi \in \mathcal{R}\}$ and $[n_2^{p,1}n_3^{p,1}]$:

$$p_m^1 = \frac{\|\bar{x}_2^{p,1} - \bar{x}_I^1\|p_3^1 + \|\bar{x}_3^{p,1} - \bar{x}_I^1\|p_2^1}{\|\bar{x}_3^{p,1} - \bar{x}_2^{p,1}\|} \quad (7)$$

Reconstruction of the Velocity at the Interface Marker m . To eventually reconstruct the velocity, we impose the equality $V_m^x \stackrel{\text{def}}{=} V_m^{x,1} = V_m^{x,2}$ and $V_m^y \stackrel{\text{def}}{=} V_m^{y,1} = V_m^{y,2}$ to satisfy the jump condition (3). Then, we substitute the linear interpolations and the pressure approximations into the jump relations (4)–(5) to get the following linear system (see [5] to get the expressions of the matrix and vector components):

$$A(1,1)V_m^x + A(1,2)V_m^y = B(1) \quad (8)$$

$$A(2,1)V_m^x + A(2,2)V_m^y = B(2) \quad (9)$$

4 Bubble Rising Test Case

This test case [4] considers an isothermal and incompressible flow of two immiscible fluids. We model a bubble rising which evolution is tracked during 3 s. No-slip boundary conditions are applied on the top and bottom walls whereas a free slip condition is used at the vertical walls. The initial configuration consists of a circular bubble centered at (0.5; 0.75) in a [1; 2] rectangular domain with a 0.15 radius. The physical parameters defining the test case are given in the first case of [4]. We have run the rising bubble simulation with the Eulerian grid sizes

$h = 1/40$, $h = 1/80$ and $h = 1/160$ and the time step $\Delta t = h/16$ with the front-tracking method presented above and the marker velocity calculated with the PERM reconstruction method (FTR-PERM-VBC), the bilinear method (FTR-Bilinear-VBC) or the jump relations velocity based method (FTR-JUMP-VBC) where the -VBC extension indicates the use of the velocity based correction for the volume conservation. A reference interface has been computed using an Eulerian grid size $h = 1/320$ and a time step $\Delta t = h/16$ with the velocity jump based relations for the marker velocity and the velocity based correction to preserve the bubble volume. Figure 1 illustrates the rising bubble interface at time $t = 3$ s for all methods compared to the reference solution with the Eulerian grid sizes $h = 1/80$. All of the velocity calculation methods slightly differs from the reference solution for this Eulerian grid size. For the FTR-PERM-VBC and the FTR-Bilinear-VBC, we observe spurious oscillations appearance at each bottom side of the ellipsoidal bubble. With the FTR-JUMP-VBC method, we do not have non physical wiggles at the interface which is an interesting point of this method.

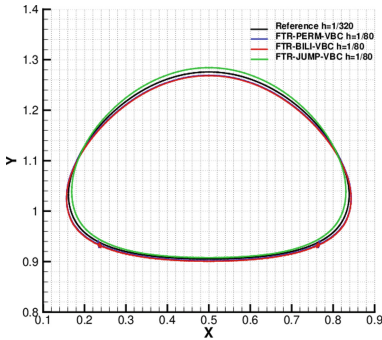


Fig. 1. Velocity interpolation method comparison on the rising bubble test case

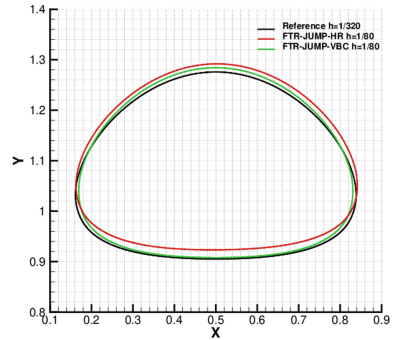


Fig. 2. Volume conservation methods comparison on the rising bubble test case

Since looking at the bubble shapes is clearly not sufficient to show the accuracy of the tracking methods for finer grids, quantities have been defined for this purpose. We use for example the vertical component of the bubble mass center Y_c , and the bubble circularity $C_b = \pi d_a / P_b$, πd_a denoting the circumference of a circle with diameter d_a , which has an area equal to a bubble with perimeter P_b . For a circular bubble, this ratio is equal to 1. Table 1 shows the relative errors ($\|E\|_1$) on the temporal evolution of the quantities Y_c and C_b to the same quantities defined for the reference solution and the respective convergence order. For Y_c and C_b , the relative error decreases with the grid refinement with comparable error levels for all the velocity calculation methods. However, even if the convergence rate is higher with $h = 1/40$ for the FTR-PERM-VBC

and the FTR-Bilinear-VBC methods, the order quickly saturates contrary to the FTR-JUMP-VBC method which converges with a more than linear convergence order approaching quadratic convergence for $h = 1/80$. These results indicate that the velocity jump based method is much more adapted to the interface velocity calculation than the other methods. We can see in Fig. 2 a comparison between the reference and the solution calculated with the FTR-JUMP method and either homothetic rescaling (HR) or the velocity based correction (VBC) for the volume correction. The location of the homothety centre at the centroid for the FTR-JUMP-HR method clearly affects the solution with a noticeable gap between the reference and the FTR-JUMP-HR solution contrary to the FTR-JUMP-VBC method. It is therefore more interesting to consider the flow characteristics (VBC) for the volume conservation.

Table 1. Relative error in norms and convergence rate for the rising bubble test case

h	FTR-JUMP-VBC		FTR-PERM-VBC		FTR-BILINEAR-VBC	
Circularity	$\ E\ _1$	Order	$\ E\ _1$	Order	$\ E\ _1$	Order
1/40	1.86E-02		4.83E-02		5.94E-02	
1/80	8.48E-03	1.1	7.67E-03	2.6	6.56E-03	3.2
1/160	2.84E-03	1.6	3.40E-03	1.2	3.53E-03	0.9
Center of mass	$\ E\ _1$	Order	$\ E\ _1$	Order	$\ E\ _1$	Order
1/40	1.10E-02		1.39E-03		1.02E-03	
1/80	4.59E-03	1.3	9.62E-04	0.5	1.52E-03	-0.6
1/160	1.48E-03	1.6	1.48E-03	-0.6	1.70E-03	-0.2

5 Conclusion

We have proposed a 2D front-tracking method for a sharp interface representation which conserves the volume while preserving the shape of the interface. Our new interface velocity reconstruction based on the jump relations provides the most accurate interface representation. In the rising bubble test case, our approach prevents the wiggles appearance which are induced by other marker velocity interpolation methods. Ongoing works and perspectives are the extension of the method to three dimensions and also an original coupling between the Navier-Stokes equations and the velocity based jump relations using directly the marker velocities and gradients in the finite volume fluxes coming from the momentum equation approximation.

References

1. Tryggvason, G., Bunner, B., Esmaeeli, A., Juric, D., Al-Rawahi, N., Tauber, W., Han, J., Nas, S., Jan, Y.J.: A front-tracking method for the computations of multi-phase flow. *J. Comput. Phys.* **169**(2), 708–759 (2001)

2. McDermott, R., Pope, S.B.: The parabolic edge reconstruction method (PERM) for Lagrangian particle advection. *J. Comput. Phys.* **227**(11), 5447–5491 (2008)
3. O’Rourke, J.: *Computational Geometry in C*, 2nd edn. Cambridge University Press, Cambridge (1998)
4. Hysing, S., Turek, S., Kuzmin, D., Parolini, N., Burman, E., Ganesan, S., Tobiska, L.: Quantitative benchmark computations of two-dimensional bubble dynamics. *Int. J. Numer. Meth. Fluids* **60**, 1259–1288 (2009)
5. Tavares, M., Bi, D.-A.K., Chénier, E., Vincent, S.: A second order conservative front-tracking method with an original marker advection method based on jump relations. To be published in *Communications in computational physics* (2020)



Bayesian Estimation of Turbulent Flow Intermittency

Adaté Tossa¹(✉) , Didier Bernard² , and Richard Emilion³

¹ CEREMADE, Université Paris Dauphine, 75775 Paris, France
oliviertossa@gmail.com

² LaRGE, Université des Antilles, 97157 Pointe-à-Pitre, Guadeloupe
didier.bernard@univ-antilles.fr

³ Institut Denis Poisson, Université d'Orléans, 45067 Orléans, France
richard.emilion@univ-orleans.fr

Abstract. Most of stochastic models for dissipation contain an intermittency parameter which is assumed to be an universal constant. However, a review of the literature reveals a very large range of values for this parameter. We present a model for dissipation with random intermittency and investigate the validity of this model on sample datasets from the Johns Hopkins Turbulence Database and a Sonic anemometer measurement.

Keywords: Turbulent flow · Intermittency · Bayesian estimation · Regimes

1 Introduction

One of the most widely used statistics characterizing the intermittent nature of turbulence is the so called “intermittency parameter”. This parameter hereafter denoted by μ , measures the discrepancy from the Kolmogorov K41 model. It is the exponent in the inertial-range power-law behavior of the autocorrelation of the turbulent energy dissipation rate ϵ , $\langle \epsilon(x)\epsilon(x+r) \rangle \sim (\frac{L}{r})^\mu$ where L is a length scale of the large structures of the flow. It is usually admitted that μ is an universal constant ($\simeq 0.2$ for the Kolmogorov lognormal model). However, a review of the literature reveals a relatively large range of measured values. According to the nature of the flow, to the domain of study, and to the particular formulations that are adopted for estimation, these values can vary from 0.15 to 0.8 [1]. This suggests that it is possible to have several levels of intermittency in a turbulent flow. D. Bernard et al. [2], investigated a possible dynamic value of μ over time for some specific flows. They considered a stochastic integral representation of the dissipation rate ϵ introduced by F. Schmitt and Marsan [9] and extended this model to a new model in a Markov Regime-Switching setting in which μ and a scale parameter λ are assumed to be random processes driven by a hidden continuous time Markov chain $X(t)$.

In this article, we investigate the validity of the model proposed in [2] on sample datasets from the Johns Hopkins Turbulence Database (JHTDB). The paper is organized as follows. Section 2 presents a description of the data used for the analysis. In Sect. 3 we recall the stochastic integral cascade model of F. Schmitt [9] and compute several hundred values of μ . A plot of the probability distribution functions (pdf) of these values shows that each pdf is a mixture of distributions. This reveals the existence of regimes (states of dissipation corresponding each to a level of intermittency with a specific value of μ) in the dissipation process. The fourth section is devoted to the model with several levels of intermittency. We precise the model and describe the Bayesian setting for the estimation of the parameters. In Sect. 5, we estimate the values of μ for the JHTDB datasets. We use the Viterbi Algorithm (a dynamic programming algorithm) to choose the number of regimes and the dynamic of these regimes in the studied time series. We finally use a Bayesian nonparametric approach to estimate the parameters. We conclude in the last section by pointing out some consequences of the possibly random nature of the intermittency in turbulence modeling, indicating some elements for future research.

2 Data Description

Two datasets are used in this paper: an active grid generated flow dataset and an atmospheric turbulence dataset. The active grid generated flow dataset is a sample data from the JHTDB. As described in [5], these data are obtained by measurements performed downstream of an active grid that generates high-Reynolds-number turbulence in a range of Taylor microscale Reynolds numbers Re_λ of about 630 to 720, with a turbulence intensity of 17.4%. The grid size M , is 0.152 m. The measurement locations in the streamwise (longitudinal) direction are at $x/M = 20, 30, 40$ and 48 distance from the grid. The signals are sampled at $f_s = 40$ kHz, low-pass filtered at a frequency of 20 kHz. We consider in this study a sampling time of 30 s, so the total number of data points for each measurement location is $12 \cdot 10^5$. The atmospheric turbulence dataset comes from a Sonic anemometer measurements conducted during two years, in a mangrove forest [3] with a Campbell CSAT3 ultrasonic anemometer. Among other variables, wind velocity was recorded at a frequency 20 Hz by its 3D components u , v and w .

3 Causal Log-Normal Cascade Model

3.1 Model Definition

Discrete multiplicative cascade models represent the dissipation rate at a position x of a turbulence developed from a larger scale L to a smaller scale l_o in n steps as a product $\epsilon(x) = \prod_{p=1}^n W_{p,x}$ of independent and identically distributed random variables $W_{p,x}$ having a common distribution W . Continuous cascade models are obtained from the discrete ones by keeping the total scale

ratio $A = L/l_0$ fixed and letting $n \rightarrow +\infty$. It has been shown [8] that for a scale ratio $1 < \lambda < A$, the process $\gamma_\lambda(x) = \log(\epsilon_\lambda(x))$ can be written in the form of a stochastic integral $\gamma_\lambda(x) = \int_1^\lambda M\left(\frac{cd\eta}{\eta}, D_\eta I_0(x)\right)$ where $c > 0$ is a parameter, M is a stochastic measure, $I_0(x)$ is an interval of length $\tau = L/\lambda$ centered at x and η is the integration variable. D_η is a dilatation operator of factor η . When considering continuous cascades developing in time, the dissipation rate can be written as $\epsilon_\lambda(t) = \lambda^{-c} \exp\left(\int_{t-\tau}^t (t-u)^{-1/\alpha} dL_\alpha(cu)\right)$ where L_α is a Lévy measure. This equation corresponds to the exponential of a fractional integration of order $1 - 1/\alpha$ of a Lévy-stable noise. The log-normal case corresponding to $\alpha = 2$ and L_α replaced by the Wiener measure, leads to the stochastic equation studied by F. Shmitt in [9]

$$\epsilon_\lambda(t) = \lambda^{-\frac{\mu}{2}} \exp\left(\mu^{\frac{1}{2}} \int_{t+1-\lambda}^t (t+1-u)^{-1/2} dB(u)\right) \quad (1)$$

where t stands for time and $B(u)$ is a standard Brownian motion. In this case,

$$\gamma_\lambda(t) = \log(\epsilon_\lambda(t)) = -\frac{\mu}{2} \log \lambda + \mu^{1/2} \int_{t+1-\lambda}^t (t+1-u)^{-1/2} dB(u)$$

is a stationary process with mean $-\frac{\mu}{2} \log \lambda$ and autocorrelation function defined for time increments ζ by

$$C_{\gamma_\lambda}(\zeta) = \langle \gamma_\lambda(t) \gamma_\lambda(t + \zeta) \rangle \approx A_\lambda - \mu \ln \zeta \quad (2)$$

where A_λ is a constant depending weakly on λ [9].

3.2 Estimating the Intermittency Parameter

We estimate the dissipation rate under the assumption of isotropic turbulence by the relation $\epsilon = \frac{15\nu}{U^2} \left\langle \left(\frac{\partial u}{\partial t}\right)^2 \right\rangle$ where ν is the kinematic viscosity, u is the longitudinal velocity and U is the mean longitudinal velocity. The angle brackets denote averaging. For this analysis, we consider the above expression normalized by the ratio $15\nu/U^2$. So, the time increments of the longitudinal velocity are used to compute the energy dissipation time series $\epsilon(t) = (V(t + \Delta t) - (t))^2 / \Delta t^2$, with $\Delta t = 2 \cdot 10^{-4}$ s for the active grid generated flow dataset and 0.05 s for the atmospheric turbulence dataset. We use Eq. (2) to estimate μ as the linear regression coefficient of $C_{\gamma_\lambda}(\zeta)$ versus $\log(\zeta)$. For the active grid turbulence, the results are almost identical for all measurement locations, that is 0.42 for $x/M = 20, 40$ and 48, and 0.41 for $x/M = 30$. The same observation can be made for the atmospheric turbulence where we obtained $\mu = 0.28$ for the low speed wind (LSW) and 0.33 for high speed wind (HSW). Figure 1 displays the pdf of μ estimated on 11000 sliding windows of 5 s lengths for the active grid datasets and 5000 windows of 5 min for the Sonic anemometer datasets. All the estimates match the known range of values of μ ; however, the form of the pdf reveals that μ is not constant. Indeed, if this was the case the distributions should be approximately Gaussian. The ones in Fig. 1 appear more like mixtures of Gaussian distributions than a unique Gaussian distribution. This reveals that there are several possible values of μ corresponding to different levels of intermittency in the dissipation process.

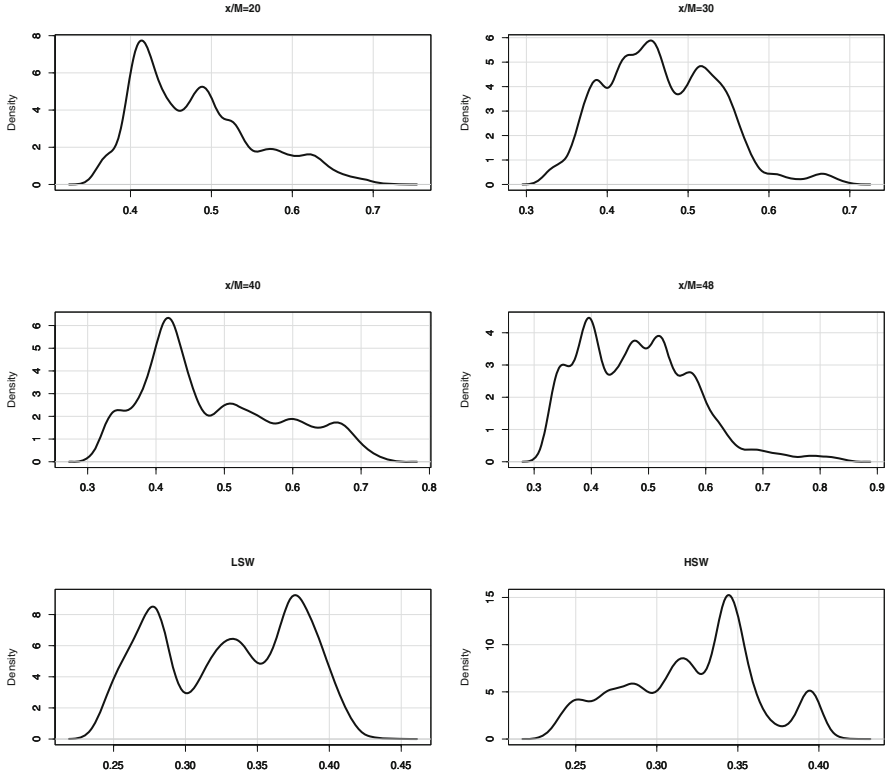


Fig. 1. Estimated pdf of μ for the active grid datasets ($x/M = 20, 30, 40$ and 48) and the atmospheric turbulence datasets (LSW and HSW)

4 Multilevel Intermittency Model

Our observation from the results of the previous section is that in some turbulent flows, the intermittency of the energy dissipation process may not be a homogeneous phenomenon. Such flows can display several levels of intermittency corresponding each to a regime in the dissipation process. The process therefore switches randomly from one regime to another over time. The D. Bernard et al. model (3) takes into account this behavior by assuming that the parameters μ and λ are themselves stochastic processes governed by a continuous-time Markov chain

$$\gamma(t) = -\frac{\mu_{X(t)}}{2} \log(\lambda_{X(t)}) + \mu_{X(t)}^{1/2} \int_{t+1-\lambda_{X(t)}}^t (t+1-u)^{-1/2} dB(u) \quad (3)$$

where $B(u)$ is a Brownian motion, $X = (X(t))_{t \geq 0}$ is a continuous time Markov chain taking values in a finite set $S = \{1, 2, \dots, K\}$ that represents the regimes. This model assumes K levels of intermittency (regimes) characterized by their

intermittency parameters (μ_1, \dots, μ_K) and the scale parameters $(\lambda_1, \dots, \lambda_K)$. The meaning of this setting is that during regime i the intermittency parameter and the scale parameter are constant and equal to μ_i and λ_i respectively. If, at a given time t , the state of the chain is i , that is if $X(t) = i$, ($i \in S$), then the dissipation process is in regime i so that $\mu_{X(t)} = \mu_i$ and $\lambda_{X(t)} = \lambda_i$.

5 Estimation of the Multilevel Intermittency Model

5.1 Procedure

From model (3), one can observe that if μ and λ are known and a sample path X of the Markov chain is given, then $\gamma(t)$ is a Gaussian process. In probabilistic terms, this model can be written in the form $(\gamma|X, \mu, \lambda) \sim \mathcal{P}$, where \mathcal{P} is a Gaussian distribution; so, using the Baye's theorem, one can make inference about μ , λ and X , if appropriate prior distributions are defined for each of these parameters. A Bayesian based algorithm proposed in [2] is used here to estimate the values of μ for the multilevel intermittency model. The estimation procedure is described as follows: first, we determine the number of states and the most likely path of the hidden Markov chain that best describes the observed data. Then, we compute the transition probability matrix of the chain and finally estimate μ and λ .

To choose the number of states of the hidden Markov chain, we try different numbers K of states and look at the model likelihood as a function of K . We pick the value of K which gives the smallest value of the Akaike Information Criterion (AIC). We use the Viterbi algorithm to find the most likely path of the chain that best fit the data. The transition probability matrix $P = (p_{i,j})_{i,j=1,\dots,K}$ is estimated as follows: let n_{ij} be the number of times the chain made a transition from state i to state j in the most likely path. We estimate the transition probability $p_{i,j}$ by maximum likelihood using the estimates $\hat{p}_{i,j} = n_{i,j} / \sum_{k=1}^K n_{i,k}$. The parameters μ and λ are estimated using the aforementioned algorithm.

5.2 Application to JHTDB Datasets

For the active grid flow dataset, our selection procedure described in Sect. 5.1 identified three regimes for the measurement locations 20 M, 40 M and 48 M and two regimes for the location 30 M. For the atmospheric turbulence measurement three regimes were identified for both the low and the high speed wind datasets. For each dataset the algorithm was run on 50,000 generated sample paths of the Markov chain. 1000 burn in iterations were executed followed by 10,000 other iterations. For each regime, we chose the mean of the values generated by the 10,000 iterations as an estimate of μ . The results are presented in Table 1 and Table 2 where the regimes are numbered in increasing order of the values of μ . This values are in accordance with the pdf of μ presented in Fig. 1. Note that during the process, the scale parameters were also estimated but are not presented here since our interest is on the intermittency parameter μ .

Table 1. Values of μ for the active grid dataset

	Regime 1	Regime 2	Regime 3
20 M	0.41	0.49	0.61
30 M	0.41	0.55	
40 M	0.42	0.53	0.65
48 M	0.38	0.50	0.70

Table 2. Values of μ for the atmospheric turbulence dataset.

	Regime 1	Regime 2	Regime 3
LSW	0.42	0.53	0.65
HSW	0.26	0.33	0.39

6 Conclusion

The datasets analyzed in this study show that, from a strictly statistical point of view, the intermittency parameter is not a constant. This means that the dissipation process in some turbulent flows can display several levels of intermittency. In such cases, it would be more appropriate to consider the intermittency parameter as a random variable. The results obtained in this analysis, confirm those presented in [2]. Furthermore, the proposed model considers a finite number of discrete values for the intermittency parameter. Future works could investigate the extension of this model to continuous processes where the number of states of the hidden Markov chain introduced in Eq. (3) becomes infinitely large.

References

1. Anselmet, F.: Turbulent flows and intermittency in laboratory experiments. *Planet. Space Sci.* **49**, 1177–1191 (2001)
2. Bernard, D., Tossa, A., Emilion, R., Iyer, S.K.: A model for dissipation: cascade SDE with Markov Regime-switching and Dirichlet prior. In: Deville, M., L e, TH., Sagaut, P. (eds.) *Turbulence and Interactions. Notes on Numerical Fluid Mechanics and Multidisciplinary Design*, vol. 110, pp 79–86. Springer, Heidelberg (2010). https://doi.org/10.1007/978-3-642-14139-3_9
3. D’Alexis, C.: Mesures exp erimentales dans les basses couches de l’atmosph ere tropicale insulaire (Guadeloupe): Micro-m eteorologie et composition chimique des masses d’air nocturnes en zone de mangrove. Th ese de doctorat, Universit e des Antilles et de la Guyane, NNT: 11GUY0438 (2011)
4. Ferguson, T.S.: A Bayesian analysis of some non parametric problems. *Ann. Stat.* **1**, 209–230 (1973)
5. Kang, H.S., Chester, S., Meneveau, C.: Decaying turbulence in an active-grid-generated flow and comparisons with large-eddy simulation. *J. Fluid Mech.* **480**(3), 129–160 (2003)
6. Mandelbrot, B.B.: Possible refinement of the lognormal hypothesis concerning the distribution of energy dissipation in intermittent turbulence. In: Rosenblatt, M., Van Atta, C. (eds.) *Statistical Models and Turbulence*, p. 333. Springer (1972)
7. Novikov, E.A., Stewart R.W.: The Intermittency of turbulence and the spectrum of energy dissipation fluctuations. In: Akad, I.Z.V., Nauk, S.S.S.R. ser., *Geofiz*, vol. 3, p. 408 (1964)
8. Schmitt, F.G., Marsan, D.: Stochastic equations generating continuous multiplicative cascades. *Eur. Phys. J. B* **20**, 3–6 (2001)
9. Schmitt, F.: A causal multifractal stochastic equation and its statistical properties. *Eur. Phys. J. B* **34**, 85–98 (2003)



Lagrangian Scheme for Scalar Advection-Diffusion. Application to Pollutant Transport

Benoît Trouette¹(✉), Georges Halim Atallah^{1,2}, and Stéphane Vincent¹

¹ Université Paris-Est, Laboratoire Modélisation et Simulation Multi Echelle, MSME UMR 8208, CNRS, UPEC, UPEM, 77454 Marne-la-Vallée, France
{benoit.trouette,georges.halimatallah,stephane.vincent}@u-pem.fr

² INRS, French National Research and Safety Institute for the Prevention of Occupational Accidents and Diseases, Lab. Aeraulic Engineering, Vandœuvre, France

Abstract. A Lagrangian scheme devoted to the approximation of advection term in advection-diffusion equation (ADE) is proposed to deal with large values of Péclet number. Advection and diffusion of circular concentration in a vortex flow are considered for validation purpose. The Lagrangian scheme reduces the numerical diffusion to almost computer error and provides better results than other Eulerian classical schemes of the literature. The injection of a pollutant in a cavity is finally illustrated.

Keywords: Lagrangian scheme · Advection-diffusion · Large Pe number

1 Introduction

The tracking of pollutants in gas and liquid is a major problem to address in atmospheric environment, air quality characterization and industrial material processes. The design of schemes for the hyperbolic advection term of the transport equation for pollutant concentration has been widely studied, with mostly Eulerian schemes relying on splines reconstruction, high-order spectral, finite difference and finite volume schemes, combined with limiters belonging to the class of TVD or WENO approaches. Reviews and comparisons of these schemes are for example given in [5,6]. The conclusion of all studies is that when the molecular or turbulent diffusion is low compared to the advection, all schemes are diffusive or dispersive, providing unexpected spreading or unphysical oscillations of the numerical solutions. In the present work, a new Lagrangian scheme [6] is proposed for the advection-diffusion equations that avoids diffusion and respects the monotonicity of the solution.

2 Model and Numerical Methods

The framework of the present work is the simulation of incompressible fluid flows with a Finite-Volume method on Cartesian staggered grids. The advection-

diffusion equation (ADE) of a quantity Φ (temperature, pollutant concentration, ...) is considered. Γ is the diffusivity and \mathbf{u} the fluid velocity, either prescribed or given by the last iteration of the Navier-Stokes resolution. Classical Eulerian Centered, Upwind, Quick, TVD or WENO schemes are generally used for discretizing the advection term. Solving the ADE with centered schemes introduce oscillations and non bounded solutions for a low diffusivity coefficient Γ or high Péclet cell number values, given by $Pe = \|\mathbf{u}\|\Delta x/\Gamma$. On the contrary, low order upwind schemes induce important numerical diffusion that alter the physical meaning of the solution, as centered schemes do. A Sequential Operator Splitting (SOS) method [2,4] is utilized. Introducing a time step Δt , ADE is split in time into two substeps: advection

$$\frac{\partial \Phi}{\partial t} + \nabla \cdot (\mathbf{u}\Phi) = 0 \quad (1)$$

is first solved along the time interval $]t, t + \Delta t]$, providing intermediate solution Φ^* . Then, diffusion

$$\frac{\partial \Phi}{\partial t} - \nabla \cdot (\Gamma \nabla \Phi) = 0 \quad (2)$$

is solved with initial condition $\Phi(t) = \Phi^*(t + \Delta t)$. It provides the approximated solution of $\Phi(t + \Delta t)$. The SOS is second-order accurate at each time step [2]. More sophisticated SOS can be found in [2,4]. Let us consider $\Phi^n = \Phi(t^n)$ as the discrete value of Φ at time $t^n = t^0 + n\Delta t$, n being the iteration number and $\Delta t = t^{n+1} - t^n$ the time step. In practice, the intermediate solution Φ^* after advection is updated solving Eq. (1) with an explicit Lagrangian scheme (see below) while Eq. (2) is discretized with an implicit Eulerian centered scheme and direct MUMPS [1] or preconditioned MILU-BICGSTAB II iterative solvers are used to obtain solutions. In addition to the Lagrangian scheme developed in this paper, a non-conservative Weno scheme of order 5 [3] will be used, coupled with a third order Runge-Kutta time integration. For comparison, results obtained with a QUICK scheme are also presented. The Lagrangian scheme for ADE is an extension of VSM scheme from [6]. A number of M markers (Lagrangian particles), located at \mathbf{X}_m and bringing volumes δV_m , are seeded in the Eulerian grid (Fig. 1) devoted to solving of conservation equations. Initially, markers are equality placed in each cell according to a number of particles per direction and per cell (*ppdpc*). A simulation then handles $ppdpc^d \times N_x \times N_y \times N_z^{d-2}$ Lagrangian objects, where d is the space dimension and N_x, N_y and N_z are the numbers of scalar cells in each space direction. Furthermore, the markers carry the local information, ϕ_m , of the Eulerian field Φ . At initial time $\phi_m^0 = \Phi^0(\mathbf{X}_m^0)$. The markers are then advected solving the Lagrangian equation $\frac{d\mathbf{X}_m}{dt} = \mathbf{u}|_{\mathbf{X}_m}$. The material derivative on marker position is integrated in time with a second order Runge-Kutta scheme. The velocities at particle positions follow a linear Q1 interpolation. As illustrated in Fig. 1 for marker 2, the volume δV_m of a marker can contribute to the computation of Φ^* on neighboring cells. The value of Φ^{n+1} is then obtained solving the unsteady diffusion equation (2). Finally, the local (marker) information is updated according to the variation of Φ during the diffusion step at the particle position:

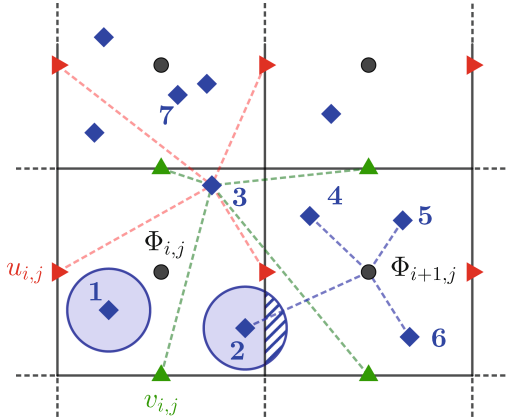


Fig. 1. Sketch of the Lagrangian particles (blue diamond) on a 2D staggered grid. Velocities at particles position are interpolated with surrounding grid velocities (see marker 3 for example, red left triangle and green triangle stand for horizontal and vertical components, respectively). The Eulerian information is computed with averages of markers included in the corresponding cell (see cell $\Omega_{i+1,j}$ for example). (Color figure online)

$$\left. \frac{\partial \phi_m}{\partial t} \right|_{\mathbf{x}_m^{n+1}} = \left. \frac{\partial \Phi}{\partial t} \right|_{\mathbf{x}_m^{n+1}} \tag{3}$$

The number of particles per cell, M_c , varies over time. It can increase or decrease according to local streamline convergence or divergence. It can be interesting to remove or add particles in each cell in order to save computational time and maintain physical relevancy of the solution. This way, M_c is reduced to a constant value at each iteration by using the following treatment:

- In each cell where $M_c > ppdp^d$, the distances between particles and its neighbors are computed for every pair. The particle having the lower distance (according to a norm, L_2 for example) is removed (particle 7 in Fig. 1) and this procedure is applied until $M_c = ppdp^d$.
- In cells where $M_c < ppdp^d$, new particles are randomly introduced until $M_c = ppdp^d$. By noting M_c^0 the initial number of markers, we have to insert $M_i = ppdp^d - M_c^0$ particles.

As discussed in the next section, these reseeding operations can lead to spurious effect on isovalues of the scalar field.

3 Advection-Diffusion of a Concentration Peak

A peak of concentration is placed in a domain defined by $(x, y) \in [0, L]^2$ with velocity field $\mathbf{u}(x, y) = -a(y - y_c) \mathbf{e}_x + a(x - x_c) \mathbf{e}_y$ corresponding to a block

rotation motion around the fixed point (x_c, y_c) . With $a = \pi/2$ and $x_c = y_c = L/2$, a marker placed in this field needs $T = 4$ s to make a complete turn and return back to its initial position. In this velocity field, a peak of concentration of radius R is initialized such that

$$\Phi(r, t = 0) = \begin{cases} \frac{R-r}{R} & \text{if } r < R \\ 0 & \text{otherwise} \end{cases} \quad (4)$$

where $r = \sqrt{(x - x_p)^2 + (y - y_p)^2}$ is the radial coordinate centered around (x_p, y_p) the position of the peak center. At the initial time, $(x_p, y_p) = (L/2, 3L/4)$. The analytical solution over time is given by

$$\Phi(r, t) = \sum_{n=1}^{\infty} A_n J_0(\lambda_n r) \exp(-\lambda_n^2 \Gamma t) \quad (5)$$

where J_0 is the zeroth order Bessel function of the first kind and λ_n the n^{th} root of $J_0(\lambda) = 0$. The A_n coefficients are obtained as:

$$A_n = \frac{2RJ_1(R\lambda_n)}{\lambda_n J_1(\lambda_n)^2} - \frac{2}{RJ_1(\lambda_n)^2 \lambda_n^3} \left((R\lambda_n)^2 J_1(R\lambda_n) - \frac{\pi R \lambda_n}{2} [H_0(R\lambda_n) J_1(R\lambda_n) - H_1(R\lambda_n) J_0(R\lambda_n)] \right) \quad (6)$$

with J_1 the first order Bessel function of the first kind, and H_0 and H_1 the Struve functions of order 0 and 1, respectively. The numerical solutions obtained with different schemes are compared to this reference solution after a simulation time of $T = 4$ s and the diffusion coefficient Γ varies from 10^{-4} to 10^{-6} m²/s. The domain is discretized with $N_x = N_y = N$ and Δt is chosen according to CFL condition defined by $\frac{a}{2} \Delta t / \Delta x$ ($a/2$ is the velocity at the peak center). A first set of results is given in Fig. 2 for $\Gamma = 10^{-6}$ m²/s and different schemes. On one hand, The QUICK scheme introduces an excessive numerical diffusion and is

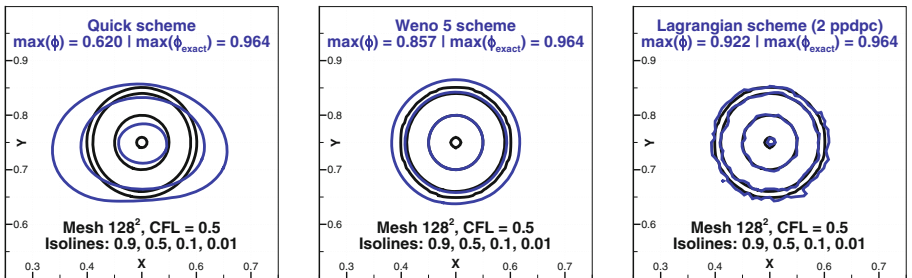


Fig. 2. Zoom on the numerical (blue lines) and reference solutions (black) after one turn for different schemes on a $N^2 = 128^2$ mesh and for $\Gamma = 10^{-6}$ m²/s. (Color figure online)

sensitive to the advection direction. The numerical diffusion is reduced with the Weno5 scheme. On the other hand, oscillations disrupt the numerical solution of the Lagrangian scheme but this latter do not introduce numerical diffusion and presents, on this mesh, a better solution than the other schemes. Note that the Lagrangian scheme, with 2 particles per direction and per cell (*ppdpc*), is able to represent 95% of the peak value. The second set of results (Fig. 3) presents, on the same mesh, the results obtained with the Lagrangian scheme and different values of *ppdpc*. The first observation is that the oscillations can be reduced increasing by the *ppdpc* value. In the same time, the quality of the solution increase, *i.e.* 99.2% of the peak value is correctly represented for *ppdpc* = 8. It has been verified that the oscillations come from the re seeding procedures. Indeed, all the markers follow circle trajectories and come back to their initial position after time T . Removing re seeding procedures in this particular rotation motion case suppress the oscillations even with a small *ppdpc* value. However, in practical cases, enrichment is mandatory to balance particle lack in sheared zones.

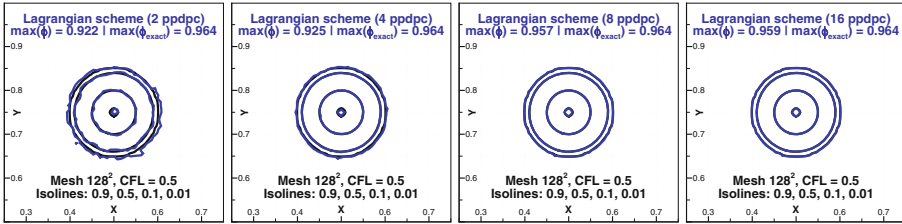


Fig. 3. Zoom on the numerical (blue lines) and reference solutions (black) after one turn for different values of *ppdpc* on a $N^2 = 128^2$ mesh and for $\Gamma = 10^{-6}$ m²/s. (Color figure online)

4 Injection of a Pollutant in a Cavity

The Lagrangian scheme is applied to polluted air injected into a rectangular enclosure containing the same fluid at rest. A round jet enters with a flow rate of 40 ℓ /min. Gas exits through an open circular outlet at atmospheric pressure. The Reynolds number based on the injector diameter is $Re = 1500$. The numerical solution is obtained on a mesh with $64 \times 32 \times 32$ cells and without any turbulence modeling. The dynamical solution is used in the ADE equation. The Fig. 4 presents the concentration fields is observed after 1.5 s. Iso-concentration for the Weno5 and Lagrangian with 4 *ppdpc* schemes are shown. The left part of the cavity presents the iso-concentration obtained with the Lagrangian scheme while the right part provides the Weno5 results. The numerical diffusion introduced by the Weno scheme prevents it from picking up the signal correctly while the Lagrangian scheme is able to represent high values of the concentration field.

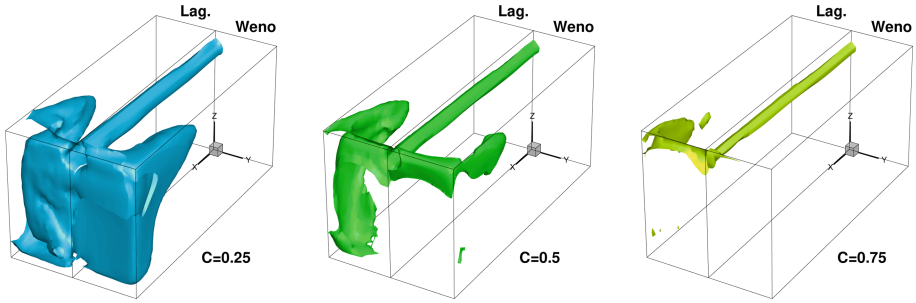


Fig. 4. Iso-concentration $C = 0.25, 0.5$ and 0.75 plotted for Lagrangian and Weno5 scheme at 1.5 s.

5 Concluding Remarks

The efficiency of a fully Lagrangian scheme has been demonstrated for the resolution of an ADE. It is even more effective than the ratio between advection and diffusion is important. The extra cost of the particle tracking method used by the Lagrangian scheme is counterbalanced by the fact that the advection process does not introduce numerical diffusion, respect monotonicity of the solution and allows coarser meshes to use in comparison to classical Eulerian schemes. The major drawback of the Lagrangian approach is the spurious oscillations introduced by the reseeding procedures. This will be considered in future works, as well as local varying Lagrangian seeding of particles in order to reduce the global cost of the scheme.

Acknowledgment. The authors are grateful for access to the computational facilities of the French GENCI under project number A0032B06115.

References

1. Amestoy, P.R., Duff, I.S., Koster, J., L'Excellent, J.-Y.: A fully asynchronous multi-frontal solver using distributed dynamic scheduling. *SIAM J. Matrix Anal. Appl.* **23**, 15–41 (2001)
2. Chertock, A., Kurganov, A., Petrova, G.: Fast explicit operator splitting method for convection-diffusion equations. *Int. J. Numer. Methods Fluids* **59**, 309–332 (2006)
3. Jiang, G.-S., Shu, S.-W.: Efficient implementation of weighted ENO schemes. *J. Comput. Phys.* **126**, 202–228 (1996)
4. Geiser, J., Elbiomy, M.: Splitting Method of Convection-Diffusion Methods with Disen- tanglement methods. Humboldt-Universität zu Berlin, Mathematisch-Naturwissenschaftliche Fakultät II, Institut für Mathematik (2011)
5. Nguyen, K., Dabdub, D.: Two-level time-marching scheme using splines for solving the advection equation. *Atmos. Environ.* **35**, 1627–1637 (2001)
6. Vincent, S., Balmigère, G., Caltagirone, J.-P., Meillot, E.: Eulerian-Lagrangian multiscale methods for solving scalar equations - application to incompressible two-phase flows. *J. Comput. Phys.* **229**, 73–106 (2010)



Spreading Time of Liquid Droplets Impacting on Non-wetting Solid Surfaces

Yang Xu^(✉), Stéphane Vincent, Q.-C. He, and H. Le-Quang

Université Paris-Est, Laboratoire de Modélisation et Simulation Multi Echelle,
UMR 8208 CNRS, 5 Bd Descartes, 77454 Marne-la-Vallée Cedex 2, France
xuyang0513@gmail.com, {stephane.vincent,
qi-chang.he, quang-hung.le}@u-pem.fr

Abstract. The spreading time that a droplet takes to reach its maximum spreading state is a parameter of paramount importance. We study the impact of a liquid droplet on a super-hydrophobic surface. A contact angle of $\theta = 170^\circ$ is used as the numerical input for the non-wetting property of the surface. Numerical simulations to understand the effects of initial impact conditions on spreading time of liquid droplets onto solid surfaces are conducted in a regime where $1 < We < 300$ and $1 < Re < 300$. We demonstrate that the spreading time t_{max} is jointly determined by the inertial, capillary and viscous forces. The spreading time t_{max} decreases exponentially with the increase of the impact velocity V_0 and surface tension σ . Regarding the influences of dynamical viscosity on spreading time, the effects of dynamic viscosity is secondary at low Weber numbers ($We < 5$), while in a moderate Weber number regime ($5 < We < 300$), the effects of dynamic viscosity should be taken into account. Finally, in our study, we successfully scale the dimensionless spreading time in the form as $t_{max}^*/Re^{1/5} \sim WeRe^{-2/5}$.

Keywords: Droplet impact · Two-phase flow · Maximum spreading

1 Introduction

Numerous studies on the impact of a liquid droplet onto solid surface have been conducted to understand the underlying physics, due to its numerous physical phenomena in nature and widespread applications in industry [3, 5, 9, 21]. The attractive dynamic process and different outcomes of droplets impacting on solid surfaces could be referred in several reviews [8, 23] and the references included. Droplet impact dynamics is largely dependent on the impact velocity, properties of the liquid, surface conditions and the environmental conditions. These parameters determine the interactions between the liquid droplet and target surface and the outcomes of droplet impact. For most of the applications, the priority is controlling the contact area between the impacting droplet and the target surface. The contact area is described by the maximum spreading diameter

Supported by a French government grant managed by ANR.

D_{max} . Numerous experimental works and numerical studies have been carried out on the maximum spreading diameter of a droplet impacting on smooth and rough solid surfaces [2, 9–11, 15, 17]. Based on energy conservation, the balance among kinetic energy, surface energy and dissipation work during spreading, several analytical models predicting the maximum spreading diameter are proposed [7, 10, 12–14, 16, 18]. The major differences between the prediction models lie in the estimation of dissipation work during spreading phase. The dissipation work is calculated by integrating the dissipation function over the spreading time and the the volume where dissipation occurs. Chandra and Avedisian (1991) assumed the dissipation work takes place in the whole droplet, Pasandideh-Fard et al. (1996) proposed that most of the dissipation occurs in the boundary layer near the target surface. Based on these previous studies, Huang and Chen (2018) take the dissipation near the contact line into account.

There are fewer studies dedicated to the investigation on spreading time t_{max} . The significance of studying the spreading time t_{max} not only lies in the calculation of the viscous dissipation energy, but also in illustrating the spreading behaviour of the droplet [1, 7, 14, 16, 18]. The spreading time t_{max} here is normalized by the ratio D_0/V_0 , denoted by t_{max}^* . In the early studies, Chandra and Avedisian (1991) approximated the spreading time t_{max} as,

$$t_{max} = D_0/V_0, \quad (1)$$

which is the time for the droplet height decreasing from its highest value D_0 to 0 at impact velocity V_0 [1]. Pasandideh-Fard et al. (1996) derived the spreading time as,

$$t_{max} = (8/3) \cdot D_0/V_0, \quad (2)$$

based on the simple geometric assumption that the splat at maximum spreading is approximated by a cylinder [14]. The Eq. (2) has been widely adopted in theoretical models predicting the maximum spreading diameter D_{max} [4, 13, 16, 18]. The models Eq. (1) and Eq. (2) are unphysical as they assume spreading time t_{max} is only determined by the initial diameter D_0 and impact velocity V_0 of the droplet by ignoring the influences of the surface tension σ , dynamic viscosity μ and the wettability of the target surface. Lee et al. (2016b) conducted experiments to show that the spreading time t_{max} decreases with surface tension σ and proposed a new scaling of t_{max} with maximum spreading factor ξ_{max} and surface tension σ as,

$$t_{max} = bD_0\xi_{max}/V_0, \quad (3)$$

where parameter b equals to the ratio of surface tension of droplet liquid to a reference liquid [11]. Recently, Huang and Chen (2018) compared their experimental results for water droplets impacting on parafilm surface with these two relations Eq. (2) and Eq. (3) [7]. The comparison shows that the dimensionless maximum spreading time can not be seen as constant, and the difference between prediction Eq. (3) and experimental results become larger with the increase of Weber number.

In this work, we use the homemade code Thetis, the modified 1-fluid model and improved Smooth VOF methods to conduct accurate two-phase flow simulations including the wetting effects, which has been validated to experimental results [6, 19, 20, 22]. We aim to quantitatively demonstrate the influences of impact velocity V_0 , surface tension σ and dynamic viscosity μ on the spreading time t_{max} in terms of Weber and Reynolds number ($We = \rho D_0 V_0^2 / \sigma$, $Re = \rho V_0 D_0 / \mu$) from our numerical simulations. The present paper starts with the influences of droplet's physical properties on the spreading time t_{max} . The droplet's major physical properties are the impact velocity V_0 , surface tension σ and dynamic viscosity μ are varied in a systematic way. The contact angle we applied between the droplet and the surface is set as 170° , i.e., the droplet impacts on a non-wetting surface. The spreading time t_{max} can be scaled as an exponential function of Weber and Reynolds number. Finally, the scaling of t_{max}^* is compared with results measured in experiments and some conclusions are made.

2 The Dependence of t_{max} on Weber and Reynolds Number

In our simulations, the droplet is chosen as a molten ceramic with initial diameter $D_0 = 30 \mu\text{m}$, density $\rho = 5700 \text{ kg/m}^3$, surface tension $\sigma = 0.5 \text{ N/m}$ and dynamic viscosity $\mu = 0.03 \text{ Pa} \cdot \text{s}$. We investigate the influences of the physical properties of a droplet on the spreading time t_{max} by varying the impact velocity V_0 , surface tension σ and dynamic viscosity μ on a non-wetting surface. The Fig. 1 plots the dimensionless spreading time t_{max}^* ($= t_{max} V_0 / D_0$) versus Reynolds number, where the impact velocity and dynamic viscosity varies while keeping surface tension constant. For the case of lower Weber number $We < 5$, the influences of Reynolds number on t_{max}^* could be ignored compared to those in moderate Weber number regime $5 < We < 300$. The explanation could be said as for higher Weber number, as the droplet spreads much larger, the viscous dissipation during spreading becomes an important role in countering the inertial force of the droplet. The dimensionless spreading time t_{max}^* remains largely dependent on the impact velocity (Weber number). For the results in the cases with lower Weber number ($We < 5$), the exponent of Re is in order of 0.02. The results obtained with moderate Weber number ($5 < We < 300$) show that

$$t_{max}^* \sim Re^{0.1}. \quad (4)$$

The Fig. 2 plots t_{max}^* versus Weber number, in which the impact velocity and the surface tension are varied. In logarithmic scale, the dimensionless spreading time t_{max}^* could be scaled as an exponential function of We . Based on these two figures Fig. 1 and Fig. 2, we observe that the dimensionless maximum spreading time t_{max}^* is an exponential function in terms We and Re . Recall the crossover function $Re^{-1/5} \cdot (WeRe^{-2/5})$ used to scale the maximum spreading factor [9], and plot the maximum spreading time results in Fig. 1 and Fig. 2 as $t_{max}^* / Re^{1/5} \sim WeRe^{-2/5}$, shown in Fig. 3,

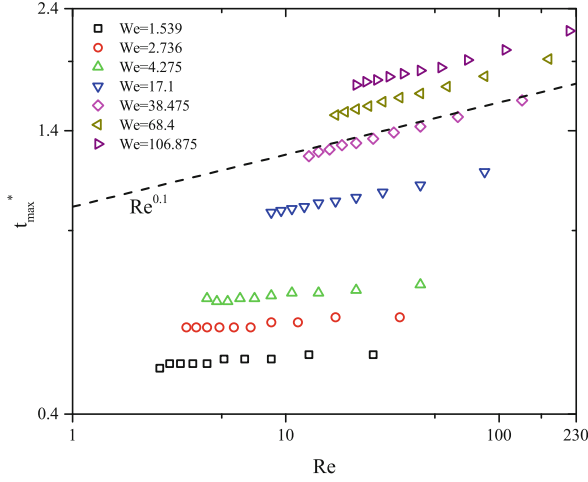


Fig. 1. The dimensionless maximum spreading time t_{max}^* plotted against Reynolds number for the impinging droplets with varied dynamic viscosity impacting on non-wetting surfaces.

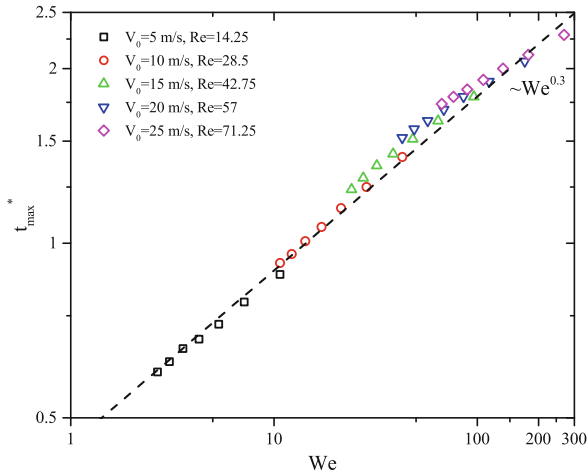


Fig. 2. The dimensionless maximum spreading time t_{max}^* plotted against Weber number for the impinging droplets with varied surface tension impacting on non-wetting surfaces.

$$t_{max}^*/Re^{1/5} = 0.375(WeRe^{-2/5})^{0.264}. \quad (5)$$

To validate this relation Eq. (5) we obtained, the experimental results of maximum spreading time measured in literature [7, 11] are rescaled and replotted in Fig. 4. Lee et al. (2016b) measured the maximum spreading time of ethanol, water and glycerol droplet on steel surfaces [11]. On steel surface, ethanol main-

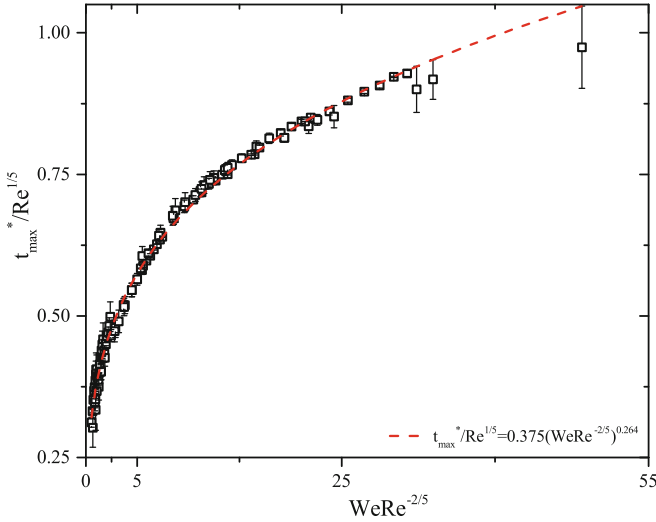


Fig. 3. The function $t_{max}^*/Re^{1/5}$ plotted versus the impact number $P = WeRe^{-2/5}$. All the data shown in Fig. 1 and Fig. 2 are included. The error bars are the difference between the value from our simulations and the estimated values provided by the the scaling.

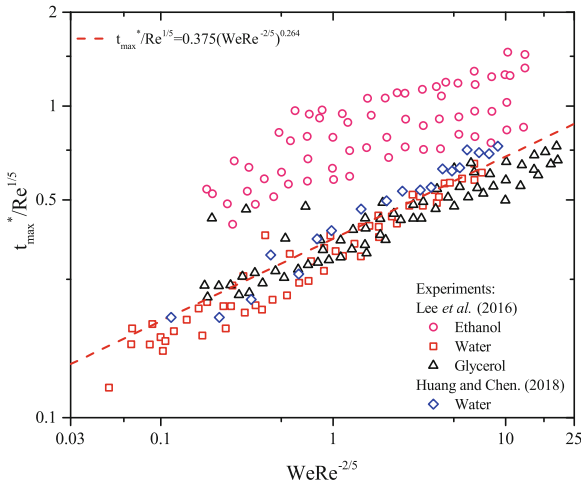


Fig. 4. Comparison between the scaling Eq. (5) (red dash line) and experimental results [7, 11] (hollow symbols) of dimensional spreading time t_{max}^* . (Color figure online)

tains a dynamic contact angle ranging from 41° to 63° and wets the surface. While the water and glycerol maintains an obtuse contact angle between 93° and 121° and are dynamically nonwetting. Huang and Chen (2018) measured the maximum spreading time of water droplet impacting onto parafilm surface

with contact angle $110^\circ \pm 7^\circ$ [7]. In Fig. 4, for clearness, we compare the scaling Eq. (5) observed from our simulations to the experimental results. The experimental results measured from, water and glycerol droplets impacting onto steel surfaces, and water droplets impacting onto parafilm, coincide into a line which follows the Eq. (5). The spreading time measured from ethanol droplets impacting on steel surface are higher than the ones obtained on hydrophobic surfaces. Lee et al. (2016b) concluded that ethanol's lower surface tension attributed to its higher maximum spreading time than the one of water and glycerol. While as the numerical simulations we performed have taken the effects of the variation of surface tension on spreading time into consideration, we draw the conclusion that the differences are caused by the different wettabilities.

3 Conclusions and Remarks

We postulate that for droplets impacting on non-wetting surfaces, the dimensionless spreading time t_{max}^* scales with no dependence on Reynolds number at lower Weber number ($We < 5$), while scales with $Re^{1/10}$ in the moderate Weber number regime $5 < We < 300$. The dimensionless maximum spreading time scales with the dependences of $We^{3/10}$ in the range of the Reynolds number, $Re < 300$. Inspired from the cross-over for ξ_{max} between capillary and viscous regimes, we found that the interpolation between $We^{1/2}$ and $Re^{1/5}$ provides a smooth cross-over for t_{max}^* as well. The scaling Eq. (5) obtained from droplets impacting on purely non-wetting surfaces fits well with experimental results obtained on hydrophobic surfaces (contact angle $\theta > 90^\circ$). For the experiments done on wetting surfaces, our prediction largely underestimates the maximum spreading time t_{max} . Based on this current work, a detailed study of the dependence of t_{max} on impact velocity, surface tension and dynamic viscosity could be carried out. A correlation between spreading time t_{max} and maximum spreading diameter D_{max} could be found, which could be used in improving the accuracy of the calculation of dissipation work, then the analytical models predicting maximum spreading diameter based on energy conservation.

References

1. Chandra, S., Avedisian, C.T.: On the collision of a droplet with a solid surface. Proc. Roy. Soc. Lond. Math. Phys. Eng. Sci. **432**, 13–41 (1991). <https://doi.org/10.1098/rspa.1991.0002>
2. Clanet, C., Béguin, C., Richard, D., Quéré, D.: Maximal deformation of an impacting drop. J. Fluid Mech. **517**, 199–208 (2004). <https://doi.org/10.1017/S0022112004000904>
3. Dhiman, R., McDonald, A.G., Chandra, S.: Predicting splat morphology in a thermal spray process. Surf. Coat. Technol. **201**(18), 7789–7801 (2007). <https://doi.org/10.1016/j.surfcoat.2007.03.010>
4. Gao, X., Li, R.: Spread and recoiling of liquid droplets impacting solid surfaces. AIChE J. **60**(7), 2683–2691 (2014). <https://doi.org/10.1002/aic.14440>

5. Ghafouri-Azar, R., Shakeri, S., Chandra, S., Mostaghimi, J.: Interactions between molten metal droplets impinging on a solid surface. *Int. J. Heat Mass Transf.* **46**(8), 1395–1407 (2003). [https://doi.org/10.1016/S0017-9310\(02\)00403-9](https://doi.org/10.1016/S0017-9310(02)00403-9)
6. Guillaument, R., Vincent, S., Caltagirone, J.P.: An original algorithm for VOF based method to handle wetting effect in multiphase flow simulation. *Mech. Res. Commun.* **63**, 26–32 (2015). <https://doi.org/10.1016/j.mechrescom.2014.11.002>
7. Huang, H.M., Chen, X.P.: Energetic analysis of drop's maximum spreading on solid surface with low impact speed. *Phys. Fluids* **30**(2), 022106 (2018). <https://doi.org/10.1063/1.5006439>
8. Josserand, C., Thoroddsen, S.T.: Droplet impact on a solid surface. *Annu. Rev. Fluid Mech.* **48**, 365–391 (2016). <https://doi.org/10.1146/annurev-fluid-122414-034401>
9. Laan, N., de Bruin, K.G., Bartolo, D., Josserand, C., Bonn, D.: Maximum diameter of impacting liquid droplets. *Phys. Rev. Appl.* **2**(4), 044018 (2014). <https://doi.org/10.1103/PhysRevApplied.2.044018>
10. Lee, J.B., Derome, D., Guyer, R., Carmeliet, J.: Modeling the maximum spreading of liquid droplets impacting wetting and nonwetting surfaces. *Langmuir* **32**(5), 1299–1308 (2016a). <https://doi.org/10.1021/acs.langmuir.5b04557>
11. Lee, J.B., et al.: Universal rescaling of drop impact on smooth and rough surfaces. *J. Fluid Mech.* **786**, R4 (2016b). <https://doi.org/10.1017/jfm.2015.620>
12. Madejski, J.: Solidification of droplets on a cold surface. *Int. J. Heat Mass Transf.* **19**(9), 1009–1013 (1976). [https://doi.org/10.1016/0017-9310\(76\)90183-6](https://doi.org/10.1016/0017-9310(76)90183-6)
13. Mao, T., Kuhn, D., Tran, H.: Spread and rebound of liquid droplets upon impact on flat surfaces. *AIChE J.* **43**, 2169–2179 (1997). <https://doi.org/10.1002/aic.690430903>
14. Pasandideh-Fard, M., Qiao, Y.M., Chandra, S., Mostaghimi, J.: Capillary effects during droplet impact on a solid surface. *Phys. Fluids* **8**(3), 650–659 (1996). <https://doi.org/10.1063/1.868850>
15. Roisman, I.V., Rioboo, R., Tropea, C.: Normal impact of a liquid drop on a dry surface: model for spreading and receding. *Proc. Roy. Soc. Lond. Math. Phys. Eng. Sci.* **458**(2022), 1411–1430 (2002). <https://doi.org/10.1098/rspa.2001.0923>
16. Ukiwe, C., Kwok, D.Y.: On the maximum spreading diameter of impacting droplets on well-prepared solid surfaces. *Langmuir* **21**(2), 666–673 (2005). <https://doi.org/10.1021/la0481288>
17. Vaikuntanathan, V., Sivakumar, D.: Maximum spreading of liquid drops impacting on groove-textured surfaces: effect of surface texture. *Langmuir* **32**(10), 2399–2409 (2016). <https://doi.org/10.1021/acs.langmuir.5b04639>
18. Visser, C.W., Tagawa, Y., Sun, C., Lohse, D.: Microdroplet impact at very high velocity. *Soft Matter* **8**(41), 10732–10737 (2012). <https://doi.org/10.1039/C2SM26323H>
19. Vincent, S., Randrianarivelo, T.N., Pianet, G., Caltagirone, J.P.: Local penalty methods for flows interacting with moving solids at high Reynolds numbers. *Comput. Fluids* **36**(5), 902–913 (2007). <https://doi.org/10.1016/j.compfluid.2006.04.006>
20. Vincent, S., Le Bot, C., Sarret, F., Meillot, E., Caltagirone, J.-P., Bianchi, L.: Penalty and Eulerian-Lagrangian VOF methods for impact and solidification of metal droplets plasma spray process. *Comput. Fluids* **113**, 32–41 (2015). <https://doi.org/10.1016/j.compfluid.2014.10.004>
21. Wirth, W., Storp, S., Jacobsen, W.: Mechanisms controlling leaf retention of agricultural spray solutions. *Pestic. Sci.* **33**, 411–420 (1991). <https://doi.org/10.1002/ps.2780330403>

22. Xu, Y., Vincent, S., He, Q.-C., Le-Quang, H.: Spread and recoil of liquid droplets impacting on solid surfaces with various wetting properties. *Surf. Coat. Technol.* **357**, 140–152 (2019). <https://doi.org/10.1016/j.surfcoat.2018.09.079>
23. Yarin, A.L.: Drop impact dynamics: Splashing, spreading, receding, bouncing. . . . *Annu. Rev. Fluid Mech.* **38**, 159–192 (2006). <https://doi.org/10.1146/annurev.fluid.38.050304.092144>

Author Index

A

Angot, Philippe, 3, 103

B

Batteux, Léa, 103

Bauer, Christian, 117

Belut, Emmanuel, 110

Bernard, Didier, 196

Bhatia, Harshit, 52

Bi, Désir-André Koffi, 144, 189

Boillod-Cerneux, France, 14

C

Caltagirone, Jean-Paul, 3

Calvin, Christophe, 14

Chénier, Éric, 144, 189

Couaillier, Vincent, 26

D

de la Llave Plata, Marta, 26

Delaby, Stéphane, 136

Dotto, Diego, 52

Dufresne, Yann, 150

E

Emilion, Richard, 196

G

Ganmbode, Paulin Sourou, 123

Guilmineau, Emmanuel, 130

H

Halim Atallah, Georges, 110, 202

He, Q.-C., 208

Herrmann, Marcus, 39

Herzog, Sebastian, 176

I

Ikardouchene, Syphax, 136

K

Kedelty, Dominic, 39

L

Laminie, Jacques, 103

Le Chenadec, Vincent, 80

Lechêne, Sullivan, 110

Le-Quang, H., 208

M

Marchioli, Cristian, 52

Masi, Enrica, 150

Mekkas, Anouar, 161

Moureau, Vincent, 150

N

Naddei, Fabio, 26

Nicolas, Xavier, 66, 123, 136

Nigmatova, Ainur, 150

O

Orlandi, Paolo, 123

Ould-Rouiss, Meryem, 123, 136

P

Pirker, Stefan, 169

Popinet, Stéphane, 80

Poulet, Pascal, [103](#)
Préa, Raphaël, [161](#)

R

Rubino, Ginevra, [130](#)

S

Saeedipour, Mahdi, [169](#), [183](#)
Sayadi, Taraneh, [80](#)
Schiepel, Daniel, [176](#)
Schneiderbauer, Simon, [183](#)
Simonin, Olivier, [150](#)
Sommerer, Yannick, [66](#)
Sun, Hua, [66](#)

T

Tavares, Mathilde, [144](#), [189](#)
Tossa, Adaté, [196](#)
Trouette, Benoît, [110](#), [202](#)

U

Uglietta, James, [39](#)

V

Verstappen, Roel, [91](#)
Vincent, Stéphane, [80](#), [110](#), [144](#), [169](#), [189](#), [202](#),
[208](#)
Visonneau, Michel, [130](#)

W

Wagner, Claus, [117](#), [176](#)

X

Xu, Yang, [208](#)

Z

Zaleski, Stéphane, [80](#)